Inference of global methane emissions from oil and gas production

Thesis by
Ariana Linnae Tribby

In Partial Fulfillment of the Requirements for the Degree of
Doctor of Philosophy

CALIFORNIA INSTITUTE OF TECHNOLOGY
Pasadena, California

2023
Defended June 1, 2023

Ariana L. Tribby
ORCID: 0000-0002-6435-4575

ABSTRACT

Atmospheric methane plays a significant role in warming the climate. Characterizing its sources and sinks is important for future climate and air quality impacts. Global methane background trends suggest a sustained increase in emissions since 2007. There is no debate that reducing anthropogenic (human-driven) emissions can lead to short-term decreases in atmospheric methane, posing an attractive avenue towards mitigating climate change. Yet, effective policy to limit emissions from energy-related activities relies on accurate emission estimates, and historically, it has been challenging to diagnose both the magnitude and origin of methane leaks from a wide range of facilities and components across production, transmission, storage, and distribution systems. We present a novel Bayesian hierarchical model to improve methane emission estimates on global and regional scales from oil and gas processes. We also present methods to optimize time and cost of model simulations of certain trace gases, including several of which have important climate implications. Finally, we present our efforts in characterizing fossil methane from burgeoning oil production in Oklahoma and Texas using long term ground-based remote-sensing observations combined with Stochastic Time-Inverted Larangian Transport modeling.

PUBLISHED CONTENT AND CONTRIBUTIONS

Tribby, A. L.; Bois, J. S.; Montzka, S. A.; Atlas, E. L.; Vimont, I.; Lan, X.; Tans, P. P.; Elkins, J. W.; Blake, D. R.; Wennberg, P. O. Hydrocarbon Tracers Suggest Methane Emissions from Fossil Sources Occur Predominately Before Gas Processing and That Petroleum Plays Are a Significant Source. *Environ. Sci. Technol.* **2022**, acs.est.2c00927. https://doi.org/10.1021/acs.est.2c00927.

A.L.T. performed research, analyzed data, and wrote the manuscript.

Tribby, A.L.; Wennberg, P.O. An analysis coordinate transform to facilitate use of in-situ aircraft observations for flux estimation. *In preparation for submission to Atmospheric Measurement Techniques.*

A.L.T. performed research, analyzed data, and wrote the manuscript.

Tribby, A.L.; Wu, Dien; Laughner, J.L.; Parker, H.A; Wennberg, P.O. Towards constraining methane emissions in southern Oklahoma using STILT analysis of remote sensing and flask observations of hydrocarbon tracers. *In preparation for submission to Atmospheric Chemistry & Physics.*

A.L.T. performed research, analyzed data, and wrote the manuscript.

TABLE OF CONTENTS

LIST OF FIGURES

Number *Page*

LIST OF TABLES

Number *Page*

Chapter 1

INTRODUCTION

1.1 Recent trends in atmospheric methane

The atmospheric surface concentration of methane (CH_4) is almost 3 times greater than its pre-industrial value.[1,2] CH_4 has a stronger global warming potential compared to CO_2, and despite having a shorter lifetime, has played a significant role in warming the climate: CH_4 has contributed about 23% to the additional radiative forcing that has accumulated in the lower atmosphere since 1750.[3] In addition to its radiative effects, CH_4 impacts background tropospheric ozone levels and the amount of stratospheric water vapor. As such, characterizing the sources and sinks of CH_4 is critical for future climate and air quality impacts.

While in situ measurements of atmospheric CH_4 are highly accurate (Figure 1), processes behind these global trends remains uncertain. There is no debate that humans have caused of the bulk of the rise in atmospheric CH_4 from preindustrial times. However, characterization of the reason for the stabilization from 1998 to 2007 and the acceleration in global CH_4 since has proved difficult. Indeed, it has been suggested that the change in observed growth rate may, in part, reflect changes in changes in the CH_4 atmospheric lifetime rather than simply changes in emissions.[4]

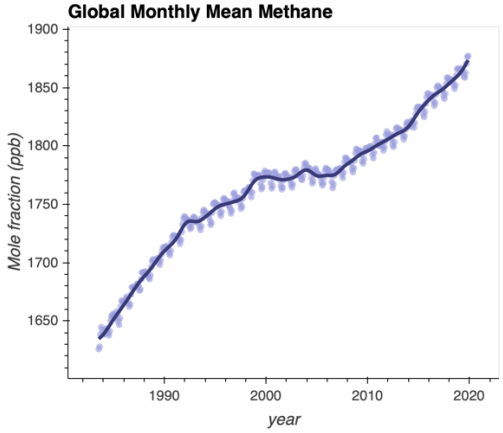

Figure a. Methane atmospheric "background" mole fraction rising worldwide. Data provided by NOAA.[2]

Nonetheless, the acceleration since 2007 unambiguously suggests a sustained increase in emissions.

Global sources of CH_4 include both natural and human-caused sources, including wetlands, fossil fuels (production, storage, transport, and incomplete combustion of oil/gas and coal), agriculture (livestock and rice cultivation), landfills and fires.[1] Globally, estimates of total CH_4 emissions are relatively certain at 572 Tg/year, of which 50-65% are attributed to anthropogenic sources.[1] Relative to the anthropogenic sector, fossil fuels are thought to make up about 35% of CH_4 emissions, while agriculture and waste are estimated at about 60%, and biomass burning at 10% from a bottom-up perspective.[1] While regional and sector emissions remain very uncertain, there is no debate that reducing anthropogenic (human-driven) emissions can lead to short-term decreases in atmospheric CH_4.

1.2 Methane Emissions from Fossil Energy

Not only do fossil fuels constitute a significant fraction of human-influenced CH_4 emissions, but a wide variety of technologies already exist to reduce such emissions from oil and gas operations; IEA estimates that almost 50% of these emissions could be avoided at zero net cost.[5] Thus, reducing uncertainty in CH_4 emission inventories to effectively reduce CH_4 emissions surrounding the energy sector presents an attractive avenue to mitigate climate change. Yet, effective policy to limit emissions from oil and gas activities relies on accurate emission estimates. Historically, it has been challenging to diagnose both the magnitude and location of emissions from a wide range of facilities and components across production, transmission, storage, and distribution systems. Past studies have generated conflicting claims about the magnitude or origin of emissions, such that top-down estimates (estimates derived from large-scale atmospheric observations) often exceed bottom-up estimates (totals based on facility-scale emission inventories). Recent work has found that divergent estimates can be largely attributed to a skewed distribution of emissions,[6] where a small number of extreme leaks account for the majority of emissions.[7–10] Recently, bottom-up[11,12] and top-down[13,14] studies have found that the majority of fossil CH_4 leaks occur mainly during the production process through planned venting/flaring and unintended leakage, with a smaller fraction originating from downstream processes such as separation, storage, and transportation. Venting and flaring of natural gas depends on many factors, including lack of proximity to a commercial market and lack of infrastructure.[15] The latter is often a challenge in burgeoning oil production sites where the value of oil can outweigh the associated natural gas byproduct, resulting in low prices for natural gas and increased venting or flaring of excess gas.

1.3 Fossil Methane Emission Monitoring

Space-based monitoring has come a long way over the years and will be invaluable for quickly identifying super-emitter leaks and increase transparency of facility-wide processes.[16] However, at this point in time, space-based monitoring is best-suited for diagnosing super-emitters rather than small-moderate leaks. Generally, this method cannot resolve point sources smaller than facility-

wide scale.[17] For this reason, ground-based monitoring is still important. There are many types of low-cost instrumentation (near infrared laser absorption spectroscopy, direct absorption mid-IR spectroscopy, metal oxide sensors) that can be mounted on stationary towers or drones that effectively capture small to moderate CH_4 emissions.[18] A widely-used method to apportion CH_4 flux is to measure atmospheric molecules that are co-emitted with CH_4 from source processes. For example, ethane (C_2H_6) is the second most abundant component of natural gas besides CH_4, but unlike CH_4, it does not have a biogenic origin, singling out CH_4 from fossil activities.

Despite being a widely used tracer for fossil activities, interpreting changes in C_2H_6 is complicated,[19,20] discussed in more detail in Chapter 2. In Chapter 2, I provide compelling evidence that propane (C_3H_8), another abundant component of natural gas, can serve as an effective tracer for production emissions from the oil and gas sector. There are few studies that characterize atmospheric trends of C_3H_8, and even fewer that attempt to quantify its emissions. Therefore, the focus of this thesis is diagnosing CH_4 emissions from oil and gas production using C_3H_8 as a tracer in addition to C_2H_6.

1.4 Thesis Overview

The work included in this thesis details my efforts to estimate global and regional fossil CH_4 emissions. In Chapter 2 (published in ES&T), I develop a novel Bayesian hierarchical model to improve global C_3H_8, C_2H_6, and CH_4 emission estimates from energy production. Chapter 3 (in preparation for submission to AMT) expands on the methods used in Chapter 2 to illustrate how using potential temperature as a diagnostic coordinate is useful for comparing observations with chemical transport models, enabling use of much lower spatial resolution, and therefore, much less costly simulations. Chapter 4 (in preparation for submission to ACP) details my initial effort to characterize fossil CH_4 emissions in Oklahoma and Texas using long term ground-based remote-sensing observations combined with Stochastic Time-Inverted Lagrangian Transport modeling.

References

(1) Saunois, M.; Stavert, A. R.; Poulter, B.; Bousquet, P.; Canadell, J. G.; Jackson, R. B.; Raymond, P. A.; Dlugokencky, E. J.; Houweling, S.; Patra, P. K.; Ciais, P.; Arora, V. K.; Bastviken, D.; Bergamaschi, P.; Blake, D. R.; Brailsford, G.; Bruhwiler, L.; Carlson, K. M.; Carrol, M.; Castaldi, S.; Chandra, N.; Crevoisier, C.; Crill, P. M.; Covey, K.; Curry, C. L.; Etiope, G.; Frankenberg, C.; Gedney, N.; Hegglin, M. I.; Höglund-Isaksson, L.; Hugelius, G.; Ishizawa, M.; Ito, A.; Janssens-Maenhout, G.; Jensen, K. M.; Joos, F.; Kleinen, T.; Krummel, P. B.; Langenfelds, R. L.; Laruelle, G. G.; Liu, L.; Machida, T.; Maksyutov, S.; McDonald, K. C.; McNorton, J.; Miller, P. A.; Melton, J. R.; Morino, I.; Müller, J.; Murguia-Flores, F.; Naik, V.; Niwa, Y.; Noce, S.; O'Doherty, S.; Parker, R. J.; Peng, C.; Peng, S.; Peters, G. P.; Prigent, C.; Prinn, R.; Ramonet, M.; Regnier, P.; Riley, W. J.; Rosentreter, J. A.; Segers, A.; Simpson, I. J.; Shi, H.; Smith, S. J.; Steele, L. P.; Thornton, B. F.; Tian, H.; Tohjima, Y.; Tubiello, F. N.; Tsuruta, A.; Viovy, N.; Voulgarakis, A.; Weber, T. S.; van Weele, M.; van der Werf, G. R.; Weiss, R. F.; Worthy, D.; Wunch, D.; Yin, Y.; Yoshida, Y.; Zhang, W.; Zhang, Z.; Zhao, Y.; Zheng, B.; Zhu, Q.; Zhu, Q.;

Zhuang, Q. The Global Methane Budget 2000–2017. *Earth Syst. Sci. Data* **2020**, *12* (3), 1561–1623. https://doi.org/10.5194/essd-12-1561-2020.
(2) Dlugokencky, E. J.; Lang, P. M.; Crotwell, A. M.; Mund, J. W.; Crotwell, M. J.; Thoning, K. W. Atmospheric Methane Dry Air Mole Fractions from the NOAA ESRL Carbon Cycle Cooperative Global Air Sampling Network, 1983-2017, Version: 2018-08-01, 2018. ftp://aftp.cmdl.noaa.gov/data/trace_gases/ch4/flask/surface/.
(3) Etminan, M.; Myhre, G.; Highwood, E. J.; Shine, K. P. Radiative Forcing of Carbon Dioxide, Methane, and Nitrous Oxide: A Significant Revision of the Methane Radiative Forcing: Greenhouse Gas Radiative Forcing. *Geophys. Res. Lett.* **2016**, *43* (24), 12,614-12,623. https://doi.org/10.1002/2016GL071930.
(4) Turner, A. J.; Frankenberg, C.; Kort, E. A. Interpreting Contemporary Trends in Atmospheric Methane. *Proc. Natl. Acad. Sci.* **2019**, 201814297. https://doi.org/10.1073/pnas.1814297116.
(5) IEA. Methane Tracker Database: Interactive Database of Country and Regional Estimates for Methane Emissions and Abatement Options, 2021. https://www.iea.org/articles/methane-tracker-database#sources.
(6) Zavala-Araiza, D.; Lyon, D. R.; Alvarez, R. A.; Davis, K. J.; Harriss, R.; Herndon, S. C.; Karion, A.; Kort, E. A.; Lamb, B. K.; Lan, X.; Marchese, A. J.; Pacala, S. W.; Robinson, A. L.; Shepson, P. B.; Sweeney, C.; Talbot, R.; Townsend-Small, A.; Yacovitch, T. I.; Zimmerle, D. J.; Hamburg, S. P. Reconciling Divergent Estimates of Oil and Gas Methane Emissions. *Proc. Natl. Acad. Sci.* **2015**, 201522126. https://doi.org/10.1073/pnas.1522126112.
(7) Zavala-Araiza, D.; Alvarez, R. A.; Lyon, D. R.; Allen, D. T.; Marchese, A. J.; Zimmerle, D. J.; Hamburg, S. P. Super-Emitters in Natural Gas Infrastructure Are Caused by Abnormal Process Conditions. *Nat. Commun.* **2017**, *8*, 14012. https://doi.org/10.1038/ncomms14012.
(8) Caulton, D. R.; Lu, J. M.; Lane, H. M.; Buchholz, B.; Fitts, J. P.; Golston, L. M.; Guo, X.; Li, Q.; McSpiritt, J.; Pan, D.; Wendt, L.; Bou-Zeid, E.; Zondlo, M. A. Importance of Superemitter Natural Gas Well Pads in the Marcellus Shale. *Environ. Sci. Technol.* **2019**, *53* (9), 4747–4754. https://doi.org/10.1021/acs.est.8b06965.
(9) Omara, M.; Zimmerman, N.; Sullivan, M. R.; Li, X.; Ellis, A.; Cesa, R.; Subramanian, R.; Presto, A. A.; Robinson, A. L. Methane Emissions from Natural Gas Production Sites in the United States: Data Synthesis and National Estimate. *Environ. Sci. Technol.* **2018**, *52* (21), 12915–12925. https://doi.org/10.1021/acs.est.8b03535.
(10) Brandt, A. R.; Heath, G. A.; Cooley, D. Methane Leaks from Natural Gas Systems Follow Extreme Distributions. *Environ. Sci. Technol.* **2016**, *50* (22), 12512–12520. https://doi.org/10.1021/acs.est.6b04303.
(11) IPCC. *2006 IPCC Guidelines for National Greenhouse Gas Inventories*; Report; Prepared by the National Greenhouse Gas Inventories Programme, 2006.
(12) Höglund-Isaksson, L. Bottom-up Simulations of Methane and Ethane Emissions from Global Oil and Gas Systems 1980 to 2012. *Environ. Res. Lett.* **2017**, *12* (2), 024007. https://doi.org/10.1088/1748-9326/aa583e.
(13) Alvarez, R. A.; Zavala-Araiza, D.; Lyon, D. R.; Allen, D. T.; Barkley, Z. R.; Brandt, A. R.; Davis, K. J.; Herndon, S. C.; Jacob, D. J.; Karion, A.; Kort, E. A.; Lamb, B. K.; Lauvaux, T.; Maasakkers, J. D.; Marchese, A. J.; Omara, M.; Pacala, S. W.; Peischl, J.; Robinson, A. L.; Shepson, P. B.; Sweeney, C.; Townsend-Small, A.; Wofsy, S. C.; Hamburg, S. P. Assessment of Methane Emissions from the U.S. Oil and Gas Supply Chain. *Science* **2018**, eaar7204. https://doi.org/10.1126/science.aar7204.

(14) Tribby, A. L.; Bois, J. S.; Montzka, S. A.; Atlas, E. L.; Vimont, I.; Lan, X.; Tans, P. P.; Elkins, J. W.; Blake, D. R.; Wennberg, P. O. Hydrocarbon Tracers Suggest Methane Emissions from Fossil Sources Occur Predominately Before Gas Processing and That Petroleum Plays Are a Significant Source. *Environ. Sci. Technol.* **2022**, acs.est.2c00927. https://doi.org/10.1021/acs.est.2c00927.
(15) International Energy Agency, (IEA). Flaring Emissions, 2020. https://www.iea.org/reports/flaring-emissions.
(16) Irakulis-Loitxate, I.; Guanter, L.; Liu, Y.-N.; Varon, D. J.; Maasakkers, J. D.; Zhang, Y.; Chulakadabba, A.; Wofsy, S. C.; Thorpe, A. K.; Duren, R. M.; Frankenberg, C.; Lyon, D. R.; Hmiel, B.; Cusworth, D. H.; Zhang, Y.; Segl, K.; Gorroño, J.; Sánchez-García, E.; Sulprizio, M. P.; Cao, K.; Zhu, H.; Liang, J.; Li, X.; Aben, I.; Jacob, D. J. Satellite-Based Survey of Extreme Methane Emissions in the Permian Basin. *Sci. Adv.* **2021**, *7* (27), eabf4507. https://doi.org/10.1126/sciadv.abf4507.
(17) Cusworth, D. H.; Jacob, D. J.; Varon, D. J.; Chan Miller, C.; Liu, X.; Chance, K.; Thorpe, A. K.; Duren, R. M.; Miller, C. E.; Thompson, D. R.; Frankenberg, C.; Guanter, L.; Randles, C. A. Potential of Next-Generation Imaging Spectrometers to Detect and Quantify Methane Point Sources from Space. *Atmospheric Meas. Tech.* **2019**, *12* (10), 5655–5668. https://doi.org/10.5194/amt-12-5655-2019.
(18) Torres, V. M.; Sullivan, D. W.; He'Bert, E.; Spinhirne, J.; Modi, M.; Allen, D. T. *Field Inter-Comparison of Low-Cost Sensors for Monitoring Methane Emissions from Oil and Gas Production Operations*; preprint; Gases/In Situ Measurement/Validation and Intercomparisons, 2022. https://doi.org/10.5194/amt-2022-24.
(19) Turner, A. J.; Frankenberg, C.; Wennberg, P. O.; Jacob, D. J. Ambiguity in the Causes for Decadal Trends in Atmospheric Methane and Hydroxyl. *Proc. Natl. Acad. Sci.* **2017**, *114* (21), 5367–5372. https://doi.org/10.1073/pnas.1616020114.
(20) Kort, E. A.; Smith, M. L.; Murray, L. T.; Gvakharia, A.; Brandt, A. R.; Peischl, J.; Ryerson, T. B.; Sweeney, C.; Travis, K. Fugitive Emissions from the Bakken Shale Illustrate Role of Shale Production in Global Ethane Shift: Ethane Emissions From the Bakken Shale. *Geophys. Res. Lett.* **2016**, *43* (9), 4617–4623. https://doi.org/10.1002/2016GL068703.
(21) Xiao, Y.; Logan, J. A.; Jacob, D. J.; Hudman, R. C.; Yantosca, R.; Blake, D. R. Global Budget of Ethane and Regional Constraints on U.S. Sources. *J. Geophys. Res.* **2008**, *113* (D21). https://doi.org/10.1029/2007JD009415.
(22) Frankenberg, C.; Kulawik, S. S.; Wofsy, S. C.; Chevallier, F.; Daube, B.; Kort, E. A.; O'Dell, C.; Olsen, E. T.; Osterman, G. Using Airborne HIAPER Pole-to-Pole Observations (HIPPO) to Evaluate Model and Remote Sensing Estimates of Atmospheric Carbon Dioxide. *Atmospheric Chem. Phys.* **2016**, *16* (12), 7867–7878. https://doi.org/10.5194/acp-16-7867-2016.
(23) Wofsy, S. C.; the HIPPO Science Team and Cooperating Modellers and Satellite Teams. HIAPER Pole-to-Pole Observations (HIPPO): Fine-Grained, Global-Scale Measurements of Climatically Important Atmospheric Gases and Aerosols. *Philos. Trans. R. Soc. Math. Phys. Eng. Sci.* **2011**, *369* (1943), 2073–2086. https://doi.org/10.1098/rsta.2010.0313.

Chapter 2

Hydrocarbon tracers suggest methane emissions from fossil sources occur predominately pre-gas processing and that petroleum plays are a significant source

Tribby, A. L.; Bois, J. S.; Montzka, S. A.; Atlas, E. L.; Vimont, I.; Lan, X.; Tans, P. P.; Elkins, J. W.; Blake, D. R.; Wennberg, P. O. Hydrocarbon Tracers Suggest Methane Emissions from Fossil Sources Occur Predominately Before Gas Processing and That Petroleum Plays Are a Significant Source. *Environ. Sci. Technol.* **2022**, acs.est.2c00927. https://doi.org/10.1021/acs.est.2c00927.

Abstract

We use global airborne observations of propane (C_3H_8) and ethane (C_2H_6) from the Atmospheric Tomography (ATom) and HIAPER Pole-to-Pole Observations (HIPPO), as well as US-based aircraft and tower observations by NOAA and from the NCAR FRAPPE campaign as tracers for emissions from oil and gas operations. To simulate global mole fraction fields for these gases, we update the default emissions configuration of C_3H_8 used by the global chemical transport model, GEOS-Chem v13.0.0, using a scaled C_2H_6 spatial proxy. With the updated emissions, simulations of both C_3H_8 and C_2H_6 using GEOS-Chem are in reasonable agreement with ATom and HIPPO observations, though the updated emissions fields underestimate C_3H_8 accumulation in the arctic wintertime pointing to additional sources of this gas in the high latitudes (e.g., Europe). Using a Bayesian hierarchical model, we estimate global emissions of C_2H_6 and C_3H_8 from fossil fuel production in 2016-2018 to be 13.3 $\pm$ 0.7 (95% CI) and 14.7 $\pm$ 0.8 (95% CI) Tg/year, respectively. We calculate bottom-up hydrocarbon emission ratios using basin composition measurements weighted by gas production, and find their magnitude is higher than expected and is similar to ratios informed by our revised alkane emissions. This suggests emissions are dominated by pre-gas processing activities in oil-producing basins.

2.1 Introduction

Many studies have diagnosed recent methane (CH_4) trends (both global and regional) using ethane (C_2H_6) atmospheric ratio signatures. However, the rejection of C_2H_6 by oil and gas producers (in the US, and presumably in countries following similar economic trends, Figure S1) results in an increase in the mole fraction of C_2H_6 in the natural gas pipelines. Thus, to the extent that losses occur in the pipelines and at the end users of natural gas, emissions of C_2H_6 may not necessarily directly reflect CH_4 emissions, adding additional uncertainty in CH_4 emission estimates from natural gas operations. In addition, a global uptick in hydraulic fracturing has shifted production

from dry to wet fields resulting in an increase in the ratios of both C_2H_6 and C_3H_8 to CH_4,[1] further complicating the use of the alkanes to diagnose the underlying CH_4 emission sources.[2–4]

Given the uncertainty in using C_2H_6 alone as a tracer for CH_4 emissions, we use both C_2H_6 and propane (C_3H_8) to diagnose whether significant CH_4 emissions from natural gas and petroleum occur pre-gas processing. Unlike C_2H_6, C_3H_8 has a much higher market value and therefore does not undergo "rejection."[5] Provided downstream losses are minimal and the raw gas ratio of C_3H_8 to CH_4 is known, C_3H_8 can provide a constraint for raw natural gas pre-gas processing CH_4 emissions.

In this study, we employ global observations from aircraft, including the 2009-2011 High-Performance Instrumented Airborne Platform for Environmental Research (HIAPER) Pole-to-Pole Observations (HIPPO)[6] and the 2016-2018 Atmospheric Tomography (ATom)[7] missions, which provide vertical profiles of a variety of constituents, including C_2H_6 and C_3H_8, around the remote atmospheres of the globe. Together with the large-scale chemical transport model GEOS-Chem, we estimate global fossil emissions of C_2H_6 and C_3H_8.

2.2 Materials and methods

Observations from the National Oceanic and Atmospheric Administration (NOAA) Global Monitoring Laboratory (GML)

Measurements of CH_4,[8–10] C_2H_6 and C_3H_8[11] from flask air collected by the NOAA GML tower[12] and aircraft[13] near oil/natural gas basins were used as pre-gas processing references. We refer to site locations using state abbreviations. More information on data processing/spatial coverage in included in Section S2, Table S1 and Figure S5. To better quantify geophysical variability and generate a confidence interval in the correlation between C_2H_6 and C_3H_8 mole fractions, we implement a pairs bootstrap to generate replicates of C_2H_6 and C_3H_8 observations. The CIs calculated from the bootstrapped samples are much broader than those calculated assuming the noise in the measurements is dominated by analytical errors. This suggests that geophysical noise induced by differences in transport and chemistry dominates the statistics. See Section S2.1 for more details.

FRAPPE Observations

FRAPPE C130 flight data were taken within the Colorado Front Range between July 26-August 19 2014. We accessed the data on October 6, 2021 from www-air.larc.nasa.gov from the WAS C130 merge file. Our data processing for FRAPPE is similar to our methods for the NOAA in situ samples. A spatial illustration of FRAPPE observations is shown in Figure S6.

HIAPER POLE-TO-POLE OBSERVATIONS (HIPPO) & ATMOSPHERIC TOMOGRAPHY (ATom) data

The HIPPO campaign was a sequence of five global measurement campaigns which sampled from near the North Pole to the coastal waters of Antarctica, covering different seasons between 2009 and 2011. Similarly, ATom took place from 2016 and 2018. Flight paths of HIPPO and ATom campaigns are illustrated in Figure S22 and specific details about the data sources are included in Section 3, SI.

Only data observed at > 20 degrees north was used since the majority of emissions of these short-lived gases of interest lie in the northern hemisphere. The lifetime of C_3H_8 and C_2H_6 are on the order of a few months or shorter during the summer, and the time it takes for mixing between the northern to southern hemispheres is on the order of a year,[14] so the mole fraction of these gases of interest is very low in the southern hemisphere.

Because C_2H_6 and C_3H_8 are relatively short-lived gases, their abundance in the stratosphere is low and poorly connected to the underlying fluxes. To exclude stratospheric observations, we use N_2O (Panther/UCATS instrument) which is inert and generally well-mixed in the troposphere, but is destroyed in the stratosphere by photolysis and reaction with O^1D.[15] Thus, we exclude from our analysis data with low N_2O mole fraction (Figure S23).

As our focus in this analysis is quantifying the global emissions of these gases, we exclude from our analysis data where local fluxes substantially influence the mole fraction of these alkanes. We use a simple land and altitude constraint, and HCN as a tracer to remove plumes from highly local sources (including both energy infrastructure and wildfires, Figure S24-26). We also exclude regions and times where the lifetime of the alkanes is very short and thus regional / local sources dominate the variance. Thus, we do not analyze the aircraft summer data (but results for the summer are shown in the SI) or data in the subtropics, where the alkane distribution is very sensitive to transport from the extratropics where most emissions of C_2H_6 and C_3H_8 originate. To exclude subtropical air, we only analyze measurements with tropopause pressure above 100 hPa (about 5% of the data was excluded under this constraint) for both ATom and HIPPO, which was sufficient to reduce the influence of tropical intrusions. See Table S1 for a comprehensive outline of the filters we use.

As in other studies,[16,17] we use potential temperature (θ, in units of Kelvin) in our analysis as a zonal coordinate. Potential temperature is conserved following adiabatic flow, and in the extra-tropics, variability within large-scale circulation can be well captured using this coordinate system. As a result, trace gases that have long lifetimes compared to synoptic-scale meteorology, which has a horizontal length scale of an order of 1000 kilometers or more and a timescale of about 10 days,[14,18] will be well correlated with θ. Using θ as a dynamical coordinate allows us to more accurately compare low spatial resolution GEOS-Chem simulations with the aircraft in situ measurements (compared with simply using altitude and latitude coordinates, Figure S27).

Potential temperature is not well-correlated with trace gases in the tropics or boundary layer, where moist convection and surface drag-driven turbulence can result in non-unique pairs, or when the photochemical lifetimes are short (summer).

GEOS-Chem Simulations

We simulated HIPPO and ATom measurements using the GEOS-Chem "classic" global 3-D chemical transport model with default settings (details about the simulations and emissions are provided in the SI, Section 4). We use the same constraints as the aircraft observations except we use a boundary layer height parameter. As described below, we use a Bayesian model to provide a best estimate for global emissions of C_2H_6 and C_3H_8 and their uncertainty. One contribution to the error estimate is transport errors in GEOS-Chem. To capture some of the uncertainty in the transport field, we sample the GEOS-Chem model several days before and after the in-situ sampling time along the aircraft flight path, which we refer to as "synoptic replicates." Finally, all GEOS-Chem simulations of C_3H_8 and C_2H_6 were interpolated on the vertical coordinate using θ to the aircraft measurements. As expected, GEOS-Chem synoptic replicates show less consistency in latitude (Figure S27), providing support for using θ as an analysis coordinate.

Bayesian Inference

We wish to quantify the global emissions of C_3H_8 and C_2H_6 using the observed mole fraction of these alkanes during ATom and HIPPO. The ambient mole fraction of C_3H_8 and C_2H_6 is most sensitive to their total northern hemisphere emissions during the winter/fall/spring when there is decreased sunlight/oxidation. As such, we assume differences between the GEOS-Chem simulations and the aircraft observations can be largely attributed to the underlying emissions grid, such that,

$$a = \mathrm{gcs} \cdot \alpha \qquad (1)$$

where a is the aircraft C_2H_6 or C_3H_8 mole fraction, gcs is the GEOS-Chem simulation of C_2H_6 or C_3H_8 mole fraction, and α is a scalar that represents the missing emissions of C_3H_8 and C_2H_6 from default emissions. We developed a Bayesian hierarchical model to estimate the missing emissions, where equation (1) forms the basis of our model. Our model only uses the GEOS-Chem simulated alkane mole fraction data (synoptic replicates), the alkane mole fractions observed by the aircraft, tropopause height, and UTC time. Our complete statistical model and its development, priors (Figure S37-41), as well as the software used, are included in the SI, section 5.

Hydrocarbon Percent Composition literature compilation and bootstrapping

We gather literature measurements of hydrocarbon composition from unprocessed gas from oil- and gas- producing basins in the U.S. and around globe to calculate emission ratios. Summary

statistics of the percent composition by region and the corresponding literature source is included in Table S4-5 (SI). Gas composition varies significantly across basins, so we perform bootstrap calculations for data samples within each basin separately. For each basin, we draw random pairs of hydrocarbon composition measurements (CH_4, C_2H_6, and C_3H_8) the size of the dataset, then take the mean and repeat this 10,000 times. We use these bootstrap samples in subsequent calculations (Equation 2), to arrive at emission ratios (Figure 6).

2.3 Results and discussion

CH_4 leaks from U.S. energy activities are dominated by pre-gas processing emissions

C_3H_8 and C_2H_6 are highly correlated at the NOAA sites (Figure 1). The data shown were obtained across 2-11 years and include tower and aircraft data (Table S1). The cross plot of C_3H_8 and C_2H_6 illustrate two distinct chemical regimes, similar to those described by Parrish et al. 2018.[19] Above 1 ppb C_3H_8, the distribution is nearly linear, consistent with the mixing of fresh non-photochemically aged emissions into the background atmosphere. At mole fractions below 1 ppb, a second regime is defined by mixing of the aged emissions (the lifetime of C_3H_8 is much less than that of C_2H_6). To explore the characteristics of pre-gas processing emissions, we study the ratio of these gases within the 50th highest percentile of C_3H_8 for the combined sites. Varying this demarcation $\pm$ 10% negligibly affects the linear fit (Figure S10). We find that the ratio of C_3H_8 to C_2H_6 in the linear regime to be [0.63, 0.70] (ppb/ppb, 95% CI), and FRAPPE observations show a similar trend at [0.76, 0.87] (Figure S9).

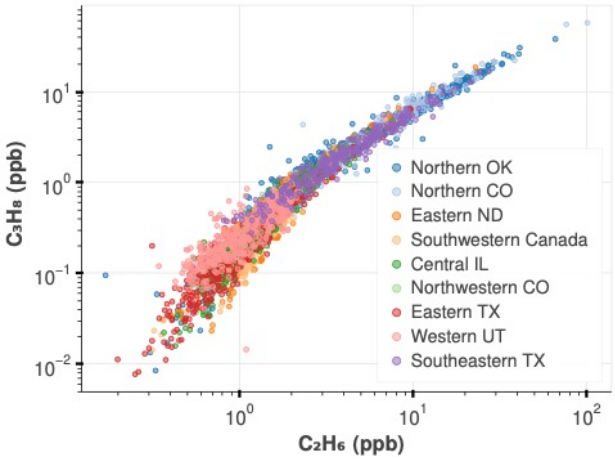

Figure 1. Measurements of C_2H_6 and C_3H_8 from ongoing NOAA GML tower and aircraft sites (Table S1) from 2005-2018. The data follow the photochemical aging distribution described in Parrish et al. 2018, where the data below 1 ppb C_3H_8 are affected by photochemically aged emissions and mixing processes. As such, we only study the ratio of these gases in the 50th highest percentile (everything above 1 ppb C_3H_8) that would indicate fresh emissions. After this filtering,

two sites, Northwestern CO and Western UT (site codes NWR and UTA), did not have any data in the fresh emission regime and are not included in further analysis (more detail in Figure S8).

Within the fresh emission chemical regime, the NOAA C_3H_8/C_2H_6 ratio changes minimally before and after 2012 ([0.62, 0.67] and [0.63, 0.71], respectively, ppb/ppb 95% CI, Figure S9) and over the entire timeseries (Figure S19). An unchanging C_3H_8/C_2H_6 ratio over time across the U.S. despite large changes in the C_3H_8/C_2H_6 ratio in processed gas during the same years (Figure S1), suggests that the majority of the alkane (and likely CH_4) emissions occur pre-gas processing when all the C_3H_8 and sometimes much of the C_2H_6 are separated from the raw gas. Conversely, post-gas processing (pipeline) composition of C_2H_6 at Playa del Rey in Southern California follows rejection trends, where the C_3H_8/C_2H_6 ratio has decreased by 8% from 2008 to 2018, and in recent years is about 18% lower in magnitude compared to the NOAA ratio (Figure S4). (Processed gas in California is a good representation of typical gas composition of domestic and globally-imported consumer-grade gas.[20]) Our results are in agreement with Rutherford et al. 2021's US-based model for CH_4 emissions, which finds that unintentional emissions from the production segment (namely, liquid storage tanks and other equipment leaks) are the largest contributors to divergence with the EPA's GHGI.[21]

We use the same chemical aging approach to construct a background for NOAA and FRAPPE CH_4 observations (Figure S7, S11). Since we only focus on the linear part of the chemical aging distribution, our analysis is not terribly sensitive to how the CH_4 anomaly is determined (it simply produces varying intercepts, Figure S10). Consistent with the analysis of Lan et al. 2019[2] (see Figure S20-21), the ratio of C_3H_8 and C_2H_6 to CH_4 has increased with time, reflecting a growing importance of oil exploration on CH_4 emissions in the US.

C_3H_8 demonstrates to be a useful tracer that constrains oil and gas related CH_4 emissions. Given that the fit of C_3H_8 vs CH_4 (and C_2H_6 vs CH_4) have similar precision over the whole record, using C_3H_8 as a tracer likely separated nearby competing non-oil and gas CH_4 emissions. However, if there were to be non-oil and gas CH_4 emissions that were spatially coherent to the NOAA observation sites, our C_3H_8 vs CH_4 and C_2H_6 vs CH_4 emission ratios would be impacted. Investigating and potentially separating spatially coherent emissions of non-fossil origins would be the topic of future studies.

NOAA observations at Oklahoma ARM site are especially impacted by nearby unprocessed gas emissions, as C_2H_6 and C_3H_8 correlations with CH_4 have less noise compared to other sites (Figure S12-13). While the ratios of C_3H_8 and C_2H_6 vs CH_4 have increased by 50% at NOAA Oklahoma site since 2010, we find that both C_2H_6 and C_3H_8 vs CH_4 ratios are fractionally increasing at the same rate (Figure 2). That the atmospheric C_2H_6 and C_3H_8 increase fractionally the same suggests that the ratio of the alkanes in the reservoirs producing these emissions do not change significantly over the time of this record. Below, we use the 2017 average C_3H_8/CH_4 and C_2H_6/CH_4 from NOAA Oklahoma site ([0.060, 0.061] ppb/ppb (C_2H_6/CH_4 is [0.086, 0.088], Figure S21) to compare our

emissions estimates for C_3H_8 and C_2H_6 to published estimates of CH_4 emissions from oil and gas exploration.

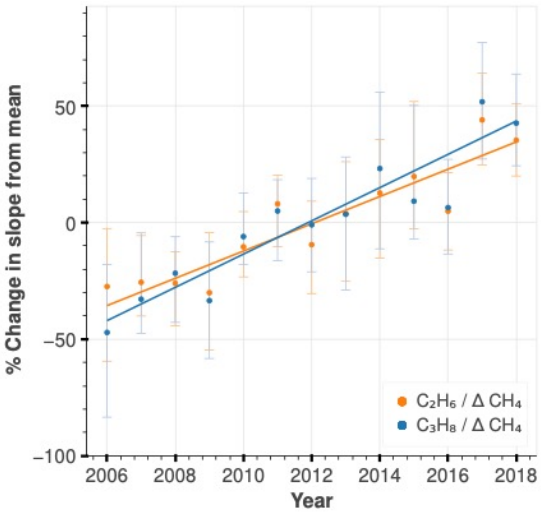

Figure 2. Yearly correlation between NOAA hydrocarbon vs CH_4 anomaly in Oklahoma**.** We show the percent change of anomalies/year with respect to the mean hydrocarbon and methane anomalies. The trend for C_3H_8/CH_4 is 7.13 $\pm$ 1.44 % with an R^2 of 0.71. The trend for C_2H_6/CH_4 is 5.87 $\pm$ 1.26 % with an R^2=0.69. The variability in the trend comes from the standard error of a linear regression. The variability in the individual points comes from the 95% confidence interval of a pairs bootstrap of the alkanes and CH_4 anomalies. (We ran a pairs bootstrap for co-measurements of C_3H_8 and ΔCH_4 and compute the slope of the correlation for each bootstrap sample and repeated this for every year in the data; please see the methods section). This trend in units of ppt/ppb/year is shown in Figure S21.

Default GEOS-Chem simulations underestimate C_3H_8 compared to aircraft observations

We compare the cross plot of C_3H_8 to C_2H_6 from the HIPPO and ATom aircraft measurements and GEOS-Chem simulations to the NOAA measurements (Figure 3). As expected, both the aircraft observations and GEOS-Chem simulations fall under the photochemically aged emissions part of the NOAA distribution. While the aircraft data overlay the NOAA measurements almost perfectly (especially in the winter when the lifetimes of both gases are longest), GEOS-Chem underestimates C_3H_8, particularly over the Atlantic curtain (Figure 3,4). The same conclusion is drawn for HIPPO time periods (Figure S31-32, S34). Because the atmospheric lifetimes of C_3H_8

and C_2H_6 are different and vary seasonally due to the much higher concentrations of OH in the summer, our estimate of global C_2H_6 and C_3H_8 emissions from GEOS-Chem comparisons are sensitive to the a priori spatial distribution of these emissions.

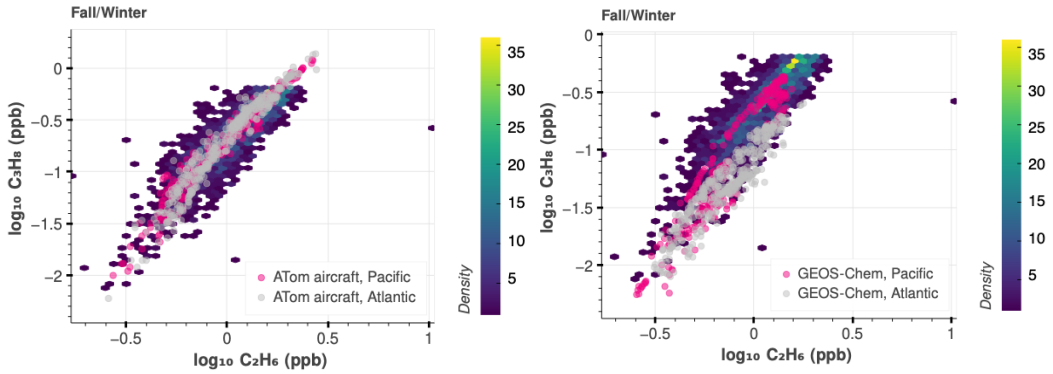

Figure 3. Comparison of C_3H_8 vs C_2H_6 for NOAA, ATom aircraft, and GEOS-Chem simulations during fall/winter seasons. NOAA photochemically-aged measurements (all sites, 2005-2018), as explained in the text, are shown on the heat map (colored by the number density of data). The spring/summer seasons are included in Figure S29-30, S33. HIPPO is shown in Figure S34.

Relative to C_2H_6, the default GEOS-Chem v13.0.0 C_3H_8 emissions result in a much larger underestimate of C_3H_8 mole fractions over the Atlantic transect compared to the Pacific (Figure 3,4) implying an underestimate over North America. This pattern is most clearly visible in the summer when the C_3H_8 lifetime is short. In contrast, the default C_2H_6 emissions produce a good simulation of the ATom data (within 5%) over both ocean basins (Figure 3,4). As such, we use the mean ratio observed in the linear regime of the NOAA data (0.67 C_3H_8/C_2H_6, ppb/ppb Figure S9) as the default global ratio of their emissions to update GEOS-Chem. In mass units (as used in the GEOS-Chem emissions), this is ≈ 0.99 kg C_3H_8 / kg C_2H_6. Given the remarkable coherence in both the large-scale fields from the aircraft over both the Atlantic and Pacific transects and in the NOAA data, the spatial distribution of the emissions ratios for both gases must be very similar upwind of the Pacific (e.g., Asia) and the Atlantic (North America). As such, in our revised emissions fields for C_3H_8, we simply used the default C_2H_6 emissions configuration used by GEOS-Chem v13.0.0. This scaling substantially altered the spatial distribution of C_3H_8 emissions (Figure S28). The effect on the C_3H_8 simulation is shown in Figure 4 using ATom 4 as an example, where updating the emissions resulted in a much better agreement between GEOS-Chem C_3H_8 and aircraft measurements (other campaigns are included in Figure S35-36). Although simulations are greatly improved using the revised emissions, it appears there is a missing high latitude source of C_3H_8 and C_2H_6 (Figure S47-48, S54-55).

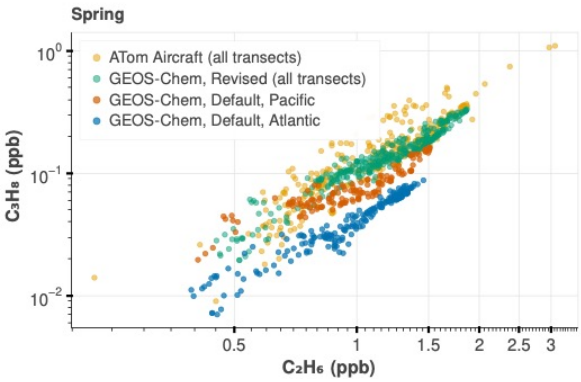

Figure 4. Impact of revised C_3H_8 emissions on GEOS-Chem simulation. Combined Pacific and Atlantic transects for ATom 4 aircraft campaign, which took place during Spring 2018, are shown in gold. The GEOS-Chem simulation using default C_3H_8 emissions are shown in blue and orange, referring to the Pacific and Atlantic transects, respectively. The GEOS-Chem simulation after implementing the revised C_3H_8 emissions is shown in green. The rest of the ATom campaigns are shown in Figure S36.

Bayesian model suggests decadal increase in global C_2H_6 and C_3H_8 anthropogenic fossil emissions

The results of our Bayesian inference were satisfactory. We had good sampling of our posterior and the sampling diagnostics were excellent (Figure S43-44, S50-51). We performed tests that verified our inference procedure could capture the ground truth (using simulated data for which the ground truth is known), and that our posterior was more concentrated around the ground truth than the prior (Figure S42). Furthermore, our model could generate the measured data reasonably well; the majority of the measured aircraft data fell into the 30th and 50th percentile of the simulated Bayesian model data (Figure S47-48, 54-55). The exception to this was the summer season, where the Bayesian model does not capture the measured aircraft data. This is expected, since during the summer we do not observe a robust relationship between potential temperature and C_3H_8 or C_2H_6. The model remained robust even when varying the sensitivity to low mole fractions of alkanes with tropical origin (Figure S58-60).

During ATom 2 (winter) Atlantic curtain, the GEOS-Chem simulations poorly capture the observed C_2H_6 and C_3H_8 at low potential temperature compared to the aircraft. These measurements are samples obtained at low altitude, high latitude, and cold temperatures (Figure S49). During the winter, these arctic airmasses are often characterized by stagnant conditions, with less mixing with the mid-latitudes.[22] As a result, emissions that occur at high latitudes during the winter can be trapped there unless the zonal flow is disrupted. Additionally, emissions of C_2H_6 and C_3H_8 near the arctic during the winter will oxidize more slowly relative to mid-latitudes due to the cold temperature and minimal sunlight. These conditions result in high C_2H_6 and C_3H_8 mole fraction over the arctic relative to remote mid-latitude chemical regimes. The measurements subject to arctic conditions during ATom were too few to make a substantial impact on the overall

Bayesian emissions estimate, but during HIPPO winter flights, few samples were obtained resulting in a large bias towards arctic data. We place much more weight on the ATom winter C_3H_8 analysis estimate of global C_3H_8 emissions since the arctic represents only a small fraction of the atmosphere.

It is likely that GEOS-Chem v13.0.0 is missing a high latitude emissions source (Figure S47-49, S54-55). Underestimation of C_3H_8 and C_2H_6 at high latitudes is consistent with other studies, which found fossil fuel emissions from Eurasia accounted for the largest underestimation.[23] It is possible that emissions from northern Europe may account for this discrepancy, as fossil emissions were found to be underestimated[23] and our revised C_3H_8 emissions decreased in that region after implementing the emission C_2H_6 proxy (Figure S28). This, combined with a relatively lower number of HIPPO aircraft observations at lower latitudes, results in a substantial positive bias on the overall Bayesian emissions estimate for C_3H_8 during winter 2009 (Figure S62).

We report our Bayesian estimates for each seasonal campaign and ocean transect during 2009-2011 and 2016-2018, and what the GEOS-Chem v13.0.0 default emissions grids should be scaled by, according to our analysis (Figure S45-46, S52-53, and SI section 5.8). We estimate global emissions of C_2H_6 and C_3H_8 from fossil fuel production from 2016-2018 to be 13.3 $\pm$ 0.7 (95% CI) and 14.7 $\pm$ 0.8 (95% CI) Tg/year, respectively. Our results compare well to other studies (Figure 5, Figure S62). Our estimates suggest emissions of C_2H_6 have increased by about 15% from 2010-2017 when comparing the mean revised C_2H_6 emissions during those time periods (Figure S61). Emissions of C_3H_8 are calculated to have increased more (65%, Figure S62), but this estimate is highly uncertain due to the few samples obtained during HIPPO and the impact of the Arctic winter pooling in both campaigns. Nevertheless, these increases are consistent with greater oil production emissions contribution. Similarly, Helmig et al. 2016, which used data from a global surface network and atmospheric column observations, found about a 22% increase in C_2H_6 emissions between 2009 and 2014.[24]

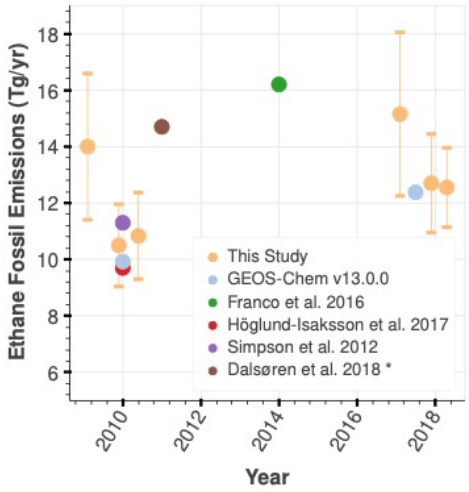

Figure 5. Global revised ethane anthropogenic fossil emissions compared to other studies. Our emissions estimate in 2016-2018 (during ATom) and 2009-2011 (during HIPPO) includes our revised emissions for winter, fall and spring seasons that we determined with our Bayesian model during each season. As discussed in the text, fewer samples were obtained during HIPPO, resulting in a sampling bias that we test by restricting observations and simulations to ± 300K potential temperature (Figure S56-S57). This test affects the estimate about ± 1 Tg during 2010-2011, but affects our estimate by up to 12 Tg in 2009. We compare our revised emissions to the default emissions from GEOS-Chem v13.0.0. The studies included here[23,25–27] represent anthropogenic fossil emissions, except Dalsøren et al. 2018 which also includes biofuel, agriculture, and waste. We obtained the CEDS CMIP6 estimate from Dalsøren et al. 2018. Our emissions estimates do not include biomass burning or biofuels. Propane emissions are included in Figure S62.

Oil exploration plays a more significant role in global CH_4 compared to dry gas

We calculate an emission ratio of C_3H_8/CH_4 for n basins or countries using the following equation,

$$E\left(\frac{C_3}{C_1}\right) = \sum_{i=1}^{n}\left(\left(\frac{P_{DNG_i} * {C_{1_i}}/{tot_i}}{P_{DNG^*} {C_1}/{tot}}\right)\left(\frac{C_{3i}}{C_{1i}}\right)\right) \quad (2)$$

where P_{DNG} is the dry natural gas production (in million tonnes), C_1 and C_3 are the bootstrapped samples of measured hydrocarbon fractions in raw natural gas samples (in mass %, details on the bootstrapping in the methods section), and tot is the sum of the bootstrapped samples of measured hydrocarbon fractions for CH_4, C_2H_6, and C_3H_8. (Note that our $E\left(\frac{C_3}{C_1}\right)$ emission ratios are inherently

weighted by natural gas production by basin, P_{DNG}.) $E\left(\frac{C_2}{C_1}\right)$ is calculated similarly. We refer to the emission ratio in Equation 2 as the "literature" emission ratio, since we combine a variety of natural gas composition measurements for wet and dry basins. We calculate a global literature emission ratio using hydrocarbon and dry natural gas production data from the top 5 producing natural gas basins around the world that made up 50% of the total natural gas production in 2019.[28,29] We also calculate a U.S. literature emission ratio using the top 7 natural gas producing basins that account for 86% of total U.S. natural gas production.[30,31] We show the relative production of the top global and U.S. basins used in our analysis in Figure S3. Additional summary statistics and sources for the composition measurements are included in Table S4-S5.

Separately, we calculate an "observationally informed emission ratio (OIER)" by taking the ratio between our revised C_3H_8 emissions with literature estimates of CH_4 emissions from oil and natural gas processes. The OIER for C_2H_6/CH_4 is calculated similarly. Previous studies have constrained global CH_4 emissions from Natural Gas/Petroleum systems to range from 63 – 91 Tg/yr.[25,32–37] Given our estimate for revised C_2H_6 and C_3H_8 emissions, this implies a mean alkane ratio of 100:[8.0, 10.0]:[6.5, 7.3] molar % (CH_4:C_2H_6:C_3H_8) in 2016-2018. We compare our literature ratio with several OIER using global estimates in Figure 6 and with U.S. estimates in Figure S63. The small abundance of spatial and temporal literature measurements of raw gas composition throughout basins most affect the final uncertainty in the emission ratio comparison.

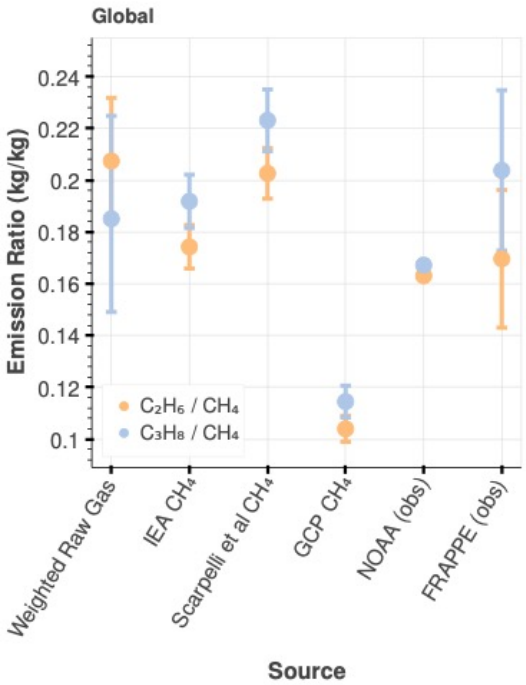

Figure 6. Global Literature and Observationally Informed Emission ratios (OIER) C_3H_8/CH_4 and C_2H_6/CH_4. The "weighted raw gas ratio" in the figure represents the "literature ratio" described in

the text, calculated using Equation 2. OIER, ratios between our revised C_2H_6 and C_3H_8 emissions and literature CH_4 emission estimates, are shown for several literature CH_4 estimates, including IEA 2021 (76.4 Tg/yr)[34], Scarpelli et al. 2020 (65.7 Tg/yr)[33], and Global Carbon Project 2020 bottom-up estimate (128 Tg/yr, 2008-2017 average)[32]. The variability in the literature ratio is attributed to the 95% CI of pairs bootstrap samples of hydrocarbon composition measurements (see text for more detail). The variability in the OIER is attributed to the 95% CI of our revised C_3H_8 and C_2H_6 emission estimates. We also compare C_3H_8/CH_4 and C_2H_6/CH_4 correlations from in-situ observations, including NOAA observations from Northern Oklahoma (2017 average from Figure S21, units of kg/kg) and FRAPPE observations from Northern Colorado (2014 from Figure S9, units of kg/kg). The variability in the NOAA ratio is relatively low because it is calculated from a multi-year average slope, and the error in the slope is low (see Figure S21, left). The variability in the FRAPPE ratio is relatively high because we use the 95% CI derived directly from our bootstrap samples, as described in the methods section.

Unprocessed dry gas has a smaller C_3H_8/CH_4 and C_2H_6/CH_4 ratio compared to unprocessed associated gas from oil-producing basins ("wet" gas). A greater contribution of emissions from dry basins would decrease the magnitude of the overall literature ratio, assuming minimal C_3H_8 leakage after separation from raw gas, given the high market value of C_3H_8. In the U.S., the basin with the highest gas production is the Appalachian (East Coast) (Figure S3). If CH_4 leaks were proportional to production, we would expect a "dry" (small) emission ratio that resembles the composition of the Appalachian region (6% mass/mass, calculated from Table S3). However, we find the production-weighted ratio to be much larger than expected (15%, Figure S63). The second-largest gas producing region, the Permian (Southwestern US), is also the largest oil producer in the U.S. and vastly overpowers the Appalachian in terms of oil production (Figure S3). The magnitude of our production-weighted raw gas "literature" emission ratios suggest a significant contribution from wet gas and emissions that are biased towards oil-producing basins. We find similar results for global emission ratios (Figure 6).

The Global Carbon Project CH_4 emissions estimate implies an OIER that is dry relative to the production-weighted raw gas ratio (literature ratio), Figure 6. Instead, the IEA (76 Tg/yr) and Scarpelli et al. 2016 (66 Tg/yr) CH_4 emissions estimates yield an OIER that is within a few percent of the production-weighted raw gas literature ratio, given our revised C_3H_8 and C_2H_6 emissions. Both of those studies estimate oil production emissions to have a relatively higher contribution to the global footprint compared to dry gas production.

The FRAPPE and NOAA Oklahoma observed emission ratios compare well to the global OIER (Figure 6) and U.S. OIER (Figure S63), suggesting high emissions from oil production. Indeed, there are substantial oil production activities (Figure S15-18) surrounding the NOAA Oklahoma and FRAPPE observation sites. Increasing tends in the Oklahoma emission ratios are consistent with production trends: oil production in Oklahoma tripled from 2010 to 2017[38,39] (compared to doubling of gas production) and in 2020, Oklahoma was the fourth-largest oil producer in the U.S.[40] (Note that Oklahoma was not included in calculations for the literature ratio, since

Oklahoma natural gas production does not rank in the top 7.) Several factors may reduce incentive or ability for oil producers to capture associated natural gas byproducts, including low market prices and lagging pipeline infrastructure.[41]

Since our findings suggest that CH_4 losses are likely greater and biased towards oil-producing sites, a significant fraction of bottom-up estimates of CH_4 emissions may be misallocated to dry CH_4 production, when they should instead be included with the oil production sector. Correctly attributing CH_4 emissions to oil production would increase the greenhouse gas footprint of petroleum-based transportation, while decreasing the greenhouse gas emissions ascribed to natural gas-powered power plants. At a minimum, the CO_2 equivalent footprint of the global transportation sector would increase by roughly 5%, using IEA's estimate of 76 Tg/year CH_4 emissions from oil and natural gas and recent transportation CO_2 emission estimates (Section 6.4, SI).[36,42] This estimate will only increase when accounting for vented and flared losses of associated natural gas that is not accounted for in marketed associated gas (which we use to calculate these numbers).

ACKNOWLEDGMENTS

This work was supported by the Resnick Sustainability Institute, including computations conducted in the Resnick High Performance Computing Center. A.L.T. received funding from NSF award No. DGE-1745301.

NOAA support was provided for HIPPO by NSF award no. AGS-0628452; California Institute of Technology support for ATom was provided by NASA grant award No. NNX15AG61A. NOAA support for ATom was provided by NASA EVS2 award No. NNH17AE26I; additional support was provided by NASA Upper Atmosphere Research Program award No. NNH13AV69I. NOAA laboratory and salary support is from NOAA Climate Change Program. S.A.M. acknowledges funding in part from NOAA Climate Program Office's AC4 Program.

NOAA flask sampling and technical support was provided by Dr. Fred Moore of NOAA/CIRES. Additional technical support was provided by C. Siso, B. Miller, M. Crotwell, C. Sweeney, A. Andrews, J. Higgs, D. Neff, J. Kofler, K. McKain, M. Madronich, P. Handley, and S. Wolter.

We thank IHS Markit for providing PointLogic economic data.

REFERENCES

(1) U.S. Energy Information Administration. *Where our natural gas comes from*. https://www.eia.gov/energyexplained/natural-gas/where-our-natural-gas-comes-from.php (accessed 2022-03-18).

(2) Lan, X.; Tans, P.; Sweeney, C.; Andrews, A.; Dlugokencky, E.; Schwietzke, S.; Kofler, J.; McKain, K.; Thoning, K.; Crotwell, M.; Montzka, S.; Miller, B. R.; Biraud, S. C. Long-Term Measurements Show Little Evidence for Large Increases in Total U.S. Methane Emissions Over the Past Decade. *Geophys. Res. Lett.* **2019**, *46* (9), 4991–4999. https://doi.org/10.1029/2018GL081731.
(3) Turner, A. J.; Frankenberg, C.; Wennberg, P. O.; Jacob, D. J. Ambiguity in the Causes for Decadal Trends in Atmospheric Methane and Hydroxyl. *Proc. Natl. Acad. Sci.* **2017**, *114* (21), 5367–5372. https://doi.org/10.1073/pnas.1616020114.
(4) Kort, E. A.; Smith, M. L.; Murray, L. T.; Gvakharia, A.; Brandt, A. R.; Peischl, J.; Ryerson, T. B.; Sweeney, C.; Travis, K. Fugitive Emissions from the Bakken Shale Illustrate Role of Shale Production in Global Ethane Shift: Ethane Emissions From the Bakken Shale. *Geophys. Res. Lett.* **2016**, *43* (9), 4617–4623. https://doi.org/10.1002/2016GL068703.
(5) U.S. Energy Information Administration. *Hydrocarbon gas liquids explained*. https://www.eia.gov/energyexplained/hydrocarbon-gas-liquids/prices-for-hydrocarbon-gas-liquids.php (accessed 2022-01-31).
(6) Wofsy, S. C. HIAPER Pole-to-Pole Observations (HIPPO): Fine-Grained, Global-Scale Measurements of Climatically Important Atmospheric Gases and Aerosols. *Philos. Trans. R. Soc. Math. Phys. Eng. Sci.* **2011**, *369* (1943), 2073–2086. https://doi.org/10.1098/rsta.2010.0313.
(7) Thompson, C. R.; Wofsy, S. C.; Prather, M. J.; Newman, P. A.; Hanisco, T. F.; Ryerson, T. B.; Fahey, D. W.; Apel, E. C.; Brock, C. A.; Brune, W. H.; Froyd, K.; Katich, J. M.; Nicely, J. M.; Peischl, J.; Ray, E.; Veres, P. R.; Wang, S.; Allen, H. M.; Asher, E.; Bian, H.; Blake, D.; Bourgeois, I.; Budney, J.; Bui, T. P.; Butler, A.; Campuzano-Jost, P.; Chang, C.; Chin, M.; Commane, R.; Correa, G.; Crounse, J. D.; Daube, B.; Dibb, J. E.; DiGangi, J. P.; Diskin, G. S.; Dollner, M.; Elkins, J. W.; Fiore, A. M.; Flynn, C. M.; Guo, H.; Hall, S. R.; Hannun, R. A.; Hills, A.; Hintsa, E. J.; Hodzic, A.; Hornbrook, R. S.; Huey, L. G.; Jimenez, J. L.; Keeling, R. F.; Kim, M. J.; Kupc, A.; Lacey, F.; Lait, L. R.; Lamarque, J.-F.; Liu, J.; McKain, K.; Meinardi, S.; Miller, D. O.; Montzka, S. A.; Moore, F. L.; Morgan, E. J.; Murphy, D. M.; Murray, L. T.; Nault, B. A.; Neuman, J. A.; Nguyen, L.; Gonzalez, Y.; Rollins, A.; Rosenlof, K.; Sargent, M.; Schill, G.; Schwarz, J. P.; Clair, J. M. St.; Steenrod, S. D.; Stephens, B. B.; Strahan, S. E.; Strode, S. A.; Sweeney, C.; Thames, A. B.; Ullmann, K.; Wagner, N.; Weber, R.; Weinzierl, B.; Wennberg, P. O.; Williamson, C. J.; Wolfe, G. M.; Zeng, L. The NASA Atmospheric Tomography (ATom) Mission: Imaging the Chemistry of the Global Atmosphere. *Bull. Am. Meteorol. Soc.* **2022**, *103* (3), E761–E790. https://doi.org/10.1175/BAMS-D-20-0315.1.
(8) Mund, J.; Thoning, K.; Tans, P.; Dlugokencky, E. NOAA ESRL/GMD Annual Period of Record Operational Carbon Cycle & Greenhouse Gases (CCGGs) from Surface Stations, 2017. https://doi.org/10.7289/V5CN725S.
(9) Mund, J.; Thoning, K.; Tans, P.; Andrews, A.; Kofler, J.; Trudeau, M. E.; Bakwin, P. S.; Fisher, M. L.; Sweeney, C.; Desai, A. R. Earth System Research Laboratory Carbon Cycle and Greenhouse Gases Group Continuous Measurements of CO2, CO, and CH4 from Tall Towers, 1992-Present, 2017. https://doi.org/10.7289/V57W69F2.
(10) Mund, J.; Thoning, K.; Tans, P.; Sweeny, C.; Higgs, J.; Wolter, S.; Crotwell, A.; Neff, D.; Dlugokencky, E.; Lang, P.; Novelli, P.; Moglia, E.; Crotwell, M. Earth System Research Laboratory Carbon Cycle and Greenhouse Gases Group Flask-Air Sample Measurements of CO2, CH4, CO, N2O, H2, and SF6 from the Aircraft Program, 1992-Present, 2017. https://doi.org/10.7289/V5N58JMF.

(11) Vimont, I.; Montzka, S.; Hall, B.; Siso, C.; Crotwell, M. Preliminary Ethane and Propane Data Used in Tribby et al. 2022. https://gml.noaa.gov/ccgg/arc/?id=155.
(12) Andrews, A. E.; Kofler, J. D.; Trudeau, M. E.; Williams, J. C.; Neff, D. H.; Masarie, K. A.; Chao, D. Y.; Kitzis, D. R.; Novelli, P. C.; Zhao, C. L.; Dlugokencky, E. J.; Lang, P. M.; Crotwell, M. J.; Fischer, M. L.; Parker, M. J.; Lee, J. T.; Baumann, D. D.; Desai, A. R.; Stanier, C. O.; De Wekker, S. F. J.; Wolfe, D. E.; Munger, J. W.; Tans, P. P. CO2, CO, and CH4 Measurements from Tall Towers in the NOAA Earth System Research Laboratory's Global Greenhouse Gas Reference Network: Instrumentation, Uncertainty Analysis, and Recommendations for Future High-Accuracy Greenhouse Gas Monitoring Efforts. *Atmospheric Meas. Tech.* **2014**, *7* (2), 647–687. https://doi.org/10.5194/amt-7-647-2014.
(13) Sweeney, C.; Karion, A.; Wolter, S.; Newberger, T.; Guenther, D.; Higgs, J. A.; Andrews, A. E.; Lang, P. M.; Neff, D.; Dlugokencky, E.; Miller, J. B.; Montzka, S. A.; Miller, B. R.; Masarie, K. A.; Biraud, S. C.; Novelli, P. C.; Crotwell, M.; Crotwell, A. M.; Thoning, K.; Tans, P. P. Seasonal Climatology of CO_2 across North America from Aircraft Measurements in the NOAA/ESRL Global Greenhouse Gas Reference Network: Vertical Climatology of CO_2 in NA. *J. Geophys. Res. Atmospheres* **2015**, *120* (10), 5155–5190. https://doi.org/10.1002/2014JD022591.
(14) Jacob, D. J. *Introduction to Atmospheric Chemistry*; Princeton University Press: Princeton, N.J, 1999; pp 52-53.
(15) Seinfeld, J. H.; Pandis, S. N. *Atmospheric Chemistry and Physics: From Air Pollution to Climate Change*, Third edition.; John Wiley & Sons: Hoboken, New Jersey, 2016; pp 129.
(16) Keppel-Aleks, G.; Wennberg, P. O.; Schneider, T. Sources of Variations in Total Column Carbon Dioxide. *Atmospheric Chem. Phys.* **2011**, *11* (8), 3581–3593. https://doi.org/10.5194/acp-11-3581-2011.
(17) Keppel-Aleks, G.; Wennberg, P. O.; Washenfelder, R. A.; Wunch, D.; Schneider, T.; Toon, G. C.; Andres, R. J.; Blavier, J.-F.; Connor, B.; Davis, K. J.; Desai, A. R.; Messerschmidt, J.; Notholt, J.; Roehl, C. M.; Sherlock, V.; Stephens, B. B.; Vay, S. A.; Wofsy, S. C. The Imprint of Surface Fluxes and Transport on Variations in Total Column Carbon Dioxide. *Biogeosciences* **2012**, *9* (3), 875–891. https://doi.org/10.5194/bg-9-875-2012.
(18) Wohltmann, I. Integrated Equivalent Latitude as a Proxy for Dynamical Changes in Ozone Column. *Geophys. Res. Lett.* **2005**, *32* (9). https://doi.org/10.1029/2005GL022497.
(19) Parrish, D. D.; Stohl, A.; Forster, C.; Atlas, E. L.; Blake, D. R.; Goldan, P. D.; Kuster, W. C.; de Gouw, J. A. Effects of Mixing on Evolution of Hydrocarbon Ratios in the Troposphere: Mixing Effects on NMHC Ratio Evolution. *J. Geophys. Res. Atmospheres* **2007**, *112* (D10). https://doi.org/10.1029/2006JD007583.
(20) Department of Energy. *Liquefied Natural Gas: Understanding the Basic Facts*; DOE/FE-0489; United States of America, 2005.
(21) Rutherford, J. S.; Sherwin, E. D.; Ravikumar, A. P.; Heath, G. A.; Englander, J.; Cooley, D.; Lyon, D.; Omara, M.; Langfitt, Q.; Brandt, A. R. Closing the Methane Gap in US Oil and Natural Gas Production Emissions Inventories. *Nat. Commun.* **2021**, *12* (1), 4715. https://doi.org/10.1038/s41467-021-25017-4.
(22) National Oceanic and Atmospheric Administration (NOAA). The Science behind the Polar Vortex: You Might Want to Put on a Sweater, 2021. https://www.noaa.gov/multimedia/infographic/science-behind-polar-vortex-you-might-want-to-put-on-sweater.

(23) Dalsøren, S. B.; Myhre, G.; Hodnebrog, Ø.; Myhre, C. L.; Stohl, A.; Pisso, I.; Schwietzke, S.; Höglund-Isaksson, L.; Helmig, D.; Reimann, S.; Sauvage, S.; Schmidbauer, N.; Read, K. A.; Carpenter, L. J.; Lewis, A. C.; Punjabi, S.; Wallasch, M. Discrepancy between Simulated and Observed Ethane and Propane Levels Explained by Underestimated Fossil Emissions. *Nat. Geosci.* **2018**, *11* (3), 178–184. https://doi.org/10.1038/s41561-018-0073-0.
(24) Helmig, D.; Rossabi, S.; Hueber, J.; Tans, P.; Montzka, S. A.; Masarie, K.; Thoning, K.; Plass-Duelmer, C.; Claude, A.; Carpenter, L. J.; Lewis, A. C.; Punjabi, S.; Reimann, S.; Vollmer, M. K.; Steinbrecher, R.; Hannigan, J. W.; Emmons, L. K.; Mahieu, E.; Franco, B.; Smale, D.; Pozzer, A. Reversal of Global Atmospheric Ethane and Propane Trends Largely Due to US Oil and Natural Gas Production. *Nat. Geosci.* **2016**, *9* (7), 490–495. https://doi.org/10.1038/ngeo2721.
(25) Höglund-Isaksson, L. Bottom-up Simulations of Methane and Ethane Emissions from Global Oil and Gas Systems 1980 to 2012. *Environ. Res. Lett.* **2017**, *12* (2), 024007. https://doi.org/10.1088/1748-9326/aa583e.
(26) Franco, B.; Mahieu, E.; Emmons, L. K.; Tzompa-Sosa, Z. A.; Fischer, E. V.; Sudo, K.; Bovy, B.; Conway, S.; Griffin, D.; Hannigan, J. W.; Strong, K.; Walker, K. A. Evaluating Ethane and Methane Emissions Associated with the Development of Oil and Natural Gas Extraction in North America. *Environ. Res. Lett.* **2016**, *11* (4), 044010. https://doi.org/10.1088/1748-9326/11/4/044010.
(27) Simpson, I. J.; Sulbaek Andersen, M. P.; Meinardi, S.; Bruhwiler, L.; Blake, N. J.; Helmig, D.; Rowland, F. S.; Blake, D. R. Long-Term Decline of Global Atmospheric Ethane Concentrations and Implications for Methane. *Nature* **2012**, *488* (7412), 490–494. https://doi.org/10.1038/nature11342.
(28) International Energy Agency. *IEA Atlas of Energy: Natural Gas Production*. http://energyatlas.iea.org/#!/tellmap/-1165808390.
(29) International Energy Agency. *IEA Atlas of Energy: Crude Oil Production*. http://energyatlas.iea.org/#!/tellmap/-1920537974.
(30) U.S. Energy Information Administration. Drilling Productivity Report for Key Tight Oil and Shale Gas Regions, 2022. https://www.eia.gov/petroleum/drilling/pdf/dpr-full.pdf.
(31) Worldwide Power Products. 10 Biggest Shale Plays in the US - New & Used Generators, Ends and Engines | Houston, TX | Worldwide Power Products. https://www.wpowerproducts.com/news/10-biggest-shale-plays-in-the-us-revised/.
(32) Saunois, M.; Stavert, A. R.; Poulter, B.; Bousquet, P.; Canadell, J. G.; Jackson, R. B.; Raymond, P. A.; Dlugokencky, E. J.; Houweling, S.; Patra, P. K.; Ciais, P. The Global Methane Budget 2000-2017. https://doi.org/10.5194/essd-2019-128.
(33) Scarpelli, T. R.; Jacob, D. J.; Maasakkers, J. D.; Sulprizio, M. P.; Sheng, J.-X.; Rose, K.; Romeo, L.; Worden, J. R.; Janssens-Maenhout, G. A Global Gridded (0.1° × 0.1°) Inventory of Methane Emissions from Oil, Gas, and Coal Exploitation Based on National Reports to the United Nations Framework Convention on Climate Change. *Earth Syst. Sci. Data* **2020**, *12* (1), 563–575. https://doi.org/10.5194/essd-12-563-2020.
(34) IEA. Methane Tracker Database: Interactive Database of Country and Regional Estimates for Methane Emissions and Abatement Options, 2021. https://www.iea.org/articles/methane-tracker-database#sources.
(35) Maasakkers, J. D.; Jacob, D. J.; Sulprizio, M. P.; Turner, A. J.; Weitz, M.; Wirth, T.; Hight, C.; DeFigueiredo, M.; Desai, M.; Schmeltz, R.; Hockstad, L.; Bloom, A. A.; Bowman, K. W.; Jeong, S.; Fischer, M. L. Gridded National Inventory of U.S. Methane Emissions. *Environ. Sci. Technol.* **2016**, *50* (23), 13123–13133. https://doi.org/10.1021/acs.est.6b02878.

(36) EPA (Environmental Protection Agency). Global Anthropogenic Non-CO2 Greenhouse Gas Emissions: 1990-2030., 2012.
(37) Turner, A. J.; Jacob, D. J.; Wecht, K. J.; Maasakkers, J. D.; Lundgren, E.; Andrews, A. E.; Biraud, S. C.; Boesch, H.; Bowman, K. W.; Deutscher, N. M.; Dubey, M. K.; Griffith, D. W. T.; Hase, F.; Kuze, A.; Notholt, J.; Ohyama, H.; Parker, R.; Payne, V. H.; Sussmann, R.; Sweeney, C.; Velazco, V. A.; Warneke, T.; Wennberg, P. O.; Wunch, D. Estimating Global and North American Methane Emissions with High Spatial Resolution Using GOSAT Satellite Data. *Atmospheric Chem. Phys.* **2015**, *15* (12), 7049–7069. https://doi.org/10.5194/acp-15-7049-2015.
(38) U.S. Energy Information Administration. Petroleum & Other Liquids: Oklahoma Field Production of Crude Oil, 2021. https://www.eia.gov/dnav/pet/hist/LeafHandler.ashx?f=M&n=PET&s=MCRFPOK1.
(39) U.S. Energy Information Administration. Natural Gas: Oklahoma Natural Gas Marketed Production, 2021. https://www.eia.gov/dnav/ng/hist/n9050ok2a.htm.
(40) U.S. Energy Information Administration. Oklahoma State Profile Analysis, 2021. https://www.eia.gov/state/analysis.php?sid=OK.
(41) Kevin Crowley; Collins, R. Oil Producers Are Burning Enough “Waste” Gas to Power Every Home in Texas. *Bloomberg*. April 10, 2019. https://www.bloomberg.com/news/articles/2019-04-10/permian-basin-is-flaring-more-gas-than-texas-residents-use-daily.
(42) Liu, Z.; Ciais, P.; Deng, Z.; Lei, R.; Davis, S. J.; Feng, S.; Zheng, B.; Cui, D.; Dou, X.; Zhu, B.; Guo, R.; Ke, P.; Sun, T.; Lu, C.; He, P.; Wang, Y.; Yue, X.; Wang, Y.; Lei, Y.; Zhou, H.; Cai, Z.; Wu, Y.; Guo, R.; Han, T.; Xue, J.; Boucher, O.; Boucher, E.; Chevallier, F.; Tanaka, K.; Wei, Y.; Zhong, H.; Kang, C.; Zhang, N.; Chen, B.; Xi, F.; Liu, M.; Bréon, F.-M.; Lu, Y.; Zhang, Q.; Guan, D.; Gong, P.; Kammen, D. M.; He, K.; Schellnhuber, H. J. Near-Real-Time Monitoring of Global CO2 Emissions Reveals the Effects of the COVID-19 Pandemic. *Nat. Commun.* **2020**, *11* (1), 5172. https://doi.org/10.1038/s41467-020-18922-7.

C h a p t e r 3

An analysis coordinate transform to facilitate use of in-situ aircraft observations for flux estimation

Ariana L. Tribby, Paul O. Wennberg

In preparation for submission to Atmospheric Measurement Techniques.

Abstract

Analysis of aircraft observations of atmospheric trace gases is key towards improving fundamental chemical processes and quantifying anthropogenic emissions. A common approach for such analysis is use of chemical transport models to produce 4-D fields for comparison with these observations together with various inversion techniques to constrain the underlying fluxes. Yet, time and monetary constraints of expensive computational jobs for chemical transport modeling can be a significant hindrance. Here, we show the advantages of using potential temperature as a dynamical coordinate to compare such simulations to aircraft observations of trace gases whose concentration fields are strongly influenced by synoptic-scale gradients. We use global observations of ethane and propane from the Atmospheric Tomography (ATom) aircraft mission and simulate globe mole fractions for these gases using GEOS-Chem High Performance v13.4.1. We show that Bayesian estimates of the fluxes of these gases to the Northern Hemisphere are invariant (± 10%) even as the simulation spatial and temporal resolution are increased 100-fold. Our approach can have broad applications for the modeling of trace gases in the extratropics, particularly those with longer lifetimes compared to synoptic timescales.

3.1 Introduction

A common approach for estimating fluxes of trace gases to the atmosphere involve comparing atmospheric simulations with in-situ observations. Such studies enable the use of sparse observations made by aircraft, for example.[1–3] However, computational load can limit the feasibility of these comparisons. Often, efforts are focused on increasing the temporal and spatial resolution of the simulations as a means of capturing the fine scale structure that adds variance to the 4-D chemical fields. This significantly increases the computational load and analysis time.

Motivated by previous analyses of column CO_2 observations,[4,5] we illustrate here how potential temperature (θ, in units of Kelvin) can be useful in model-observation comparisons, particularly when the trace gases under analysis have fluxes that are largely dependent on synoptic-scale dynamics. Variability in the extra-tropics within large-scale circulation can be well-captured since θ is conserved following adiabatic flow. Trace gases that have longer lifetimes compared to

synoptic-scale meteorology (about 10 days),[6] will be well correlated with θ. (The correlation does not hold in the tropics or boundary layer, or when the photochemical lifetimes are short, i.e., during the summer months.)

In this study, we use global aircraft observations of ethane (C_2H_6) and propane (C_3H_8) from Atmospheric Tomography (ATom) mission during 2016-2017 and simulate those global fields using the chemical transport model, GEOS-Chem High Performance v13.4.1. We show that when used a zonal coordinate, θ improves model/observation correlation compared with using classical latitude, longitude, altitude and time coordinates. We use the Bayesian hierarchical model from Tribby et al. 2022 to evaluate flux estimates from simulations performed at 4x5, 2x2.5, and 0.5x0.625 resolutions, and find that when using θ, the comparisons have negligible difference. As such, θ offers an opportunity to optimize time and cost of model simulations for certain trace gases, including several of which have important climate implications.

3.2 Methods

3.2.1 ATom observations

The Atmospheric Tomography (ATom) aircraft campaign comprised of four sequential global flights. We use two flight campaigns during July-August 2016 and January-February 2017.

As in Tribby et al. 2022, we exclude from our analysis stratospheric observations (using N_2O) and data influenced by highly local emission sources (boundary layer and biomass burning).[7] When using θ as a vertical interpolation coordinate, we exclude the summer months from our analysis, since the lifetime of C_2H_6 and C_3H_8 are reduced, and regional/local sources dominate the variance. Further, we exclude subtropical transport by limiting observations with tropopause pressure above 100 hPa (only about 5% of data was affected by this constraint), which sufficiently reduced subtropical influence.

We show flight paths for the data above 20 degrees north in Figure 7, as we only consider northern fluxes since most emissions of short-lived C_2H_6 and C_3H_8 originate in the northern hemisphere, and their lifetimes are shorter than northern-southern hemispheric exchange rate.

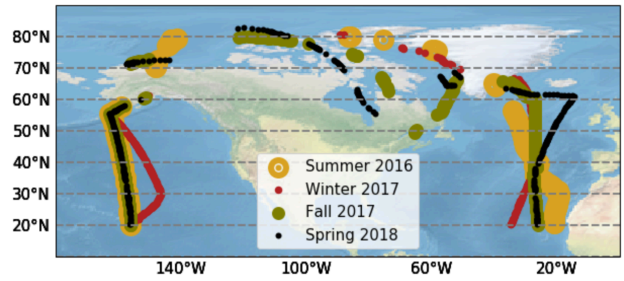

Figure 7. Flight paths during ATom flight campaign. We use summer 2016 and winter 2017 campaigns over the Atlantic Ocean in our analysis. We only consider observations above 20 degrees north, as explained in the methods.

3.2.2 GEOS-Chem simulations

We simulated ATom aircraft observations using the GEOS-Chem classic global3-D chemical transport model in v13.4.1 (doi:10.5281/zenodo.6564702) on Amazon Web Services (AWS) using a public GEOS-Chem Amazon Machine Image (ami-0491da4eeba0fe986).[8] We used the standard full-chemistry option and 3 horizontal resolutions to simulate ATom1 & 2, including 4x5, 2x2.5, and 0.5x0.625, all with the native 72 hybrid sigma/pressure levels using MERRA-2 reanalysis meteorology products by the Global Modeling and Assimilation Office (GMAO) at NASA Goddard Space Flight Center,[9] available on the AMI. For all 3 horizontal resolution simulations, we output hourly simulations over the ATom 1 and 2 flight campaign periods.

We conducted a global simulation for 4x5 and 2x2.5 horizontal resolutions before sampling to the aircraft path, except for 0.5x0.625, detailed below. Default chemistry and configurations were used for 2x2.5 and 4x5, except for custom C_2H_6 and C_3H_8 emissions, described below. We used a 1-year spin-up at 4x5 horizontal resolution, followed by a 10-day spin-up with the 2x2.5 or 0.5x0.625 meteorological files.

The 0.5x0.625 simulations were conducted using a nested-grid over a custom box that encompassed the ATom Atlantic curtain transect. The vertices of our custom grid included a minimum/maximum latitude of (18.0, 88.0) and a minimum/maximum longitude of (-90.0, -15.0) with 3-grid buffer for all sides. We generated global boundary condition tri-hourly daily files for our custom grid using a 4x5 simulation and custom emissions for C_2H_6 and C_3H_8, described below. In addition, we re-used the 4x5 spin-up restart files when generating boundary condition files. During the nested run, several species were flagged as having negative values during PBL mixing in GEOS-Chem, including HNO_3, NH_3, NO, NO_2, O_3, and halogen chemistry sea salt alkalinity variables, SALAAL and SALCAL, causing the simulations to end. Manually increasing the background concentrations or reducing the transport/convection timestep to 150 seconds and the chemistry/emission timestep to 300 seconds did not prevent these issues. We kept the timesteps at

those reduced values and edited the wrapper module, mixing_mod.F90, to replace negative values with zero to allow the model to run. No other species were flagged as having negative values.

Emissions for C_2H_6 and C_3H_8 were computed using the Harmonized Emissions Component (HEMCO)[10] Standalone version 3.5.0-rc.1 and GEOS-Chem 14.0.0-rc.1 on AWS using a public Amazon Machine Image (ami-0491da4eeba0fe986). We revised the default emissions using the same methods from Tribby et al. 2022: we scaled all sectors of default C_2H_6 by 1.1, and we substituted C_3H_8 with default C_2H_6 before scaling by 1.2.

3.3 Results

In Figure 8, we show curtain plots for C_3H_8 for 4x5, 2x2.5, and 0.5x0.625 horizontal resolution GEOS-Chem simulations. We interpolate 4x5 and 2x2.5 along pressure and latitude to the 0.5x0.625 scale. As expected, 0.5x0.625 show more defined structures. However, if we instead create the same curtain plots but using θ as the vertical coordinate (without interpolation), the three simulations look very similar (SI). This holds true for the winter 2017 observations, but not for the summer 2016 observations, since the increased sunlight/oxidation reduces the chemical lifetime of C_2H_6 and C_3H_8, resulting in a poor relationship with θ (Figures A5, A6).

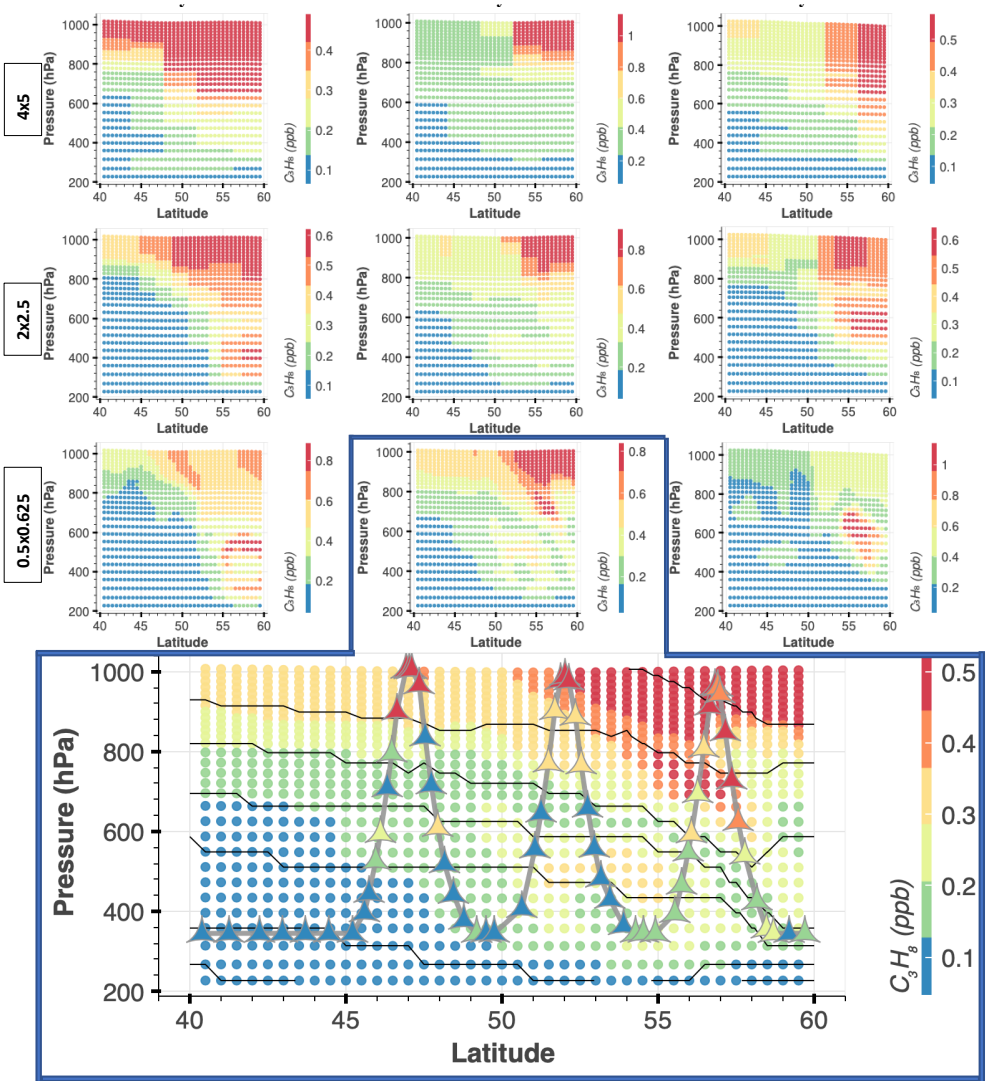

Figure 8. GEOS-Chem-simulated C_3H_8 "curtain" during ATom 2 winter 2017 campaign, along pressure and latitude. All GEOS-Chem simulations were sampled along aircraft latitude and a single median time/longitude during the flight over the Atlantic ocean. Column 1 shows simulations sampled 5 days before the median aircraft time; Column 2 shows simulations sampled on the median aircraft time; Column 3 shows simulations sampled 5 days after the median aircraft time. FIRST row: 4x5 resolution, interpolated to 0.5x0.625 grid using latitude and pressure coordinates. SECOND row: 2x2.5 resolution, interpolated to 0.5x0.625 grid using latitude and pressure coordinates. THIRD row: 0.5x0.625 resolution. FOURTH row: a more detailed illustration of plot number r3,c2, with aircraft flight path shown in grey, the aircraft observations shown by triangle markers, and potential temperature contours shown in black. C_2H_6 is included in the SI.

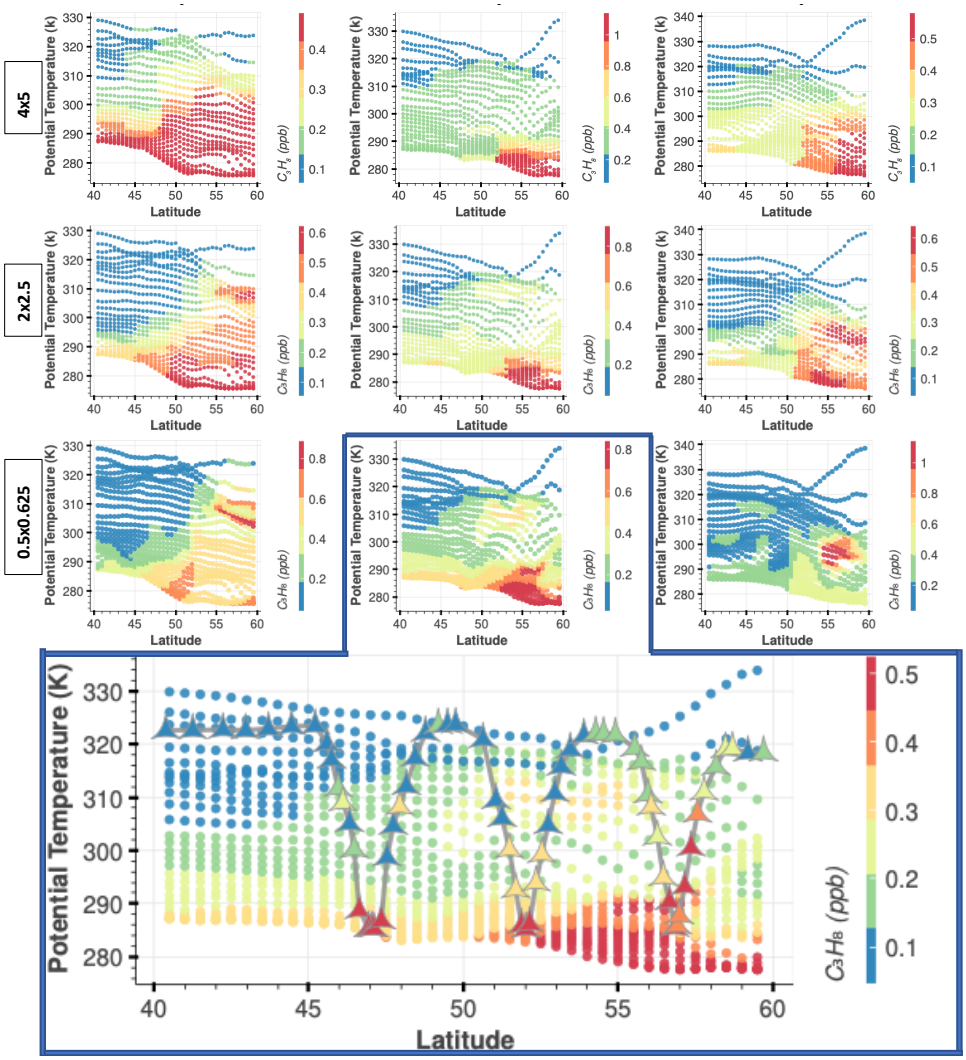

Figure 9. GEOS-Chem-simulated C_3H_8 "curtain" during ATom 2 winter 2017 campaign, along potential temperature and latitude. All GEOS-Chem simulations were sampled along aircraft latitude and a single median time/longitude during the flight over the Atlantic ocean. Column 1 shows simulations sampled 5 days before the median aircraft time; Column 2 shows simulations sampled on the median aircraft time; Column 3 shows simulations sampled 5 days after the median aircraft time. FIRST row: 4x5 resolution. SECOND row: 2x2.5 resolution. THIRD row: 0.5x0.625 resolution. FOURTH row: a more detailed illustration of plot number r3,c2, with aircraft flight path shown in grey, the aircraft observations shown by triangle markers, and potential temperature contours shown in black. C_2H_6 is included in the SI.

When we interpolate the GEOS-Chem simulations along aircraft latitude, longitude, time, and θ, we see excellent agreement between simulations and the aircraft observations, consistent across all 3 horizontal resolutions (Figure 10). Furthermore, there is generally good agreement between the aircraft observations and simulations 5 days before and after the flight path, which is expected during the winter months when C_3H_8 and C_2H_6 have longer lifetimes and higher abundance.

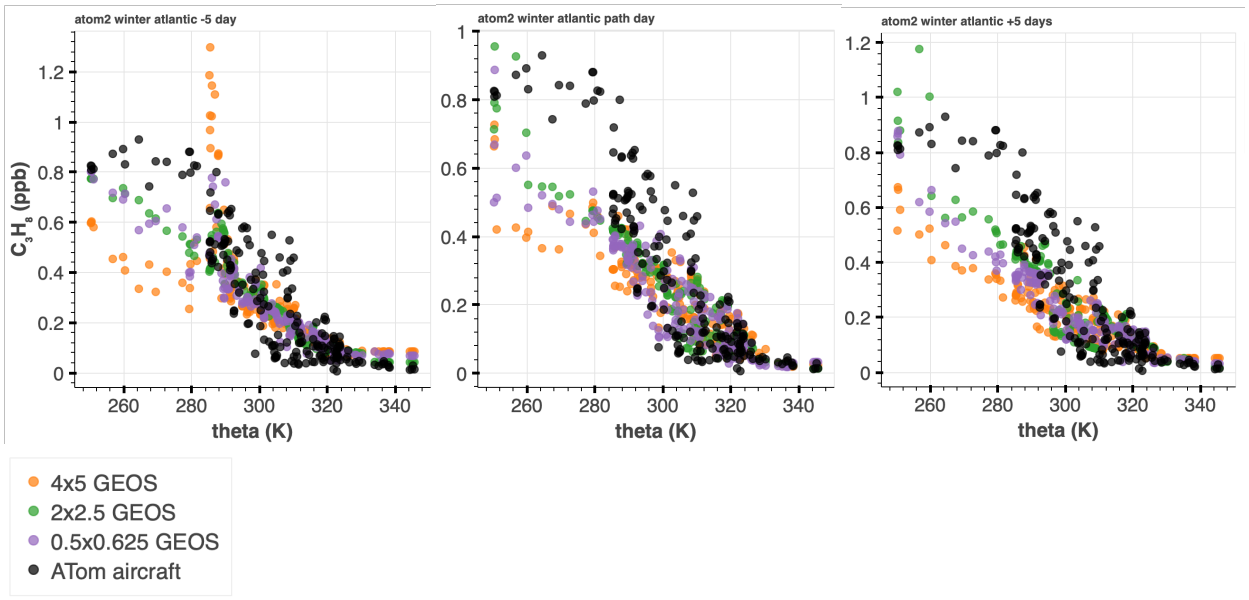

Figure 10. GEOS-Chem simulations and ATom aircraft C_3H_8 vs potential temperature. Left: Includes aircraft observations and simulations sampled 5 days after the aircraft flight path. Middle: Includes aircraft observations and simulations sampled during the aircraft flight path. Right: Includes aircraft observations and simulations 5 days before the aircraft flight path. C_2H_6 included in the SI.

We compare the aircraft observations with the GEOS-Chem simulations using the same Bayesian hierarchical model from Tribby et al. 2022 to capture the contribution of uncertainty due to transport in GEOS-Chem. In summary, Tribby et al. 2022 assumed differences between the GEOS-Chem simulations and aircraft observations are largely dependent on the underlying emissions grid during the winter when there is decreased sunlight/oxidation, such that

$$a = \mathrm{gcs} \cdot \alpha \quad (1)$$

where a is the aircraft mole fraction, gcs is the GEOS-Chem simulation, and α is a scalar that quantifies the difference between the simulations and the aircraft observations (that directly attributes the missing emissions). Since in our simulations here, we updated the fluxes to those estimated in Tribby et al. 2022, we expect α to be close to 1. We follow all methods of the previous study, including sampling the GEOS-Chem simulations several days before and after the aircraft flight latitude, longitude, and time before interpolating on the vertical level using θ. Please refer to Tribby et al. 2022 for the complete statistical model and its derivation, the software, and the development of the priors.

With θ as the interpolation coordinate, the Bayesian results are similar regardless of the simulation grid scale (Figure 11): the mean posterior varies 10% or less between all horizontal resolutions for both C_3H_8 and C_2H_6. Furthermore, the confidence interval spread was about the same for the finest and coarsest resolutions, illustrating the value of using θ as the analysis coordinate.

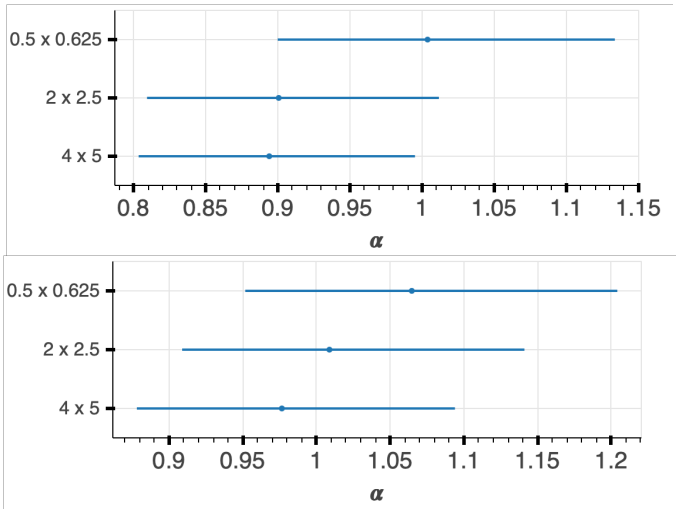

Figure 11. Bayesian inference results, 97.5% confidence interval. **Top**: C_3H_8. **Bottom**: C_2H_6.

References

(1) Xiao, Y.; Logan, J. A.; Jacob, D. J.; Hudman, R. C.; Yantosca, R.; Blake, D. R. Global Budget of Ethane and Regional Constraints on U.S. Sources. *J. Geophys. Res.* **2008**, *113* (D21). https://doi.org/10.1029/2007JD009415.

(2) Zhou, M.; Langerock, B.; Wells, K. C.; Millet, D. B.; Vigouroux, C.; Sha, M. K.; Hermans, C.; Metzger, J.-M.; Kivi, R.; Heikkinen, P.; Smale, D.; Pollard, D. F.; Jones, N.; Deutscher, N. M.; Blumenstock, T.; Schneider, M.; Palm, M.; Notholt, J.; Hannigan, J. W.; De Mazière, M. An Intercomparison of Total Column-Averaged Nitrous Oxide between Ground-Based FTIR TCCON and NDACC Measurements at Seven Sites and Comparisons with the GEOS-Chem Model. *Atmospheric Meas. Tech.* **2019**, *12* (2), 1393–1408. https://doi.org/10.5194/amt-12-1393-2019.

(3) Frankenberg, C.; Kulawik, S. S.; Wofsy, S. C.; Chevallier, F.; Daube, B.; Kort, E. A.; O'Dell, C.; Olsen, E. T.; Osterman, G. Using Airborne HIAPER Pole-to-Pole Observations (HIPPO) to Evaluate Model and Remote Sensing Estimates of Atmospheric Carbon Dioxide. *Atmospheric Chem. Phys.* **2016**, *16* (12), 7867–7878. https://doi.org/10.5194/acp-16-7867-2016.

(4) Keppel-Aleks, G.; Wennberg, P. O.; Schneider, T. Sources of Variations in Total Column Carbon Dioxide. *Atmospheric Chem. Phys.* **2011**, *11* (8), 3581–3593. https://doi.org/10.5194/acp-11-3581-2011.

(5) Keppel-Aleks, G.; Wennberg, P. O.; Washenfelder, R. A.; Wunch, D.; Schneider, T.; Toon, G. C.; Andres, R. J.; Blavier, J.-F.; Connor, B.; Davis, K. J.; Desai, A. R.; Messerschmidt, J.; Notholt, J.; Roehl, C. M.; Sherlock, V.; Stephens, B. B.; Vay, S. A.; Wofsy, S. C. The Imprint of Surface Fluxes and Transport on Variations in Total Column Carbon Dioxide. *Biogeosciences* **2012**, *9* (3), 875–891. https://doi.org/10.5194/bg-9-875-2012.
(6) Wohltmann, I. Integrated Equivalent Latitude as a Proxy for Dynamical Changes in Ozone Column. *Geophys. Res. Lett.* **2005**, *32* (9), L09811. https://doi.org/10.1029/2005GL022497.
(7) Tribby, A. L.; Bois, J. S.; Montzka, S. A.; Atlas, E. L.; Vimont, I.; Lan, X.; Tans, P. P.; Elkins, J. W.; Blake, D. R.; Wennberg, P. O. Hydrocarbon Tracers Suggest Methane Emissions from Fossil Sources Occur Predominately Before Gas Processing and That Petroleum Plays Are a Significant Source. *Environ. Sci. Technol.* **2022**, acs.est.2c00927. https://doi.org/10.1021/acs.est.2c00927.
(8) Zhuang, J.; Jacob, D. J.; Gaya, J. F.; Yantosca, R. M.; Lundgren, E. W.; Sulprizio, M. P.; Eastham, S. D. Enabling Immediate Access to Earth Science Models through Cloud Computing: Application to the GEOS-Chem Model. *Bull. Am. Meteorol. Soc.* **2019**, *100* (10), 1943–1960. https://doi.org/10.1175/BAMS-D-18-0243.1.
(9) Gelaro, R.; McCarty, W.; Suárez, M. J.; Todling, R.; Molod, A.; Takacs, L.; Randles, C. A.; Darmenov, A.; Bosilovich, M. G.; Reichle, R.; Wargan, K.; Coy, L.; Cullather, R.; Draper, C.; Akella, S.; Buchard, V.; Conaty, A.; da Silva, A. M.; Gu, W.; Kim, G.-K.; Koster, R.; Lucchesi, R.; Merkova, D.; Nielsen, J. E.; Partyka, G.; Pawson, S.; Putman, W.; Rienecker, M.; Schubert, S. D.; Sienkiewicz, M.; Zhao, B. The Modern-Era Retrospective Analysis for Research and Applications, Version 2 (MERRA-2). *J. Clim.* **2017**, *30* (14), 5419–5454. https://doi.org/10.1175/JCLI-D-16-0758.1.
(10) Lin, H.; Jacob, D. J.; Lundgren, E. W.; Sulprizio, M. P.; Keller, C. A.; Fritz, T. M.; Eastham, S. D.; Emmons, L. K.; Campbell, P. C.; Baker, B.; Saylor, R. D.; Montuoro, R. Harmonized Emissions Component (HEMCO) 3.0 as a Versatile Emissions Component for Atmospheric Models: Application in the GEOS-Chem, NASA GEOS, WRF-GC, CESM2, NOAA GEFS-Aerosol, and NOAA UFS Models. *Geosci. Model Dev.* **2021**, *14* (9), 5487–5506. https://doi.org/10.5194/gmd-14-5487-2021.

C h a p t e r 4

Towards constraining methane emissions in southern Oklahoma using STILT analysis of remote sensing and flask observations of hydrocarbon tracers

Ariana L. Tribby, Dien Wu, Josh L. Laughner, Harrison A. Parker, Paul O. Wennberg

In preparation for submission to Atmospheric Chemistry and Physics.

4.1 Introduction

Previous studies have seen evidence for significant, nearby oil and gas production hydrocarbon emissions using ethane and propane flask observations from the NOAA station in Lamont, Oklahoma (Tribby et al. 2022). Their reported decadal trend is consistent with Oklahoma oil and gas production activities that tripled during the same time.[1,2] We develop a methodology to quantify emissions of methane from this region using long-term measurements of ethane and propane tracers, in conjunction with NOAA flask. Finally, we will quantify regional emissions using STILT. This analysis is in preparation for submission to ACP.

4.2. Methods

4.2.1 TCCON measurements of ethane and propane

Remote sensing observations from ground-based Fourier transform spectrometer located in Lamont, Oklahoma are part of the Total Carbon Colomn Observing Network (TCCON), which includes 29 active sites located around the world.[3] The TCCON instruments are solar-viewing Bruker 125HR (high-resolution) FT-IR spectrometers (near-infrared) that record an interferogram every few minutes that are converted to spectra. The volume mixing ratio (VMR) of numerous trace gases are derived from the measured spectra using a nonlinear least-squares algorithm that minimizes the residuals between a measured spectrum and one that is the product of the a priori profile and a uniform scalar.[4] Column abundances of atmospheric gases are computed by integrating the optimally-scaled prior profiles.[5] The column abundances are converted to column dry mole fractions (DMF) by dividing by the column of O_2. In this analysis, we take advantage of new retrievals of ethane and propane together with standard retrievals of methane.

The a priori profiles are constructed using correlations between meteorological variables and observations (i.e., balloon) of trace gas DMFs in the atmosphere. While these a priori are satisfactory for remote observations typical of TCCON sites, in the context of intense oil and gas emissions, they are not appropriate for regions such as Oklahoma. Here, we use GEOS-Chem simulations of C_2H_6 and C_3H_8 (see configurations for GEOS-Chem below) at Oklahoma to update

the a priori profiles for the TCCON retrievals using the newly-developed ginput-devel algorithm (https://github.com/WennbergLab/py-ginput-devel.git), Figure 12. This product was developed for TCCON users to derive a priori profiles using custom trace gas column profiles. The algorithm samples custom trace gas profiles (at a frequency of every 3 hours) and interpolates along geopotential height to arrive at the same vertical coordinates as the meteorology used in TCCON GGG2020, which uses the Goddard Earth Observing System Forward Product for Instrument Teams (GEOS FP-IT) reanalysis product. The geopotential height is computed by normalizing the geometric height by gravity and linearly interpolated in log(pressure) from the model's level edge pressures. The edge heights are calculated using the hydrostatic equation, $\frac{1}{g}\left(PHIS + c_p \sum_{l=L}^{LM} \theta_v \Delta P\right)$, where ΔP is the difference in $\left(\frac{p}{p_0}\right)^k$ at the lower and upper edges of layer l, PHIS is the surface geopotential, c_p is the specific heat, and θ_v is the virtual potential temperature in the layer (https://gmao.gsfc.nasa.gov/GMAO_products/documents/GEOS-5_Filespec_Glossary.pdf). We calculate θ_v using the virtual temperature ("TV") and water profile. All profiles of interfering species in the spectra of C_2H_6 and C_3H_8 are taken from the default a priori profiles used in GGG2020. Below is a comparison of an example of the updated VMR for C_2H_6 and C_3H_8.

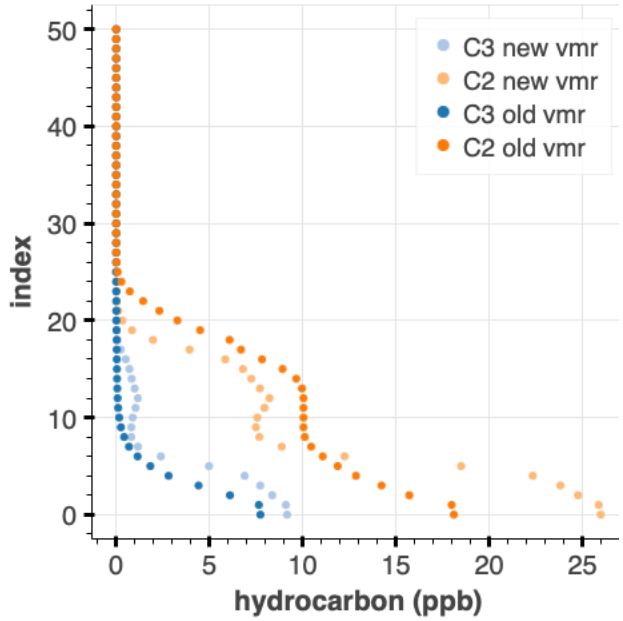

Figure 12. Updated ethane and propane volume mixing ratios (VMR) for TCCON retrievals. Updated VMR are derived using the new ginput-devel algorithm (see Methods) and GEOS-Chem profiles made using revised hydrocarbon emissions from Tribby et al. 2022. Index is a proxy for the hybrid pressure level. Shown in blue are the standard a priori profiles used in ggg.

We obtain column average dry mole fractions (DMF) with high temporal frequency for ethane and propane at the Lamont site from 2017-2020 (see Results). We also filter for scaling factor (VSF) error less than 10 to reduce solar zenith angle dependence.

4.2.2 GEOS-Chem simulations

We use GEOS-Chem simulations to develop custom priors for our TCCON retrievals of C_2H_6 and C_3H_8. We ran GEOS-Chem classic global3-D chemical transport model in v13.4.1 (doi:10.5281/zenodo.6564702) on Amazon Web Services (AWS) using a public GEOS-Chem Amazon Machine Image (ami-0491da4eeba0fe986). We used the standard full-chemistry option at 4x5 degree horizontal resolution at the native 72 hybrid sigma/pressure levels using GEOS-FP meteorology products available on AWS to simulate C_2H_6 and C_3H_8 from June 1 – October 1 2017-2020, with output frequency of every 3 hours. Default chemistry and configurations were used except for custom C_2H_6 and C_3H_8 emissions, described below. We used a 1-year spin up at 4x5 horizontal resolution.

Emissions for C_2H_6 and C_3H_8 were computed using the Harmonized Emissions Component (HEMCO) Standalone version 3.5.0-rc.1 and GEOS-Chem 14.0.0-rc.1 on AWS using a public Amazon Machine Image (ami-0491da4eeba0fe986). We revised the default emissions using the same methods from Tribby et al. 2022: we scaled all sectors of default C_2H_6 by 1.1 and substituted C_3H_8 with default C_2H_6 before scaling by 1.2.

4.2.3 NOAA flask observations

We use observations from the NOAA Oceanic and Atmospheric Administration (NOAA) Global monitoring Laboratory (GML) measurements of C_3H_8, C_2H_6 and CH_4 from flask air samples collected by the NOAA GML tower and aircraft at the Southern Great Plains (SGP) location in Lamont, Oklahoma from 2017-2020. The C_3H_8 and C_2H_6 were accessed from https://gml.noaa.gov/aftp/data/trace_gases/, while CH_4 was accessed from https://gml.noaa.gov/aftp/data/trace_gases/ch4/pfp/. We use measurement quality flags labeled as either preliminary or good sampling analysis only. There were unequal number of quality measurements for all 3 alkane species, so we matched UTC time stamps that were shared between all 3 to avoid sampling bias. As in Tribby et al. 2022 we use 1 ppb C_3H_8 as a threshold for photochemically aged samples. We restrict our analysis to samples associated with fresh emissions (unaged). We only use summer data between June 1-October 1 2017-2020.

Wind speed and direction for Lamont NOAA flasks was obtained from the nearby Blackwell station at https://mesonet.agron.iastate.edu/sites/windrose.phtml?station=WDG&network=OK_ASOS. We interpolated the speed and direction using the nearest neighbor UTC time.

4.2.4 STILT modeling

We use the Stochastic Time-Inverted Lagrangian Transport (STILT) model,[6] which simulates atmospheric transport backward in time by releasing an ensemble of representative air parcels at a receptor location, and simulating their stochastic transport by extracting parameters from assimilated meteorological fields. Only flask NOAA observations are modeled at this time, and plans for using TCCON retrievals with STILT are described in future directions. 1000 air parcels are released per tower receptor longitude/latitude/time/altitude. Our model area is defined as 20-50N latitude, 90-110W longitude. To transport the air parcels, we use the North American Mesoscale Forecast System (NAM) (12 km resolution) run by the National Centers for Environmental Prediction (NCEP). The impact on wind error is a topic of future work, but we utilize a generous uncertainty of 50% in modeled mole fractions for preliminary Bayesian estimates below.[7]

STILT generates a footprint, which describes the influence of potential upwind source regions to downwind receptor mole fraction anomaly, in units of ppm/($\mu molm^{-2}$). Each footprint has a horizontal resolution of 0.1x0.1 degrees. The footprints, multiplied by emissions, describes the contribution to the mole fraction anomaly at the receptor, in units of ppb.

4.2.5 Emissions prior

Oil and gas wells shapefiles were downloaded from https://www.fractracker.org/map/us/ in April 2023 for the following regions: Oklahoma, Colorado, Kansas, Missouri, new Mexico, Oklahoma and Texas (see SI for visualization). We use geopandas (v 0.12.2) for processing and analysis. After converting all coordinates to WGS 84, we compute well density for every 0.1x0.1 cell (figure, SI). We then use Zhang et al. 2020's[8] CH_4 emission estimates in the Permian basin to derive a CH_4 emission rate for our entire footprint area using our computed well density, Figure 13. We use the mean C_3H_8/CH_4 and C_2H_6/CH_4 emission ratios from 2017 at Lamont Oklahoma (Tribby et al. 2022) to estimate C_3H_8 and C_2H_6 emissions at 0.1x0.1 degrees (Figures in SI). Integrated emissions over our footprint area are as follows: CH_4 at 7.6 ± 1.4 Tg/yr, C_3H_8 at 1.3 ± 0.5 Tg/yr, and C_2H_6 at 1.2 ± 0.5 Tg/yr, where uncertainty is the propagated error between Zhang et al. 2020 CH_4 emission rate uncertainty and the variability in the hydrocarbon emission ratio from Tribby et al. 2022. We compare our area totals with other studies in the SI.

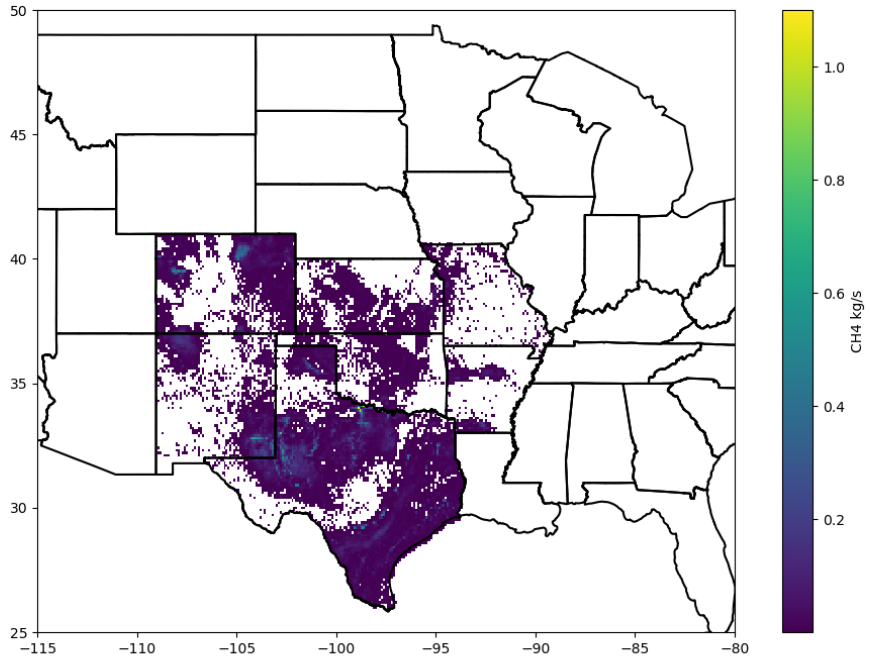

Figure 13. CH_4 emissions constructed using wellhead density, used for computing STILT contribution. C_2H_6 and C_3H_8 are included in the SI.

We convert from latitude/longitude coordinates to units of meters using pyproj Geod package (v3.5.0). Finally, we filled any zero values in the emissions grid with 1e-15 to avoid issues with log(0) before scaling by the STILT footprint in the Bayesian modeling below.

4.2.6 Bayesian modeling

We assume a linear relationship between the STILT-modeled mole fraction (y_m) and the observed mole fractions (y_0) such that $y_0 = xy_m$, where x is the state vector representing the emissions scaling factor. This assumption holds because the lifetime of ethane and propane are on the order of weeks during the summertime and longer at other times of year. This is sufficiently long with respect to transport over a 3-day footprint period that we can assume these gases are passive tracers. We can reasonably approximate ethane and propane as lognormally distributed:

$$\sigma \sim Norm(0.9, 0.15)$$
$$log_{10}x \sim Norm(0,1)$$
$$\Delta y_{0_j} \sim \text{LogNorm}\left(x\Delta y_{m_j}, \sigma\right)$$

where Δy_{0_i} is the *j*th observed enhancement hydrocarbon mole fraction, and Δy_{m_i} is the *j*th modeled enhancement mole fraction, which are the STILT $\text{footprints}_{j,k}$ (of k spatial grid cells)

scaled by the emissions $prior_k$. We define x_k on a log scale for its prior for two reasons. First, it is well documented that emissions from oil and gas follow a heavy-tail distribution, [9–12] so this will generate scaling factors on an appropriate scale. Second, the emissions $prior_k$ is likely an underestimate since we use well density to linearly scale our derived emission rate and do not account for super emitters. The prior for σ is sufficiently broad to allow for an error estimate of 50% in ppb enhancement (the generated samples are in log scale). Figures for our priors are shown in the SI.

We run our statistical model using Stan software[13] (version 2.26) with CmdStanPy Python interface (version 0.9.67).[14] Stan is a probabilistic programming language that uses Hamiltonian Monte Carlo (HMC),[15] which allows for more efficient sampling of the posterior. We parse Markov chain sampling using ArviZ (version 0.11.1).[16] We use bebi103 package (version 0.1.0)[17] to prepare data for Stan sampling, parse MCMC samples, plot posteriors and plot posterior predictive checks. Finally, other software we use in our analysis includes Holoviews version 1.14.5,[18] Bokeh version 2.3.3,[19] Pandas version 1.3.1,[20] SciPy version 1.6.2,[21] and NumPy version 1.20.3.[22] We set the warmup iterations to 2000 and conducted 1000 samples.

4.3. Results & analysis

The TCCON dry mole fractions (DMF) of C_3H_8 and C_2H_6 are very well correlated (Figure 14). In anticipation of performing a STILT run using TCCON columns, we have prepared a TCCON dataset in which TCCON and NOAA flask observations overlap in day of measurement (SI). We have not yet completed the algorithm for executing STILT for TCCON column receptors at the time of this thesis preparation, and this task is left for future work prior to submission of this study for peer review.

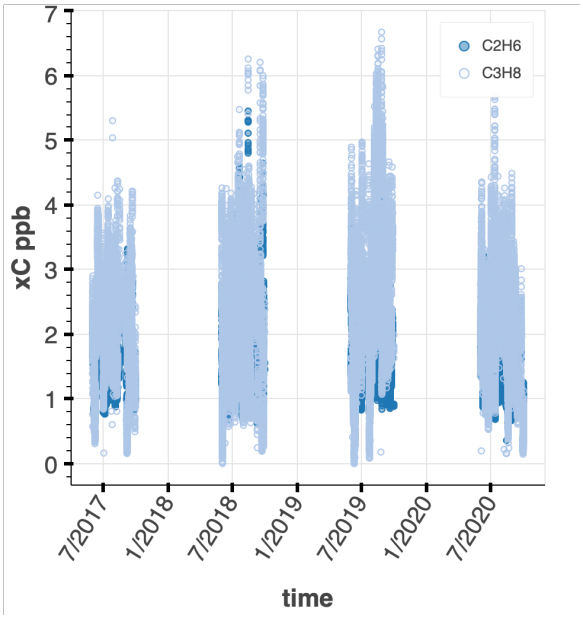

Figure 14. TCCON dry mole fractions of C_2H_6 and C_3H_8.

We show NOAA flask tower and plane C_3H_8 and C_2H_6 for Lamont in the 'fresh emission' regime (Figure 15). Most samples with highly elevated C_3H_8 and C_2H_6 are associated with wind direction vector originating from a south/south-westerly direction.

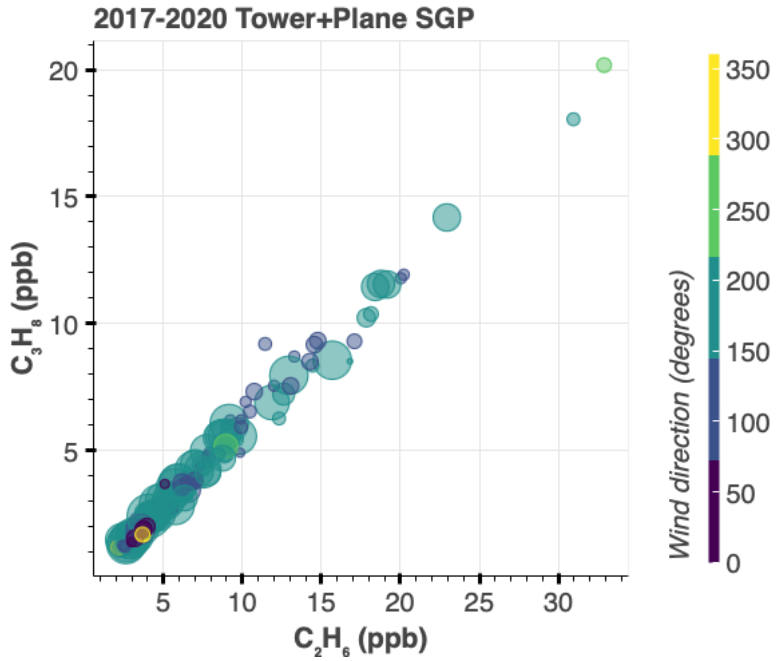

Figure 15. C_3H_8 and C_2H_6 NOAA flask data. Data filtered for fresh emission chemical regime. Not yet background corrected. Marker size correlates to relative wind magnitude.

Below we show an example of our modeled mole fraction anomaly (y_m) contribution to the NOAA tower flask receptor (STILT footprint scaled by our emissions prior), over the 3 day back-trajectory (Figure 16). At first glance though all the receptor days, there seem to be a significant number of footprints from North, South-East origin contributing to the receptor mole fraction. However, more analysis is needed, as some footprints show a spread-out influence compared to others.

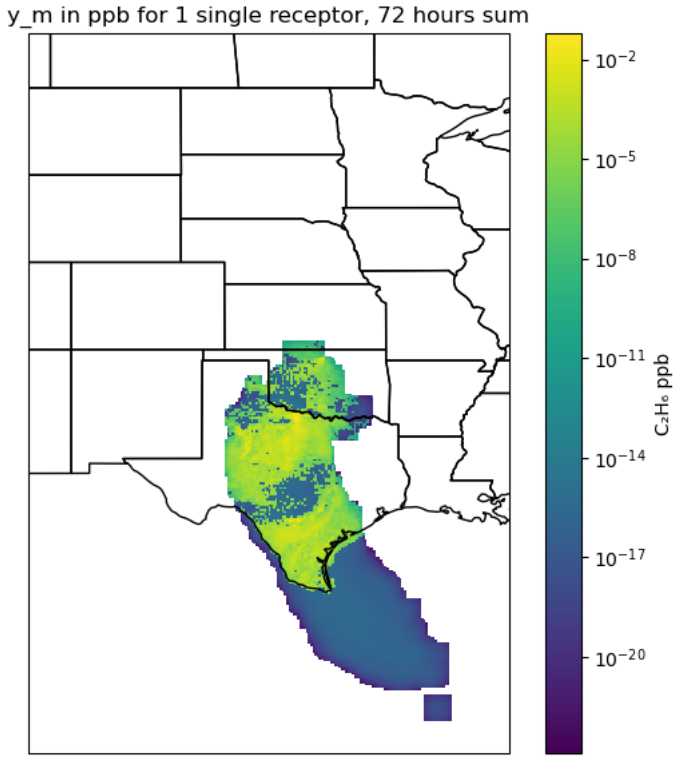

Figure 16. Example of mole fraction contribution to the NOAA tower flask receptor over the 3-day back trajectory.

The y_m summed across the entire footprint area represents the total modeled mole fraction anomaly at the receptor location after influence from neighboring regions. We show this estimate for every receptor day and compare this to NOAA tower flask background-corrected anomalies (Figure 17). STILT underestimates NOAA flask observations significantly. More analysis is needed to determine the validity of these estimates, as we cannot unambiguously determine whether the emission estimates are significantly underestimated or there are other factors contributing to these low anomalies. Incorporating the aircraft data and the TCCON retrievals in our STILT analysis will be helpful in determining whether the high C_3H_8 and C_2H_6 we see in the tower data is due to the presence of highly local emissions (as this will result in highly elevated mole fractions at the surface) or whether our emissions prior is underestimated.

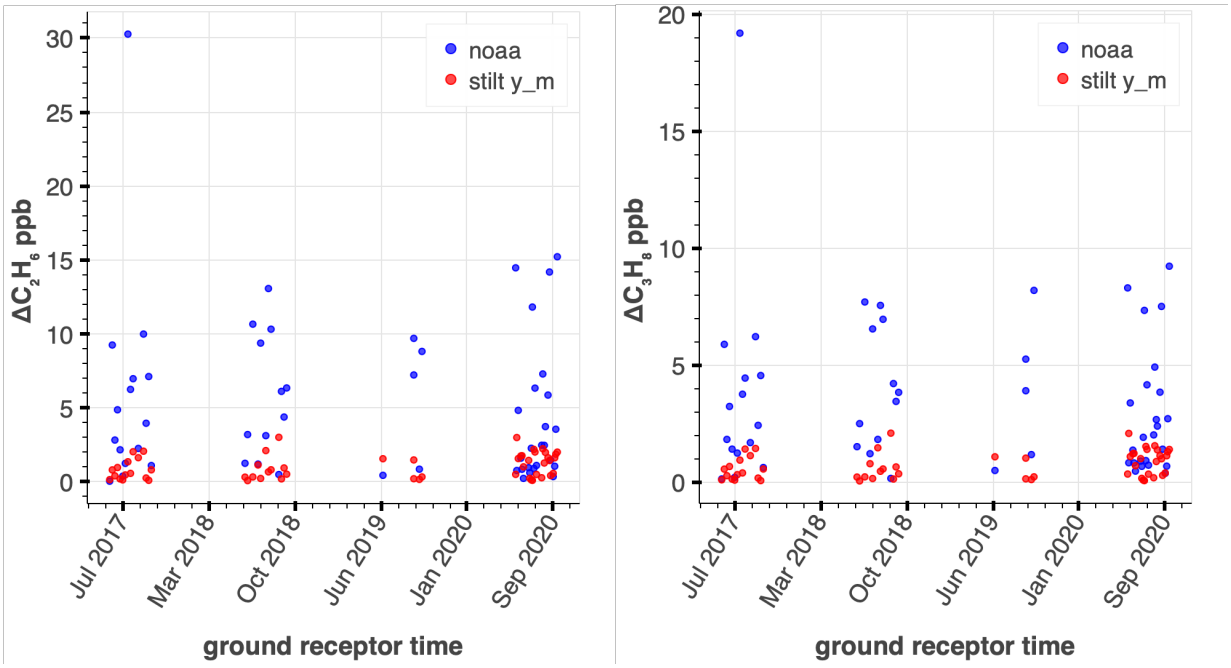

Figure 17. STILT-modeled receptor anomaly mole fraction compared to NOAA flask background-corrected anomaly. Only including tower observations here. Background described in the methods.

We estimate a scaling factor directly related to the missing emissions using our Bayesian model. We start by estimating a scaling factor for the entire footprint region (all oil and gas basins included in the emissions grid, Figure 13). We simply use the receptor anomalies (Figure 17) to do this. Our HMC sampling was successful; using bebi103's stan.check_all_diagnostics function, our sampling had effective sample size for all parameters (based on the suggestion of 50 effective samples per split chain)[23] and 0 out of 4000 iterations ended with a divergence or saturated the maximum tree depth with no other indication of pathological behavior. The 95% credible interval of the scaling factor parameter samples is [2.9, 5.8] for C_2H_6 and [3.2, 6.2] for C_3H_8 (Figure 18). Using the 50th percentile of the samples, this corresponds to 5-6 Tg/yr of C_3H_8 and C_2H_6 for the entire footprint area. Based on previous studies, this is likely an overestimate. Incorporating additional datasets in our STILT analysis such as aircraft and TCCON will be invaluable in determining the magnitude of these regional emissions.

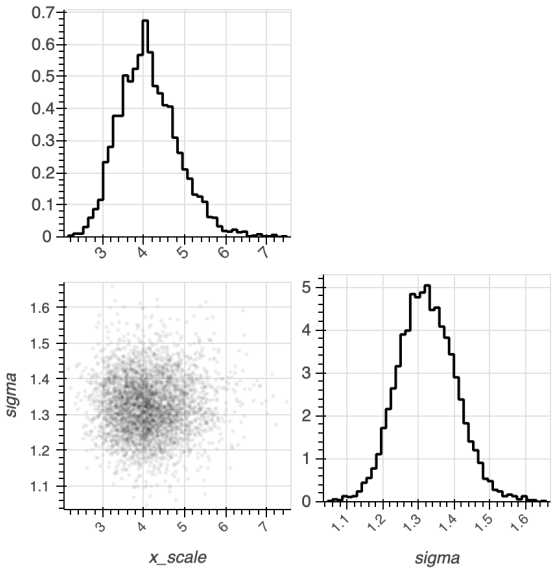

Figure 18. Posterior samples for x scalar parameter and σ for C_2H_6.

We performed posterior predictive checks, which involve drawing parameter values out of the posterior, using those parameters in the likelihood to generate a pseudo dataset, and repeat. This allows us to see whether our Bayesian model can produce the observed data. Below, we show the posterior predictive checks for our analysis (Figure 19). The majority of the measured C_3H_8 and C_2H_6 NOAA data fell into the 30th and 50th percentile of the simulated Bayesian model data.

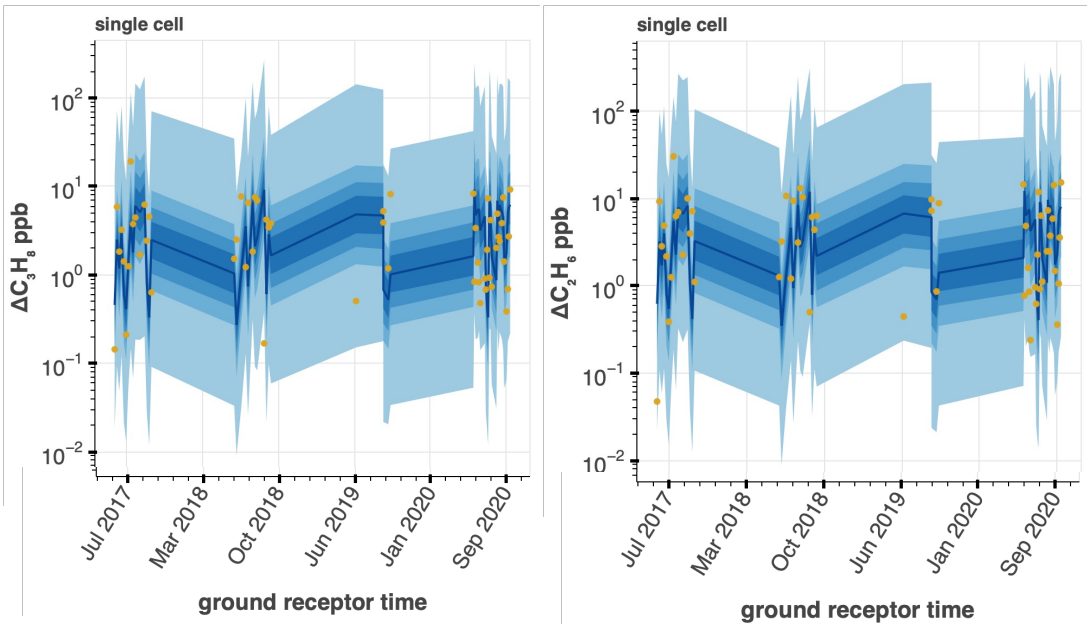

Figure 19. Posterior predictive check of C_3H_8 and C_2H_6 NOAA flask anomalies. Posterior predictive checks are explained in the text above. The pseudo data are shown in blue with 30, 50, 70, and 99th percentiles.

4.4. Future work

We plan to extend the STILT-modeled framework to the column and aircraft measured C_2H_6 and C_3H_8 to diagnose why STILT produces very low mole fraction anomalies compared with the tower observations. One hypothesis, is that a large emission is occurring in close proximity to the site that is not captured in our emissions prior. If this is the case, we anticipate that the column observations and those obtained in situ at higher altitudes will show much less of a divergence from these observaitons. We also plan to expand our Bayesian analysis to find independent emissions scalars for each basin (ie, which basin has the most impact on the observations and what emissions lead to the observations). We will further constrain our prior by including TCCON in the inversion, and need to finish STILT modeling for TCCON columns. This is more computationally intense as we need to advect air from multiple altitude levels.

Author Contributions

J.L.L. created ginput-devel to incorporate chemical profiles into VMR. H.A.P. employed GGG2020 to create TCCON retrievals and conducted additional post-processing. D.W. provided guidance in running STILT for NOAA flasks, and working on code to run STILT using DMF columns from TCCON. A.L.T. ran GEOS-Chem simulations for TCCON priors, processed NOAA flask and TCCON data, ran STILT, prepared y_m, created Bayesian model and ran HMC calculations.

References

(1) U.S. Energy Information Administration. Petroleum & Other Liquids: Oklahoma Field Production of Crude Oil, 2021. https://www.eia.gov/dnav/pet/hist/LeafHandler.ashx?f=M&n=PET&s=MCRFPOK1 (accessed 2021-12-17).

(2) U.S. Energy Information Administration. Natural Gas: Oklahoma Natural Gas Marketed Production, 2021. https://www.eia.gov/dnav/ng/hist/n9050ok2a.htm.

(3) Wunch, D.; Toon, G. C.; Blavier, J.-F. L.; Washenfelder, R. A.; Notholt, J.; Connor, B. J.; Griffith, D. W. T.; Sherlock, V.; Wennberg, P. O. The Total Carbon Column Observing Network. *Philos. Trans. R. Soc. Math. Phys. Eng. Sci.* **2011**, *369* (1943), 2087–2112. https://doi.org/10.1098/rsta.2010.0240.

(4) Laughner, J. L.; Roche, S.; Kiel, M.; Toon, G. C.; Wunch, D.; Baier, B. C.; Biraud, S.; Chen, H.; Kivi, R.; Laemmel, T.; McKain, K.; Quéhé, P.-Y.; Rousogenous, C.; Stephens, B. B.; Walker, K.; Wennberg, P. O. A New Algorithm to Generate a Priori Trace Gas Profiles for the

GGG2020 Retrieval Algorithm. *Atmospheric Meas. Tech.* **2023**, *16* (5), 1121–1146. https://doi.org/10.5194/amt-16-1121-2023.
(5) Parker, H. A.; Laughner, J. L.; Toon, G. C.; Wunch, D.; Roehl, C. M.; Iraci, L. T.; Podolske, J. R.; McKain, K.; Baier, B.; Wennberg, P. O. *Inferring the Vertical Distribution of CO and CO $_2$ from TCCON Total Column Values Using the TARDISS Algorithm*; preprint; Gases/Remote Sensing/Data Processing and Information Retrieval, 2022. https://doi.org/10.5194/amt-2022-322.
(6) Lin, J. C. A Near-Field Tool for Simulating the Upstream Influence of Atmospheric Observations: The Stochastic Time-Inverted Lagrangian Transport (STILT) Model. *J. Geophys. Res.* **2003**, *108* (D16), ACH 2-1-ACH 2-17. https://doi.org/10.1029/2002JD003161.
(7) Wu, D.; Lin, J. C.; Oda, T.; Kort, E. A. Space-Based Quantification of per Capita CO_2 Emissions from Cities. *Environ. Res. Lett.* **2020**, *15* (3), 035004. https://doi.org/10.1088/1748-9326/ab68eb.
(8) Zhang, Y.; Gautam, R.; Pandey, S.; Omara, M.; Maasakkers, J. D.; Sadavarte, P.; Lyon, D.; Nesser, H.; Sulprizio, M. P.; Varon, D. J.; Zhang, R.; Houweling, S.; Zavala-Araiza, D.; Alvarez, R. A.; Lorente, A.; Hamburg, S. P.; Aben, I.; Jacob, D. J. Quantifying Methane Emissions from the Largest Oil-Producing Basin in the United States from Space. *Sci. Adv.* **2020**, *6* (17), eaaz5120. https://doi.org/10.1126/sciadv.aaz5120.
(9) Kort, E. A.; Smith, M. L.; Murray, L. T.; Gvakharia, A.; Brandt, A. R.; Peischl, J.; Ryerson, T. B.; Sweeney, C.; Travis, K. Fugitive Emissions from the Bakken Shale Illustrate Role of Shale Production in Global Ethane Shift: Ethane Emissions From the Bakken Shale. *Geophys. Res. Lett.* **2016**, *43* (9), 4617–4623. https://doi.org/10.1002/2016GL068703.
(10) Alvarez, R. A.; Zavala-Araiza, D.; Lyon, D. R.; Allen, D. T.; Barkley, Z. R.; Brandt, A. R.; Davis, K. J.; Herndon, S. C.; Jacob, D. J.; Karion, A.; Kort, E. A.; Lamb, B. K.; Lauvaux, T.; Maasakkers, J. D.; Marchese, A. J.; Omara, M.; Pacala, S. W.; Peischl, J.; Robinson, A. L.; Shepson, P. B.; Sweeney, C.; Townsend-Small, A.; Wofsy, S. C.; Hamburg, S. P. Assessment of Methane Emissions from the U.S. Oil and Gas Supply Chain. *Science* **2018**, eaar7204. https://doi.org/10.1126/science.aar7204.
(11) Zavala-Araiza, D.; Alvarez, R. A.; Lyon, D. R.; Allen, D. T.; Marchese, A. J.; Zimmerle, D. J.; Hamburg, S. P. Super-Emitters in Natural Gas Infrastructure Are Caused by Abnormal Process Conditions. *Nat. Commun.* **2017**, *8*, 14012. https://doi.org/10.1038/ncomms14012.
(12) Omara, M.; Zavala-Araiza, D.; Lyon, D. R.; Hmiel, B.; Roberts, K. A.; Hamburg, S. P. Methane Emissions from US Low Production Oil and Natural Gas Well Sites. *Nat. Commun.* **2022**, *13* (1), 2085. https://doi.org/10.1038/s41467-022-29709-3.
(13) Stan Development Team. Stan Modeling Language Users Guide and Reference Manual, 2021. https://mc-stan.org.
(14) Stan Dev Team. CmdStanPy (0.9.76), 2021. https://pypi.org/project/cmdstanpy.
(15) Gelman, A. *Bayesian Data Analysis*, Third edition.; Chapman & Hall/CRC texts in statistical science; CRC Press: Boca Raton, 2014.

(16) Kumar, R.; Carroll, C.; Hartikainen, A.; Martin, O. ArviZ a Unified Library for Exploratory Analysis of Bayesian Models in Python. *J. Open Source Softw.* **2019**, *4* (33), 1143. https://doi.org/10.21105/joss.01143.
(17) Bois, J. Justinbois/Bebi103: 0.1.0, 2020. https://doi.org/10.22002/D1.1615.
(18) Rudiger, P.; Stevens, J.-L.; Bednar, J. A.; Nijholt, B.; Mease, J.; Andrew; B, C.; Randelhoff, A.; Tenner, V.; Maxalbert; Kaiser, M.; Ea42gh; Stonebig; Hoxbro; Samuels, J.; Pevey, K.; LB, F.; Tolmie, A.; Stephan, D.; Bois, J.; Lowe, S.; Bampton, J.; Henriqueribeiro; Ruoyu0088; Lustig, I.; Klein, A.; Van De Ven, B.; Raillard, D.; Signell, J.; Talirz, L. Holoviz/Holoviews: Version 1.14.5, 2021. https://doi.org/10.5281/ZENODO.5114034.
(19) Brendan Collins, B. V. D. V. Bokeh: Essential Open Source Tools for Science. **2020**. https://doi.org/10.5281/ZENODO.4317717.
(20) Reback, J.; Jbrockmendel; McKinney, W.; Van Den Bossche, J.; Augspurger, T.; Cloud, P.; Hawkins, S.; Gfyoung; Sinhrks; Roeschke, M.; Klein, A.; Terji Petersen; Tratner, J.; She, C.; Ayd, W.; Hoefler, P.; Naveh, S.; Garcia, M.; Schendel, J.; Hayden, A.; Saxton, D.; Shadrach, R.; Gorelli, M. E.; Jancauskas, V.; Fangchen Li; Attack68; McMaster, A.; Battiston, P.; Skipper Seabold; Kaiqi Dong. Pandas-Dev/Pandas: Pandas 1.3.1, 2021. https://doi.org/10.5281/ZENODO.5136416.
(21) Virtanen, P.; Gommers, R.; Burovski, E.; Oliphant, T. E.; Weckesser, W.; Cournapeau, D.; Alexbrc; Reddy, T.; Peterson, P.; Haberland, M.; Wilson, J.; Nelson, A.; Endolith; Mayorov, N.; Walt, S. V. D.; Ilhan Polat; Laxalde, D.; Brett, M.; Larson, E.; Millman, J.; Lars; Mulbregt, P. V.; Eric-Jones; CJ Carey; Moore, E.; Kern, R.; Peterbell10; Leslie, T.; Perktold, J.; Striega, K. Scipy/Scipy: SciPy 1.6.2, 2021. https://doi.org/10.5281/ZENODO.4635380.
(22) Harris, C. R.; Millman, K. J.; van der Walt, S. J.; Gommers, R.; Virtanen, P.; Cournapeau, D.; Wieser, E.; Taylor, J.; Berg, S.; Smith, N. J.; Kern, R.; Picus, M.; Hoyer, S.; van Kerkwijk, M. H.; Brett, M.; Haldane, A.; del Río, J. F.; Wiebe, M.; Peterson, P.; Gérard-Marchant, P.; Sheppard, K.; Reddy, T.; Weckesser, W.; Abbasi, H.; Gohlke, C.; Oliphant, T. E. Array Programming with NumPy. *Nature* **2020**, *585* (7825), 357–362. https://doi.org/10.1038/s41586-020-2649-2.
(23) Talts, S.; Betancourt, M.; Simpson, D.; Vehtari, A.; Gelman, A. Validating Bayesian Inference Algorithms with Simulation-Based Calibration. *ArXiv180406788 Stat* **2020**.

Appendix S

Supplementary Information for "Hydrocarbon Tracers Suggest Methane Emissions from Fossil Sources Occur Predominately Before Gas Processing and that Petroleum Plays Are a Significant Source"

S1. Economics and Production of Oil & Natural Gas

The development of the hydraulic fracturing (fracking) technique has led to a widespread increase in the production of associated and non-associated natural gas,[1] as well as natural gas liquids, or NGLs (Figure S1, left and Figure S2). NGLs are extracted with raw gas and are, just after extraction, often separated from the stream to yield consumer-grade natural gas and the more valuable alkane liquids.[2] Basins with petroleum typically have a larger composition of ethane and propane and other NGLs, whereas "dry" basins, such as Fayetteville and Appalachian in the U.S., tend to provide mostly dry natural gas with low fractions of NGLs.[3] By volume, ethane, C_2H_6, is the second most abundant component of natural gas after CH_4, while propane (C_3H_8) is the third most abundant.[4] The fraction of C_2H_6 (but not C_3H_8) removed during gas processing changes significantly over time. Over the last 10 years, the dramatic increase of C_2H_6 production (Figure S1, left) has exceeded domestic demand or ability to export it abroad,[5] resulting in C_2H_6 prices generally at or below natural gas since 2012 (Figure S1, right).[6,7] As a result, it is often more economical to sell C_2H_6 as natural gas rather than separate it from the raw stream. Producers can increase the amount of C_2H_6 they sell as natural gas by "rejecting" it (not recovering it). Rejection of C_2H_6 has continued to grow almost continuously over the past decade (Figure S1, right) resulting in increasing abundance of C_2H_6 in the natural gas distribution system.

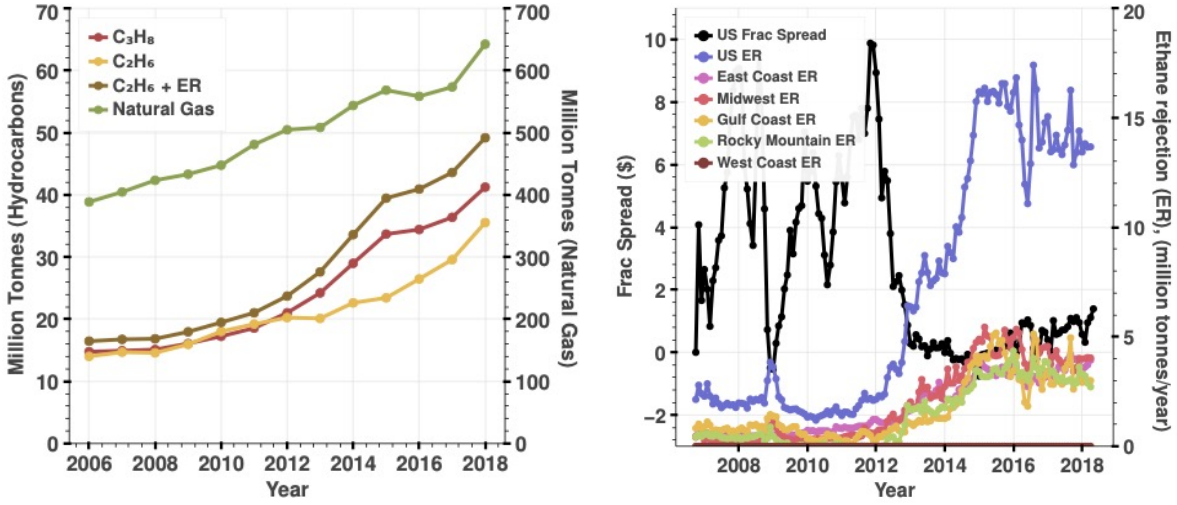

Figure S1. Economic trends of natural gas and natural gas liquids. **Left**: Trends in natural gas and hydrocarbon production (EIA) and total ethane summed with rejected ethane modeled by OPIS, Point Logic, provided by IHS Markit. **Right**: The value of ethane compared to natural gas

represented by fractionation spread (frac spread) on the left axis. Ethane rejection in the U.S. and major U.S. refining areas is plotted on the right axis. (Data by OPIS, Point Logic, provided by IHS Markit.)

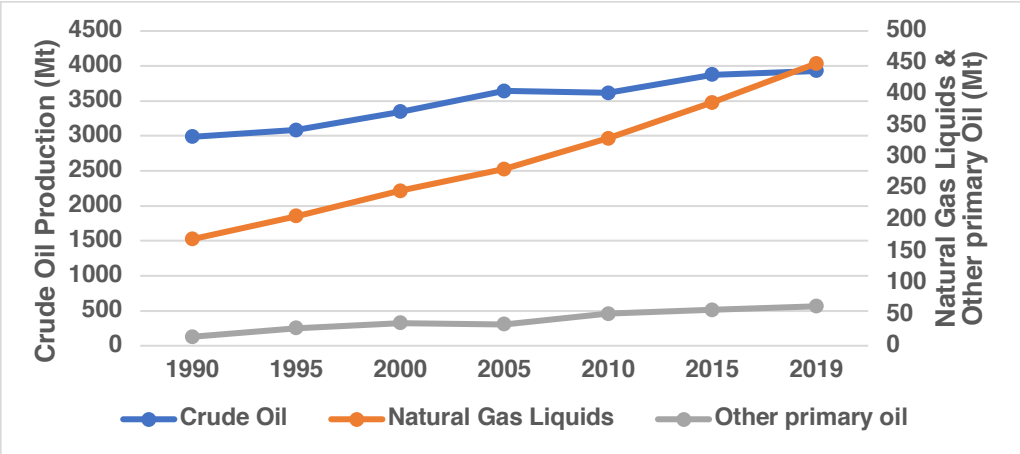

Figure S2. Global oil production. Data provided by IEA (https://www.iea.org/fuels-and-technologies/oil).

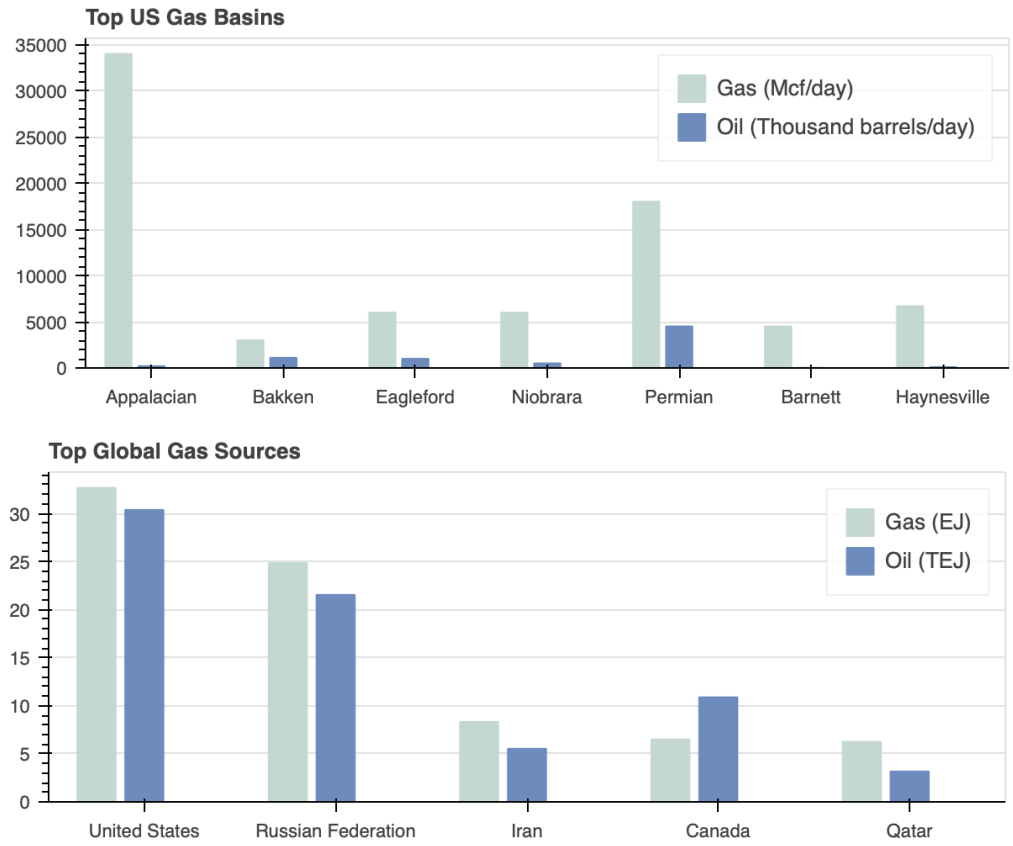

Figure S3. Top Natural Gas-Producing US basins/Countries and their corresponding oil production. **Top**: Oil and gas production for the top 7 natural gas producing basins that account for 86% of total U.S. natural gas production.[8,9] **Bottom**: Global oil and gas production for the top 5 natural gas producing countries that account for 50% of global natural gas production.[10,11]

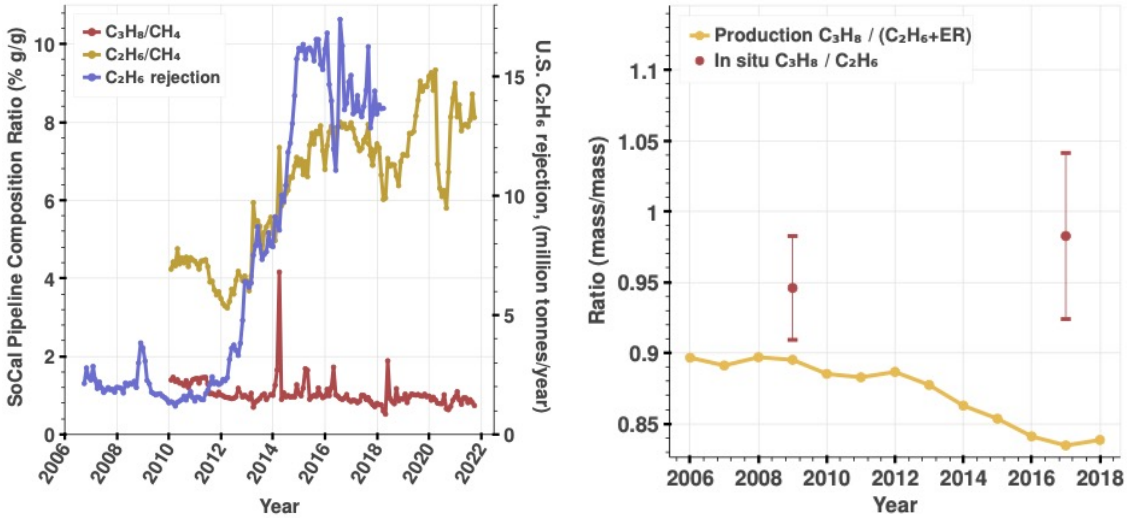

Figure S4. Observed pipeline composition in Playa del Rey and ethane rejection trends. **Left:** The ratio of propane/methane and ethane/methane measured in natural gas withdrawn from Playa del Rey in Southern California,[12] compared to U.S. ethane rejection (see Figure S1 for more

information on rejection; data provided by IHS Markit). **Right**: The ratio of U.S. propane production and total ethane production (including rejection, ER). The production data is provided by EIA[13,14]s and the rejection data is provided by IHS Markit. The in-situ observed ratio is calculated from NOAA-ongoing observations, see Figure S9.

S2. NOAA & FRAPPE Observations

S2.1 Processing and statistical methods

Ethane and propane mole fraction data from aircraft measurements, tall tower, and surface flasks are publicly available at https://gml.noaa.gov/ccgg/arc/?id=155. Methane mole fraction data is publicly available at https://gml.noaa.gov/ccgg/obspack/data.php?Id=obspack_multi-species_1_CCGGAircraftFlask_v2.0_2021-02-09, https://gml.noaa.gov/ccgg/obspack/data.php?Id=obspack_multi-species_1_CCGGSurfaceFlask_v2.0_2021-02-09, and https://gml.noaa.gov/ccgg/obspack/data.php?Id=obspack_multi-species_1_CCGGTowerInsitu_v1.0_2018-02-08.

We first discuss NOAA ongoing observations. We use measurement quality flags labeled as either preliminary or good sampling and analysis only. Some sites had an unequal number of quality measurements between alkane species, so we match UTC time stamps that are shared between each species to avoid sampling bias. We drop any corresponding paired measurements of CH_4, C_2H_6 and C_3H_8 that are labeled as NaN (all three pairs are dropped). Figure S5 shows the spatial location of the NOAA ongoing observation sites used in this analysis, and Table S1 lists the temporal and spatial coverage offered at each site. Most sites offered a few measurements each week for the years indicated.

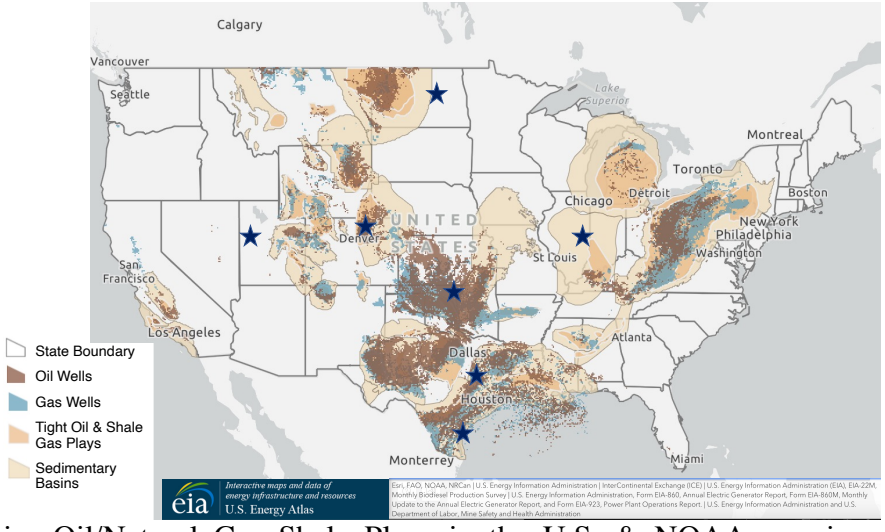

Figure S5. Major Oil/Natural Gas Shale Plays in the U.S. & NOAA ongoing measurement locations. Approximate geographical locations of NOAA ongoing measurement locations are shown in the blue stars on the map. Not pictured is East Trout Lake (ETL) site, located in

Saskatchewan, Canada (54.3541N, 104.9868W). Well and basin layers provided by https://atlas.eia.gov/apps/all-energy-infrastructure-and-resources/explore .

Table S1. Sites for NOAA Ongoing Observations in the U.S.

Site Location	**Site Abbreviation**	**Years**	**Measurement Method**	**Processing lab**
Homer, IL	HIL	2015 - 2018	Aircraft/Tower	CCGG, HATS
Lamont, OK	SGP	2006 - 2017	Aircraft/Tower	CCGG
Dahlen, ND	DND	2014 - 2016	Aircraft/Tower	CCGG, HATS
East Trout Lake, Canada	ETL	2014 - 2018	Aircraft/Tower	CCGG, HATS
Wendover, UT	UTA	2006 - 2016	Tower	CCGG, ARL
Boulder, CO	BAO	2014 - 2016	Tower	CCGG, HATS
Moody, TX	WKT	2015 - 2018	Tower	CCGG, HATS
Sinton, TX	TGC	2015 - 2018	Aircraft/Tower	CCGG, HATS
Niwot Ridge, CO	NWR	2005-2014	Tower	CCGG, ARL

For FRAPPE, we also use 1000 meters as a marker for the boundary layer, and analyze measurements taken above it. We also drop any corresponding paired measurements of CH_4, C_2H_6 and C_3H_8 that are labeled as NaN (all three pairs are dropped). Figure S6 shows the spatial location of the FRAPPE observations (after filtering) in Colorado.

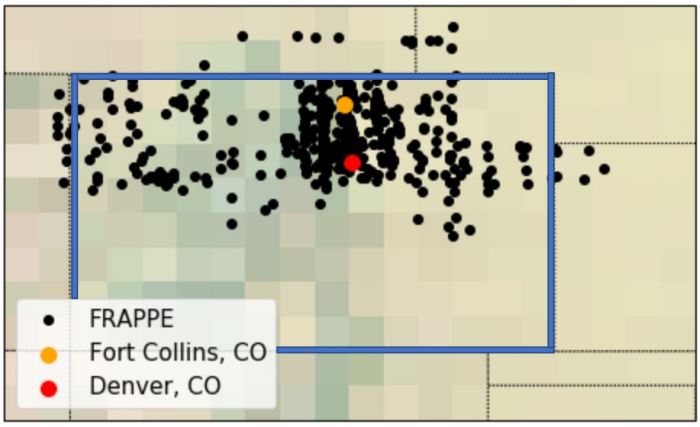

Figure S6. FRAPPE observations. The outline of Colorado state is shown in blue. We show data already pre-processed and filtered for fresh emissions, as discussed in this section.

To better quantify geophysical variability and generate a confidence interval in the correlation in measured mole fractions between C_2H_6 and C_3H_8, we implement a pairs bootstrap to generate replicates of C_2H_6 and C_3H_8 observations for NOAA and FRAPPE observations. We draw random samples of pairs of C_2H_6 and C_3H_8, where instead of drawing two random samples of each array, we draw the same indices from both arrays so we end up with paired samples, since C_2H_6 and C_3H_8 were measured together and we want to compute the correlation. We draw samples the size of the dataset, then compute the slope of the correlation. We repeat this 10,000 times. As shown for different scenarios below, we perform this bootstrap for individual sites separately, as well as all sites combined. The confidence interval reported for correlations between C_2H_6, C_3H_8, and CH_4 anomalies is the 95% CI of the 10,000 samples. The CIs calculated from the bootstrapped samples are much broader than those calculated assuming the noise in the measurements is dominated by analytical errors. This suggests that geophysical noise induced by differences in transport and chemistry dominates the statistics.

S2.2 Chemical aging approach to determining methane background

We take a chemical aging approach to defining the threshold between samples associated with fresh emissions (unaged) and photochemically aged emissions. As in Parrish et al 2018,[15] we observe both fresh and aged regimes (Figure S7 below). We chose the 50th percentile of C_3H_8 as the demarcation between these regimes (about 10^3 ppt) and show in Figure S10 that our analysis of the ethane and propane ratio to methane is not terribly sensitive to the choice. This threshold will clearly depend on the fraction of samples obtained in the two regimes.

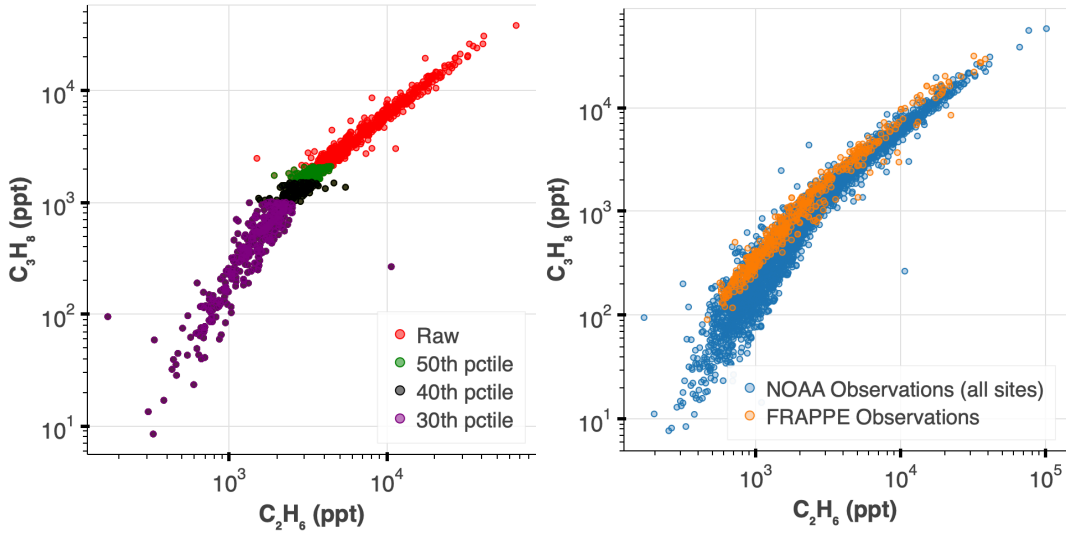

Figure S7. Identifying fresh emission chemical regime in NOAA and FRAPPE campaigns. **Left**: Varying C_3H_8 percentiles at the NOAA SGP site. The inflection point between aged and fresh emission regime is visually contained within varying the C_3H_8 percentile cutoff by $\pm$ 10%. We chose the 50th percentile of C_3H_8 as the demarcation between these regimes (about 10^3 ppt). **Right**: C_3H_8 vs C_2H_6 using FRAPPE data (already pre-processed, as described in the methods in the main text). FRAPPE observations are quite consistent with NOAA, hence we use the same C_3H_8 demarcation between the aged and fresh chemical regime.

After filtering for fresh emissions using C_3H_8 percentile method, two NOAA observation sites (NWR and UTA) only showed aged emissions (Figure S8). Consequently, these sites were not used in the subsequent analysis.

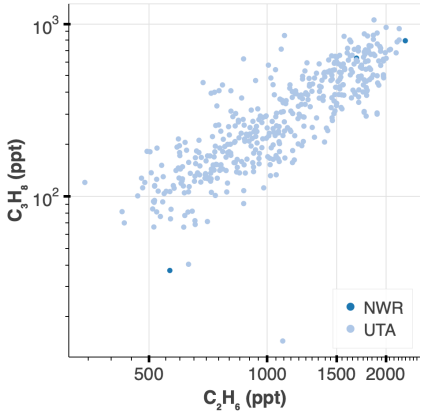

Figure S8. NOAA C_3H_8 vs C_2H_6 after filtering for fresh emissions. We used C_3H_8 50th percentile as a marker for fresh emissions (please see details in text above). Sites NWR and UTA only had C_3H_8 mole fractions below this demarcation and were assumed to be affected only by aged emissions, and as such, were excluded from further analysis.

After filtering for fresh emissions using C_3H_8 percentile method, the cross plot of C_3H_8 vs C_2H_6 is similar for all NOAA sites, NOAA SGP only, and FRAPPE observations (Figure S9).

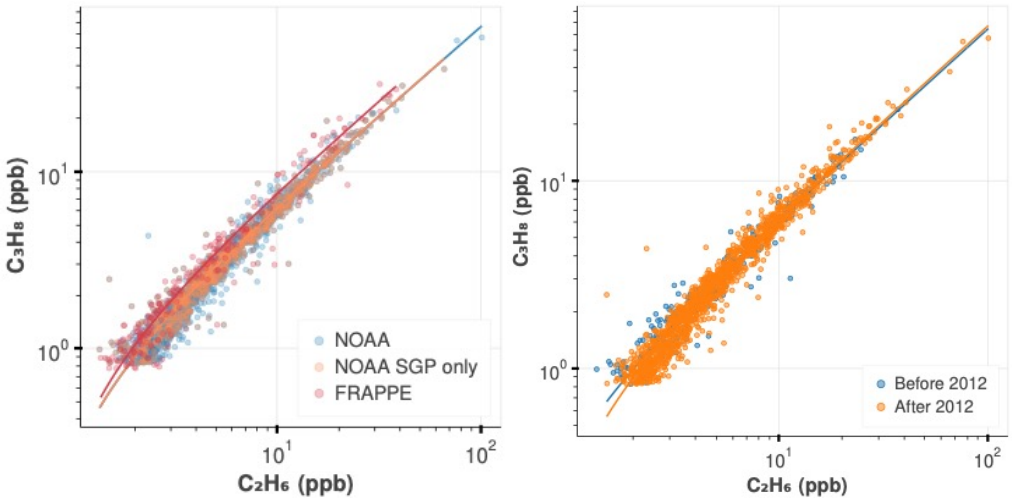

Figure S9. C_3H_8 vs C_2H_6 after filtering for fresh oil and gas emissions. **Left**: The filtering method is described in Section 3.1. We show observations for all NOAA sites (2005-2018, see Table S1), NOAA for SGP site only (2006-2018 Oklahoma tower and aircraft observations), and FRAPPE campaign (2014 aircraft observations around Colorado). Top: FRAPPE linear least squares slope 95% CI is [0.76, 0.87] (ppb/ppb, $R^2 = 0.97$) compared to [0.63, 0.70] (ppb/ppb, $R^2 = 0.98$) for all NOAA sites. Variability in the slope for both FRAPPE and NOAA is given by a pairs bootstrap analysis, described in Section 2.1. **Right**: Slope before 2012 (2005-2011): [0.62, 0.67] (95% CI), $R^2 = 0.98$. Slope after 2012 (2012-2018): [0.63, 0.71] (95% CI), $R^2 = 0.98$. We use data from SGP, TGC, ETL, HIL, DND, BAO, and WKT sites (see Table S1) before filtering for air influenced by fresh oil/gas emissions, which is shown here. We use both tower and aircraft data. We use pairs bootstrapping to arrive at confidence intervals, described in detail in Section 2.1.

After identifying the fresh emissions, we defined a background for CH_4 observations and constructed CH_4 anomalies by doing the following:

- Find corresponding co-CH_4 measurements in the aged air regime as identified by C_3H_8 mole fraction (below 10^3 ppt C_3H_8).
- Interpolate this CH_4 array to the full timeseries using time to obtain a CH_4 background.
- Subtract this interpolated background from the full CH_4 array to obtain a CH_4 anomaly. Note that because the CH_4 lifetime is much longer than either C_2H_6 or C_3H_8, the differences are much smaller.

Since we only focus on the linear part of the curve, our analysis is not terribly sensitive to how the CH_4 anomaly is determined (it simply produces varying intercepts, see our quantitative analysis on the impact on the slope in Figure S10). Again, to get C_3H_8/ C_2H_6, we only consider the fresh emission

regime (beyond 10^3 ppt C_3H_8). Figure S10 shows our calculated CH_4 background and CH_4 anomalies for the NOAA SGP site (near Lamont, OK).

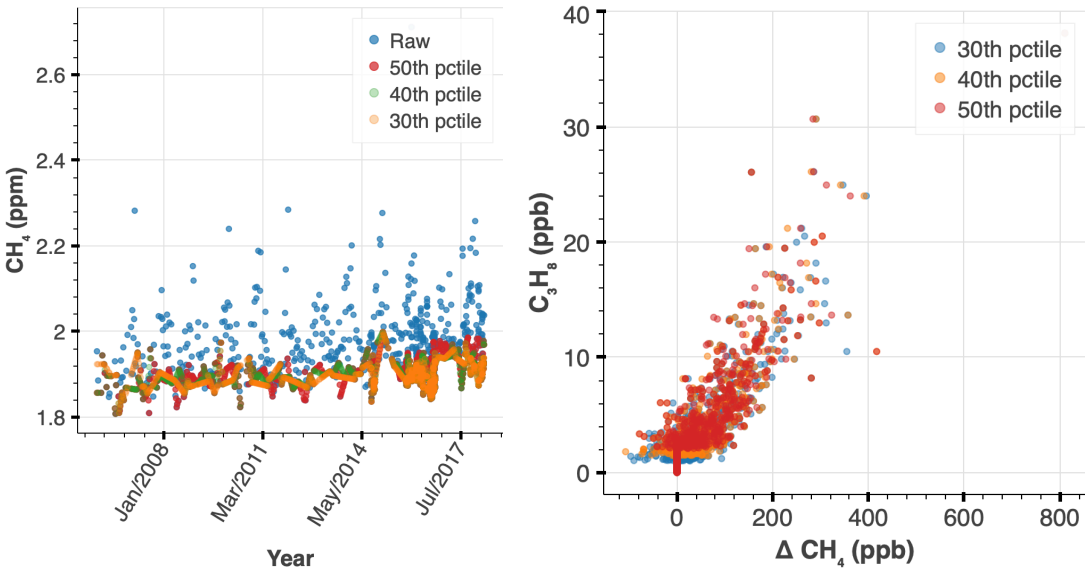

Figure S10. Background estimate for CH_4 at NOAA SGP site**. Left**: Using 50% ±10% percentile cutoff of C_3H_8 has a minimal effect on the background CH_4 estimation. **Right**: C_3H_8 vs CH_4 Anomaly at NOAA SGP site. A CH_4 anomaly is calculated by linearly interpolating the estimated CH_4 background to the raw CH_4 measurement timescale. The interpolated background is then subtracted from the raw CH_4 measurements. Using 50% ±10% percentile cutoff of C_3H_8 has a minimal effect on CH_4 anomaly cross plots. Using a pairs bootstrap approach (see Section S2.1), we generate thousands of slope replicates and calculate the following 95% CIs for the slope using the following C_3H_8 percentile cutoffs: [0.0458, 0.0526] (30^{th} percentile); [0.0460, 0.0534] (40^{th} percentile); [0.0481, 0.0563] (50^{th} percentile).

Below in Figure S11, we show the result of our CH_4 background calculations for each NOAA site.

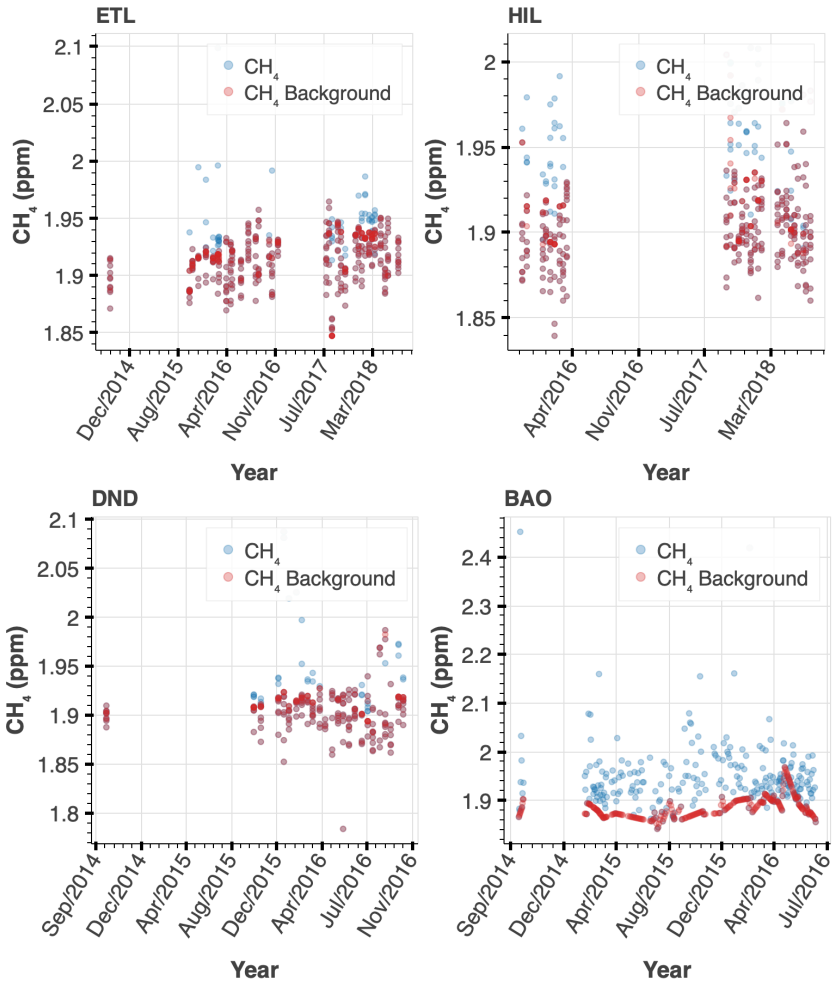
ETL
HIL
DND
BAO
CH4
CH4 Background
CH4 (ppm)
Year
Dec/2014
Aug/2015
Apr/2016
Nov/2016
Jul/2017
Mar/2018
Sep/2014
Dec/2015
Jul/2016

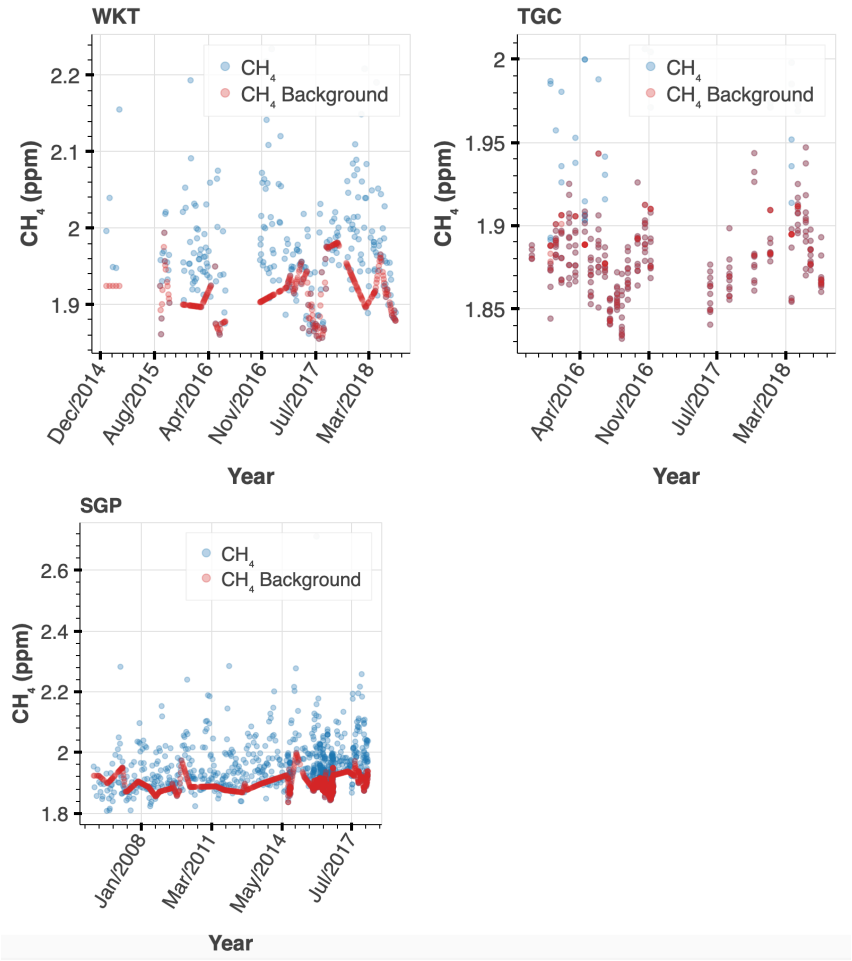

Figure S11. Methane vs time for NOAA sites. The estimated background is shown in red. Raw CH_4 data is shown in blue. The background was calculated using 50% C_3H_8 percentile cutoff method.

S2.3 Methane anomaly plots for NOAA and FRAPPE campaigns

Below, we show the results of our CH_4 anomaly calculations for NOAA and FRAPPE observations using the methods described in Section 2.2 (above). First, we show correlations for individual NOAA sites (Figures S12, S13), followed by a comparison between NOAA SGP site (Oklahoma site) and FRAPPE observations (Figure S14).

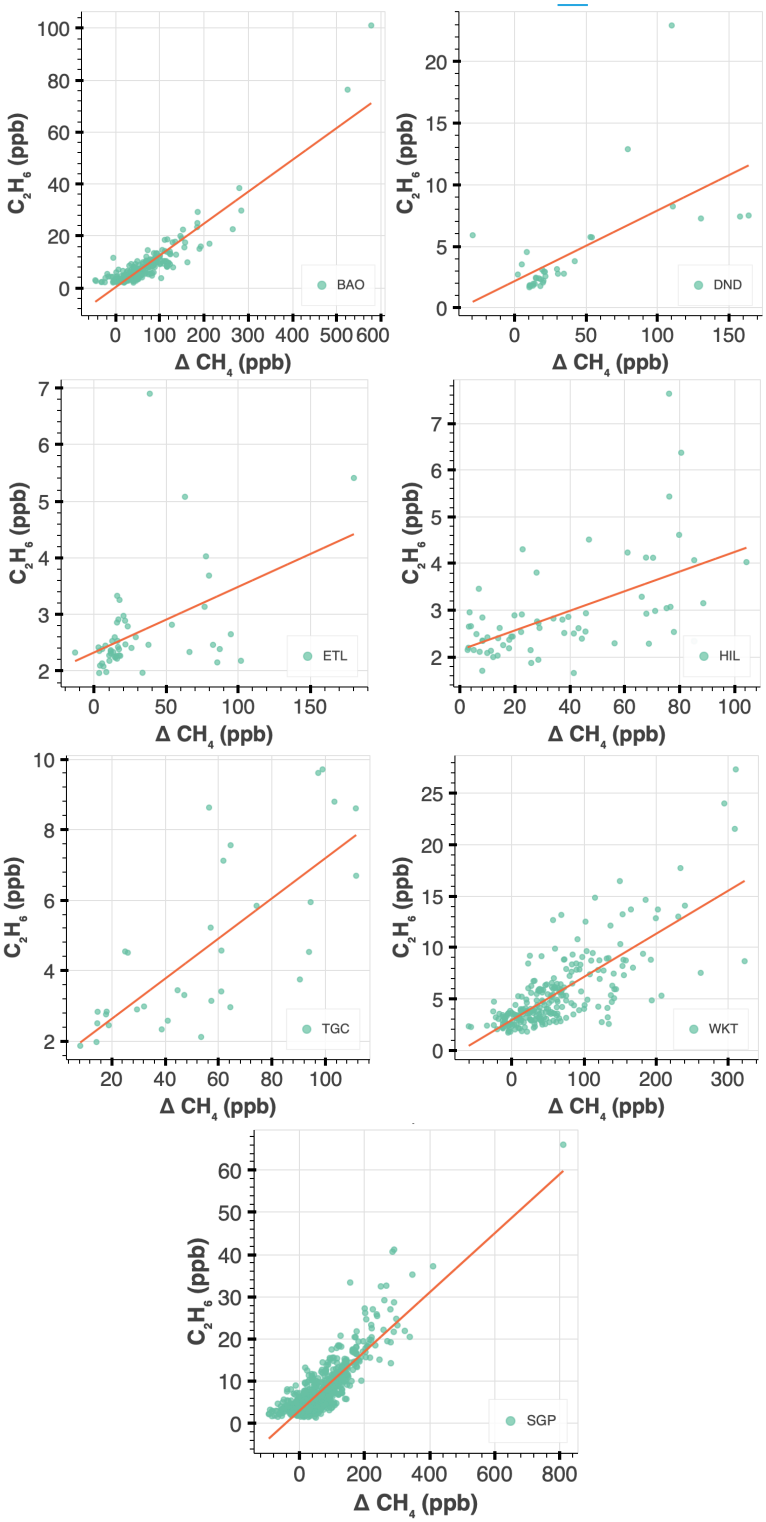

Figure S12. C_2H_6 vs CH_4 anomaly for NOAA sites. The data for each site were filtered using the chemical aging regime to filter for fresh emissions and to construct CH_4 anomalies (Section 2.2). See Table S1 for a description of site location/observation type. We also ran a bootstrap for each individual site (bootstrapping methods, main text). The 95% CI slopes (ppb/ppb) are as follows: BAO: [0.0833, 0.1449], R^2 = 0.91; DND: [0.0289, 0.1205], R^2 = 0.63; ETL: [0.0030, 0.0176], R^2

= 0.46; HIL: [0.0116, 0.0313], R^2 = 0.56; TGC: [0.0400, 0.0730], R^2 = 0.74; WKT: [0.0324, 0.0510], R^2 = 0.75; SGP: [0.0645, 0.0749], R^2 = 0.86.

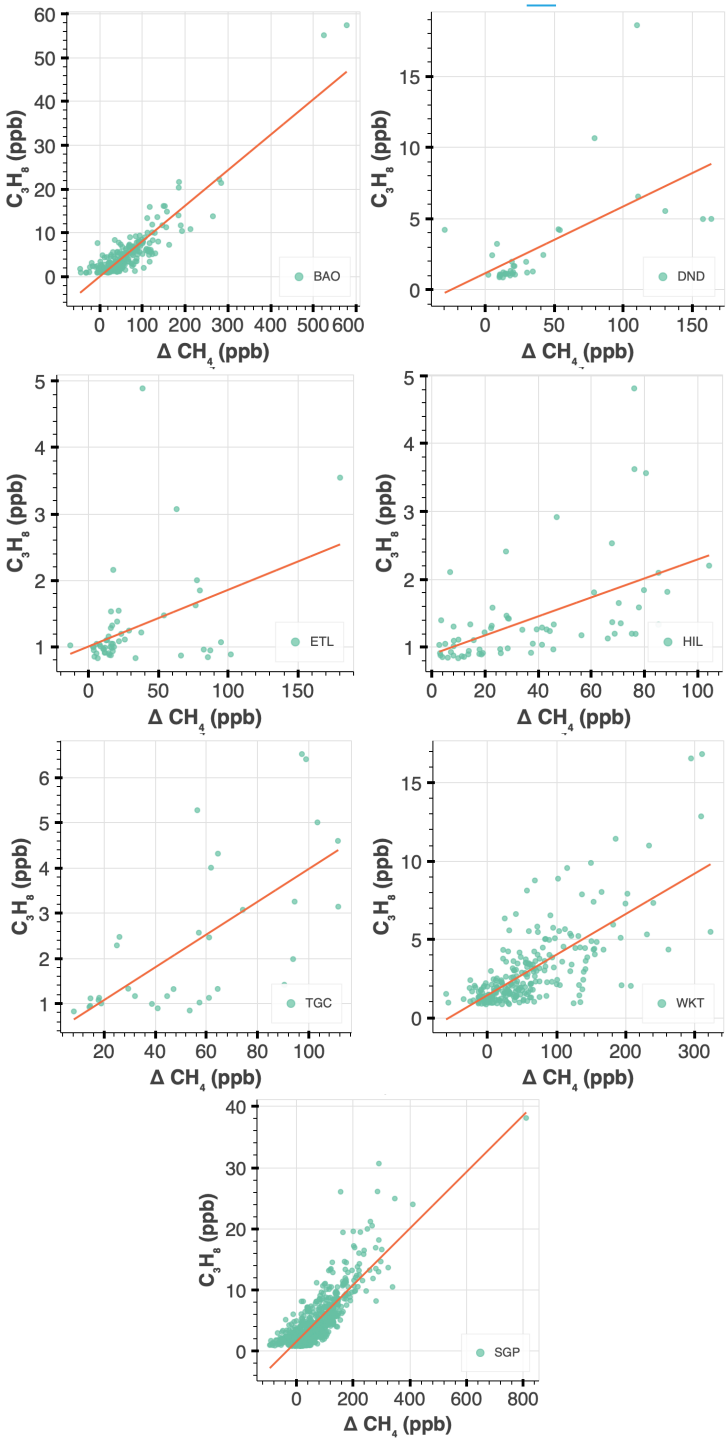

Figure S13. C_3H_8 vs CH_4 anomaly for NOAA sites. The data for each site were filtered using the chemical aging regime to filter for fresh emissions and to construct CH_4 anomalies (Section 2.2). See Table S1 for a description of site location/observation type. We also ran a bootstrap for each individual site (bootstrapping methods, main text). The 95% CI slopes (ppb/ppb) are as follows: BAO: [0.0587, 0.0922], $R^2 = 0.91$; DND: [0.0221, 0.1003], $R^2 = 0.61$; ETL: [0.0013, 0.0136], $R^2 = 0.41$; HIL: [0.0078, 0.0216], $R^2 = 0.54$; TGC: [0.0228, 0.0506], $R^2 = 0.68$; WKT: [0.0195, 0.0321], $R^2 = 0.71$; SGP: [0.0426, 0.0499], $R^2 = 0.83$.

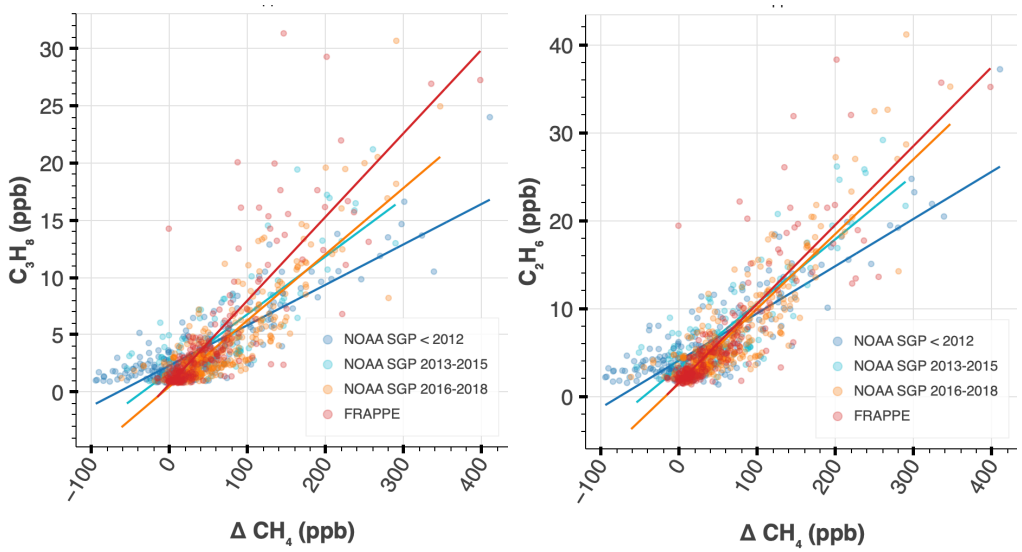

Figure S14. C_2H_6 vs CH_4 anomaly for NOAA SGP site and FRAPPE study. We use the chemical aging approach defined in Section 3.1 to identify C_3H_8 and CH_4 observations within a fresh oil and gas emissions chemical regime. We construct CH_4 background-corrected anomalies as described in SI Section S2. Results with C_2H_6 are similar and shown in Figure S9. NOAA observations for SGP site (Oklahoma, Table S1) are shown here. We show correlations between 2006-2011, labeled as "NOAA SGP < 2012" (HIPPO takes place between 2009-2011), 2013-2015 (FRAPPE takes place in 2014), and 2016-2018 (ATom time period). **Left**: The slope of the correlation between C_3H_8 and CH_4 anomaly for NOAA observations before 2012 is [0.031, 0.040] ppb/ppb, $R^2 = 0.85$; between 2013-2015 is [0.045, 0.084], $R^2 = 0.82$; and between 2016-2018 is [0.039, 0.059], $R^2 = 0.86$. FRAPPE is [0.063, 0.085] ppb/ppb, $R^2 = 0.83$. The slope of the correlation for all years of NOAA is [0.043, 0.050] ppb/ppb, $R^2 = 0.83$. C_3H_8 vs CH_4. **Right**: C_2H_6 vs CH_4 The FRAPPE slope (95% CI, ppb/ppb) is [0.0763, 0.1047], $R^2 = 0.85$. C_2H_6 vs CH_4 NOAA slope for all years is [0.0647, 0.0749], $R^2 = 0.86$. The C_2H_6 vs CH_4 slope before 2012 is [0.047, 0.060], $R^2 = 0.85$; from 2013-2015 is [0.066, 0.143], $R^2 = 0.85$; and from 2016-2018 is [0.058, 0.084], $R^2 = 0.88$.

S2.4 Maps of FRAPPE and NOAA SGP observations compared to oil and gas sites

Below, we show the location of the NOAA samples taken at the SGP site in Oklahoma, which include a combination of aircraft and tower measurements (Figure S15). We add the approximate location on top of a USGS map of oil and gas sites in Oklahoma, using coordinates for Lamont and Billings for reference (Figure S16), where we see that the SGP measurements are taken around a mix of oil and gas sites. We include a figure of Oklahoma oil and gas production by county (Figure S17), where we see widespread surrounding oil and gas production.

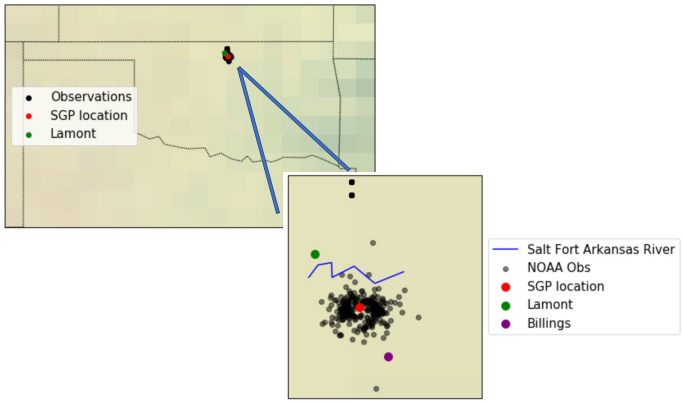

Figure S15. NOAA observations at SGP site (Oklahoma). The observations shown here are pre-processed and filtered for fresh emissions as discussed in the methods section in the main body.

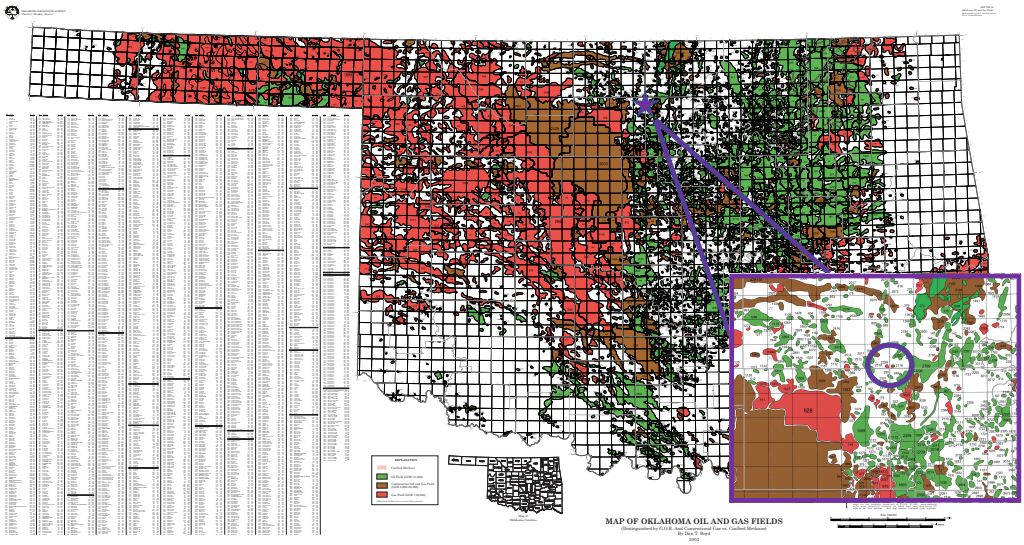

Figure S16. Oklahoma oil and gas wells. Plot adapted from Oklahoma Geological Survey[16]: http://www.ogs.ou.edu/fossilfuels/MAPS/GM-36.pdf.

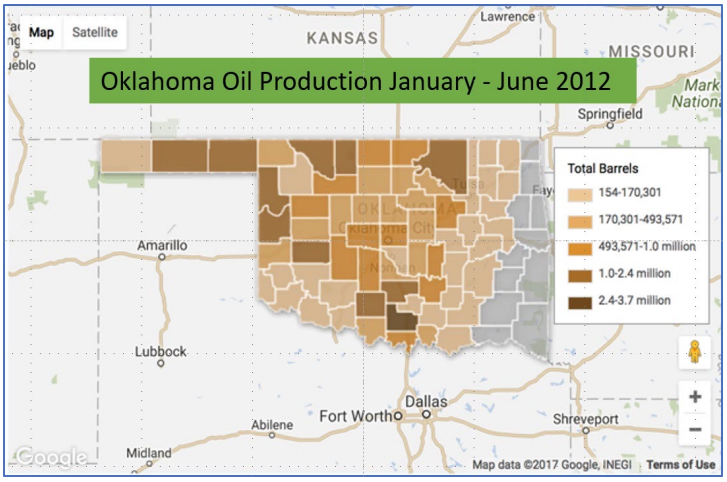

Figure S17. Oklahoma oil and gas production by county**.** Plot was created by Joe Wertz of StateImpact Oklahoma[17].

Below, we include a plot by Water Education Colorado showing the value of oil and gas production value by county (Figure S18). If we compare it to Figure S6, it is evident that much of the FRAPPE observations were taken around nearby oil-producing wells that produce significant revenue. This is consistent with the large C2 and C3 to C1 emission ratios observed during the FRAPPE campaign (Figure 13, main text).

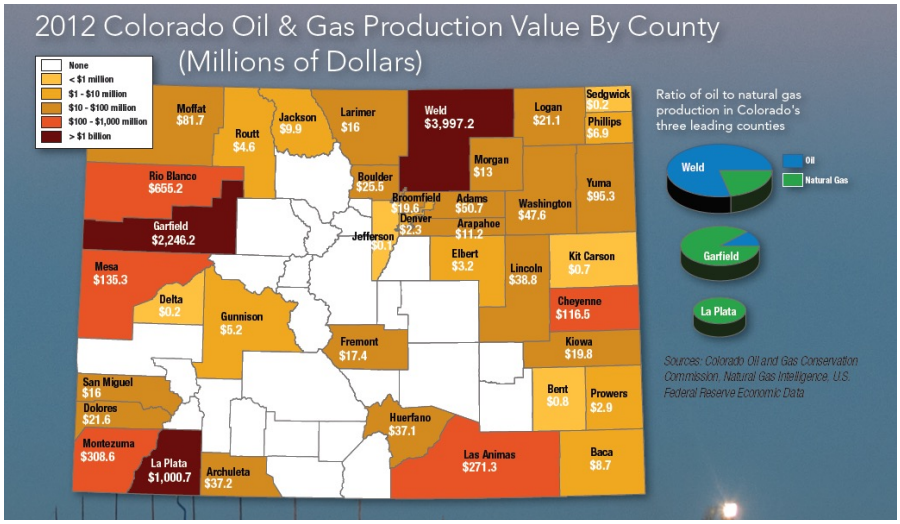

Figure S18. Oil and gas production value by county in Colorado. The plot was obtained from Water Education Colorado (founded by Colorado State Legislature).[18]

S2.5 Comparison to Lan et al. 2019 study

Lan et al. 2019 investigated C_3H_8/CH_4 and C_2H_6/CH_4 ratios using NOAA-ongoing observations. Consistent with their study, we find increasing C_3H_8/CH_4 and C_2H_6/CH_4 ratios over time with relatively similar slopes. However, we find no statistically significant temporal trend in C_3H_8/C_2H_6. As shown in Figure S9 and in the additional cross plot of C_3H_8 and C_2H_6 colored by time (Figure S19, left), the correlation of these gases in the 'fresh emissions' regime is identical within error. Even when excluding aircraft data for SGP site, the ratio remains nearly the same (Figure S19, right).

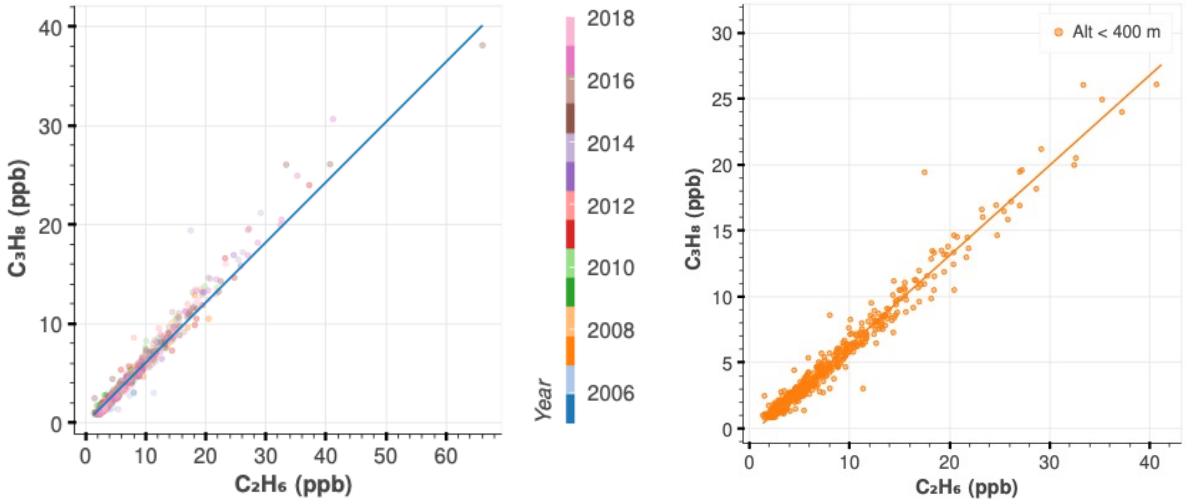

Figure S19. C_3H_8 and C_2H_6 correlation at NOAA SGP site– yearly and tower observations. **Left**: C_3H_8 vs C_2H_6 colored by all years for the NOAA SGP site. Slope: [0.63, 0.70] (95% CI), R^2=0.98. **Right**: Slope of C_3H_8 vs C_2H_6 for ground- and tower-based measurements NOAA SGP site. (The highest tower sampling is 374m sampling at SGP.) The slope is [0.66, 0.70], and R^2=0.99, comparable to [0.63, 0.70] 95% CI slope of the correlation that includes both aircraft and tower observations (this Figure, left side). We bootstrapped the samples to obtain a 95% CI (see methods, main text).

Our C_3H_8 anomalies are calculated in a different fashion than in Lan et al. 2019. Given the curvature of the correlation (Figure 1, main text) and its seasonal dependence, we determine the slope of the C_3H_8 and CH_4 anomalies only within the fresh emission regime ($C_3H_8 > 10^3$ ppt, along with co-measurements of CH_4, see Section 2.2). Since we only focus on the linear part of the curve, our analysis is not terribly sensitive to how the CH_4 anomaly is determined (it simply produces varying intercepts). To estimate C_3H_8/C_2H_6, we also only consider the fresh emission regime (beyond 10^3 ppt C_3H_8).

We replicate Figure 3a,b from Lan et al. 2019 using our methods in Figure S20. Even with very different methodology, our results for the central value of the emissions ratio between C_3H_8 and C_2H_6 and CH_4 anomalies are similar, albeit Lan et al. claims a much smaller uncertainty in these

ratios (51.2 ± 0.6ppt/ppb and 80.5 ± 2.5ppt/ppb, respectively) such that the interannual variation and the trend over the record far exceed the stated uncertainty. Our 95% CI of the slope for C_3H_8/CH_4 is [42.57, 49.87] and for C_2H_6/CH_4 is [64.66, 74.89] (both in ppt/ppb) where most of the CI spread results from the temporal trend (see Figure S20).

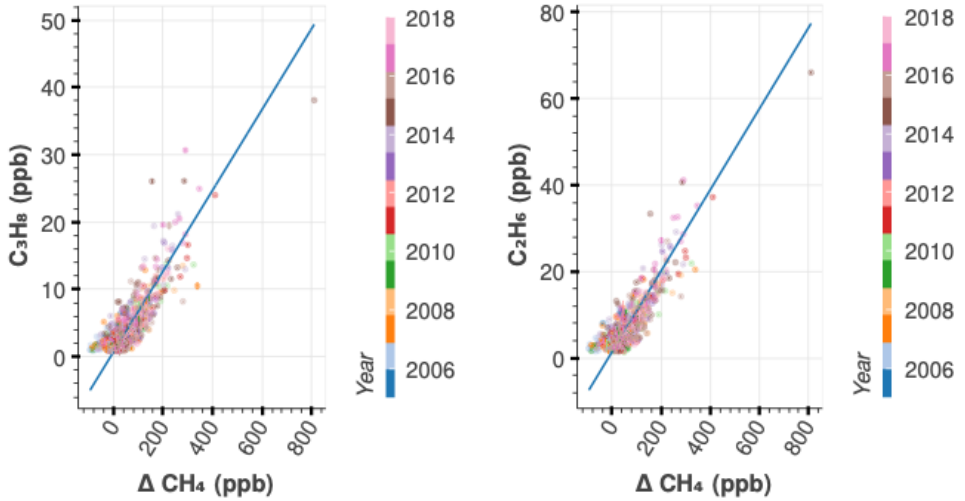

Figure S20. NOAA C_3H_8 and C_2H_6 vs CH_4 anomaly colored by year. Data is for SGP site only. $C_3H_8/\Delta CH_4$ slope: [0.43, 0.50] ppb/ppb, R^2= 0.83. $C_2H_6/\Delta CH_4$ slope: [0.65, 0.75] ppb/ppb, R^2= 0.86. We use data within the fresh emission regime (see Section 2.2). Our methods for determining CH_4 anomalies are described in detail in section 2.3, and our methods for determining the 95% CI via bootstrapping is described in the methods section of the main text.

We reproduce Figure 3e from Lan et al. 2019 in Figure S21, below. In Figure S21, the variability in ratios each year is constructed from the 95% confidence interval of the slopes from samples of a pairs bootstrap, described in more detail in section 2.1 As in Lan et al., we find significant trends in C_3H_8/CH_4 anomalies (3.12 ± 0.63 ppt/ppb/year), and C_2H_6/CH_4 anomalies (3.89 ± 0.84 ppt/ppb/year), which are comparable to their result. On the right side of Figure S21, we plot the fractional change relative to the mean. Instead, we find that both ratios are fractionally increasing at the same rate. The reported error in the slope is simply the standard error calculated from a linear regression of the yearly slopes vs year (that includes the upper and lower CI points). We use the linear trend of anomalies/year (Figure S21, left) to calculate mean anomaly ratios for SGP during 2016-2018 to be [0.060, 0.061] ppb/ppb (and C_2H_6/CH_4 to be 0.086, 0.088]), where the interval is determined using the standard error in the slope.

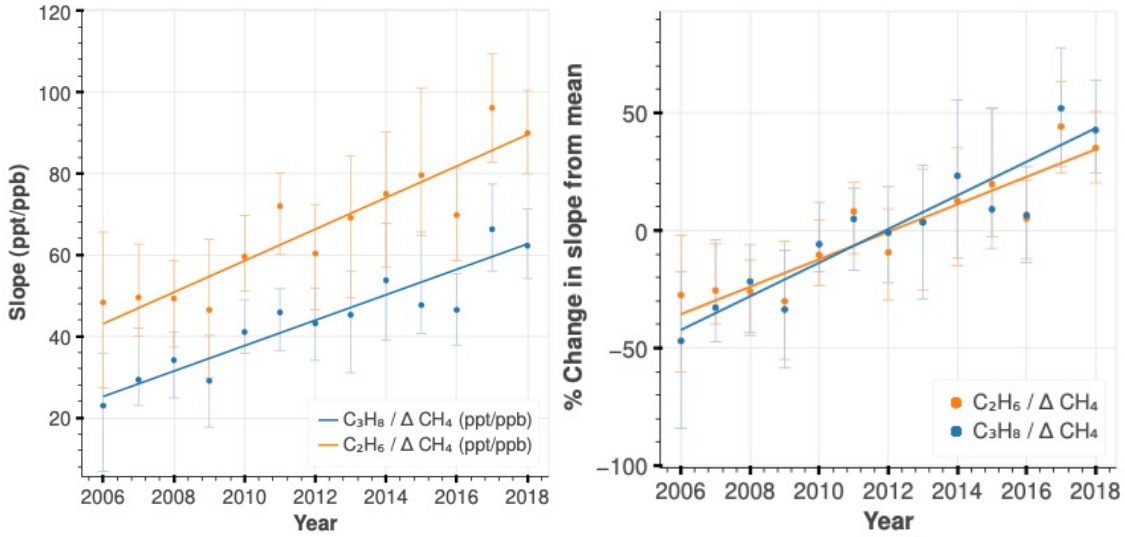

Figure S21. Yearly correlation between NOAA hydrocarbon vs CH_4 anomaly. **Left**: Average hydrocarbon vs CH_4 anomaly for each year for NOAA SGP site. C_3H_8/CH_4 anomaly slope: 3.12 ± 0.63 ppt/ppb/year (R^2=0.71), and C_2H_6/CH_4 anomaly trend is 3.89 ± 0.84 ppt/ppb/year (R^2=0.69). The variability in the trend (ppt/ppb/year) comes from the standard error of a linear regression. The variability in the yearly slope (ppt/ppb) comes from the 95% confidence interval of a pairs bootstrap (we ran a pairs bootstrap for co-measurements of C_3H_8 and ΔCH_4 and compute the slope of the correlation for each bootstrap sample and repeated this for every year in the data; please see the methods section of the main text for more information about pairs bootstrapping). **Right**: Same as left, but in units of percent change with respect to the mean hydrocarbon and methane anomalies. The resulting trend for C_3H_8/CH_4 is 7.13 ± 1.44 % with an R^2 of 0.71. The trend for C_2H_6/CH_4 is 5.87 ± 1.26 % with an R^2=0.69. Both trends are calculated in the same way as the left figure.

Our analysis of the NOAA data suggests that the C_3H_8/C_2H_6 ratio is quite static in the U.S. over this 12-year record. That the ratios C_2H_6/CH_4 (and C_3H_8/CH_4) are increasing over time is completely consistent with Lan et al. 2019, and as they point out, studies that assume these ratios are invariant will overestimate the rate of oil/gas CH_4 emissions. Here, we use C_3H_8 vs CH_4 and C_2H_6 vs CH_4 between 2012 and 2018 to estimate the CH_4 emissions from the US as this is the period when most of the top-down and bottom-up estimates of CH_4 have been performed. That the ratios are getting "wetter" (higher hydrocarbon content in pre-processed gas) over time is consistent with an increasing contribution from oil exploration. That the atmospheric C_2H_6 and C_3H_8 increase fractionally the same, suggests that the ratio of the alkanes in the reservoirs producing these emissions do not change significantly over the time of this record.

S3. ATom & HIPPO aircraft observations

The HIPPO campaign was a sequence of five global measurement campaigns which sampled from near the North Pole to the coastal waters of Antarctica, covering different seasons and years:

HIPPO 1: 8-30 January 2009, HIPPO 2: 31 October – 22 November 2009, HIPPO 3: 24 March – 16 April, HIPPO 4: 14 June – 11 July 2011. ATom was a sequence of four global campaigns that took place from 29 July – 12 August 2016, 26 January – 10 February 2017, 28 September 2017-11 October 2017, and 24 April 2018 – 6 May 2018. Flight paths of HIPPO and ATom campaigns are illustrated in Figure S22.

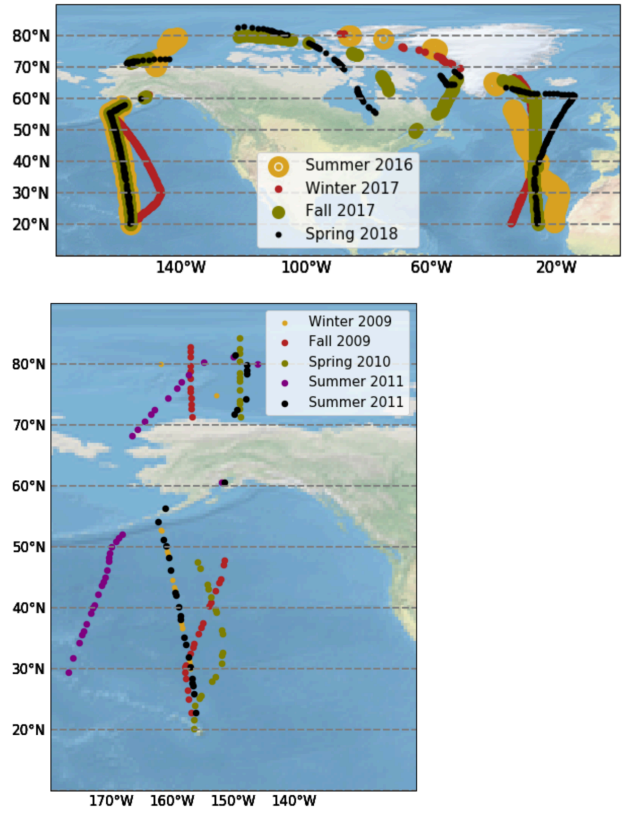

Figure S22. Truncated ATom and HIPPO flight paths. Flight paths used in this analysis are shown above (**Top**: ATom, **Bottom**: HIPPO). We split the data into Pacific (left column) and Atlantic (right column) "curtains" shown above for ATom, but HIPPO only offered Pacific curtains over remote ocean. The flight paths shown above do not encompass the entire dataset due to filtering out measurements south of 20 latitude north, those obtained over land, and those associated with very recent emissions. A summary of the filtering parameters we use in the main text are shown in Table S2.

Table S2. Filters for Aircraft Measurements.

Parameter	**ATom Aircraft**	**HIPPO Aircraft**
Altitude	> 1000 meters	> 1000 meters
N_2O	> 0.327 ppb	> 0.320 ppb
Tropopause Pressure	> 100 hPa	> 100 hPa

Summer season	exclude	exclude

HIPPO data were accessed from https://www.eol.ucar.edu/field_projects/hippo on 12/18/18, using the "discrete continuous merge" file. ATom data were accessed from the WAS-Discrete merged file from espo.nasa.gov/atom/archive/browse/atom/DC8/MER-WAS in August, 2021. Data taken over landmass for both aircraft campaigns were filtered away using global-land-mask version 1.0.0,[19] available from Python Package Index.

Here, we outline additional information on processing ATom and HIPPO aircraft observations used to compare with the GEOS-Chem model. HIPPO measurements were filtered for AWAS/UM instrument measurements to avoid measurement bias in C_3H_8 over C_2H_6, as the NOAA instrument only measured one of those species. All measurement species of HIPPO and ATom were filtered for consistent measurements of C_3H_8 and C_2H_6 within their respective campaigns; i.e., when those constituents were either both null or non-zero. This requires filtering data to remove plumes from highly local sources (including both energy infrastructure and wildfires), and to exclude regions and times where the lifetime of the alkanes is very short and thus regional / local sources dominate the variance. To reduce the influence of local sources, we only analyze observations in the free troposphere over the ocean at altitudes above 1000 meters (this filter excludes less than 20% of the dataset). To diagnose tropical air, we use tropopause pressure as a filter. We use the NASA Global Modeling and Assimilation Office GEOS FP-IT (version 5.12.4) tropopause pressure product at 0.5 x 0.67 resolution,[20] and linearly interpolate it to the HIPPO aircraft path (for ATom, we use the product already included in the dataset). We only analyze measurements with tropopause pressure above 100 hPa (about 5% of the data was excluded under this constraint) for both ATom and HIPPO, which was sufficient to reduce the influence of tropical intrusions.

Because C_2H_6 and C_3H_8 are relatively short-lived gases, their abundance in the stratosphere is low and poorly connected to the underlying fluxes. To exclude stratospheric observations, we use N_2O which is inert and generally well-mixed in the troposphere, but is destroyed in the stratosphere by photolysis and reaction with O^1D.[21] Thus, we exclude data associated with low N_2O mole fraction (Figure S23). We use nearest neighbor interpolation to estimate missing N_2O observations. In Figure S23, we compare N_2O observations and GEOS-Chem simulations of N_2O and determine a common filter for both datasets. (Note that we generate GEOS-Chem N_2O simulations shown in Figure S23 by interpolating GEOS-Chem to aircraft latitude, longitude, time and potential temperature, but for all subsequent analysis, we filter GEOS-Chem by N_2O before interpolating to the aircraft potential temperature). To account for biomass burning, we use HCN as a tracer and did not use data with high HCN (Figure S24-26) for ATom observations only, as HIPPO did not provide HCN observations.

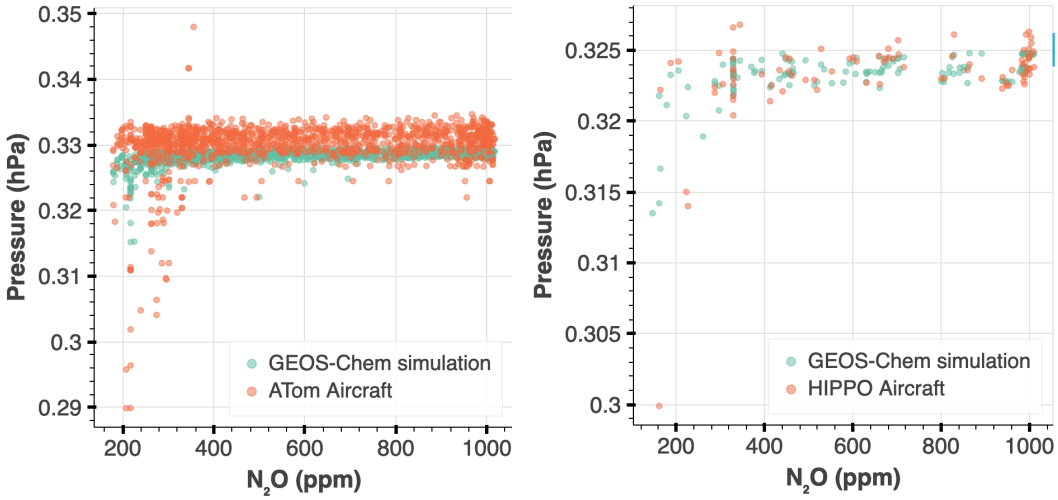

Figure S23. Stratospheric filter using N_2O. **Left**: ATom. **Right**: HIPPO. In both figures, GEOS-Chem simulations were interpolated to aircraft latitude, longitude, time, and potential temperature in order to compare N_2O. However, for all subsequent analysis, GEOS-Chem was filtered by N_2O before interpolating simulations to aircraft potential temperature. We use these figures to arbitrarily choose 0.327 and 0.320 N_2O mole fractions as a filter cutoff for ATom and HIPPO, respectively, as described in the main text.

To account for biomass burning, we use HCN as a tracer. We see elevated HCN over the Atlantic ocean on several campaigns (Figure S21). In the cross plot of HCN and C_2H_6 (Figure S23), we observe distinct plumes of elevated HCN and C_2H_6 that suggest biomass burning, and we de-weighted and excluded samples with high HCN (see description in Figure S23).

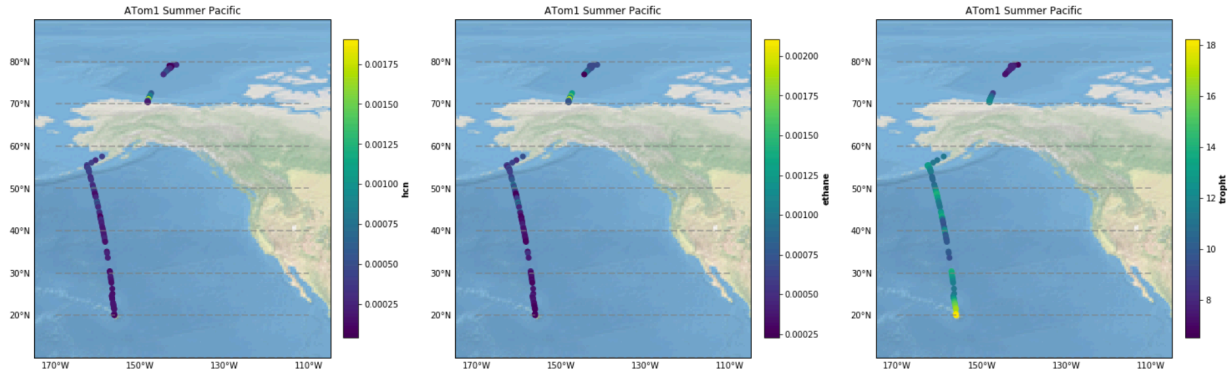

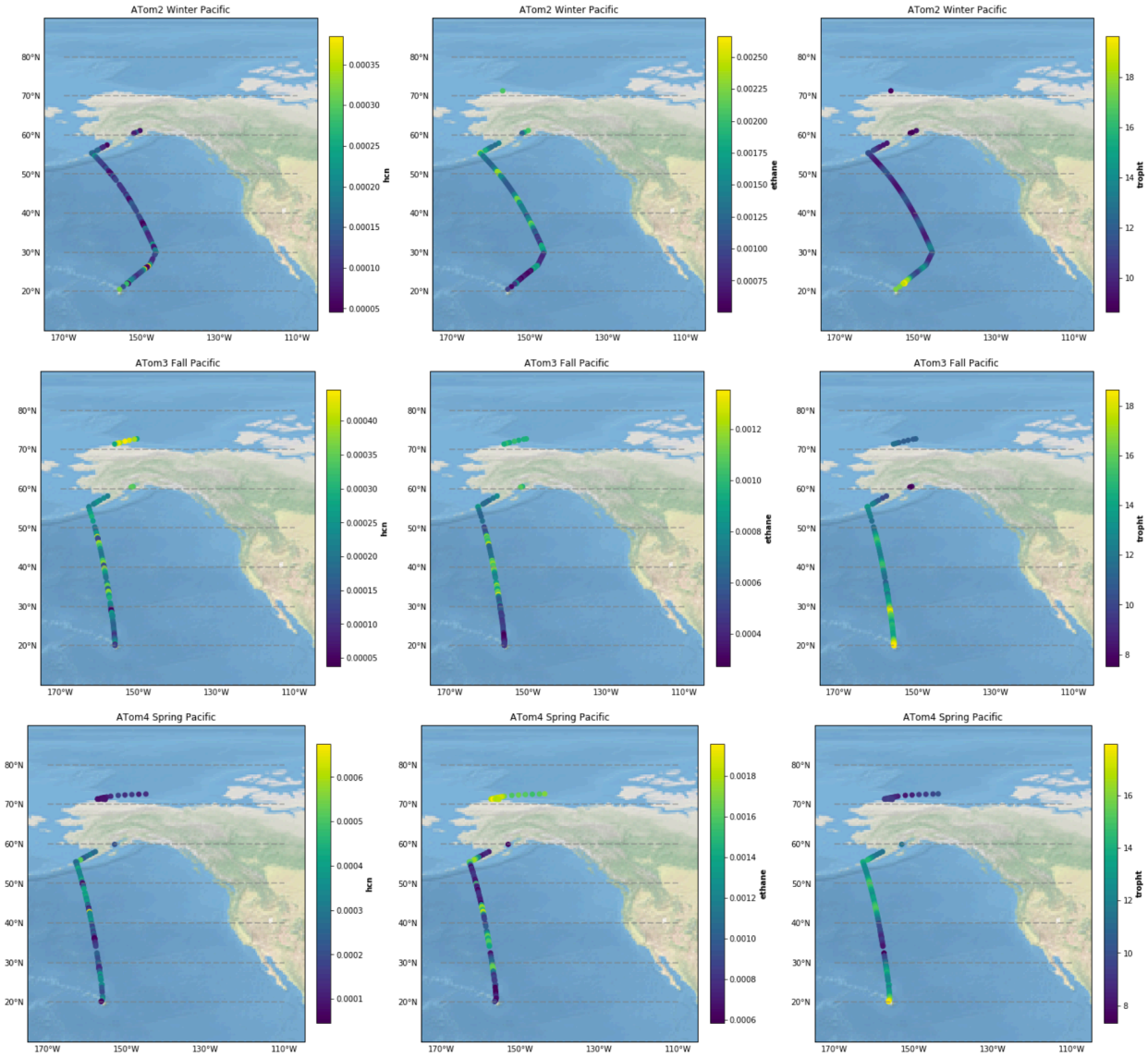

Figure S24. ATom HCN Pacific transects. HCN (left column), Ethane (middle column), and tropopause height (right column).

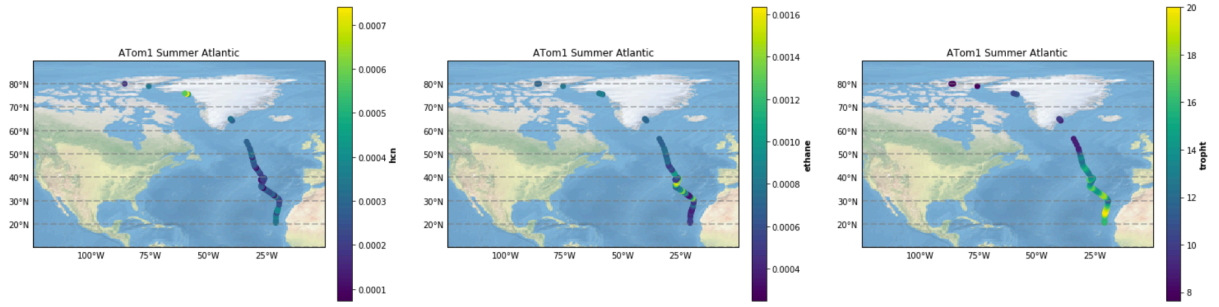

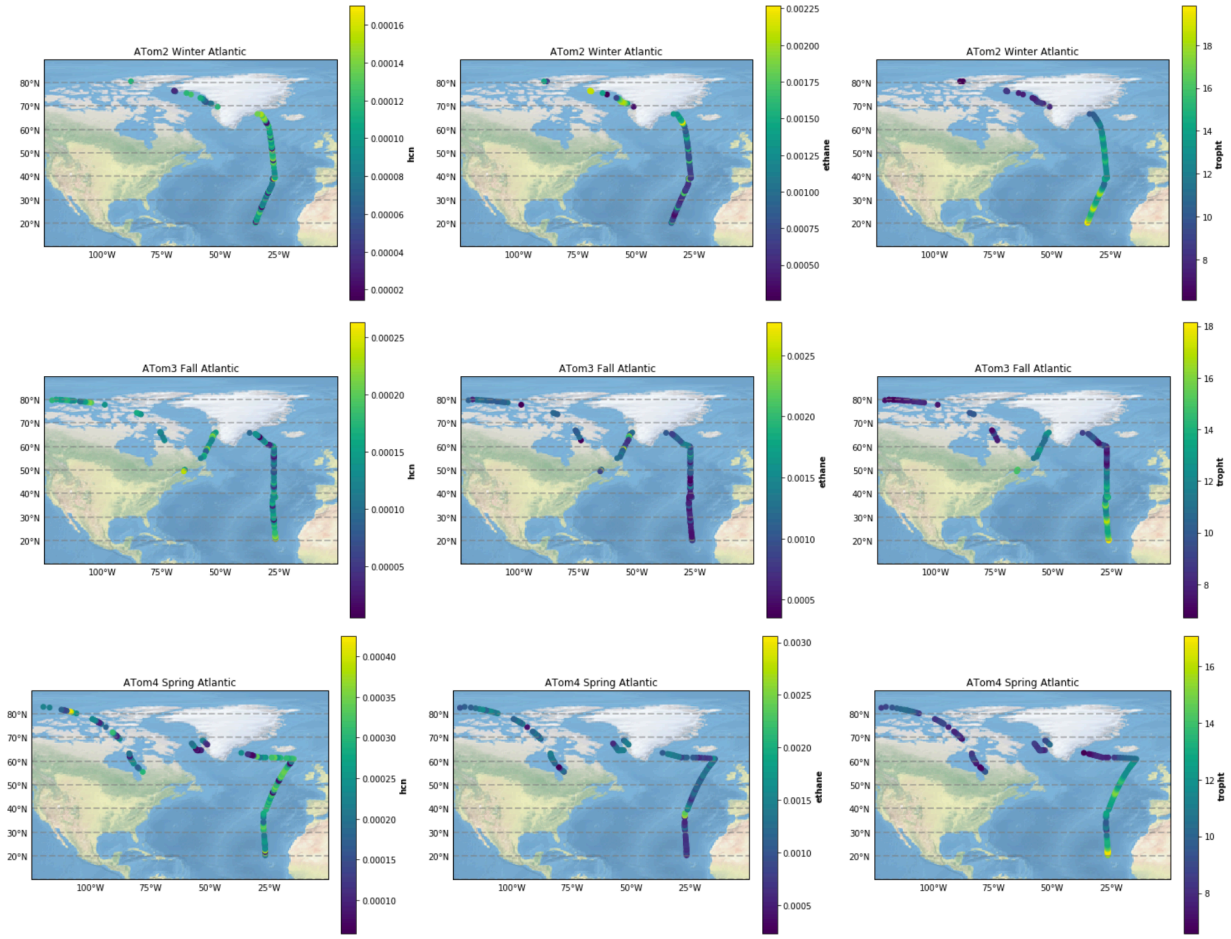

Figure S25. ATom HCN Atlantic transects. HCN (left column), Ethane (middle column), and tropopause height (right column).

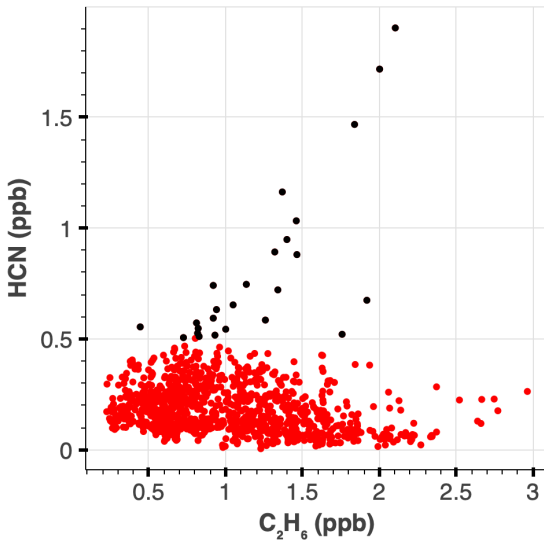

Figure S26. ATom HCN vs C_2H_6. This data includes all four ATom campaigns and ocean transects and has been filtered using the specifications outlined in the methods section in the main text. The

few points with very high HCN and C_2H_6 are associated with biomass burning. We assigned a weak percentile score for each datapoint, and the values greater than or equal to equal to the 87th percentile are highlighted in black. Those points were replaced with NaN and then interpolated using the "backfill" method for C_3H_8 and C_2H_6.

S4. GEOS-Chem Simulations

We simulated HIPPO and ATom measurements using the GEOS-Chem "classic" global 3-D chemical transport model in v12.1.1 (doi:10.5281/zenodo.2249246). The simulations were driven by MERRA-2 reanalysis meteorology product by the Global Modeling and Assimilation Office (GMAO) at NASA Goddard Space Flight Center.[22] MERRA-2 has a native resolution of 0.5 lat x 0.625 lon x 72 hybrid sigma/pressure levels, of which we degrade to a 4 x 5 x 72 resolution. We simulate time periods that encompass the HIPPO and ATom aircraft measurements with a 1-year spin-up period. In all cases, we use a standard chemistry simulation with no changes to the chemistry regimes. Simulations were collected over every hour over every day of each campaign period (~2 months of results for each campaign time period). Hydrocarbons were converted from units of carbon to $mol_x/mol_{dry\ air}$.

All emissions are computed using the Harmonized Emissions Component (HEMCO) Standalone[23] version 3.0.0 (DOI: 10.5281/zenodo.4429214)[24] with GEOS-Chem development version 13.0.0, cloned on 9/2020 at https://github.com/geoschem/geos-chem). This Standalone utilizes the most up-to-date versions of emissions as of September, 2020. As such, even though we utilize an older version of GEOS-Chem classic for the simulations, we implement up-to-date emissions. Relevant inventories that cover the oil and natural gas sector that are used in the default emissions configuration for GEOS-Chem v13.0.0 are Tzompa-Sosa et al. 2017 for C_2H_6, and Xiao et al. 2008 for C_3H_8.[4,25]

In Figure S27, we show that GEOS-Chem "synoptic replicates" (GEOS-Chem sampled several days before and after the aircraft in situ sampling time) show less consistency in latitude compared to the coordinate, potential temperature.

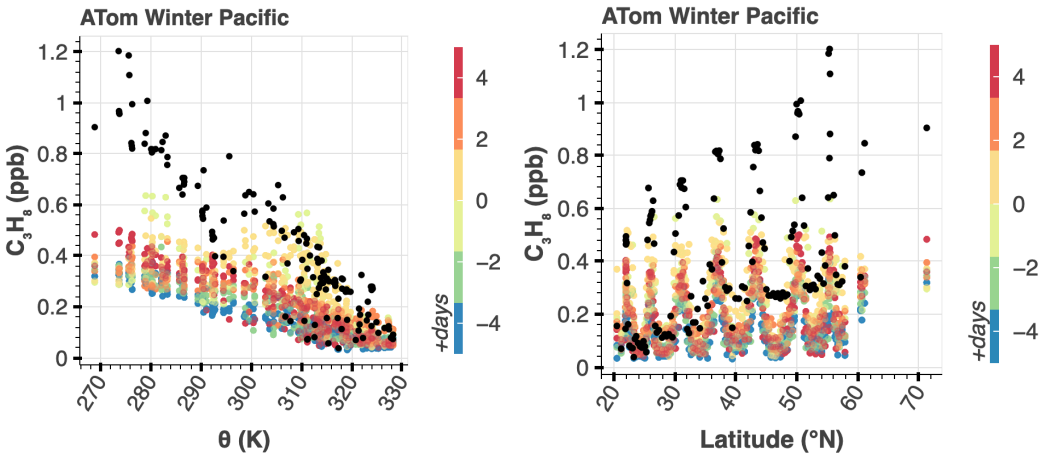

Figure S27. GEOS-Chem simulated C_2H_6 vs potential temperature and latitude during 2017. These data are analyzed for Pacific and Atlantic transects during January-Feburary 2017. Aircraft observations are shown in black. GEOS-Chem simulations are colored by the sampling time, in days beyond the flight path. (We found the median time of in-situ sampling of the aircraft, and then sampled the GEOS-Chem model for several days before and after the median to generate what we call "synoptic replicates" here. Each of the synoptic replicates were sampled along the flight path latitude, longitude, time and potential temperature using nearest neighbor interpolation.) In this figure we include $\pm$ 5 days to demonstrate the variance, but we use up to $\pm$ 2 days of the GEOS-Chem replicates in the Bayesian model. All remaining simulations of ATom and HIPPO C_2H_6 and C_3H_8 are included in the SI.

As discussed in Section 3.2 in the main text, we revise C_3H_8 emissions using GEOS-Chem v13.0.0 default C_2H_6 emissions scaled by the observed C_3H_8/C_2H_6 ratio estimated from the NOAA data. In Figure S28, we show the default C_2H_6 and C_3H_8 emissions, as well as the revised C_3H_8 emissions.

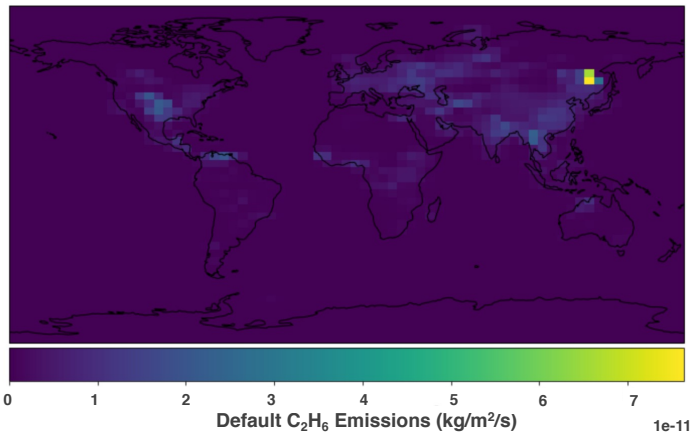

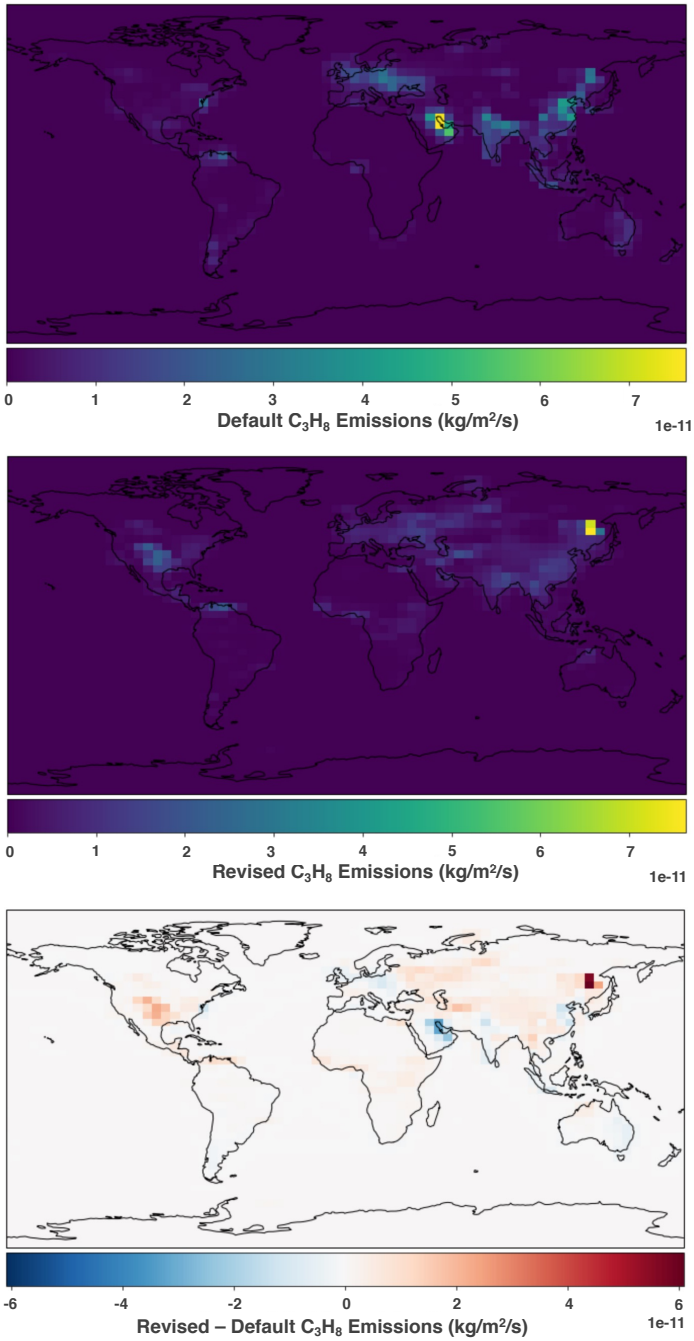

Figure S28. GEOS-Chem v13.0.0 default and revised emissions. **Top**: Default C_3H_8 emissions. **Upper middle**: Default C_2H_6 emissions. **Bottom middle**: Revised C_3H_8 emissions scaled by the observed NOAA C_3H_8/C_2H_6 ratio (0.67 mol/mol, Figure S9). **Bottom**: Difference between revised and default C3H8 emissions used by GEOS-Chem v13.0.0.

In the GEOS-Chem simulations, both ethane and propane have the most variability and lowest mole fraction, as expected, since their oxidative chemistry is much faster. During the summer,

tropical intrusions with very low mixing ratios are prominent (see Atom summer Pacific transect, Figure S29.).

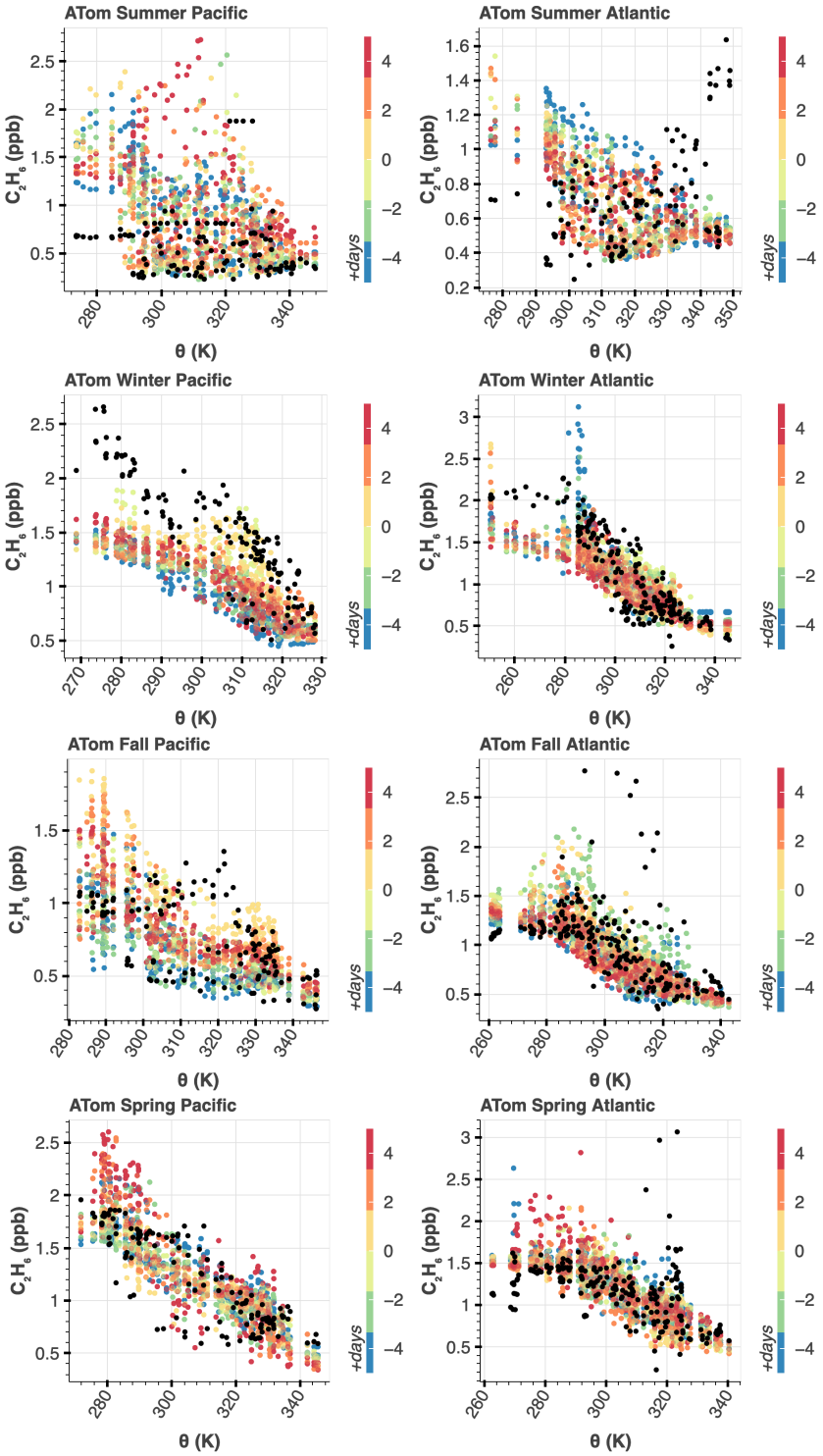

Figure S29. GEOS-Chem simulated C_2H_6 vs potential temperature during ATom campaign**.** Each plot is specific to the ocean transect. GEOS-Chem simulations are colored by the sampling time,

in the number of days from the day of the flight. (We found the median time of in-situ sampling of the aircraft, and then sampled the GEOS-Chem model for several days before and after the median to generate “synoptic replicates.” Each of the synoptic replicates were sampled along the flight path latitude, longitude, time of day and potential temperature using nearest neighbor interpolation.)

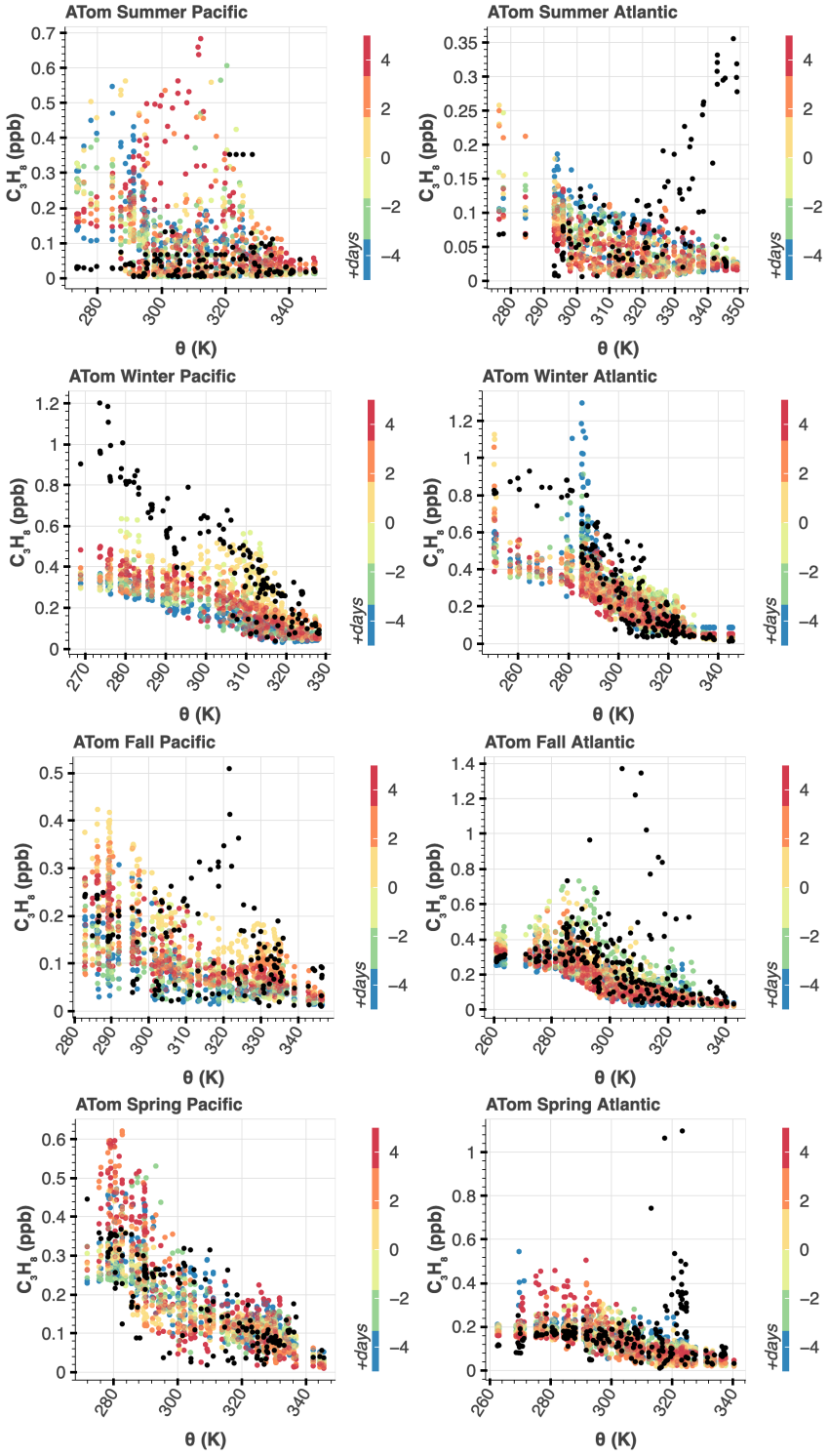

Figure S30. GEOS-Chem simulated C_3H_8 vs potential temperature during ATom campaign. Each plot is specific to the ocean transect. GEOS-Chem simulations are colored by the sampling time, in the number of days from the day of the flight. (We found the median time of in-situ sampling of the aircraft, and then sampled the GEOS-Chem model for several days before and after the median to generate "synoptic replicates." Each of the synoptic replicates were sampled along the

flight path latitude, longitude, time of day and potential temperature using nearest neighbor interpolation.)

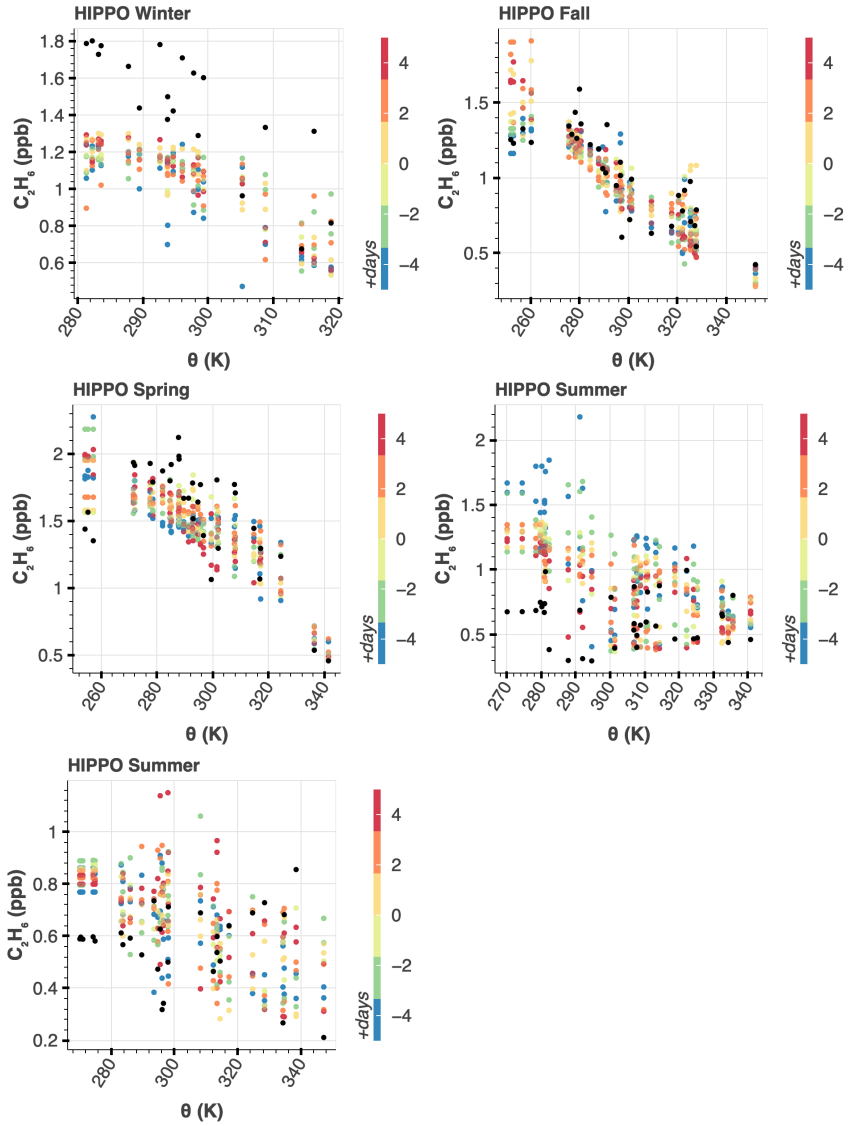

Figure S31. GEOS-Chem simulated C_2H_6 vs potential temperature during HIPPO aircraft campaign. Each plot is specific to the ocean transect. GEOS-Chem simulations are colored by the sampling time, in the number of days from the day of the flight. (We found the median time of in-situ sampling of the aircraft, and then sampled the GEOS-Chem model for several days before and after the median to generate "synoptic replicates." Each of the synoptic replicates were sampled along the flight path latitude, longitude, time of day and potential temperature using nearest neighbor interpolation.)

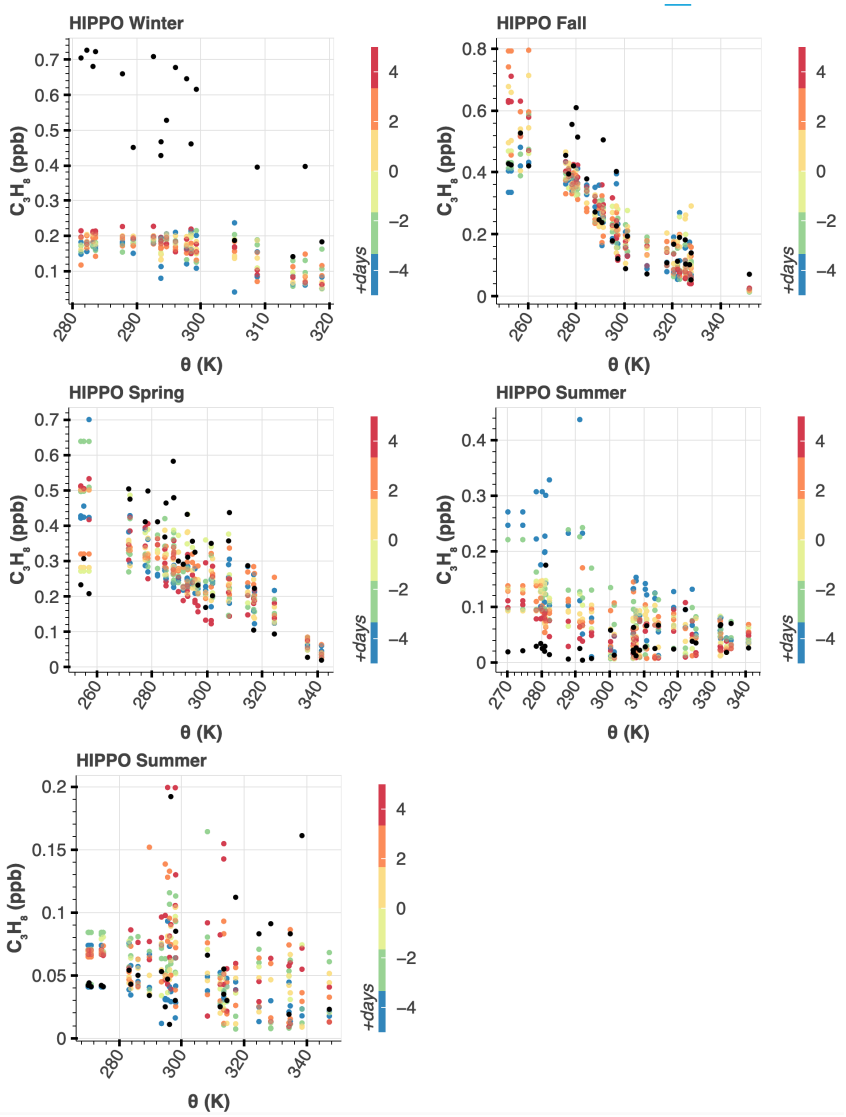

Figure S32. GEOS-Chem simulated C_3H_8 vs potential temperature during HIPPO aircraft campaign. Each plot is specific to the ocean transect. GEOS-Chem simulations are colored by the sampling time, in the number of days from the day of the flight. (We found the median time of in-situ sampling of the aircraft, and then sampled the GEOS-Chem model for several days before and after the median to generate "synoptic replicates." Each of the synoptic replicates were sampled along the flight path latitude, longitude, time of day and potential temperature using nearest neighbor interpolation.)

We compare the cross plot of C_3H_8 to C_2H_6 from the aircraft measurements and GEOS-Chem simulations to the NOAA measurements. As expected, both the aircraft and GEOS-Chem simulations fall under the photochemically aged emissions part of the NOAA curve. While the aircraft data overlays the NOAA measurements almost perfectly (especially in the winter when the lifetimes of both gases are longest), GEOS-Chem underestimates C_3H_8, particularly over the Atlantic curtain (Figure S33). The same conclusion is drawn for HIPPO time periods (Figure S 34).

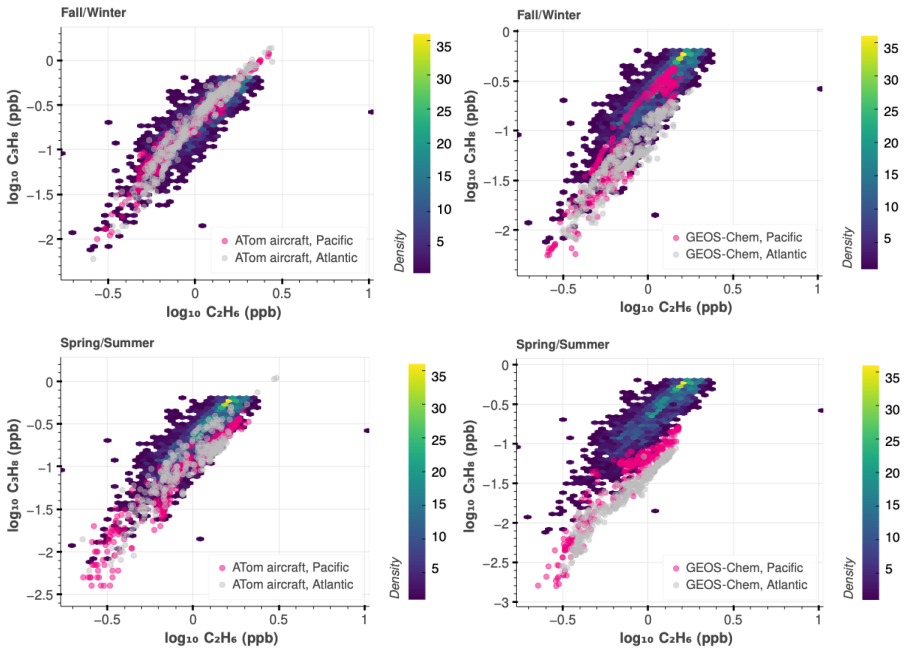

Figure S33. Comparison of C_3H_8 vs C_2H_6 for NOAA, ATom aircraft, and GEOS-Chem (GC) simulations. NOAA photochemically-aged measurements (all sites, 2005-2018), as explained in the text, are shown on the heat map (colored by density of data). Note the distinction between winter/fall and spring/summer seasons. HIPPO is included in the SI, Section 3.

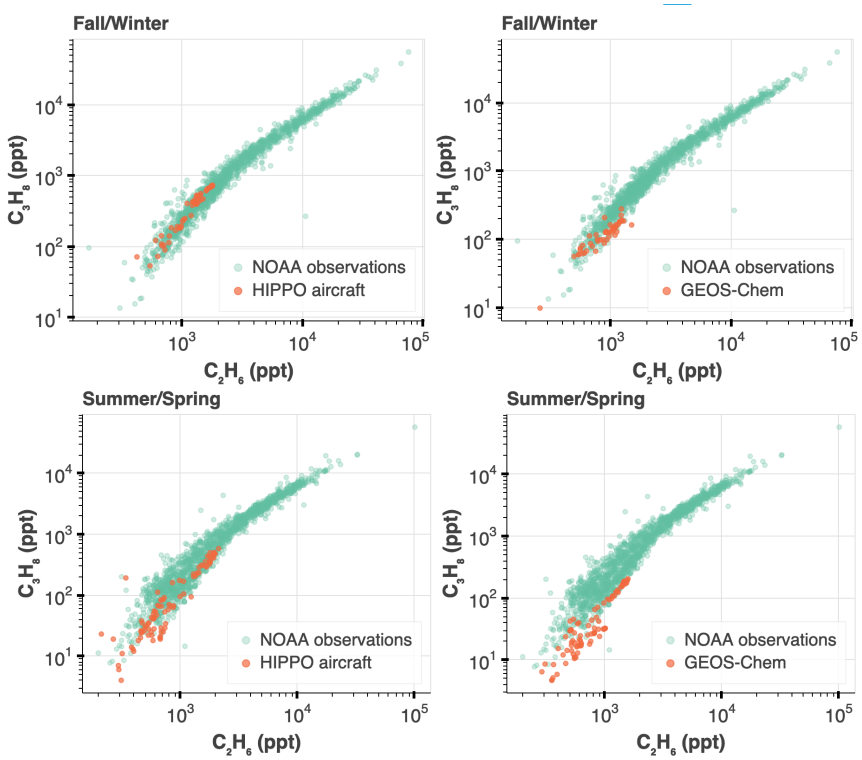

Figure S34. C_3H_8 vs C_2H_6 for HIPPO aircraft and GEOS-Chem simulations. Please see section 3.2 in the main text for a discussion.

In the main text, we show, in Figure 4, the impact of the revised C_3H_8 emissions on GEOS-Chem simulations during the ATom 4 campaign time period. Below, in Figure S35, we show the impact of the revised C_3H_8 emissions for all four ATom campaigns. In Figure S36, we show the impact of the revised C_3H_8 emissions during all 5 HIPPO campaigns.

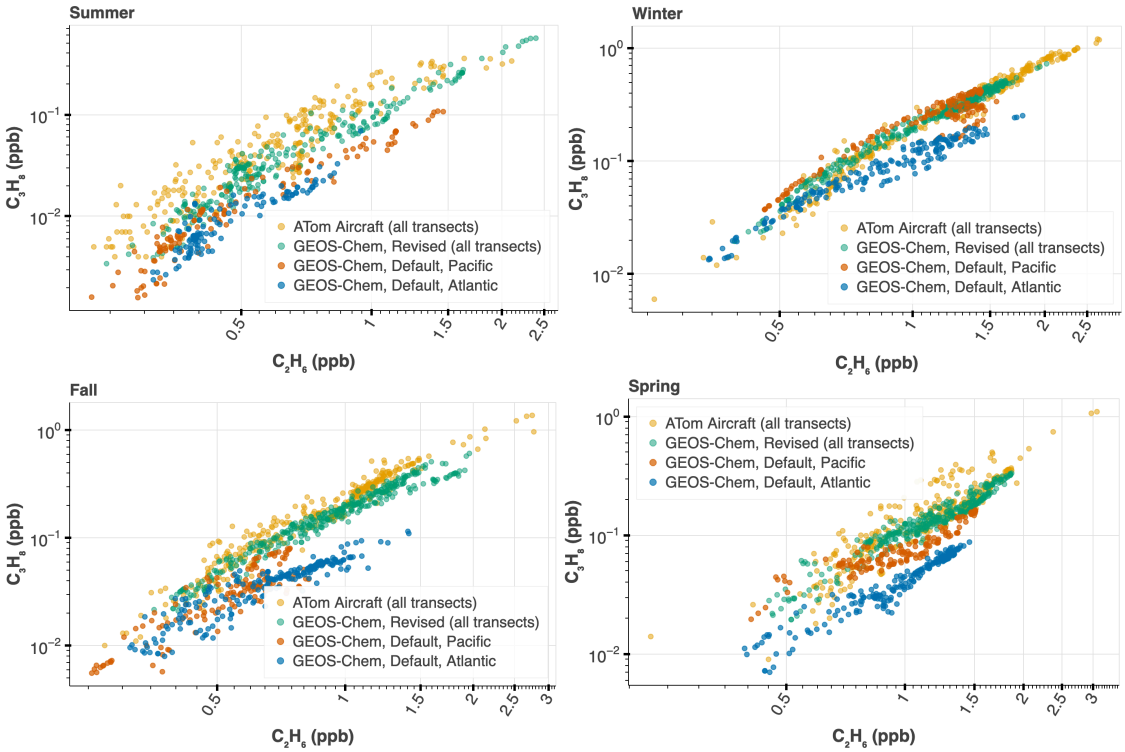

Figure S35. GEOS-Chem simulations using the default and revised C_3H_8 emissions during all four ATom campaigns. Please see section 3.2 in the main text for more discussion.

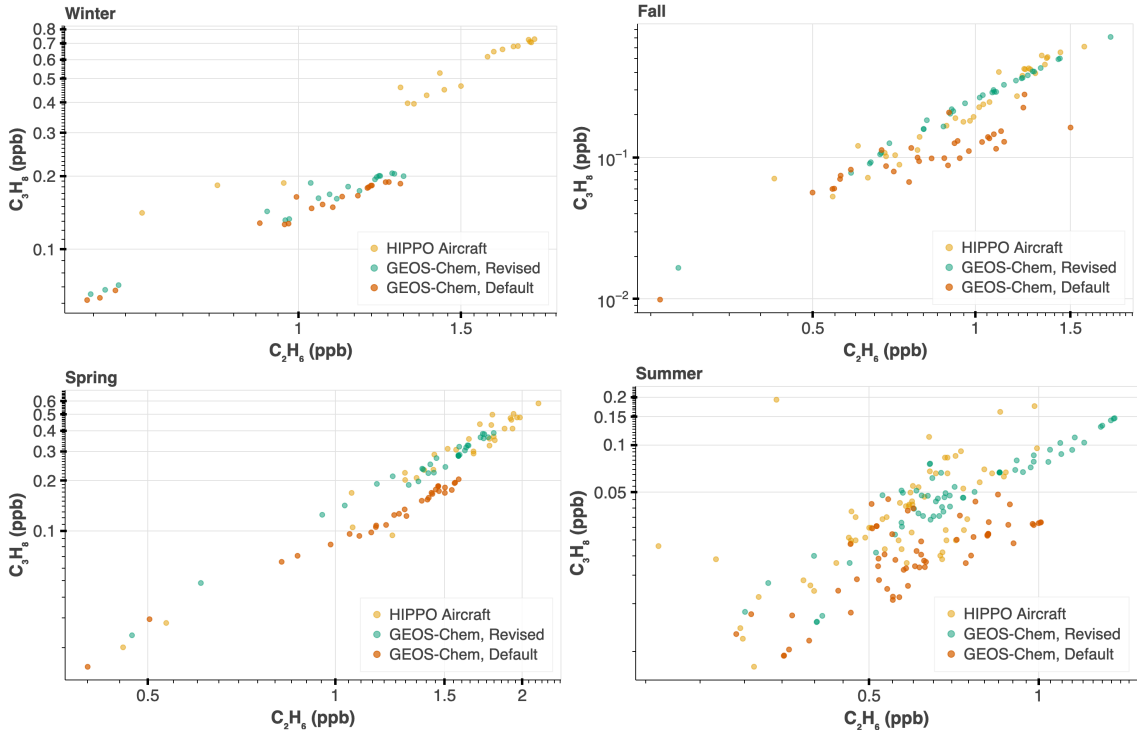

Figure S36. GEOS-Chem simulations using the default and revised C_3H_8 emissions during all 5 HIPPO campaigns. Please see section 3.2 in the main text for more discussion.

S5. Bayesian Inference

S5.1 Background and Priors

We wish to use the ATom and HIPPO aircraft observations to quantify C_3H_8 and C_2H_6 emissions. We use hierarchical Bayesian modeling to estimate what global scalar would minimize the difference between the simulated C_3H_8 and C_2H_6 from the updated GEOS-Chem v13.0.0 emissions and the observations made during the ATom and HIPPO aircraft campaigns. Using Bayesian probability, we can quantify a degree of certainty about a hypothesis or parameter value. Using probability rules, one can derive Bayes's Theorem:

$$P(\theta \mid y) = \frac{P(y \mid \theta)P(\theta)}{P(y)}$$

$$posterior = \frac{likelihood \times prior}{evidence}$$

The likelihood tells us how likely it is to acquire the observed data, y, given the parameter, θ. The prior is a measure of plausibility of the hypothesis θ before the experiment was conducted. The evidence is a marginal likelihood that is computed from the likelihood and the prior. The posterior contains the information we want about the parameters we are after. The ambient mole fraction of C_3H_8 and C_2H_6 is more linearly related to its underlying emissions pattern during the winter/fall/spring when there is decreased sunlight/oxidation. As such, we assume differences between the GEOS-Chem simulations and the aircraft observations can largely be attributed to the underlying emissions grid, such that,

$$\mathrm{a} = \mathrm{gcs} \cdot \alpha \tag{1}$$

where a is the aircraft C_2H_6 or C_3H_8, gcs stands for GEOS-Chem simulation of C_2H_6 or C_3H_8, and α is a scalar that represents the most likely mismatch between the underlying C_3H_8 and C_2H_6 emissions as transported through GEOS-Chem v13.0.0 relative to ATom and HIPPO observations. This assumption forms the heart of our hierarchical Bayesian model.

We can reasonably approximate C_2H_6 and C_3H_8 measured by the aircraft to be Lognormally distributed with an approximate error. Lognormal distributions have longer tails, which is appropriate given the outliers we see in the measurements. We can model the GEOS-Chem simulated results as follows:

$$\begin{aligned} \mathrm{gcs}_j &\sim \mathrm{LogNorm}(\beta \cdot \mathrm{a}_j, \sigma) \\ \sigma &\sim \mathrm{Prior} \\ \beta &\sim \mathrm{Prior} \end{aligned} \tag{2}$$

where gcs_j represents GEOS-Chem simulated C_3H_8 and C_2H_6, a_j represents the jth datum of aircraft-observed C_3H_8 or C_2H_6. Here, β parameter (equivalent to $1/\alpha$) estimates error in the default GEOS-Chem emissions, and σ is the approximate uncertainty in the GEOS-Chem simulations. In this case, we expect β to be less than one since the aircraft observations are usually greater than the GEOS-Chem simulations. We organized the Bayesian model this way because we consider the aircraft observations to be unchanging, while treating the GEOS-Chem simulations as the experimental dataset. To obtain the GEOS-Chem missing emissions, we can invert the β parameter.

We sampled the GEOS-Chem model several days before and after the aircraft path to estimate uncertainty in the simulations due to meteorology, as explained in Section 2.3 in the main text. If we were to pool all the data together, each experiment would be governed by identical parameters. However, each replicate is subject to differences mainly due to meteorology and we conclude that the parameters in each replicate experiment should vary from one another, such that we have i separate models to fit, each looking like equations 2, above. Under this scenario, we organize our model into a hierarchical structure, pictured in Figure S37.

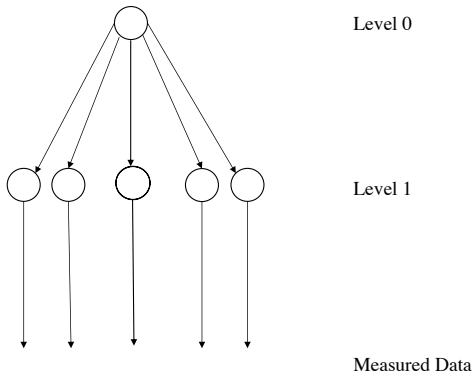

Figure S37. Schematic of hierarchical Bayesian model. Level 0 contains the hyperparameter β, the parameter we ultimately wish to get estimates for. Level 1 corresponds to the day the GEOS-Chem model was sampled (there are 5 days because we sampled 2 days before and after the mean flight path). There will be variability from day to day, and the location and scale parameters for a given day are conditioned on the hyperparameters.

We can consider a hierarchical model in which there is a hyperparameter, which we call β (corresponds to level 0, Figure S32), and the values of the scaling parameters of the replicates,

which we now call β_1 (corresponds to level 1, Figure S37), may vary from this β according to some probability distribution, $g(\beta_{1,i}|\beta)$. We now have parameters $\beta_{1,1}, \beta_{1,2}, \ldots \beta_{1,i}$ and β. The posterior can be written using Bayes' theorem, defining $\beta_1 = (\beta_{1,1}, \beta_{1,2}, \ldots)$,

$$g(\beta, \beta_1|\mathrm{a}, \mathrm{gcs}) = \frac{f(\mathrm{a}, \mathrm{gcs}|\beta, \beta_1)g(\beta, \beta_1)}{f(\mathrm{a}, \mathrm{gcs})} \tag{3}$$

Note though that the observed values of gcs do not directly depend on β, only on β_1 and as such, the observations are only indirectly dependent on β. So, we can write:

$$g(\beta, \beta_1|\mathrm{a}, \mathrm{gcs}) = \frac{f(\mathrm{a}, \mathrm{gcs}|\beta_1)g(\beta, \beta_1)}{f(\mathrm{a}, \mathrm{gcs})} \tag{4}$$

Next, we can rewrite the prior using the definition of conditional probability:

$$g(\beta, \beta_1) = g(\beta_1|\beta)g(\beta) \tag{5}$$

Substituting this back into the previous expression for the posterior, we have:

$$g(\beta, \beta_1|\mathrm{a}, \mathrm{gcs}) = \frac{f(\mathrm{a}, \mathrm{gcs}|\beta_1)g(\beta_1|\beta)g(\beta)}{f(\mathrm{a}, \mathrm{gcs})} \tag{6}$$

In the numerator, we see a chain of dependencies. The gcs simulations depend on β_1. Parameters β_1 depend on hyperparameter β. Hyperparameter β then has some hyperprior distribution. As such, this hierarchical model captures both the sample day-to-day variability, as well as the hyperparameter.

We must specify a hyperprior, and a conditional prior, $g(\beta_1|\beta)$. Here, we have no reason to believe that we can distinguish any one $\beta_{1,i}$ from another prior to the experiment. As such, we can assume the conditional prior to behave in an exchangeable manner, where the label i is not dependent on the permutations of the indices. Our expression for the posterior is:

$$g(\beta_1, \beta \mid \mathrm{a}, \mathrm{gcs}) = \frac{f(\mathrm{a}, \mathrm{gcs} \mid \beta_1)\left(\prod_{i=1}^{k} g(\beta_{1,i} \mid \beta)\right)g(\beta)}{f(\mathrm{a}, \mathrm{gcs})} \tag{7}$$

The full hierarchical model is given by one additional level above Level 0 in Figure 37 that corresponds to individual aircraft campaign/season and ocean transect. This additional level

contains the parameter α, the overall parameter that is a result of the sampling replicates and the season/ocean transect. It is very difficult to sample the full hierarchical model with so many levels, and for practical reasons, we were not able to. However, given that each season/ocean transect is assumed to be independent, we can treat each season/ocean transect with a separate hierarchical model (that is shown in Figure 37), and then sample the posterior samples of those separate models to define a credible interval for overall α. Our statistical model is defined for campaign/transect, i, and the observed mole fraction, j, as follows:

$$\begin{gathered}\tau_{ij} = 0.05|\Delta t|_{ij} + 0.01 \\ \beta_i \sim \text{Norm}(0.7,0.2) \\ \beta_{1,ij} \sim \text{Norm}(\beta_i, \tau_{ij}) \\ \alpha_i = 1/\beta_i \\ \sigma_{ij} = 0.14 \cdot \text{tropht}_{ij} + 0.8 \\ \text{gcs}_{ij} \sim \text{LogNorm}(\beta_{1,ij} \cdot \text{a}_{ij}, \sigma_{ij})\end{gathered} \tag{8}$$

The likelihood is given by gcs_{ij}, which represents the *ij*th mole fraction of GEOS-Chem simulated C_3H_8 and C_2H_6, and a_{ij} represents the *ij*th C_3H_8 or C_2H_6 mole fraction observed by the aircraft. The uncertainty in gcs_{ij} is given by σ_{ij}, which increases linearly with tropopause height, tropht_{ij}, since we expect more variability in C_3H_8 or C_2H_6 mole fraction with high tropopause height that is often related with tropical intrusions. The conditional parameter, $\beta_{1,ij}$, depends on a hyperprior distribution for the emissions scalar, β_i (which is equivalent to $1/\alpha_i$), and τ_{ij}, which describes variability in the emissions scalar due to transport errors in GEOS-Chem. As such, τ_{ij} depends on the difference between the original aircraft sampling time and the GEOS-Chem sampling replicate time (Δt_{ij}) and increases with deviation between them. Development of this hierarchical model and our process for selecting priors are included in the SI.

We assume each α_i parameter from individual aircraft campaign season and ocean transect to be independent of one another. As such, to estimate a credible interval for an overall α, we draw a random sample of the posterior of hyperparameter α_i for each campaign season and ocean transect. We take the mean of these samples and repeat this 10,000 times. (Note that we do not use the summer estimates for this calculation, for reasons described in Section 2.2, main text.) Details on the software used are described below.

The τ_{ij} parameter has the effect of weighting the GEOS-Chem simulation replicate that falls on the plane path higher than the other replicates that do not. As such, GEOS-Chem simulation replicate that falls on the exact aircraft data collection time has more influence on the final result of β_i parameter (the emission scalar). We would not expect meteorology to cause more than $\pm$ 0.5

variation in parameter $\beta_{1,ij}$, as this would imply a very large variation in Tg after scaling emissions. As such, we vary τ_{ij} from 0.05 (the plane path day), to 0.33 for the furthest day from the plane path ($\pm$ 2 days), (Figure S38).

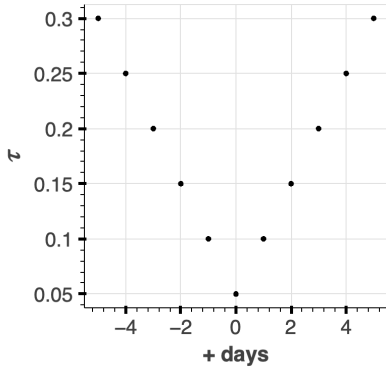

Figure S38. Prior for τ_{ij} parameter for the GEOS-Chem simulations in the Bayesian hierarchical model. The x-axis corresponds to the GEOS-Chem sample replicate, in units of days above or below the aircraft path (day 0).

We define σ_{ij} parameter as a function of tropopause height. As discussed earlier, tropical air masses are characterized by very low mole fractions of C_3H_8 and C_2H_6 because in the tropics they have short lifetimes relative to transport. We assign higher σ_{ij} (lower weight) to GEOS-Chem simulations that have higher tropopause height, which extends the width of the lognormal distribution likelihood for those measurements. This de-weights the samples that have more tropical influence. (In practice, the model is quite robust against changes in σ_{ij}, so this implementation has a small impact – see results of the sampling the posterior in Section 4.7). We somewhat arbitrarily define $\sigma_{ij} = 0.14 \cdot \mathrm{tropht}_{ij} + 0.8$, where tropht_{ij} is the tropopause height in km associated for the *j*th aircraft observation. This equation results in σ_{ij} typically ranging from 1- 1.5 and implementing this range as the variance in a lognormal distribution centered at $1x10^{-3}$ or $1x10^{-4}$ (typical of C_2H_6 or C_3H_8 measured mole fractions in remote atmospheres) results in a broad distribution that is consistent with mole fractions that we would expect for short-lived gases in remote atmospheres. The 1st and 99th percentiles of the resulting C_3H_8 distribution are $3x10^{-6}$ and $3x10^{-3}$, respectively, which is two orders of magnitude below and one order of magnitude above an average C_3H_8 mole fraction we would expect in the remote atmosphere. We find similar results for C_2H_6, except that it is centered at a value that is one magnitude larger. We use the same σ_{ij} when modeling both C_3H_8 and C_2H_6. An example of the value of σ_{ij} for ATom 2 observations over the Atlantic is shown in Figure S39.

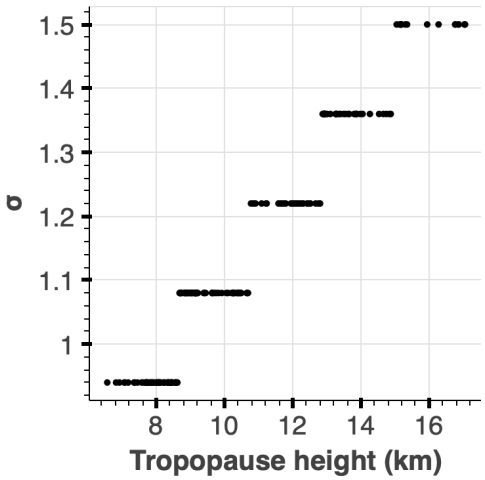

Figure S39. Prior for the $\boldsymbol{\sigma_{ij}}$ parameter for ATom 2 observations in the Bayesian hierarchical model.

We expect the β_i to be less than 1 since GEOS-Chem typically underestimates the aircraft observations. The prior for β_i is weakly informative, centered at 0.7 with the 1st percentile at 0.23 and 99th percentile at 1.17 (Figure S40).

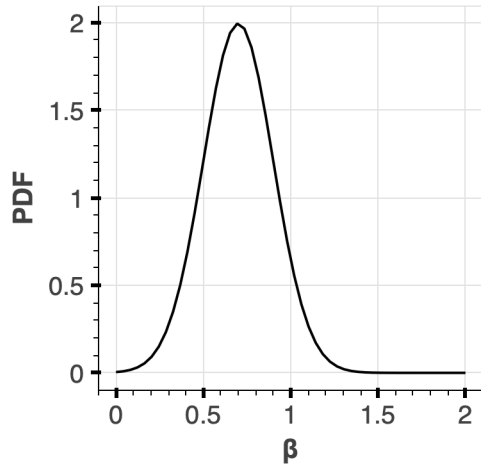

Figure S40. Prior distribution for $\boldsymbol{\beta_i}$ parameter in the Bayesian hierarchical model.

We performed prior predictive checks[26] to visualize the data our Bayesian model would generate given our priors. This check includes drawing parameter values from the prior distributions, plugging those parameters into the likelihood to generate pseudo data, and saving those data. These simulations gave us insight as to whether this was an appropriate model given our prior knowledge. The results of are satisfactory, as the empirical cumulative distribution functions are within what we expect given our prior knowledge. The results are shown in Figure S41.

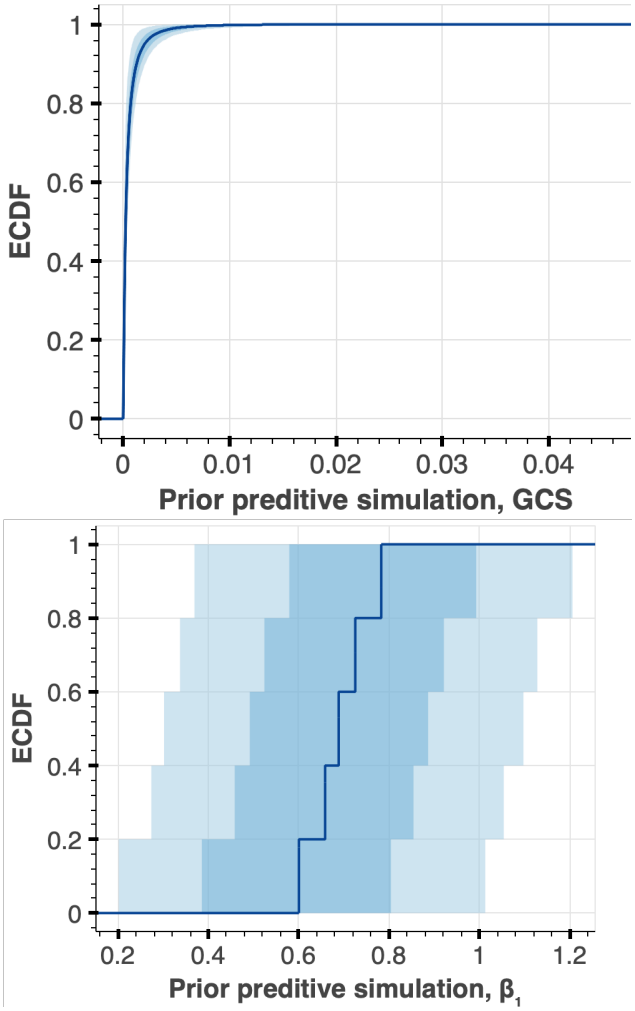

Figure S41. Prior predictive checks during ATom 2, Atlantic curtain. **Top**: Empirical cumulative distribution function of pseudo data of GEOS-Chem simulations given our priors. **Bottom**: Empirical cumulative distribution function of pseudo data of the $\beta_{1,ij}$ parameter given our priors.

We run our statistical model using Stan software[27] (version 2.26) with CmdStanPy Python interface (version 0.9.67)[28]. We parse Markov chain sampling using ArviZ (version 0.11.1).[29] We validate our hierarchical model using simulation-based calibration,[30] and posterior predictive checks[26] (described more below). We use bebi103 package (version 0.1.0)[31] to execute simulation-based calibration, prepare data for Stan sampling, parse MCMC samples, plot posteriors and plot posterior predictive checks. We also use iqplot (version 0.1.6)[32] to visualize empirical cumulative distribution functions of our priors. Finally, other software we use in our analysis includes Holoviews version 1.14.5,[33] Bokeh version 2.3.3,[34] Pandas version 1.3.1,[35] SciPy version 1.6.2,[36] and NumPy version 1.20.3.[37]

S5.2 Simulation based calibration

Often, the posterior distribution is impossible to calculate analytically. Markov chain Monte Carlo (MCMC) allows us to sample out of an arbitrary probability distribution, where the probability of choosing a given value of a parameter is proportional to the posterior probability or probability density. Here, we use Stan to sample the posterior. Stan is a free, open source, state-of-the-art probabilistic programming language that has interfaces for many other programming languages. Stan translates the model into C++, which is then compiled into machine code. It uses Hamiltonian Monte Carlo (HMC),[26] which allows for more efficient sampling of the posterior by taking large step sizes while taking into account the shape of the target distribution and tracing trajectories along it. We use CmdStanPy to install Stan, version 0.9.67. We use the bebi103 package[31] to execute simulation-based calibration.

Simulation-based calibration[30] consists of the following general steps: 1) Draw a parameter set $\tilde{\theta}$ out of the prior; 2) Use $\tilde{\theta}$ to draw a data set $\tilde{y}$ out of the likelihood; 3) Perform HMC sampling of the posterior using $\tilde{y}$ as if it were the actual measured data set, and draw L HMC samples of the parameters; 4) Do steps 1-3 N times, on order of N = 1000. In step 3, we are using a data set for which we know the underlying parameters that generated it. Because the data were generated using $\tilde{\theta}$ as the parameter set, $\tilde{\theta}$ is now the ground truth parameter set. As such, we can check to see if we uncover the ground truth in the posterior sampling by calculating the z-score. We can also check whether the posterior is narrower than the prior (shrinkage), indicating that the data are informing the model. We compute a z-score for each parameter, θ_i, which measures how close the mean sampled parameter value is to the ground truth, relative to the posterior uncertainty in the parameter value:

$$z_i = \frac{\langle \theta_i \rangle_{post} - \tilde{\theta}_i}{\sigma_{i,post}} \tag{9}$$

Here, $\langle \theta_i \rangle_{post}$ is the average value of θ_i over all posterior samples, and $\sigma_{i,post}$ is the standard deviation of θ_i over all posterior samples. The z-score should be symmetric about zero to indicate that there is no bias in estimating the ground truth, and should have a magnitude less than 5.[30] Our z-score calculations are satisfactory, shown in Figure S42.

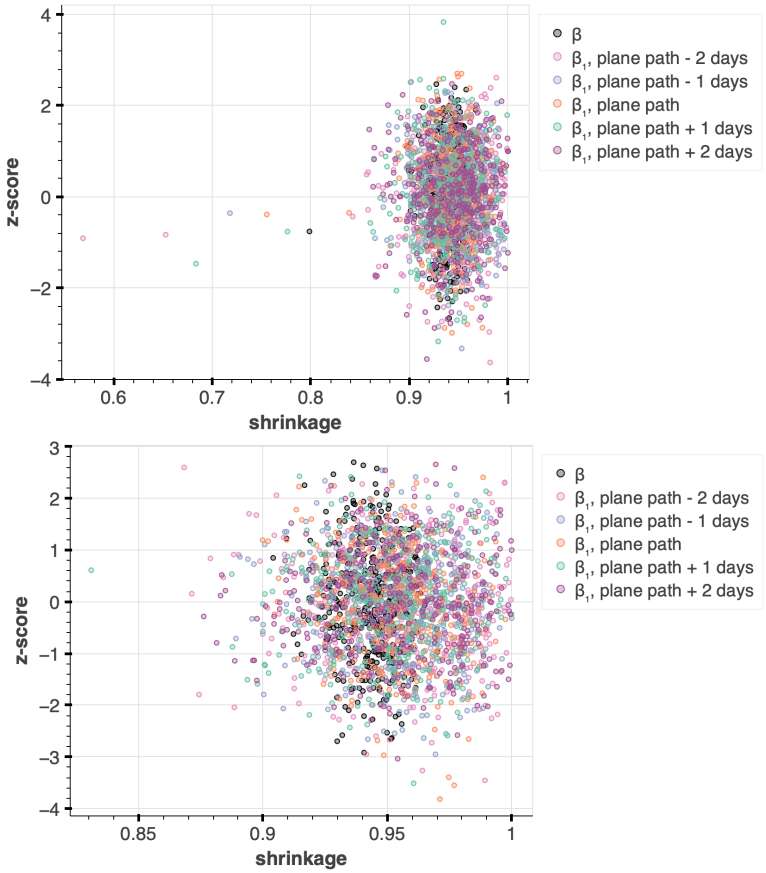

Figure S42. Z-score and shrinkage. **Top**: C_2H_6 during ATom 2 Atlantic curtain. **Bottom**: C_3H_8 during ATom 4 Atlantic curtain. Satisfactory z-score is symmetric about zero with a magnitude less than 5, while shrinkage should be around 1.

S5.3 Posterior samples – ATom observations

Below are our results for our HMC sampling of the posterior (Figure S43 and S44). The posterior of hierarchical models inherently has regions of high curvature, which can cause difficulties for HMC sampling. If HMC trajectories veer sharply due to this curvature, the Monte Carlo step ends in a divergence. We decreased the step size of the sampler to sample the areas of high curvature (increased the adapt_delta parameter to 0.99 in Stan). To further reduce problems with high curvature, we implemented a non-centered parametrization of $\beta_{1,ij}$. We also set the warmup iterations to 2000 and conducted 1000 samples. Using bebi103's stan.check_all_diagnostics() function, our sampling had effective sample size for all parameters (based on the suggestion of 50 effective samples per split chain):[30] 0 out of 4000 iterations ended with a divergence or saturated the maximum tree depth and the energy-Bayes fraction of missing information indicated no pathological behavior. We achieved these diagnostics for all runs of ATom and HIPPO.

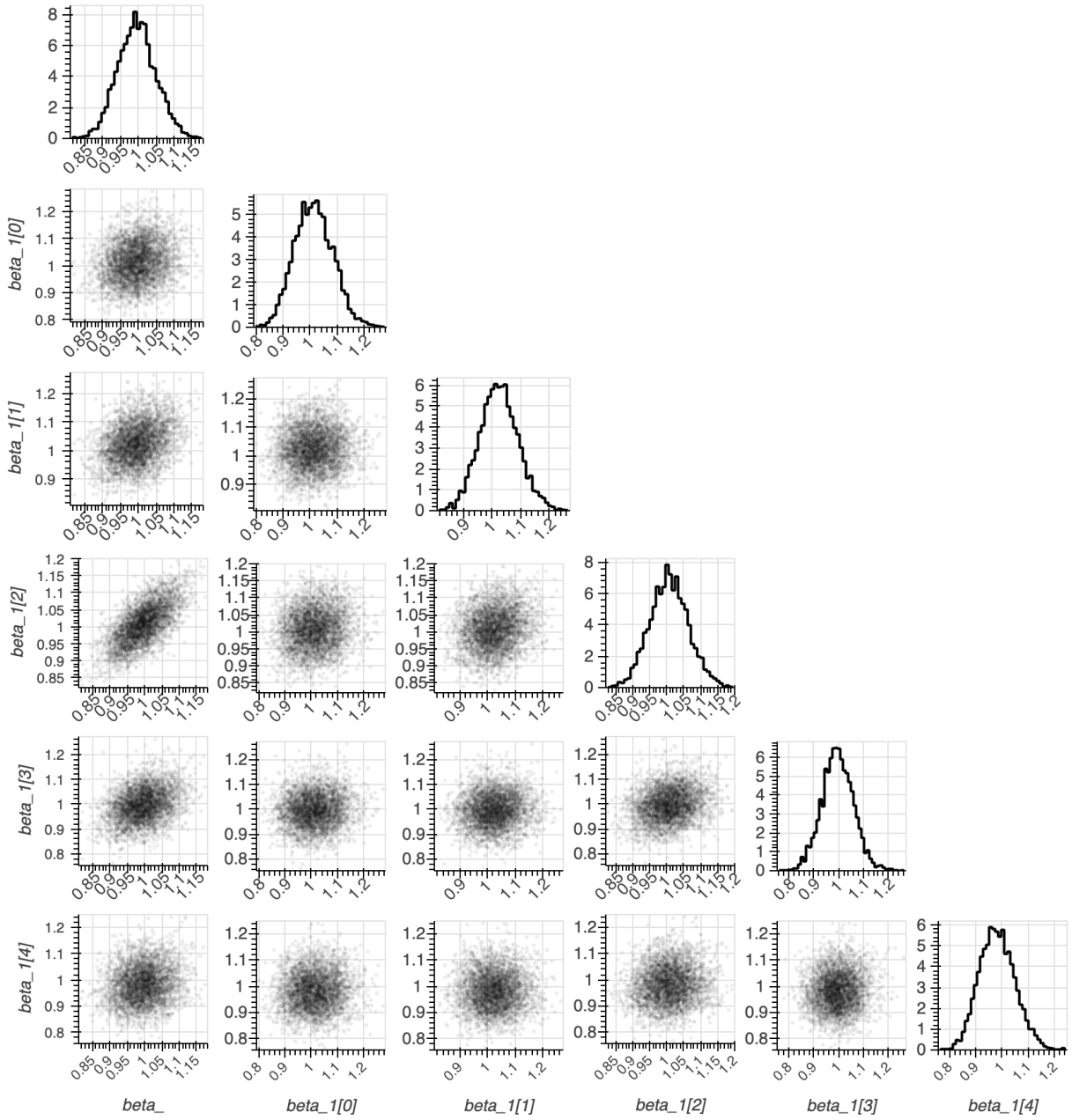

Figure S43. HMC Posterior samples for $\beta_{1,ij}$ and β_i parameters using C_2H_6 ATom 4 aircraft and GEOS-Chem simulations. Beta_1 parameter is a vector of length 5, corresponding to the synoptic replicates of GEOS-Chem. Beta_1[0] and beta_1[1] correspond to 2 days before the aircraft, beta_1[2] is the plane path, and beta_1[3] and beta_1[4] correspond to 2 days after the aircraft. The hyperparameter β_i is represented by beta_.

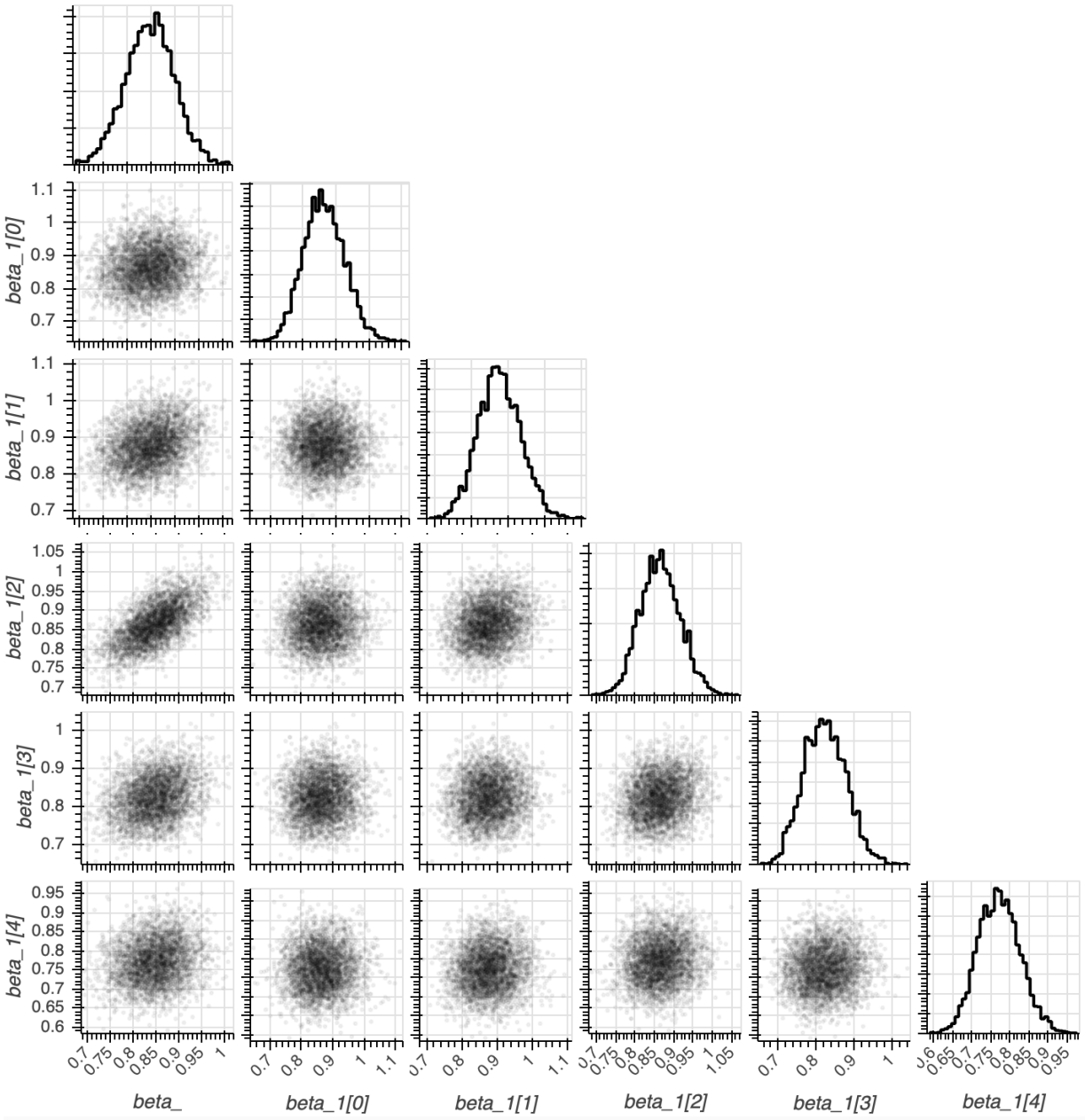

Figure S44. HMC Posterior samples for $\beta_{1,ij}$ and β_i parameters using C_3H_8 ATom 4 aircraft and GEOS-Chem simulations. Beta_1 parameter is a vector of length 5, corresponding to the synoptic replicates of GEOS-Chem. Beta_1[0] and beta_1[1] correspond to 2 days before the aircraft, beta_1[2] is the plane path, and beta_1[3] and beta_1[4] correspond to 2 days after the aircraft. The hyperparameter, β_i, is represented by beta_.

In Figure S45, we show a cross plot of our hyperparameter, β_i and $\beta_{1,ij}$, in inverse form, for a single ATom campaign, which directly corresponds to the scaling of our adjusted default emissions under the GEOS-Chem v13.0.0 simulations. This shows an example of the variability due to GEOS-Chem meteorology compared to the hyperparameter that we use to scale the emissions. In

Figure S46, we show the results of the Bayesian model for the α_i emissions scalar estimate for all 4 ATom campaigns and ocean transects.

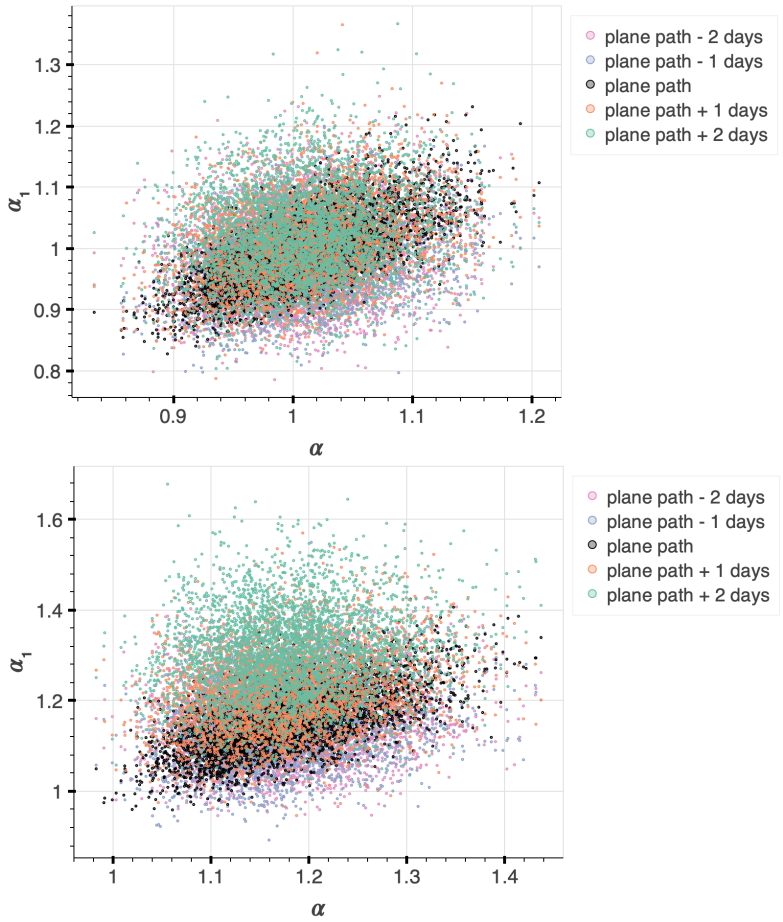

Figure S45. Posterior samples of $\alpha_{1,ij}$ vs α_i during ATom 4. **Top**: C_2H_6 observations. **Bottom**: C_3H_8 observations.

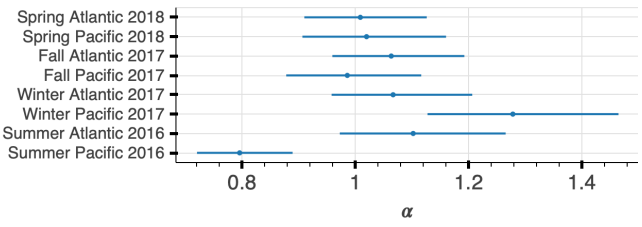

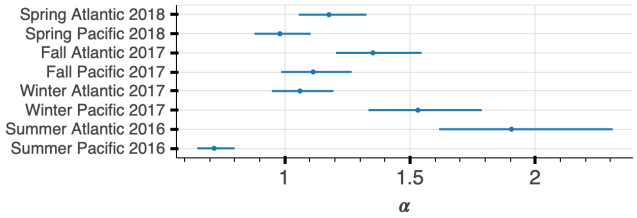

Figure S46. α_i hyperparameter estimate for each season during the ATom campaign. We do not include the summer values to calculate an overall α estimate as discussed in the methods in the main text. **Top**: C_2H_6, **Bottom**: C_3H_8.

S5.4 Posterior predictive check – ATom observations

Posterior predictive checks involve drawing parameter values out of the posterior, using those parameters in the likelihood to generate a pseudo dataset, and repeat. We can see whether our Bayesian model can produce the observed data. Below, we show all posterior predictive checks for all ATom aircraft campaigns (Figures S47, S48). The majority of the measured data fell into the 30th and 50th percentile of the simulated Bayesian model data. The exception to this was the summer season, where the Bayesian model does not capture the measured aircraft data. This is expected, since during the summer we do not observe a robust relationship between potential temperature and C_3H_8 or C_2H_6.

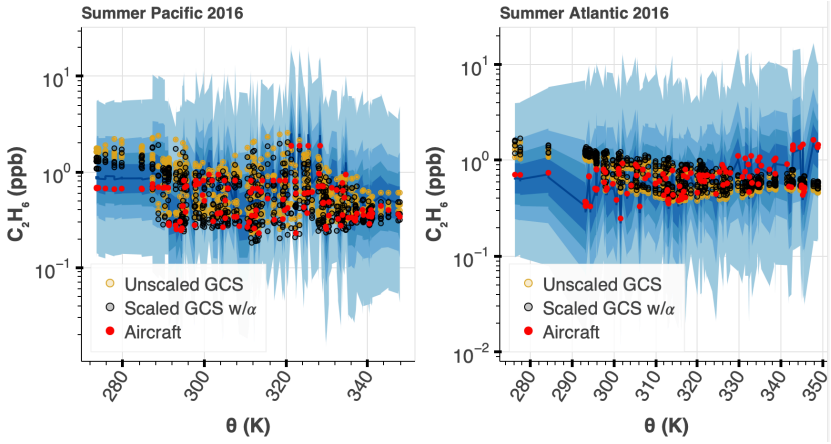

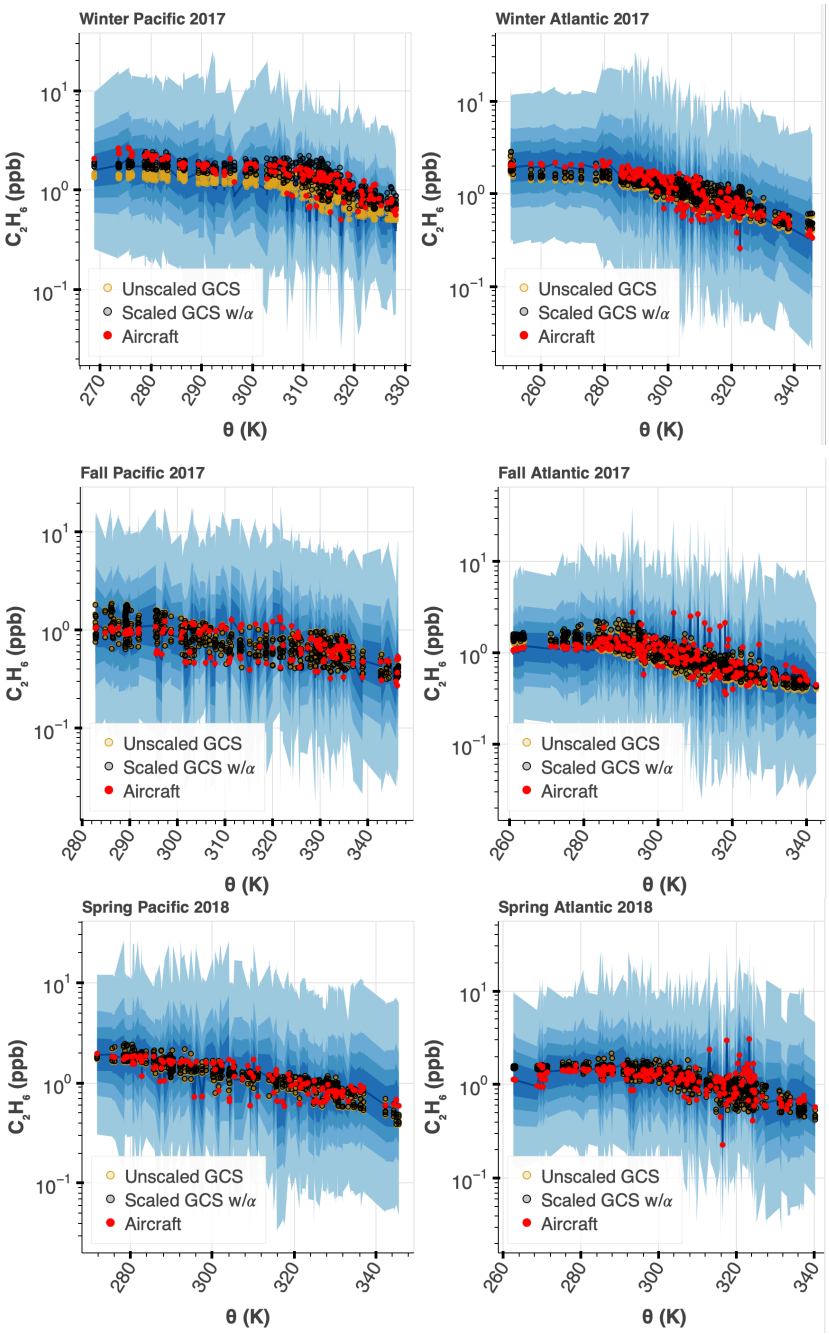

Figure S47. Posterior predictive check of C_2H_6 using ATom data. Posterior predictive checks are explained in the text above. The pseudo data are shown in blue with 30, 50, 70, 99th percentiles. Please see Figure S46 for the estimated values of α_i that were used to scale the GCS data in each season/transect.

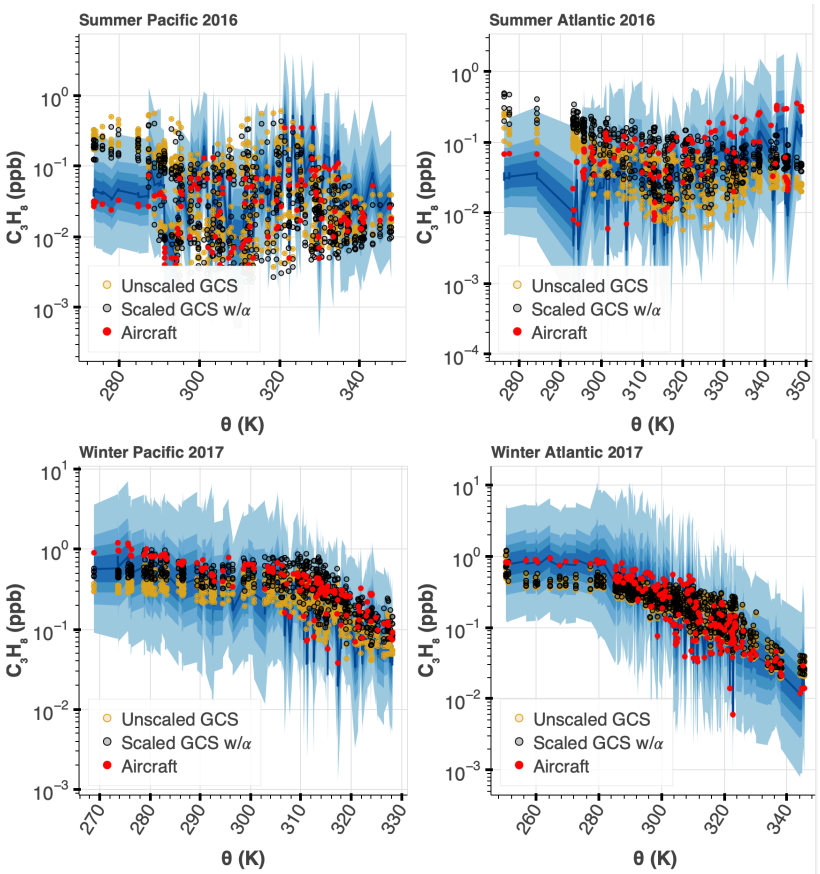
Summer Pacific 2016
Summer Atlantic 2016
Winter Pacific 2017
Winter Atlantic 2017
C_3H_8 (ppb)
θ (K)
Unscaled GCS
Scaled GCS w/α
Aircraft

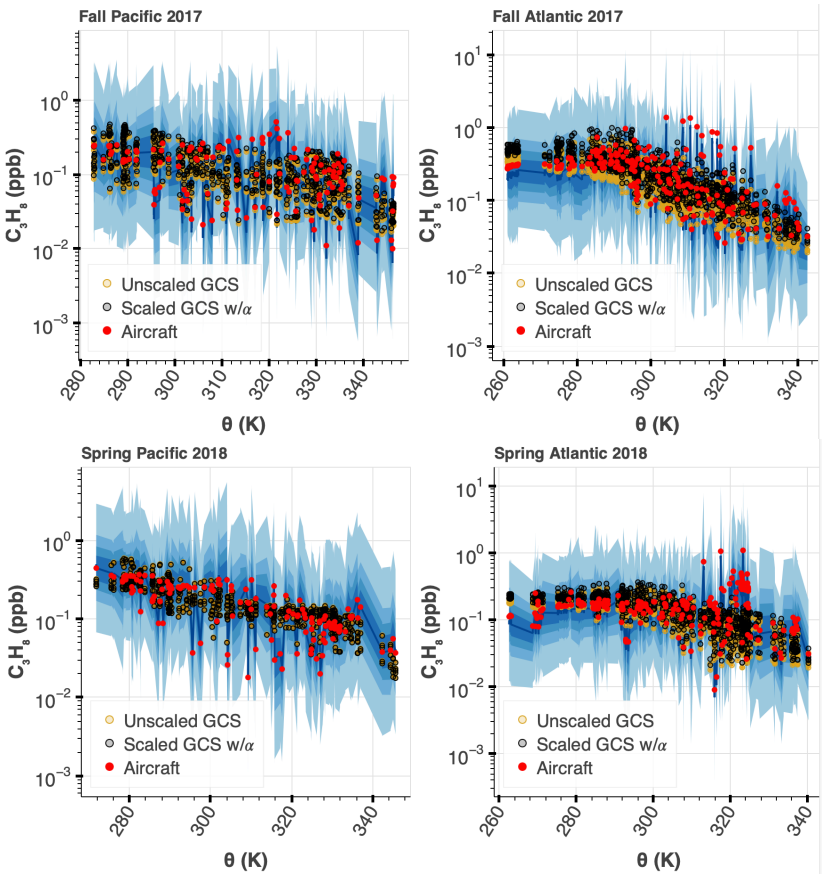

Figure S48. Posterior predictive check of C_3H_8 using ATom data. (Posterior predictive checks are explained in the text above.) The pseudo data are shown in blue with 30, 50, 70, 99th percentiles. Please see Figure S46 for the estimated values of α_i that were used to scale the GCS data in each season/transect.

Both C_3H_8 and C_2H_6 aircraft observations feature high mole fractions during ATom 2 winter measurements at low potential temperature. The largest differences between the aircraft and GEOS-Chem simulations occur at high latitude and low altitude (Figure S49), subject to low altitude and cold environments. GEOS-Chem does not able to capture this variability, as discussed in Section 3.3 in the main text.

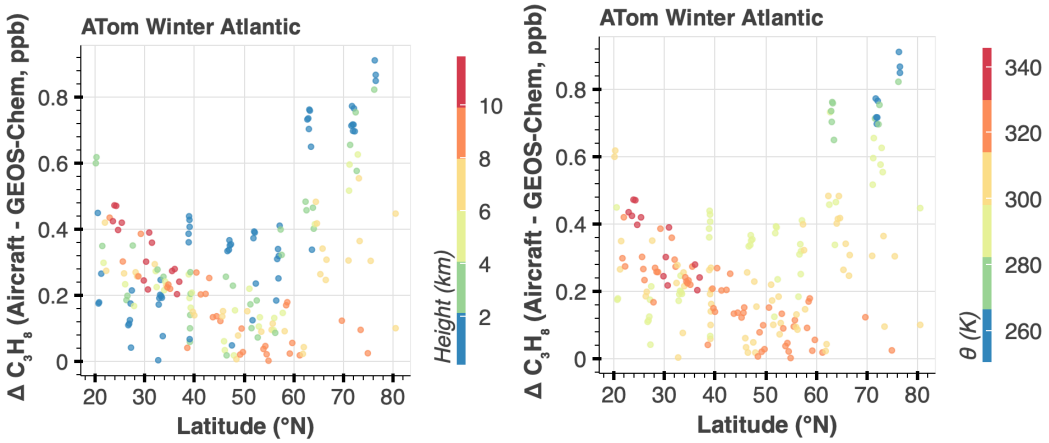

Figure S49. Difference between aircraft and GEOS-Chem C_3H_8 simulations. Simulations and aircraft observations during ATom 2, Atlantic transect, are shown. Points are colored by altitude (left) and potential temperature (right).

S5.5 Posterior samples – HIPPO observations

We show an example of our posterior sampling for our Bayesian model using HIPPO C_2H_6 and C_3H_8 observations in Figures S50 and S51 below.

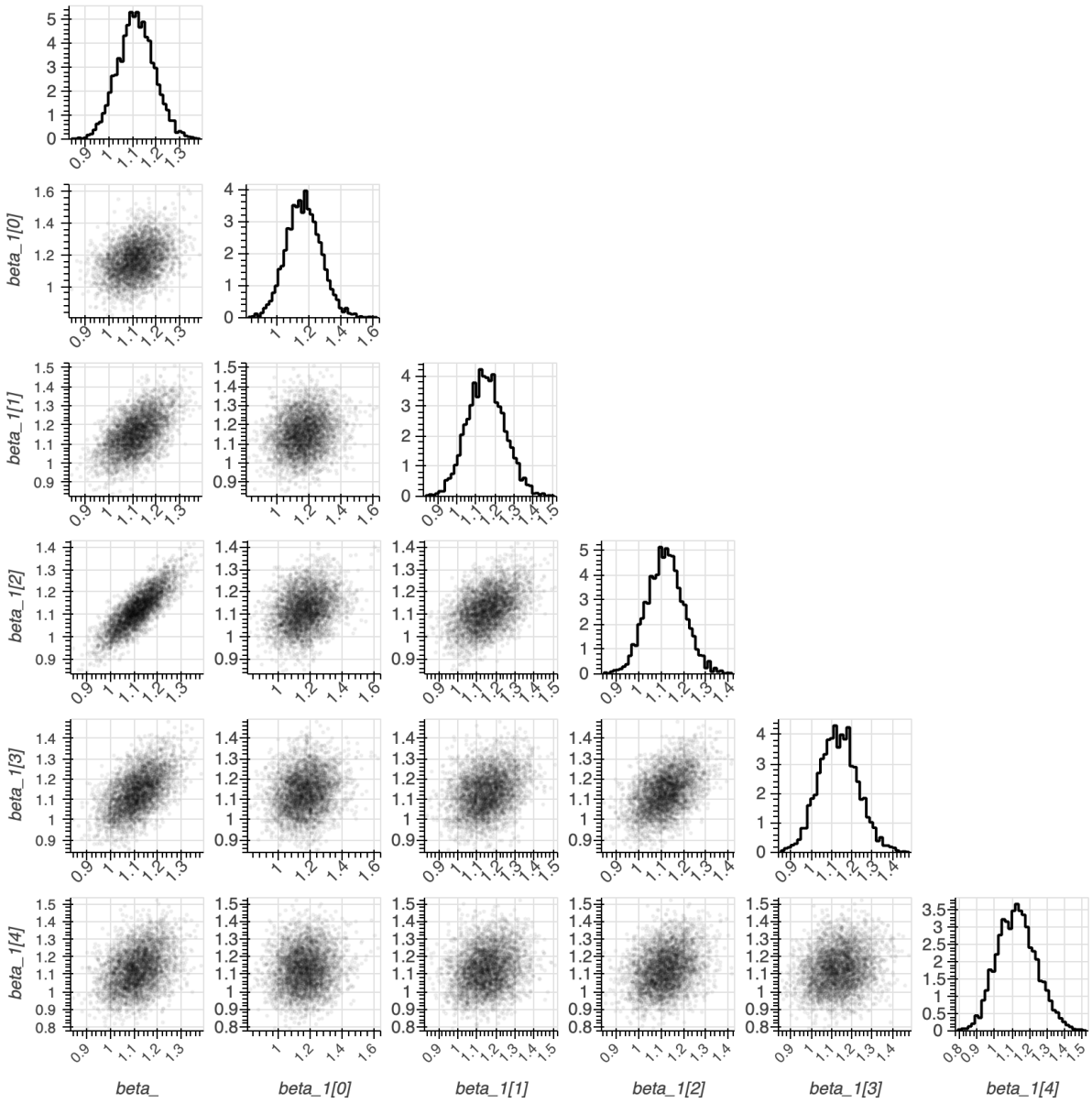

Figure S50. HMC Posterior samples for $\beta_{1,ij}$ and β_i parameters using C_2H_6 HIPPO 5 aircraft and GEOS-Chem simulations. Beta_1 parameter is a vector of length 5, corresponding to the synoptic replicates of GEOS-Chem. Beta_1[0] and beta_1[1] correspond to 2 days before the aircraft, beta_1[2] is the plane path, and beta_1[3] and beta_1[4] correspond to 2 days after the aircraft. The hyperparameter, β_i, is represented by beta_.

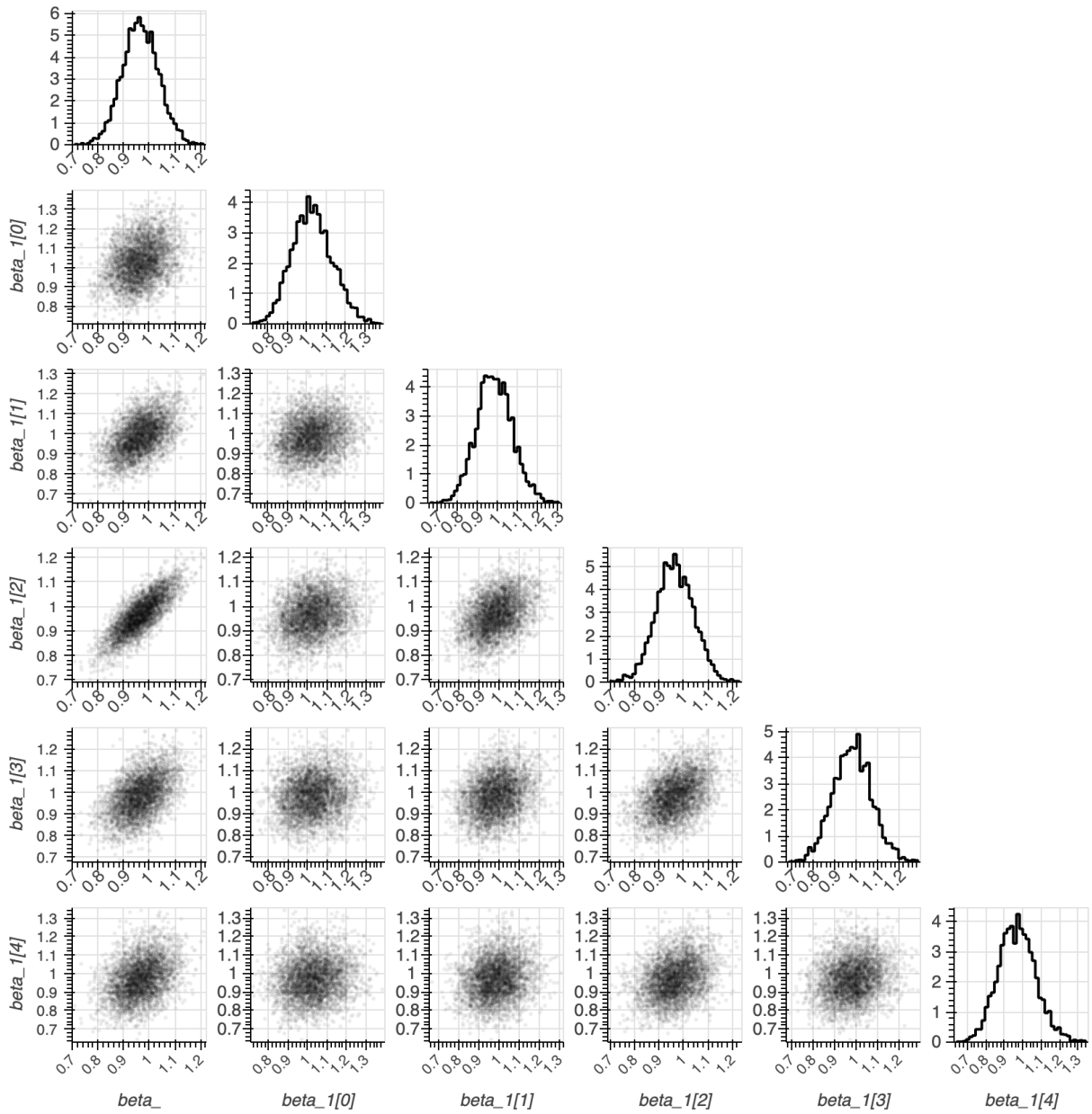

Figure S51. HMC Posterior samples for $\beta_{1,ij}$ and β_i parameters using C_3H_8 HIPPO 5 aircraft and GEOS-Chem simulations. Beta_1 parameter is a vector of length 5, corresponding to the synoptic replicates of GEOS-Chem. Beta_1[0] and beta_1[1] correspond to 2 days before the aircraft, beta_1[2] is the plane path, and beta_1[3] and beta_1[4] correspond to 2 days after the aircraft. The hyperparameter, β_i, is represented by beta_.

In Figure S52, we show a cross plot of our hyperparameter, $\beta_{1,ij}$ **and** β_i, in inverse form, for a single HIPPO campaign, which directly corresponds to the scaling of the GEOS-Chem v13.0.0 emissions. This shows an example of the variability due to GEOS-Chem meteorology compared

to the hyperparameter that we use to scale the emissions. In Figure S53, we show the results of the Bayesian model for the α_i emissions scalar estimate for all 5 HIPPO campaigns.

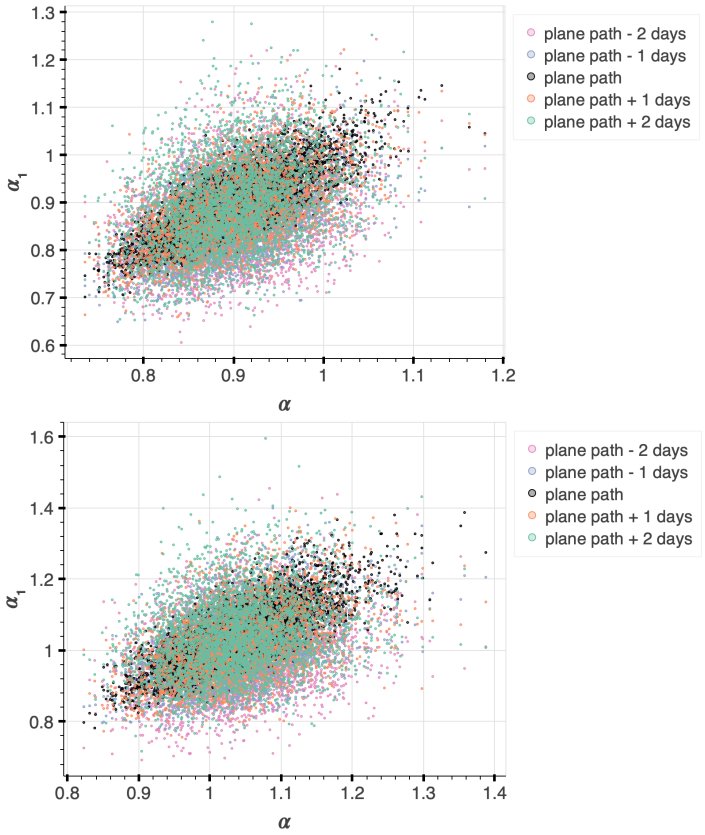

Figure S52. Posterior samples of $\alpha_{1,ij}$ vs α_i during HIPPO 5. **Top**: C_2H_6 observations. **Bottom**: C_3H_8 observations.

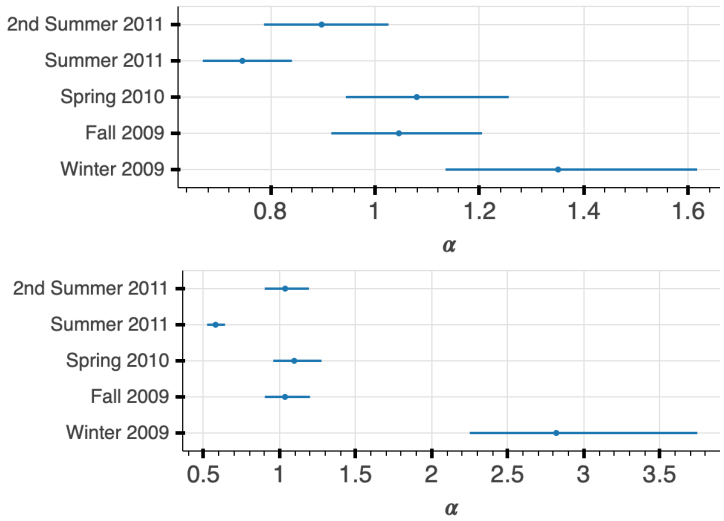

Figure S53. α_i hyperparameter estimate for each season during the HIPPO campaign. We do not include the summer values to calculate an overall α estimate as discussed in the methods in the

main text. **Top**: C_2H_6, **Bottom**: C_3H_8. There are many fewer observations during HIPPO than ATom resulting in a much larger spread and bigger uncertainty in defining α_i.

S5.6. Posterior predictive check – HIPPO observations

Posterior predictive checks involve drawing parameter values out of the posterior, using those parameters in the likelihood to generate a pseudo dataset, and repeat. We can see whether our Bayesian model can produce the observed data. Below, we show all posterior predictive checks for all HIPPO aircraft campaigns (Figures S54, S55).

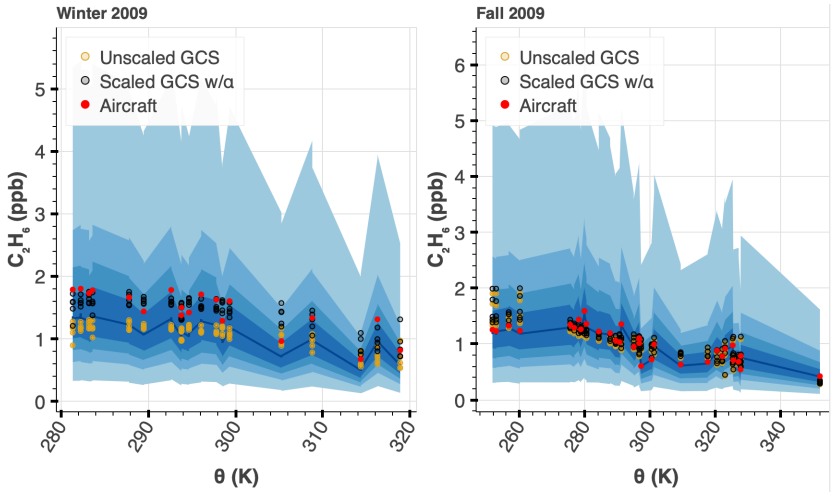

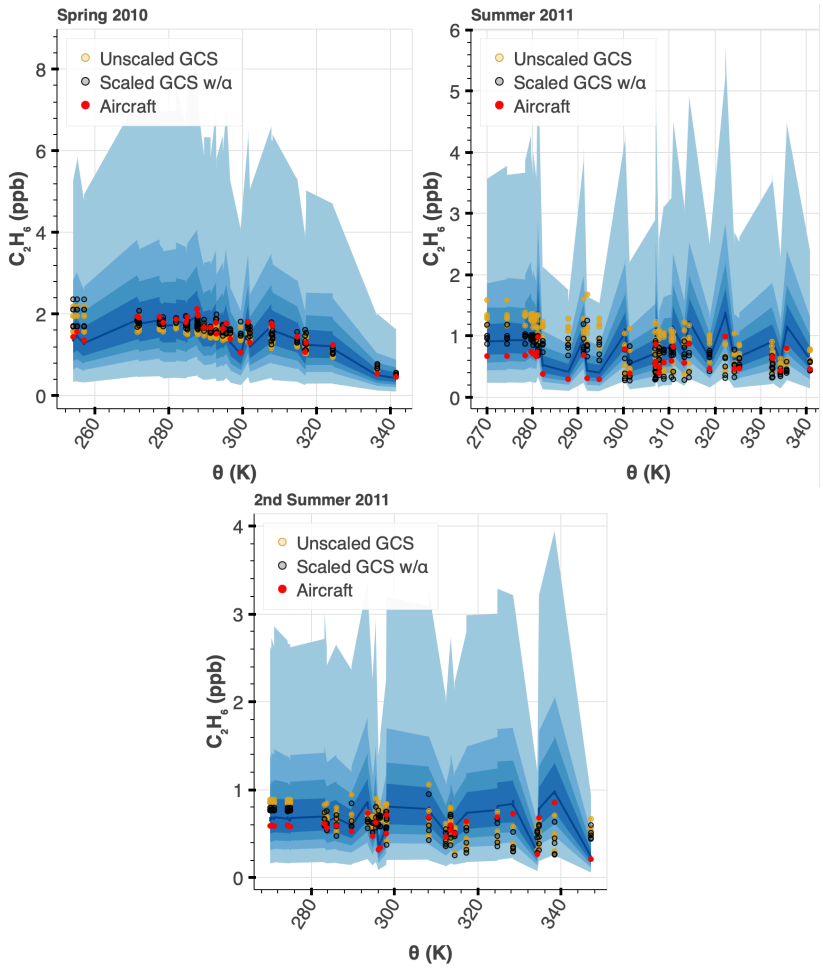

Figure S54. Posterior predictive check of C_2H_6 using HIPPO data. (Posterior predictive check method is described in the text above.) The pseudo data are shown in blue with 30, 50, 70, 99th percentiles. Please see Figure S53 for the estimated values of α_i that were used to scale the GCS data in each season/transect.

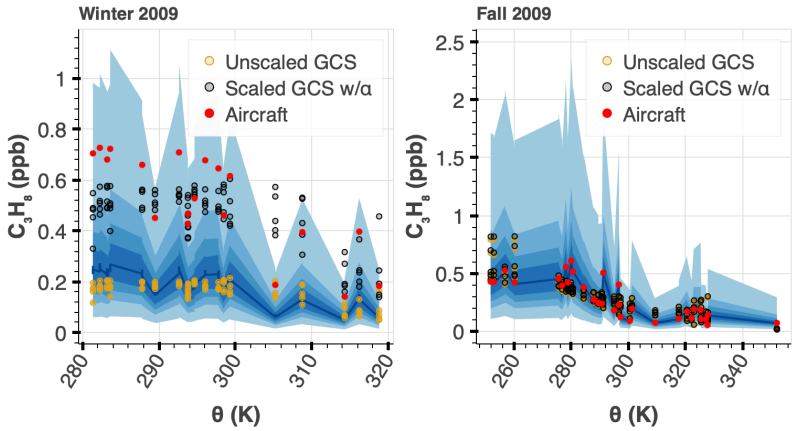

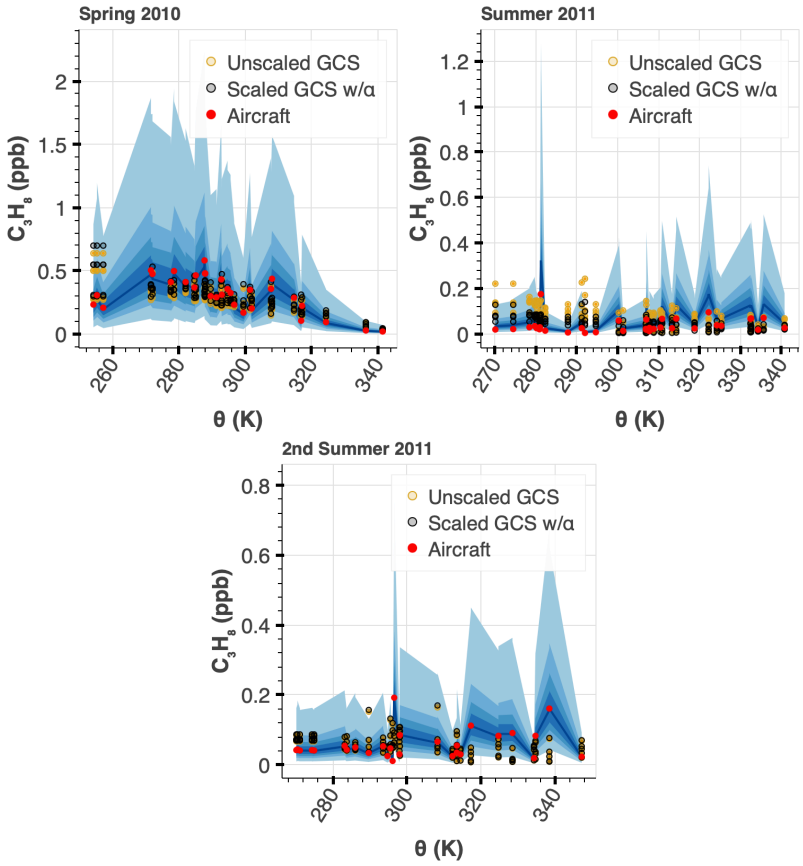

Figure S55. Posterior predictive check of C_3H_8 using HIPPO data. (Posterior predictive check method is described in the text above.) The pseudo data are shown in blue with 30, 50, 70, 99th percentiles. Please see Figure S53 for the estimated values of α_i that were used to scale the GCS data in each season/transect.

During HIPPO 1 (winter 2009), observations are biased towards high latitudes and are subject to arctic conditions. Furthermore, the revised emissions may be missing a high latitude source. This, combined with a relatively lower number of HIPPO aircraft observations at lower latitudes, results in a substantial bias on the overall Bayesian emissions scalar estimate for C_3H_8 during winter 2009 (Figure S53). To illustrate sampling biases at high latitudes during the winter 2009 campaign, we obtain two Bayesian estimates of α_i during each season: one estimate using aircraft observations restricted above 300 K (potential temperature) and those below 300 K. We see that observations restricted to values less than 300 K result in very high α_i estimates that bias the overall α scalar estimate (Figure S56-S57).

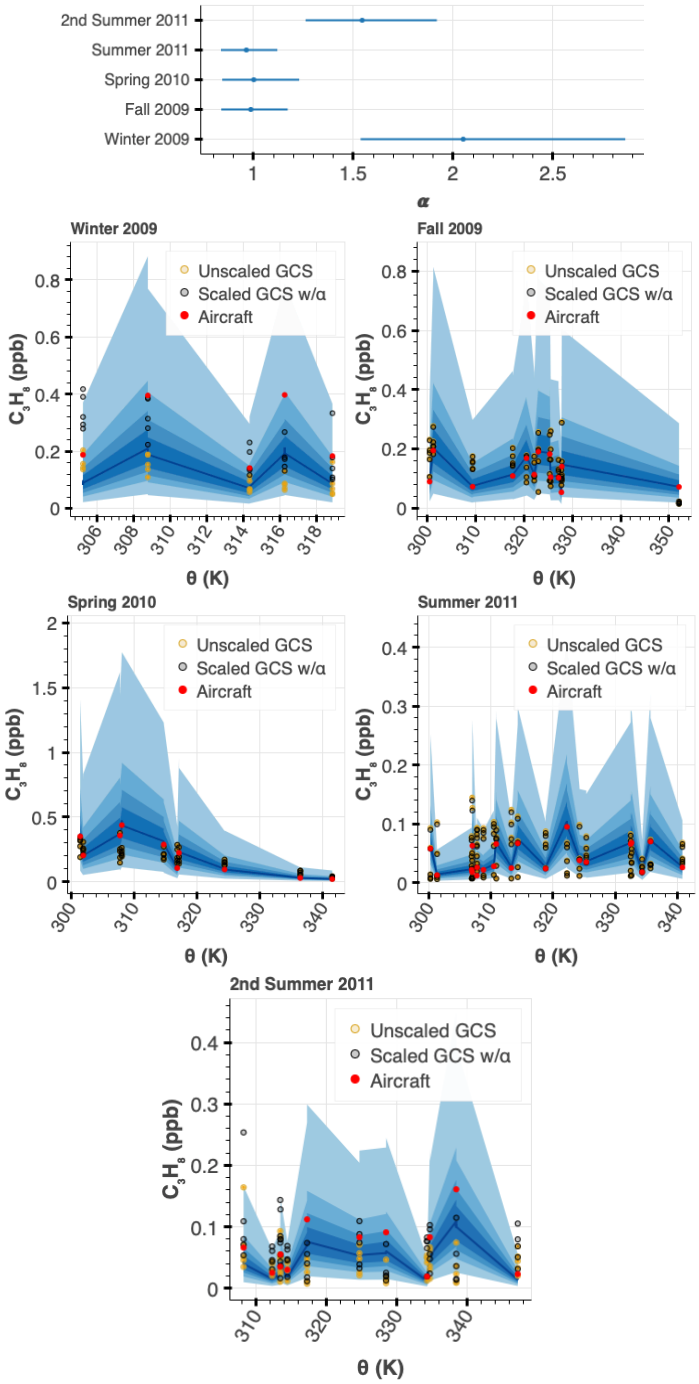

Figure S56. Bayesian α_i hyperparameter estimate and posterior predictive checks using HIPPO aircraft observations > 300 K.

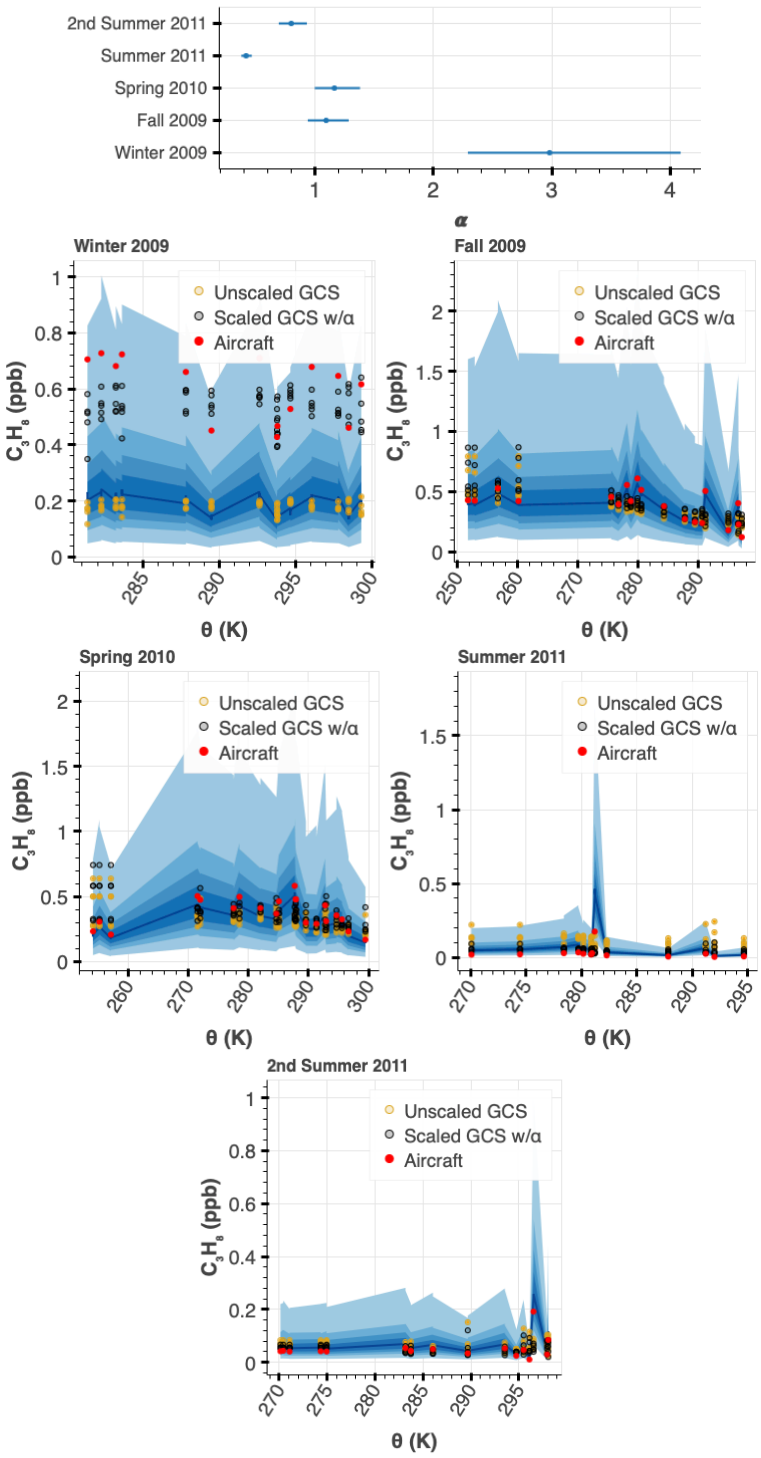

Figure S57. Bayesian $\boldsymbol{\alpha_i}$ hyperparameter estimate and posterior predictive checks using HIPPO aircraft observations < 300 K.

S5.7. Sigma parameter sensitivity analysis

We use ATom aircraft/GEOS-Chem simulations of C_3H_8 to observe the effect of implementing an unchanging, large σ_{ij} parameter. (As a reminder, the σ_{ij} parameter has the effect of de-weighting GEOS-Chem simulations with higher tropopause height, since samples with high tropopause height tend to originate from the tropics, which is not useful for the purposes of our study. Please see Section 5.1 for more background on the parameters and the selected prior.) Here, we show that in practice, our model is quite robust against changes in σ_{ij}.

Using an unchanging, relatively large σ_{ij} parameter equal to 3.5 in the lognormal likelihood yields α_i hyperparameter estimates (Figure S58, S59) that are nearly identical to our results shown previously in which σ_{ij} varies according to tropopause height (Figure S45, S46). Furthermore, we obtain similar posterior predictive checks (Figure S60) as our previous results (Figure S48).

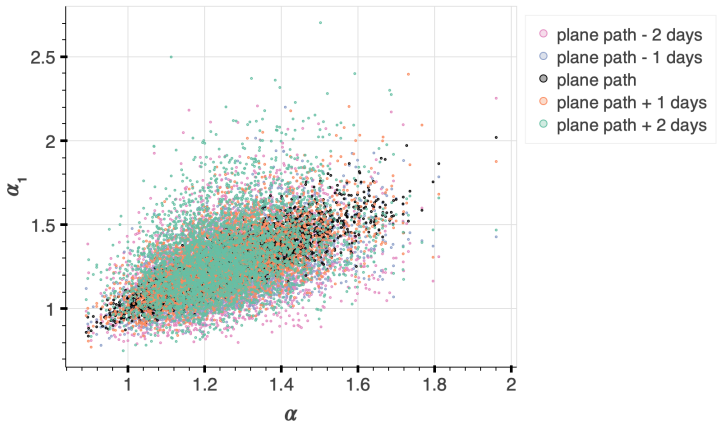

Figure S58. Posterior samples of $\alpha_{1,ij}$ vs α_i using a scalar σ_{ij} parameter. We use σ_{ij} = 3.5 instead of the usual distribution in the lognormal likelihood during ATom 4 time period.

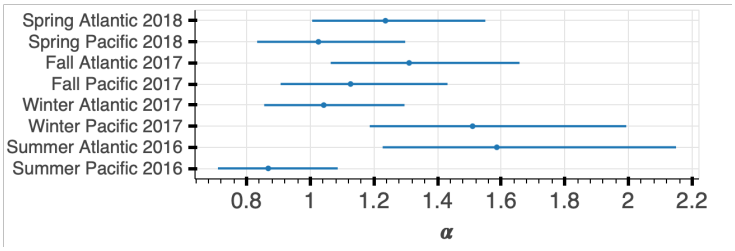

Figure S59. Estimate of α hyperparameter after using a scalar σ_{ij} parameter. We use σ_{ij} = 3.5 in the lognormal likelihood during ATom 4 time period.

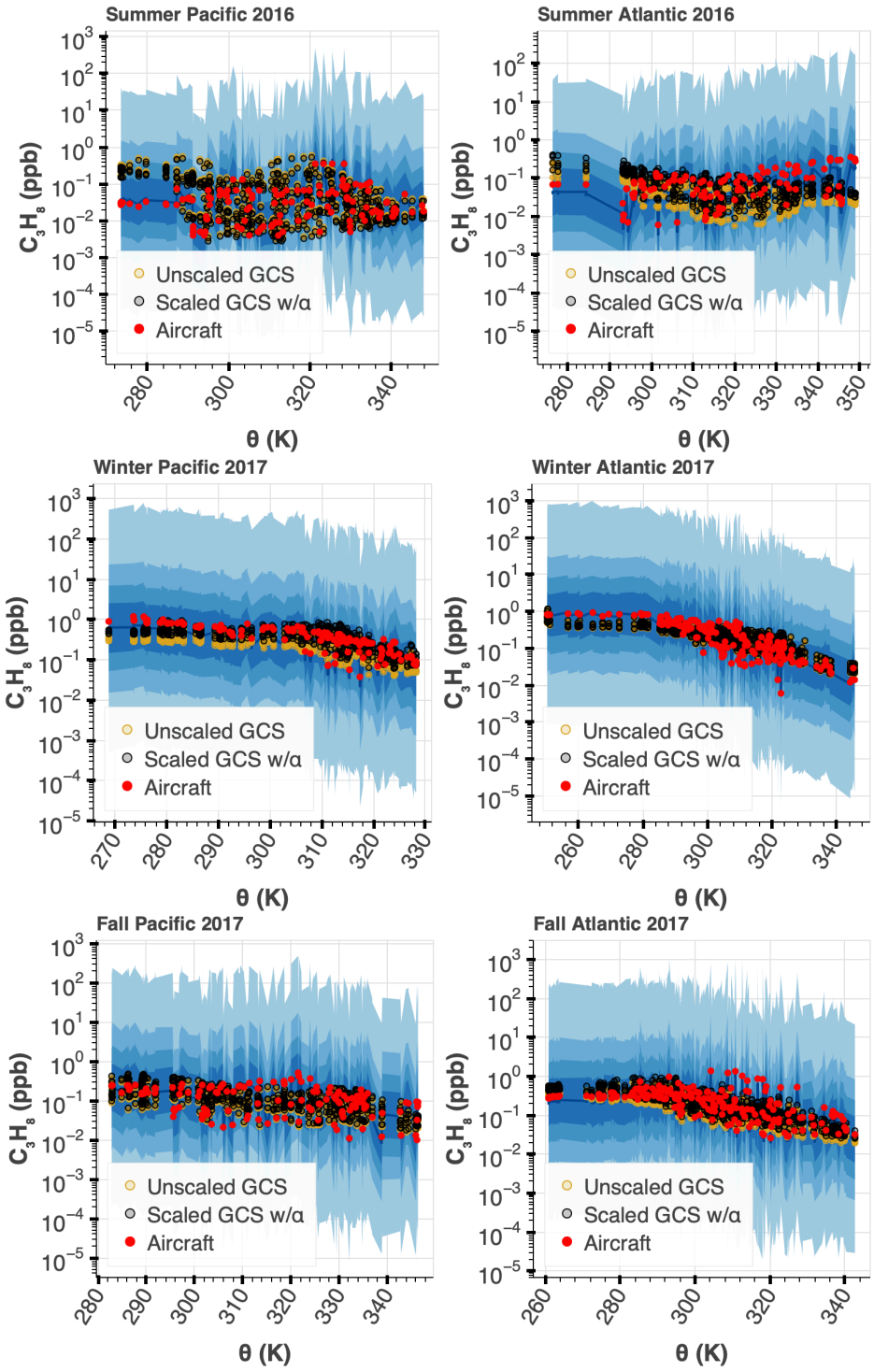
Summer Pacific 2016
Summer Atlantic 2016
Winter Pacific 2017
Winter Atlantic 2017
Fall Pacific 2017
Fall Atlantic 2017
C_3H_8 (ppb)
θ (K)
Unscaled GCS
Scaled GCS w/α
Aircraft

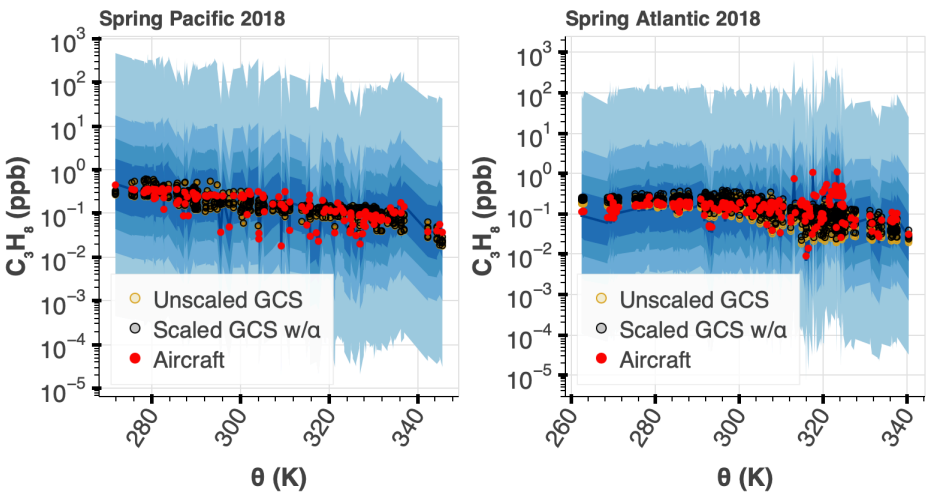

Figure S60. Posterior predictive check for C_3H_8 using a scalar σ_{ij} parameter. We use σ_{ij} = 3.5 in the lognormal likelihood.

S5.8. Estimating an overall emissions scalar

To estimate a credible interval for an overall α, we draw a random sample of the posterior of hyperparameter α_i for each campaign season and ocean transect. We take the mean of these samples and repeat this 10,000 times. (Note that we do not use the summer estimates for this calculation, for reasons described in the main text.) For ATom, the 95% confidence interval for α of C_2H_6 is [1.02, 1.13] and for α of C_3H_8, [1.15, 1.27]. For HIPPO, the confidence interval for α of C_2H_6 is [1.06, 1.28] and for α of C_3H_8, [1.45, 1.98].

S5.9 Estimating C_2H_6 and C_3H_8 Emissions

GEOS-Chem v13.0.0 emissions were calculated using the Harmonized Emissions Component (HEMCO) v3.0.0, as described in section 2.3 in the main text. To estimate emissions over the Northern Hemisphere and the U.S., we calculate a simple integration by defining a rectangle that describes the latitude and longitude boundaries that approximately encloses the geographical region of interest. (Table S3 shows those boundary estimates.) We approximate latitude and longitude to meters using the Haversine formula. We then integrate the region of the emission grid computed by HEMCO of the anthropogenic variable using trapezoidal integration along latitude and longitude. When estimating global emissions, we do not impose any boundaries on latitude or longitude. After integration, we simply convert the resulting units of kg/second to Tg/year.

Table S3. Boundary estimates for emissions grid.

Region	Latitude Min	Latitude Max	Longitude Min	Longitude Max
US	20	50	-130	-60
Northern Hemisphere	0	80	-165	180

The anthropogenic variable does not include biomass burning or biofuel emissions, according to GEOS-Chem documentation. Finally, we scale the emissions estimate for each boundary region with an overall hyperparameter, α, estimated during ATom from section 5.8. We report fossil emissions using 95% CI of α to define the variability. Our estimates for global fossil fuel emissions of C_2H_6 and C_3H_8 are [12.67, 13.98] (13.3 $\pm$ 0.7, 95% CI) and [13.89, 15.44] (14.7 $\pm$ 0.8, 95% CI) Tg/year, respectively (during the median year of 2017). Northern hemisphere emissions of C_2H_6 and C_3H_8 from fossil fuel production to be [11.18, 12.30] and [12.23, 13.60] Tg/year, respectively. In the U.S., we estimate C_2H_6 and C_3H_8 fossil fuel emissions at [1.29, 1.42] and [1.41, 1.56] Tg/year. Note that the global C_2H_6 emissions estimated in 2016-2018 are about 15% larger than in 2009-2011 ([10.55, 12.57] Tg/yr, Figure S61). Our C_3H_8 emissions are about 65% larger than in 2009-2011 ([7.31, 12.2] Tg/yr when not including the biased winter 2009 estimate that is impacted by arctic conditions and few observations. Our results are comparable to other studies (Figure S62).

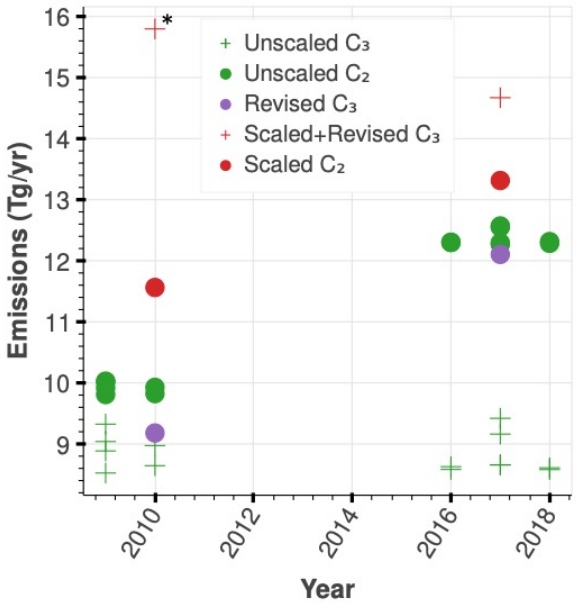

Figure S61. Global ethane and propane emissions during 2009-2018. "Unscaled" represent integrated default emissions from GEOS-Chem v13.0.0. "Revised C_3" represent the revised C_3H_8 emissions after implementing the default v13.0.0 C_2H_6 proxy. "Scaled+Revised C_3" represents the revised C_3H_8 emissions after scaling with our mean Bayesian estimate (Section 5.8). "Scaled C_2" represent the revised emissions after scaling with our mean Bayesian estimate (Section 5.8). $*$: Note that our mean scaled C_3 estimate shown here are skewed, as the 2009 winter HIPPO

observations are latitudinally biased. We show that C_3 emissions increase by 65% from 2010 to 2017 when excluding the bias below in Figure S62.

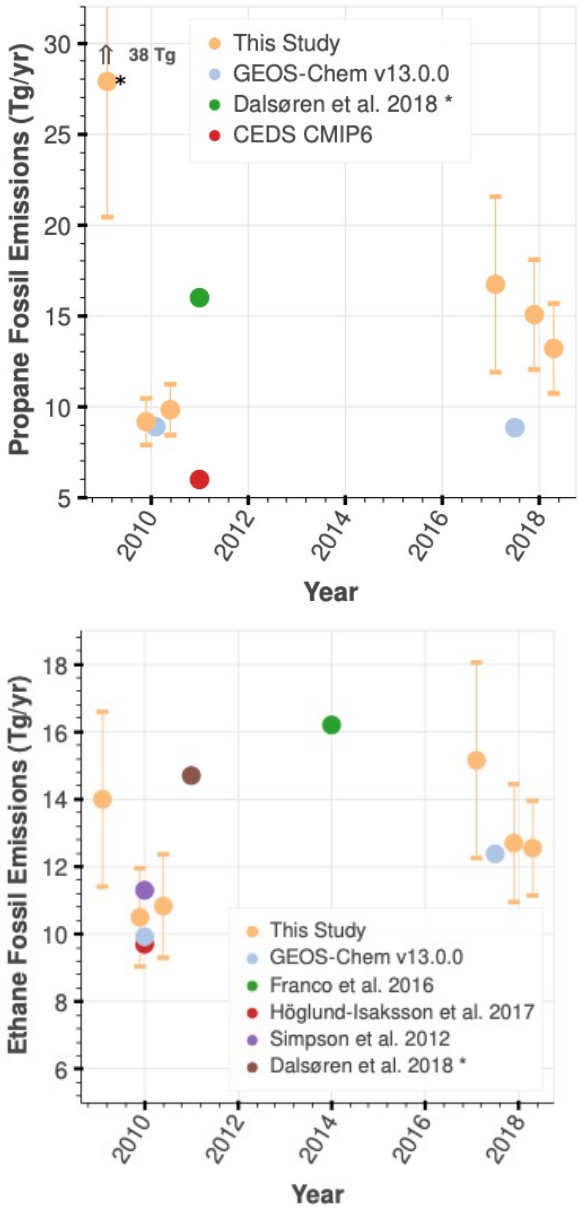

Figure S62. Global revised ethane and propane anthropogenic fossil emissions compared to other studies. Our emissions estimate in 2016-2018 (during ATom) and 2009-2011 (during HIPPO) includes GEOS-Chem v13.0.0 emissions for winter, fall and spring seasons scaled by α, that we determined with our Bayesian model during each season. As discussed in the text, fewer samples were obtained during HIPPO, resulting in a sampling bias that we test by restricting observations and simulations to $\pm$ 300K potential temperature (Figure S51-S52). This test affects the estimate about $\pm$ 1 Tg during 2010-2011 but affects our estimate by up to 12 Tg in 2009. $*$: This 2009 estimate is highly biased, as the latitudinal coverage of aircraft observations is not representative

of the global spatial distribution of methane emissions from oil and gas processes and the confidence interval stretches to nearly 40 Tg (please see Section 3.3 text and Figure S51-52). We compare our revised ethane and propane emissions to the default emissions from GEOS-Chem v13.0.0 (relevant anthropogenic inventories include Tzompa-Sosa et al. 2017[25] for C_2H_6, and Xiao et al. 2008[4] for C_3H_8). ‡: The studies included here[38–41] represent anthropogenic fossil emissions, except Dalsøren et al. 2018 which also includes biofuel, agriculture, and waste. We obtained the CEDS CMIP6 estimate from Dalsøren et al. 2018. Our emissions estimates do not include biomass burning or biofuels. Please see Section 5 in the SI for more information on estimating these emissions.

S6. Oil & Gas Emissions

S6.1. Hydrocarbon wellhead composition

We gathered hydrocarbon wellhead compositions reported in the literature for the top five natural gas-producing countries in the world (Table S4 and S5).

Table S4. Statistical summaries of hydrocarbon wellhead composition for the globe. Units are in mole % for the US,[42–49] Russia,[50–56] Qatar,[57] Iran,[58] and Canada [59–62]. **Top**: C_1; **Middle**: C_2; **Bottom**: C_3.

region	count	mean	std	min	25%	50%	75%	max
CANADA	22.0	74.090909	10.962747	54.00	65.2500	77.000	83.000	89.00
IRAN	45.0	89.531333	4.071936	74.16	89.2700	90.870	91.860	93.53
QATAR	1.0	89.900000	-	89.90	89.9000	89.900	89.900	89.90
RUSSIA	18.0	88.278778	12.873191	65.00	75.6875	95.685	98.500	100.00
US	63.0	85.718413	9.687639	52.67	78.3550	88.170	93.835	98.44

region	count	mean	std	min	25%	50%	75%	max
CANADA	22.0	14.909091	4.849242	7.0000	10.250	15.00	18.00	24.00
IRAN	45.0	5.624667	1.506998	4.0300	5.110	5.32	5.60	11.71
QATAR	1.0	6.000000	-	6.0000	6.000	6.00	6.00	6.00
RUSSIA	18.0	7.075722	7.677314	0.0000	0.750	4.50	11.95	26.00
US	63.0	7.029257	5.513786	0.0912	2.525	5.30	11.84	24.60

region	count	mean	std	min	25%	50%	75%	max
CANADA	22.0	11.000000	7.244045	4.00	5.0000	6.500	15.75	24.00
IRAN	45.0	2.250222	1.081225	1.37	1.7500	1.970	2.12	6.78
QATAR	1.0	2.200000	-	2.20	2.2000	2.200	2.20	2.20
RUSSIA	18.0	6.242111	7.98688	0.00	0.5600	1.945	11.95	26.00
US	63.0	2.792530	3.044868	0.00	0.1535	1.930	4.88	12.86

Table S5. Statistical summaries of hydrocarbon wellhead composition in the U.S. Units are in mole %.[42–49] **Top**: C_1; **Middle**: C_2; **Bottom**: C_3.

region	count	mean	std	min	25%	50%	75%	max
Appalachian	22.0	88.089091	7.121542	76.38	82.5250	88.180	94.1925	98.440
Bakken	1.0	52.670000	-	52.67	52.6700	52.670	52.6700	52.670
Barnett	5.0	84.962000	7.248256	77.81	80.3000	81.200	91.8000	93.700
Eagleford	13.0	80.726923	7.325718	66.20	77.8000	80.270	82.9900	91.790
Haynesville	15.0	94.344000	2.323018	89.40	92.5950	95.000	96.2100	97.100
Niobrara	4.0	77.447500	6.680047	68.49	74.2725	79.350	82.5250	82.600
Permian	3.0	70.140000	3.86114	66.26	68.2190	70.178	72.0800	73.982

region	count	mean	std	min	25%	50%	75%	max
Appalachian	22.0	6.558182	4.71379	1.1000	2.6325	5.235	10.6600	16.10
Bakken	1.0	24.600000	-	24.6000	24.6000	24.600	24.6000	24.60
Barnett	5.0	7.544000	3.983802	2.6000	4.4000	8.100	10.8200	11.80
Eagleford	13.0	10.045385	4.711809	0.2500	9.1900	11.880	12.6200	16.30
Haynesville	15.0	1.585613	1.58007	0.0912	0.2160	0.419	2.8800	4.10
Niobrara	4.0	10.877500	2.185869	8.5000	9.7000	10.655	11.8325	13.70
Permian	3.0	12.786333	1.172344	11.4540	12.3495	13.245	13.4525	13.66

region	count	mean	std	min	25%	50%	75%	max
Appalachian	22.0	2.069295	1.88617	0.020	0.15175	1.9000	3.3750	6.070
Bakken	1.0	12.860000	-	12.860	12.86000	12.8600	12.8600	12.860
Barnett	5.0	2.584000	2.465011	0.000	0.40000	2.3000	5.0200	5.200
Eagleford	13.0	3.813077	2.550161	0.030	2.06000	4.0500	5.1000	8.520
Haynesville	15.0	0.370527	0.417251	0.000	0.00850	0.0325	0.8355	0.927
Niobrara	4.0	5.777500	3.298488	2.700	4.05000	5.0000	6.7275	10.410
Permian	3.0	8.795667	1.469655	7.352	8.04850	8.7450	9.5175	10.290

Using Equation 2 (main text), we combine literature estimates of dry natural gas production and hydrocarbon composition measurements from a variety of basins (Table S4 and Table S5) to arrive at a global and U.S. C_3/C_1 emission ratio. We refer to this value as a "literature" emission ratio. For our global literature emission ratio, we use hydrocarbon and dry natural gas production data from the top 5 producing natural gas basins around the world that made up 50% of the total natural gas production in 2019. For our U.S. emission ratio, we include the top 7 natural gas producing basins that account for 86% of total U.S. natural gas production. The literature emission ratio of C_2/C_1 is calculated similarly. We arrive at a single literature emission estimate for both the US and globe (Figure 13, main text). Due to the limited published data on hydrocarbon composition, we compile data we found for a range of years: U.S. (2003-2020), Russia (1995-2018), Qatar (2005), Iran (2006), Canada (2004-2020). We calculate confidence intervals for each basin by performing a pairs bootstrap with co-measurements of hydrocarbon composition using the same bootstrap methods used with the NOAA and FRAPPE data as described in the methods section of the main text.

Separately, we calculate an "implied" emission ratio by taking the ratio between our revised C_3H_8 emissions with several literature estimates of CH_4 emissions from oil and natural gas processes. The results are shown in Figure S63. The implied emission ratio for our revised C_2H_6 is calculated similarly. For the EPA U.S. CH_4 emissions estimate,[63] we sum the categories "Natural Gas Systems", "Petroleum Systems", and "Abandoned Oil and Gas Wells" from Table 3-1 using the 2017 estimates (to match NOAA/ATom time period during 2016-2018).

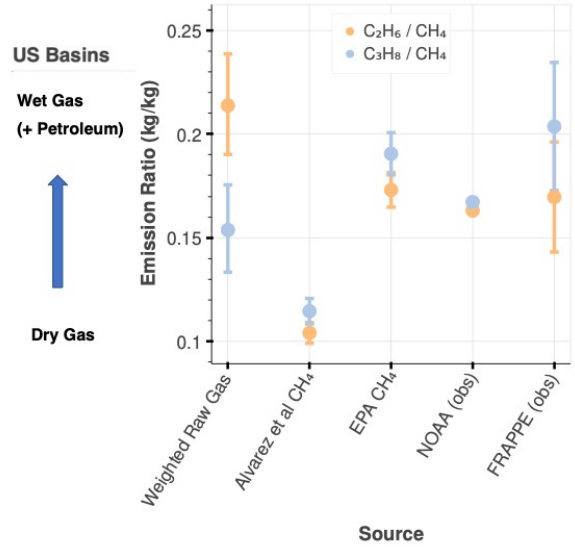

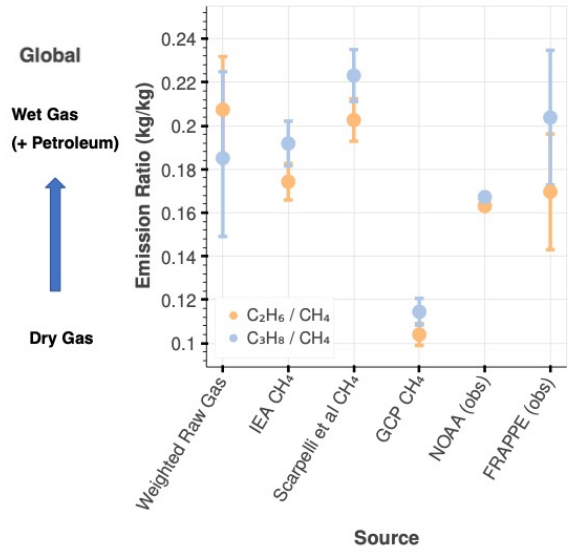

Figure S63. Literature and Observationally-Informed Emission ratios. **Top**: U.S. basins; **Bottom**: Global basins. The weighted raw gas ratio represents the "literature ratio" described in the main text. OIER, ratios between our revised C_2H_6 and C_3H_8 emissions and literature CH_4 emission estimates, are shown for several literature CH_4 estimates, including Alvarez et al. 2018 (13 Tg/yr)[64] and EPA 2017 estimate (7.8 Tg/yr, 2021 report)[63] for U.S. basins, and IEA 2021 (76.4 Tg/yr),[65] Scarpelli et al. 2020 (65.7 Tg/yr),[66] and Global Carbon Project 2020 bottom-up estimate[67] (128 Tg/yr, 2008-2017 average) for global basins. The variability in the literature ratio is attributed to the 95% CI of pairs bootstrap samples of hydrocarbon composition measurements (see main text for more detail). The variability in the OIER is attributed to the 95% CI of our revised C_3H_8 and C_2H_6 emission estimates. We also compare C_3H_8/CH_4 and C_2H_6/CH_4 correlations from in-situ observations, including NOAA observations from Northern Oklahoma (2017 average from Figure S21, units of kg/kg) and FRAPPE observations from Northern Colorado (2014 from Figure S9, units of kg/kg). The variability in the NOAA ratio is relatively low because it is calculated from a multi-year average slope, and the error in the slope is low (see Figure S21, left). The variability in the FRAPPE ratio is relatively high because we use the 95% CI derived directly from our bootstrap samples described in the main text.

S6.2. Impact of reallocation of CH4 emissions on the transportation sector footprint

There has been much debate about the greenhouse gas mitigation impact of switching from coal to natural gas energy in electricity production. The impact depends on how much CH_4 is lost during natural gas production, processing, and transport as these losses will offset some of the benefits of the lower CO_2 emissions. A study by the Environmental Defense Fund suggested that a CH_4 leak rate greater than 3% would negate the climate benefits of switching from coal to gas in the near term (the current leak rate is estimated at 2.3%).[68] As described here and in other studies, although CH_4 emissions associated with dry natural gas production likely remain underestimated, flared and

vented associated gas from petroleum exploration contributes significantly to the total emissions. Since global oil production has continually increased over the past 3 decades (Figure S2), and our findings suggest that CH_4 losses are at least proportional to production (but likely greater and biased towards oil-producing sites), a significant fraction of the estimated CH_4 emissions may be misallocated to dry CH_4 production and should instead be included with the oil production sector. Correctly attributing CH_4 emissions from oil production to the transportation sector, rather than the power sector, increases the greenhouse gas footprint of petroleum-based transportation, while decreasing the greenhouse gas emissions ascribed to natural gas-powered power plants. As an example, if we assume that 20% of natural gas losses are associated with petroleum exploration (associated natural gas makes up 20% of total natural gas marketed production in the U.S.[69]), the CO_2 equivalent footprint of the global transportation sector would increase by roughly 5%, using IEA's estimate of 76 Tg/year CH_4 emissions from oil and natural gas and recent transportation CO_2 emission estimates.[70,71] Equivalently, the U.S. transportation sector CO_2 footprint would increase by 2%, using the EPA's U.S. 2017 estimate (2021 report)[63] of 7.8 Tg/year CH_4 emissions and the U.S. petroleum/transportation sector CO_2 (equivalent) footprint as reported by the EPA (2017 estimate, 2021 report)[63]. Both of our estimates are lower bounds that will only increase when accounting for vented and flared losses of associated natural gas that is not accounted for in marketed associated gas.

Methods:

For a global estimate, we estimate the transportation footprint from Figure 4 from Liu et al. 2020[71] and multiply it by 365 to get 7,300 Mmt (million metric tones) CO_2 equivalents/year. We use 76 Tg/year of CH_4 from (IEA)[65] as a global estimate from oil and natural gas and find that 20% of that number results in 15.2 Tg, multiplied by 25 GWP, yields 6% of the transportation sector. Using the same process for the U.S., the EPA estimates the transportation sector at 1,740.2 Mmt CO_2/year (Table 3-5, Petroleum fuel/Transportation sector for 2017).[63] We use the EPA's 7.8 Tg/year[64] of CH_4 for the oil and gas estimate and find that 20% of 7.8 Tg/year multiplied by 25 GWP results in 2.2% of the U.S. transportation sector.

References

(1) U.S. Energy Information Administration. Where our natural gas comes from https://www.eia.gov/energyexplained/natural-gas/where-our-natural-gas-comes-from.php (accessed 2022 -03 -18).

(2) U.S. Energy Information Administration. Natural gas explained https://www.eia.gov/energyexplained/natural-gas/.

(3) Keller, A. NGL 101- The Basics, 2012. https://www.eia.gov/conference/ngl_virtual/EIA-NGL_workshop-Anne-Keller.pdf

(4) Xiao, Y.; Logan, J. A.; Jacob, D. J.; Hudman, R. C.; Yantosca, R.; Blake, D. R. Global Budget of Ethane and Regional Constraints on U.S. Sources. *J. Geophys. Res.* **2008**, *113* (D21). https://doi.org/10.1029/2007JD009415.
(5) MacIntyre, S., Wilczewski, W. U.S. Ethane Consumption, Exports to Increase as New Petrochemical Plants Come Online. U.S. Energy Information Administration April 2018.
(6) U.S. Energy Information Administration. Natural Gas Weekly Update. July 7, 2016. https://www.eia.gov/naturalgas/weekly/archivenew_ngwu/2016/07_07/.
(7) U.S. Energy Information Administration. Natural Gas Weekly Update. March 1, 2018. https://www.eia.gov/naturalgas/weekly/archivenew_ngwu/2018/03_01/.
(8) U.S. Energy Information Administration. Drilling Productivity Report for Key Tight Oil and Shale Gas Regions, 2022. https://www.eia.gov/petroleum/drilling/pdf/dpr-full.pdf.
(9) Worldwide Power Products. 10 Biggest Shale Plays in the US - New & Used Generators, Ends and Engines | Houston, TX | Worldwide Power Products.
(10) International Energy Agency. IEA Atlas of Energy: Natural Gas Production http://energyatlas.iea.org/#!/tellmap/-1165808390.
(11) International Energy Agency. IEA Atlas of Energy: Crude Oil Production http://energyatlas.iea.org/#!/tellmap/-1920537974.
(12) SoCalGas. Playa Del Rey Withdrawn Natural Gas Composition, 2021.
(13) U.S. Energy Information Administration. Natural Gas Gross Withdrawals and Production (U.S.), 2020. https://www.eia.gov/dnav/ng/ng_prod_sum_dc_NUS_mmcf_a.htm.
(14) U.S. Energy Information Administration. Natural Gas Plant Field Production, 2020. https://www.eia.gov/dnav/pet/pet_pnp_gp_dc_nus_mbbl_a.htm.
(15) Parrish, D. D.; Stohl, A.; Forster, C.; Atlas, E. L.; Blake, D. R.; Goldan, P. D.; Kuster, W. C.; de Gouw, J. A. Effects of Mixing on Evolution of Hydrocarbon Ratios in the Troposphere: Mixing Effects on NMHC Ratio Evolution. *J. Geophys. Res. Atmospheres* **2007**, *112* (D10). https://doi.org/10.1029/2006JD007583.
(16) Boyd, D. T.; Mankin, C. J. Map of Oklahoma Oil and Gas Fields - Oklahoma Geological Survey, 2002.
(17) Parker, J.; Wertz, J. Oklahoma Oil Production in the Last Five Years: Has It Changed?, 2017.
(18) Best, A. Water Education Colorado: Do Oil and Water Mix?, 2013.
(19) toddkarin. global-land-mask (1.0.0) https://pypi.org/project/global-land-mask/ (accessed 2022 -08 -22).
(20) NASA Global Modeling and Assimilation Office. GEOS5124 FP-IT 2d Assimilated State.
(21) Seinfeld, J. H.; Pandis, S. N. *Atmospheric Chemistry and Physics: From Air Pollution to Climate Change*, Third edition.; John Wiley & Sons: Hoboken, New Jersey, 2016.
(22) Gelaro, R.; McCarty, W.; Suárez, M. J.; Todling, R.; Molod, A.; Takacs, L.; Randles, C. A.; Darmenov, A.; Bosilovich, M. G.; Reichle, R.; Wargan, K.; Coy, L.; Cullather, R.; Draper, C.; Akella, S.; Buchard, V.; Conaty, A.; da Silva, A. M.; Gu, W.; Kim, G.-K.; Koster, R.; Lucchesi, R.; Merkova, D.; Nielsen, J. E.; Partyka, G.; Pawson, S.; Putman, W.; Rienecker, M.; Schubert, S.

D.; Sienkiewicz, M.; Zhao, B. The Modern-Era Retrospective Analysis for Research and Applications, Version 2 (MERRA-2). *J. Clim.* **2017**, *30* (14), 5419–5454. https://doi.org/10.1175/JCLI-D-16-0758.1.

(23) Lin, H.; Jacob, D. J.; Lundgren, E. W.; Sulprizio, M. P.; Keller, C. A.; Fritz, T. M.; Eastham, S. D.; Emmons, L. K.; Campbell, P. C.; Baker, B.; Saylor, R. D.; Montuoro, R. Harmonized Emissions Component (HEMCO) 3.0 as a Versatile Emissions Component for Atmospheric Models: Application in the GEOS-Chem, NASA GEOS, WRF-GC, CESM2, NOAA GEFS-Aerosol, and NOAA UFS Models. *Geosci. Model Dev.* **2021**, *14* (9), 5487–5506. https://doi.org/10.5194/gmd-14-5487-2021.

(24) Community, T. I. G.-C. U. *Geoschem/HEMCO: HEMCO 3.0.0-Rc (HEMCO 3.0.0 Release Candidate)*; Zenodo, 2021. https://doi.org/10.5281/ZENODO.4429214.

(25) Tzompa-Sosa, Z. A.; Mahieu, E.; Franco, B.; Keller, C. A.; Turner, A. J.; Helmig, D.; Fried, A.; Richter, D.; Weibring, P.; Walega, J.; Yacovitch, T. I.; Herndon, S. C.; Blake, D. R.; Hase, F.; Hannigan, J. W.; Conway, S.; Strong, K.; Schneider, M.; Fischer, E. V. Revisiting Global Fossil Fuel and Biofuel Emissions of Ethane. *J. Geophys. Res. Atmospheres* **2017**, *122* (4), 2493–2512. https://doi.org/10.1002/2016JD025767.

(26) Gelman, A. *Bayesian Data Analysis*, Third edition.; Chapman & Hall/CRC texts in statistical science; CRC Press: Boca Raton, 2014.

(27) Stan Development Team. Stan Modeling Language Users Guide and Reference Manual, 2021.

(28) Stan Dev Team. CmdStanPy (0.9.76), 2021.

(29) Kumar, R.; Carroll, C.; Hartikainen, A.; Martin, O. ArviZ a Unified Library for Exploratory Analysis of Bayesian Models in Python. *J. Open Source Softw.* **2019**, *4* (33), 1143. https://doi.org/10.21105/joss.01143.

(30) Talts, S.; Betancourt, M.; Simpson, D.; Vehtari, A.; Gelman, A. Validating Bayesian Inference Algorithms with Simulation-Based Calibration. *ArXiv180406788 Stat* **2020**.

(31) Bois, J. *Justinbois/Bebi103: 0.1.0*; CaltechDATA, 2020. https://doi.org/10.22002/D1.1615.

(32) Bois, J. S. *Justinbois/Iqplot: 0.1.6*; CaltechDATA, 2020. https://doi.org/10.22002/D1.1614.

(33) Rudiger, P.; Stevens, J.-L.; Bednar, J. A.; Nijholt, B.; Mease, J.; Andrew; B, C.; Randelhoff, A.; Tenner, V.; Maxalbert; Kaiser, M.; Ea42gh; Stonebig; Hoxbro; Samuels, J.; Pevey, K.; LB, F.; Tolmie, A.; Stephan, D.; Bois, J.; Lowe, S.; Bampton, J.; Henriqueribeiro; Ruoyu0088; Lustig, I.; Klein, A.; Van De Ven, B.; Raillard, D.; Signell, J.; Talirz, L. *Holoviz/Holoviews: Version 1.14.5*; Zenodo, 2021. https://doi.org/10.5281/ZENODO.5114034.

(34) Brendan Collins, B. V. D. V. Bokeh: Essential Open Source Tools for Science. **2020**. https://doi.org/10.5281/ZENODO.4317717.

(35) Reback, J.; Jbrockmendel; McKinney, W.; Van Den Bossche, J.; Augspurger, T.; Cloud, P.; Hawkins, S.; Gfyoung; Sinhrks; Roeschke, M.; Klein, A.; Terji Petersen; Tratner, J.; She, C.; Ayd, W.; Hoefler, P.; Naveh, S.; Garcia, M.; Schendel, J.; Hayden, A.; Saxton, D.; Shadrach, R.;

Gorelli, M. E.; Jancauskas, V.; Fangchen Li; Attack68; McMaster, A.; Battiston, P.; Skipper Seabold; Kaiqi Dong. *Pandas-Dev/Pandas: Pandas 1.3.1*; Zenodo, 2021. https://doi.org/10.5281/ZENODO.5136416.

(36) Virtanen, P.; Gommers, R.; Burovski, E.; Oliphant, T. E.; Weckesser, W.; Cournapeau, D.; Alexbrc; Reddy, T.; Peterson, P.; Haberland, M.; Wilson, J.; Nelson, A.; Endolith; Mayorov, N.; Walt, S. V. D.; Ilhan Polat; Laxalde, D.; Brett, M.; Larson, E.; Millman, J.; Lars; Mulbregt, P. V.; Eric-Jones; CJ Carey; Moore, E.; Kern, R.; Peterbell10; Leslie, T.; Perktold, J.; Striega, K. *Scipy/Scipy: SciPy 1.6.2*; Zenodo, 2021. https://doi.org/10.5281/ZENODO.4635380.

(37) Harris, C. R.; Millman, K. J.; van der Walt, S. J.; Gommers, R.; Virtanen, P.; Cournapeau, D.; Wieser, E.; Taylor, J.; Berg, S.; Smith, N. J.; Kern, R.; Picus, M.; Hoyer, S.; van Kerkwijk, M. H.; Brett, M.; Haldane, A.; del Río, J. F.; Wiebe, M.; Peterson, P.; Gérard-Marchant, P.; Sheppard, K.; Reddy, T.; Weckesser, W.; Abbasi, H.; Gohlke, C.; Oliphant, T. E. Array Programming with NumPy. *Nature* **2020**, *585* (7825), 357–362. https://doi.org/10.1038/s41586-020-2649-2.

(38) Höglund-Isaksson, L. Bottom-up Simulations of Methane and Ethane Emissions from Global Oil and Gas Systems 1980 to 2012. *Environ. Res. Lett.* **2017**, *12* (2), 024007. https://doi.org/10.1088/1748-9326/aa583e.

(39) Dalsøren, S. B.; Myhre, G.; Hodnebrog, Ø.; Myhre, C. L.; Stohl, A.; Pisso, I.; Schwietzke, S.; Höglund-Isaksson, L.; Helmig, D.; Reimann, S.; Sauvage, S.; Schmidbauer, N.; Read, K. A.; Carpenter, L. J.; Lewis, A. C.; Punjabi, S.; Wallasch, M. Discrepancy between Simulated and Observed Ethane and Propane Levels Explained by Underestimated Fossil Emissions. *Nat. Geosci.* **2018**, *11* (3), 178–184. https://doi.org/10.1038/s41561-018-0073-0.

(40) Franco, B.; Mahieu, E.; Emmons, L. K.; Tzompa-Sosa, Z. A.; Fischer, E. V.; Sudo, K.; Bovy, B.; Conway, S.; Griffin, D.; Hannigan, J. W.; Strong, K.; Walker, K. A. Evaluating Ethane and Methane Emissions Associated with the Development of Oil and Natural Gas Extraction in North America. *Environ. Res. Lett.* **2016**, *11* (4), 044010. https://doi.org/10.1088/1748-9326/11/4/044010.

(41) Simpson, I. J.; Sulbaek Andersen, M. P.; Meinardi, S.; Bruhwiler, L.; Blake, N. J.; Helmig, D.; Rowland, F. S.; Blake, D. R. Long-Term Decline of Global Atmospheric Ethane Concentrations and Implications for Methane. *Nature* **2012**, *488* (7412), 490–494. https://doi.org/10.1038/nature11342.

(42) Howard, T.; Ferrara, T. W.; Townsend-Small, A. Sensor Transition Failure in the High Flow Sampler: Implications for Methane Emission Inventories of Natural Gas Infrastructure. *J. Air Waste Manag. Assoc.* **2015**, *65* (7), 856–862. https://doi.org/10.1080/10962247.2015.1025925.

(43) Thiagarajan, N.; Xie, H.; Ponton, C.; Kitchen, N.; Peterson, B.; Lawson, M.; Formolo, M.; Xiao, Y.; Eiler, J. Isotopic Evidence for Quasi-Equilibrium Chemistry in Thermally Mature Natural Gases. *Proc. Natl. Acad. Sci.* **2020**, *117* (8), 3989–3995. https://doi.org/10.1073/pnas.1906507117.

(44) Burruss, R. C.; Ryder, R. T. *Open-File Report*; Composition of crude oil and natural gas produced from 14 wells in the Lower Silurian “Clinton” sandstone and Medina Group,

northeastern Ohio and northwestern Pennsylvania; Open-File Report; U.S. Geological Survey: Reston, Virginia 20192, 2003.
(45) Fairhurstm, B.; Hanson, M. L. Evolution and Development of the WolfBone Play, Southern Delaware Basin, West Texas: An Emerging Frontier, An Oil-Rich Unconventional Resource; #10411 (2012). **2012**, 64.
(46) Bullin, K.; Krouskop, P. *Composition Variety Complicates Processing Plans from US Shale Gas*; Bryan Research and Engineering Inc., 2008.
(47) Higley, D. K.; Cox, D. O. *Oil and Gas Exploration and Development along the Front Range in the Denver Basin of Colorado, Nebraska, and Wyoming*; Petroleum Systems and Assessment of Undiscovered Oil and Gas in the Denver Basin Province, Colorado, Kansas, Nebraska, South Dakota, and Wyoming - USGS Province 39; Digital Data Series DDS-69-P; U.S. Geological Survey, 2007; p Ch.2.
(48) Laughrey, C. D. *Comparative Natural Gas Geochemistry of the Hanson 31-5054z Water Well and Select Upper Jurassic - Lower Cretaceous Oil and Gas Wells, Northwest Louisiana*; OilTracers Updated Report No. 18-2422; Louisiana Department of Natural Resources, 2018.
(49) Ghandi, A.; Yeh, S.; Brandt, A.; Vafi, K.; Cai, H.; Wang, M. Q.; Scanlon, B. R.; Reedy, R. C. *Energy Intensity and Greenhouse Gas Emissions from Crude Oil Production in the Eagle Ford Region: Input Data and Analysis Methods*; Institute of Transportation Studies, University of California, Davis, 2015.
(50) Kurchatova, A.; Rogov, V.; Taratunina, N. Geochemical Anomalies of Frozen Ground Due to Hydrocarbon Migration in West Siberian Cryolithozone. *Geosciences* **2018**, *8* (12), 430. https://doi.org/10.3390/geosciences8120430.
(51) Klyusov, V. A.; Ershov, A. A. Experience in Operation of Processing Equipment for Gas Pretreating Systems at the Yamburg Gas-Condensate Field. *Chem. Pet. Eng.* **1995**, *31* (12), 759–761. https://doi.org/10.1007/BF01155172.
(52) Andreev, O. P.; Arabsky, A. K.; Bashkin, V. N.; Priputina, I. V.; Barsukov, P. A. *Assessment of the Life Cycle of Nitrogen and Carbon Compounds Emitted in the Arctic: The Example of Natural Gas Fields of Gazprom Dobycha Yamburg*; International Gas Union Research Conference, 2011.
(53) Seligman, B. J. Key Factors Influencing the Reliability of Trunk Gas Pipelines in the West Siberian North, Pembroke College, 1998. https://core.ac.uk/download/pdf/237398547.pdf.
(54) Lechtenbömer, S.; Assonov, S. S.; Dienst, C.; Brenninkmeijer, C.; Fischedick, M.; Hanke, T.; Langrock, T. *Greenhouse Gas Emissions from the Russian Natural Gas Export Pipeline System*; Wuppertal Institute for Climate, Enivornment, Energy/Max-Planck-Institute for Chemistry.
(55) Batalin, O.; Vafina, N. Condensation Mechanism of Hydrocarbon Field Formation. *Sci. Rep.* **2017**, *7* (1), 10253. https://doi.org/10.1038/s41598-017-10585-7.
(56) *Biogeochemical Technologies for Managing Pollution in Polar Ecosystems*, 1st ed. 2017.; Bashkin, V. N., Ed.; Environmental Pollution; Springer International Publishing : Imprint: Springer: Cham, 2017. https://doi.org/10.1007/978-3-319-41805-6.

(57) Department of Energy. *Liquefied Natural Gas: Understanding the Basic Facts*; DOE/FE-0489; United States of America, 2005.
(58) Aali, J.; Rahimpour-Bonab, H.; Kamali, M. R. Geochemistry and Origin of the World's Largest Gas Field from Persian Gulf, Iran. *J. Pet. Sci. Eng.* **2006**, *50* (3–4), 161–175. https://doi.org/10.1016/j.petrol.2005.12.004.
(59) Murillo, C. A. *Natural Gas Liquids in North America: Overview and Outlook to 2035*; 130; Canadian Energy Research Institute, 2012.
(60) Natural Gas Intelligence. Information about the Duvernay Shale https://www.naturalgasintel.com/information-about-the-duvernay-shale/.
(61) Dieckmann, V.; Fowler, M.; Horsfield, B. Predicting the Composition of Natural Gas Generated by the Duvernay Formation (Western Canada Sedimentary Basin) Using a Compositional Kinetic Approach. *Org. Geochem.* **2004**, *35* (7), 845–862. https://doi.org/10.1016/j.orggeochem.2004.02.010.
(62) Alberta Energy Regulator. Natural Gas, 2021.
(63) U.S. Environmental Protection Agency (EPA). Inventory of U.S. Greenhouse Gas Emissions and Sinks: 1990-2019, 2021. https://www.epa.gov/sites/production/files/2021-04/documents/us-ghg-inventory-2021-main-text.pdf.
(64) Alvarez, R. A.; Zavala-Araiza, D.; Lyon, D. R.; Allen, D. T.; Barkley, Z. R.; Brandt, A. R.; Davis, K. J.; Herndon, S. C.; Jacob, D. J.; Karion, A.; Kort, E. A.; Lamb, B. K.; Lauvaux, T.; Maasakkers, J. D.; Marchese, A. J.; Omara, M.; Pacala, S. W.; Peischl, J.; Robinson, A. L.; Shepson, P. B.; Sweeney, C.; Townsend-Small, A.; Wofsy, S. C.; Hamburg, S. P. Assessment of Methane Emissions from the U.S. Oil and Gas Supply Chain. *Science* **2018**, eaar7204. https://doi.org/10.1126/science.aar7204.
(65) IEA. Methane Tracker Database: Interactive Database of Country and Regional Estimates for Methane Emissions and Abatement Options, 2021. https://www.iea.org/articles/methane-tracker-database#sources.
(66) Scarpelli, T. R.; Jacob, D. J.; Maasakkers, J. D.; Sulprizio, M. P.; Sheng, J.-X.; Rose, K.; Romeo, L.; Worden, J. R.; Janssens-Maenhout, G. A Global Gridded (0.1° × 0.1°) Inventory of Methane Emissions from Oil, Gas, and Coal Exploitation Based on National Reports to the United Nations Framework Convention on Climate Change. *Earth Syst. Sci. Data* **2020**, *12* (1), 563–575. https://doi.org/10.5194/essd-12-563-2020.
(67) Saunois, M.; Stavert, A. R.; Poulter, B.; Bousquet, P.; Canadell, J. G.; Jackson, R. B.; Raymond, P. A.; Dlugokencky, E. J.; Houweling, S.; Patra, P. K.; Ciais, P.; Arora, V. K.; Bastviken, D.; Bergamaschi, P.; Blake, D. R.; Brailsford, G.; Bruhwiler, L.; Carlson, K. M.; Carrol, M.; Castaldi, S.; Chandra, N.; Crevoisier, C.; Crill, P. M.; Covey, K.; Curry, C. L.; Etiope, G.; Frankenberg, C.; Gedney, N.; Hegglin, M. I.; Höglund-Isaksson, L.; Hugelius, G.; Ishizawa, M.; Ito, A.; Janssens-Maenhout, G.; Jensen, K. M.; Joos, F.; Kleinen, T.; Krummel, P. B.; Langenfelds, R. L.; Laruelle, G. G.; Liu, L.; Machida, T.; Maksyutov, S.; McDonald, K. C.; McNorton, J.; Miller, P. A.; Melton, J. R.; Morino, I.; Müller, J.; Murguia-Flores, F.; Naik, V.; Niwa, Y.; Noce, S.; O'Doherty, S.; Parker, R. J.; Peng, C.; Peng, S.; Peters, G. P.; Prigent, C.; Prinn, R.; Ramonet,

M.; Regnier, P.; Riley, W. J.; Rosentreter, J. A.; Segers, A.; Simpson, I. J.; Shi, H.; Smith, S. J.; Steele, L. P.; Thornton, B. F.; Tian, H.; Tohjima, Y.; Tubiello, F. N.; Tsuruta, A.; Viovy, N.; Voulgarakis, A.; Weber, T. S.; van Weele, M.; van der Werf, G. R.; Weiss, R. F.; Worthy, D.; Wunch, D.; Yin, Y.; Yoshida, Y.; Zhang, W.; Zhang, Z.; Zhao, Y.; Zheng, B.; Zhu, Q.; Zhu, Q.; Zhuang, Q. The Global Methane Budget 2000–2017. *Earth Syst. Sci. Data* **2020**, *12* (3), 1561–1623. https://doi.org/10.5194/essd-12-1561-2020.

(68) Alvarez, R. A.; Pacala, S. W.; Winebrake, J. J.; Chameides, W. L.; Hamburg, S. P. Greater Focus Needed on Methane Leakage from Natural Gas Infrastructure. *Proc. Natl. Acad. Sci.* **2012**, *109* (17), 6435–6440. https://doi.org/10.1073/pnas.1202407109.

(69) Clemente, J. The Rise of U.S. Associated Natural Gas. *Forbes*. June 3, 2018.

(70) EPA (Environmental Protection Agency). Global Anthropogenic Non-CO2 Greenhouse Gas Emissions: 1990-2030, 2012. https://www.epa.gov/sites/default/files/2016-08/documents/summary_global_nonco2_projections_dec2012.pdf.

(71) Liu, Z.; Ciais, P.; Deng, Z.; Lei, R.; Davis, S. J.; Feng, S.; Zheng, B.; Cui, D.; Dou, X.; Zhu, B.; Guo, R.; Ke, P.; Sun, T.; Lu, C.; He, P.; Wang, Y.; Yue, X.; Wang, Y.; Lei, Y.; Zhou, H.; Cai, Z.; Wu, Y.; Guo, R.; Han, T.; Xue, J.; Boucher, O.; Boucher, E.; Chevallier, F.; Tanaka, K.; Wei, Y.; Zhong, H.; Kang, C.; Zhang, N.; Chen, B.; Xi, F.; Liu, M.; Bréon, F.-M.; Lu, Y.; Zhang, Q.; Guan, D.; Gong, P.; Kammen, D. M.; He, K.; Schellnhuber, H. J. Near-Real-Time Monitoring of Global CO2 Emissions Reveals the Effects of the COVID-19 Pandemic. *Nat. Commun.* **2020**, *11* (1), 5172. https://doi.org/10.1038/s41467-020-18922-7.

Appendix A

Supplementary Information for "An Analysis Coordinate Transform to Facilitate Use of in-situ Aircraft Observations for Flux Estimation"

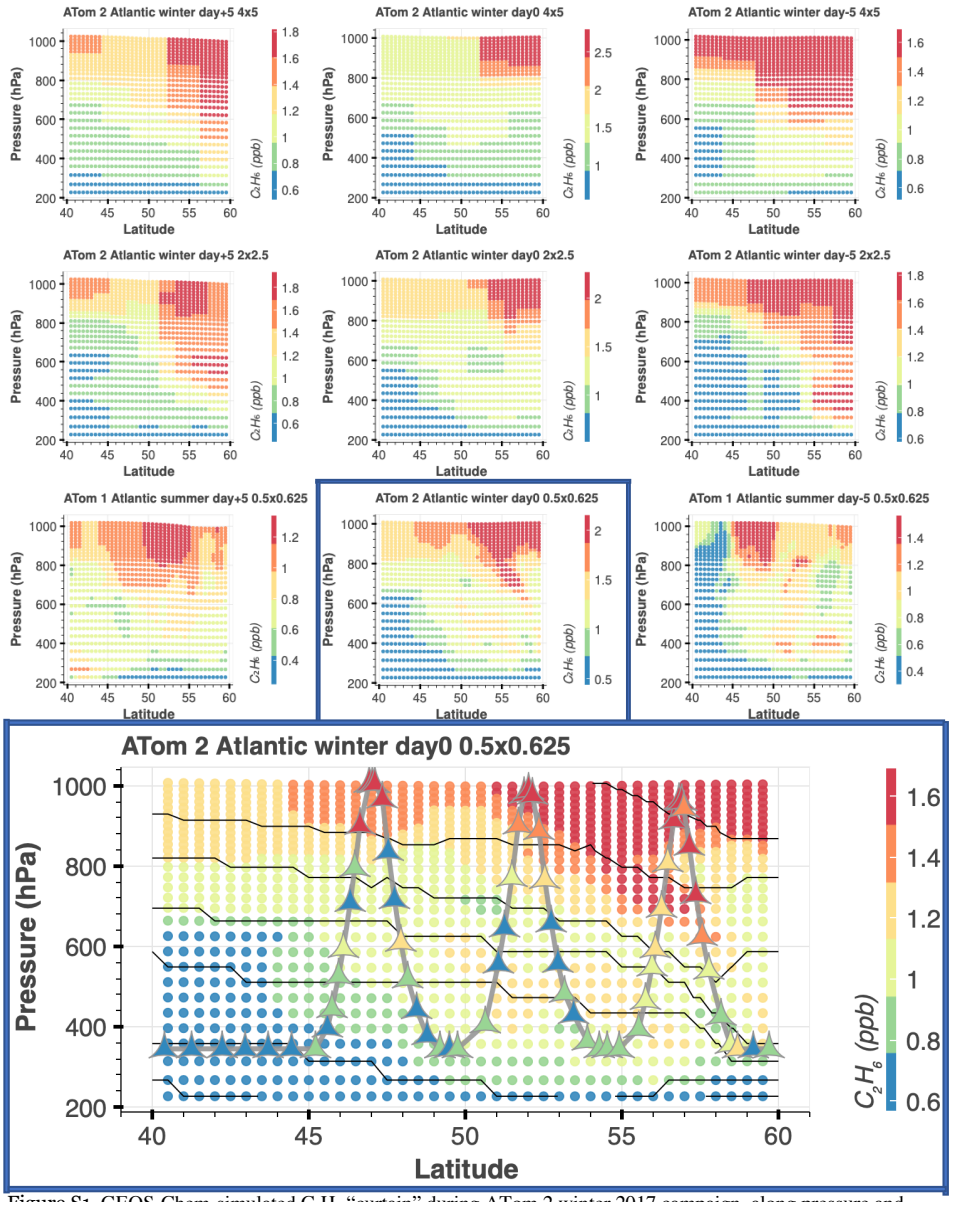

Figure A1. GEOS-Chem-simulated C_2H_6 "curtain" during ATom 2 winter 2017 campaign, along pressure and latitude. All GEOS-Chem simulations were sampled along aircraft latitude and a single median time/longitude during the flight over the Atlantic ocean. Column 1 shows simulations sampled 5 days after the median aircraft time; Column 2 shows simulations sampled on the median aircraft time; Column 3 shows simulations sampled 5 days before the median aircraft time. FIRST row: 4x5 resolution, interpolated to 0.5x0.625 grid using latitude and pressure coordinates. SECOND row: 2x2.5 resolution, interpolated to 0.5x0.625 grid using latitude and pressure coordinates. THIRD row: 0.5x0.625 resolution. FOURTH row: a more detailed

illustration of plot number r3,c2, with aircraft flight path shown in grey, the aircraft observations shown by triangle markers, and potential temperature contours shown in black. C_3H_8 is included in the main body.

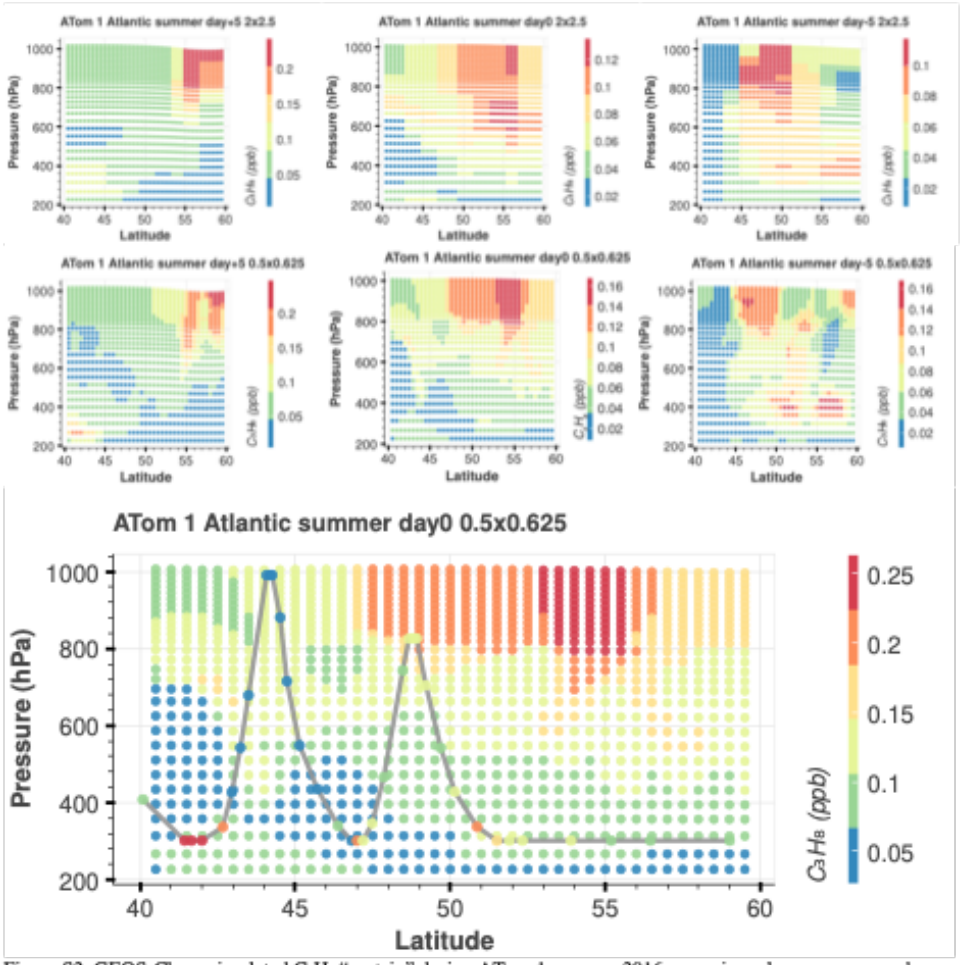

Figure A2. GEOS-Chem-simulated C_3H_8 "curtain" during ATom 1 summer 2016 campaign, along pressure and latitude. All GEOS-Chem simulations were sampled along aircraft latitude and a single median time/longitude during the flight over the Atlantic ocean. Column 1 shows simulations sampled 5 days after the median aircraft time; Column 2 shows simulations sampled on the median aircraft time; Column 3 shows simulations sampled 5 days before the median aircraft time. FIRST row: 4x5 resolution, interpolated to 0.5x0.625 grid using latitude and pressure coordinates. SECOND row: 2x2.5 resolution, interpolated to 0.5x0.625 grid using latitude and pressure coordinates. THIRD row: 0.5x0.625 resolution. FOURTH row: a more detailed illustration of plot number r3,c2, with aircraft flight path shown in grey, the aircraft observations shown by triangle markers, and potential temperature contours shown in black.

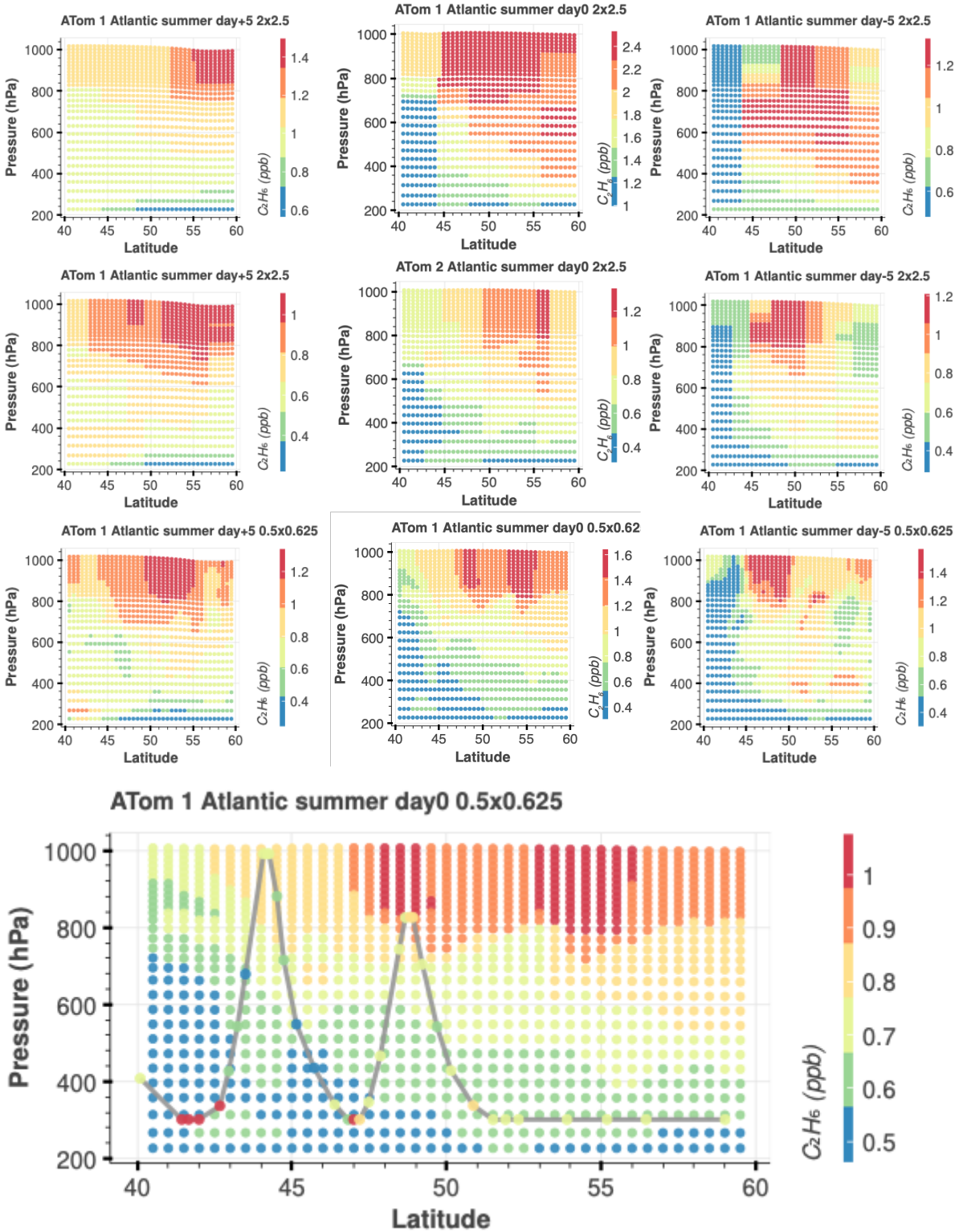

Figure A3. GEOS-Chem-simulated C_2H_6 "curtain" during ATom 1 summer 2016 campaign, along pressure and latitude. All GEOS-Chem simulations were sampled along aircraft latitude and a single median time/longitude during the flight over the Atlantic ocean. Column 1 shows simulations sampled 5 days after the median aircraft time; Column 2 shows simulations sampled on the median aircraft time; Column 3 shows simulations sampled 5 days before the median

aircraft time. FIRST row: 4x5 resolution, interpolated to 0.5x0.625 grid using latitude and pressure coordinates. SECOND row: 2x2.5 resolution, interpolated to 0.5x0.625 grid using latitude and pressure coordinates. THIRD row: 0.5x0.625 resolution. FOURTH row: a more detailed illustration of plot number r3,c2, with aircraft flight path shown in grey, the aircraft observations shown by triangle markers, and potential temperature contours shown in black.

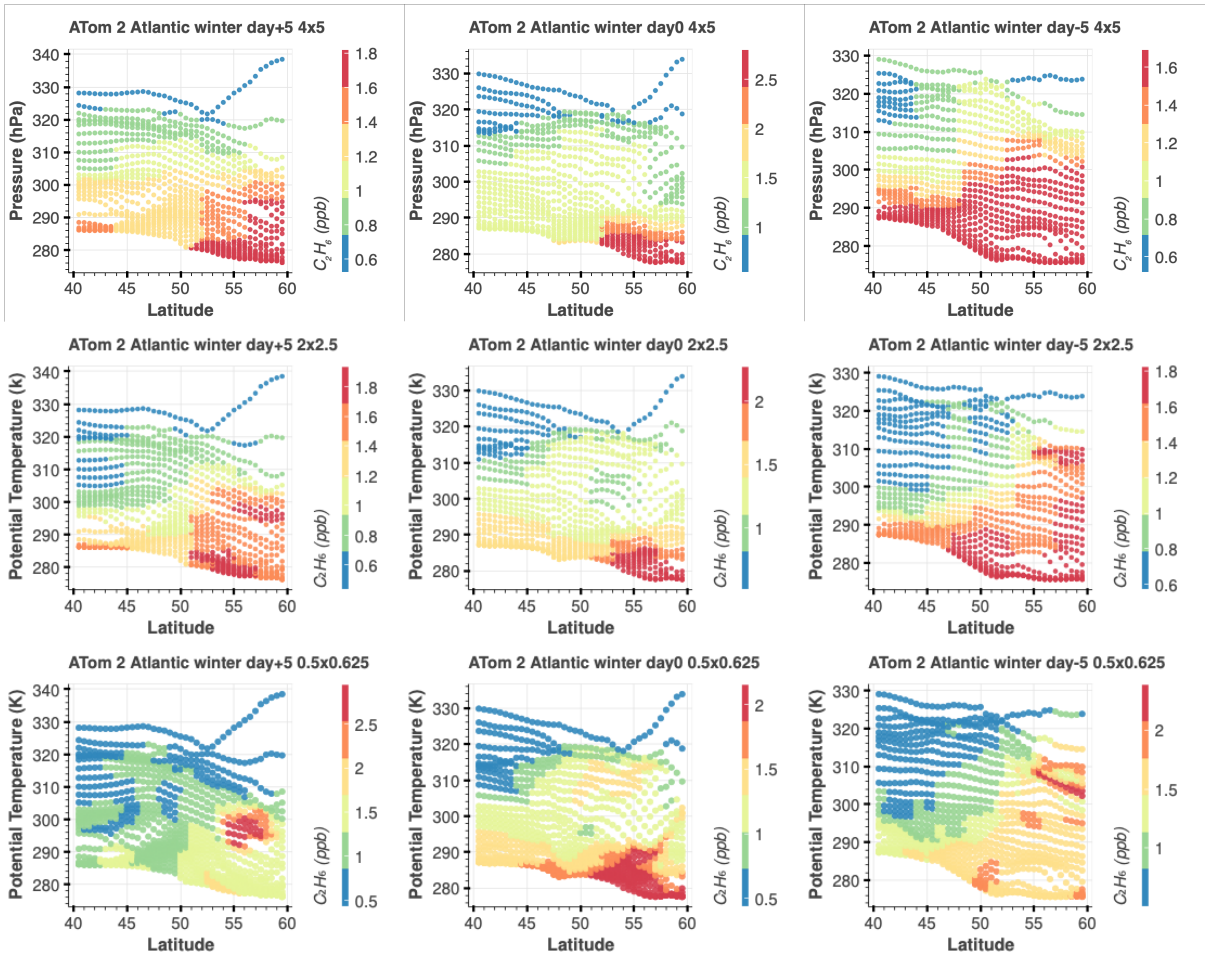

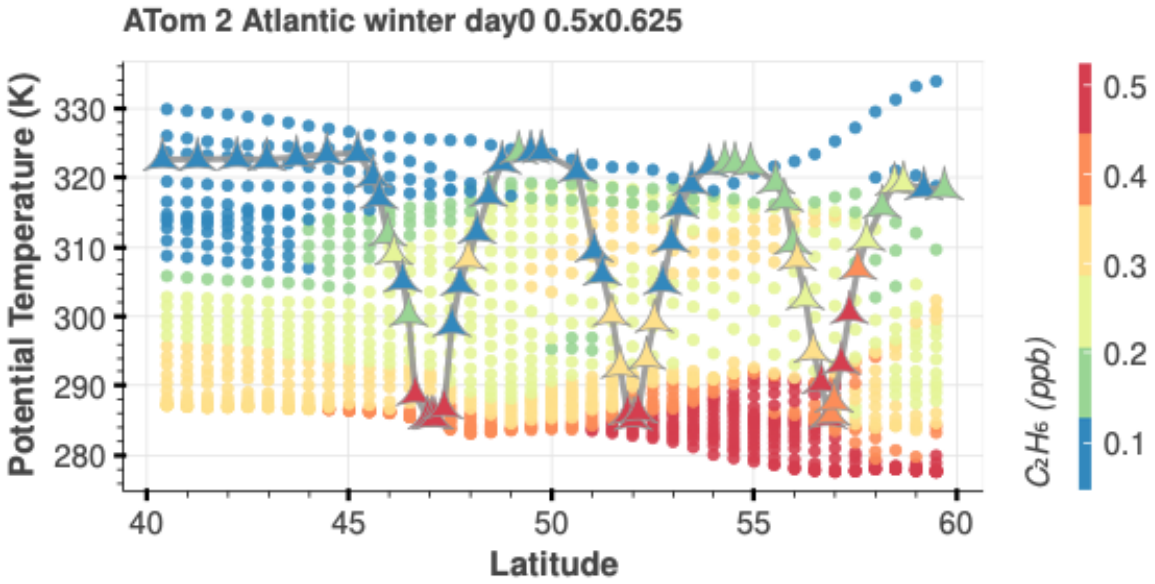

Figure A4. GEOS-Chem-simulated C_2H_6 "curtain" during ATom 2 winter 2017 campaign, along potential temperature and latitude. All GEOS-Chem simulations were sampled along aircraft latitude and a single median time/longitude during the flight over the Atlantic ocean. Column 1 shows simulations sampled 5 days after the median aircraft time; Column 2 shows simulations sampled on the median aircraft time; Column 3 shows simulations sampled 5 days before the median aircraft time. FIRST row: 4x5 resolution. SECOND row: 2x2.5 resolution. THIRD row: 0.5x0.625 resolution. FOURTH row: a more detailed illustration of plot number r3,c2, with aircraft flight path shown in grey, the aircraft observations shown by triangle markers, and potential temperature contours shown in black. C_3H_8 is included in the main body.

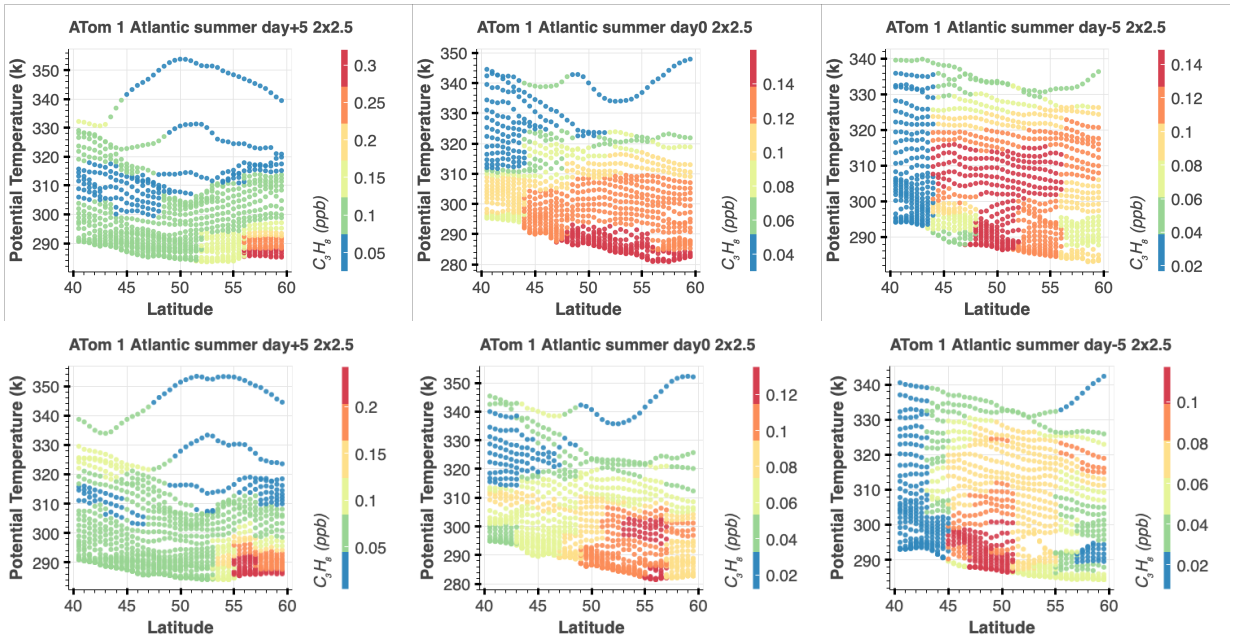

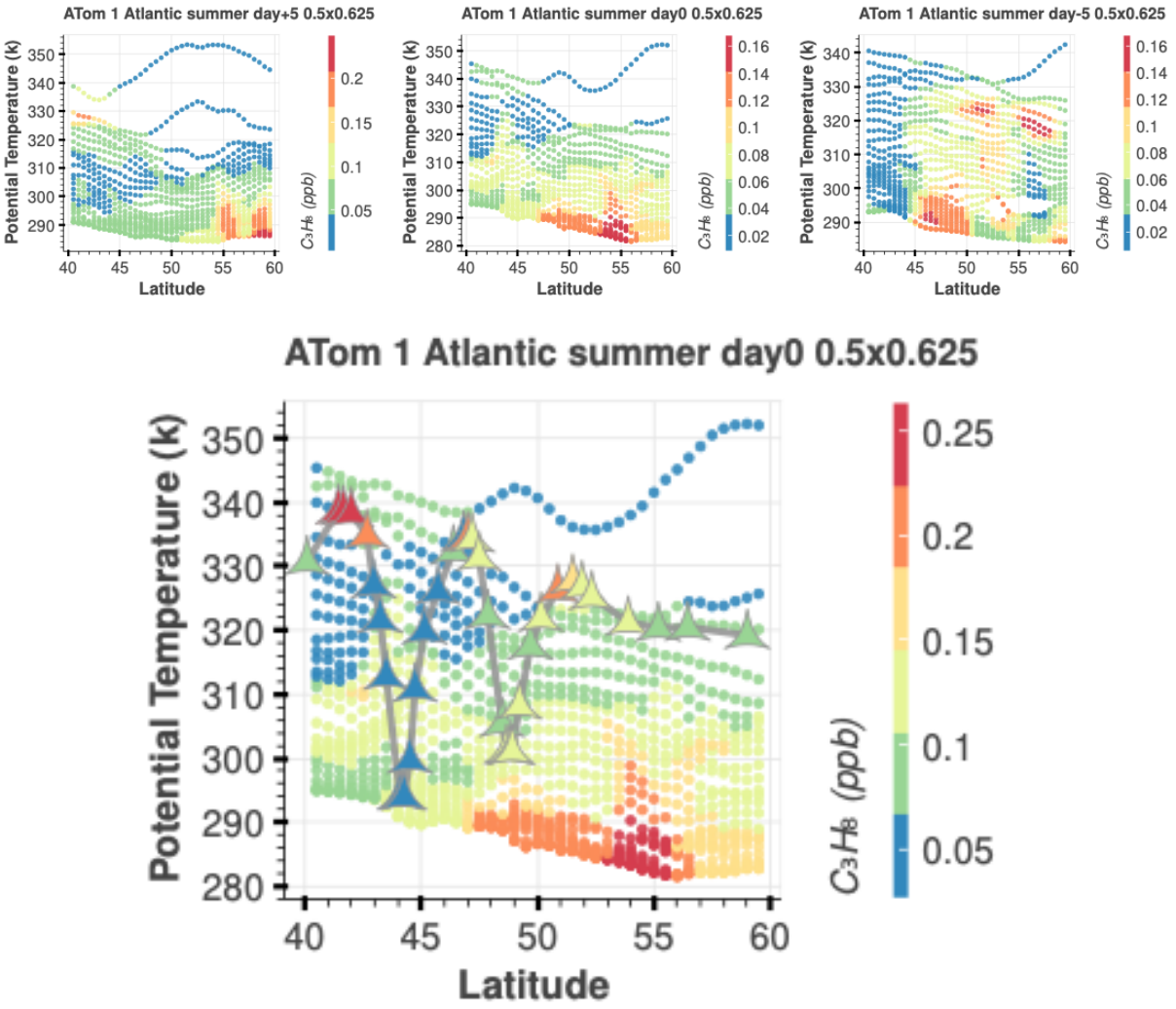

Figure A5. GEOS-Chem-simulated C_3H_8 "curtain" during ATom 1 summer 2016 campaign, along potential temperature and latitude. All GEOS-Chem simulations were sampled along aircraft latitude and a single median time/longitude during the flight over the Atlantic ocean. Column 1 shows simulations sampled 5 days after the median aircraft time; Column 2 shows simulations sampled on the median aircraft time; Column 3 shows simulations sampled 5 days before the median aircraft time. FIRST row: 4x5 resolution. SECOND row: 2x2.5 resolution. THIRD row: 0.5x0.625 resolution. FOURTH row: a more detailed illustration of plot number r3,c2, with aircraft flight path shown in grey, the aircraft observations shown by triangle markers, and potential temperature contours shown in black.

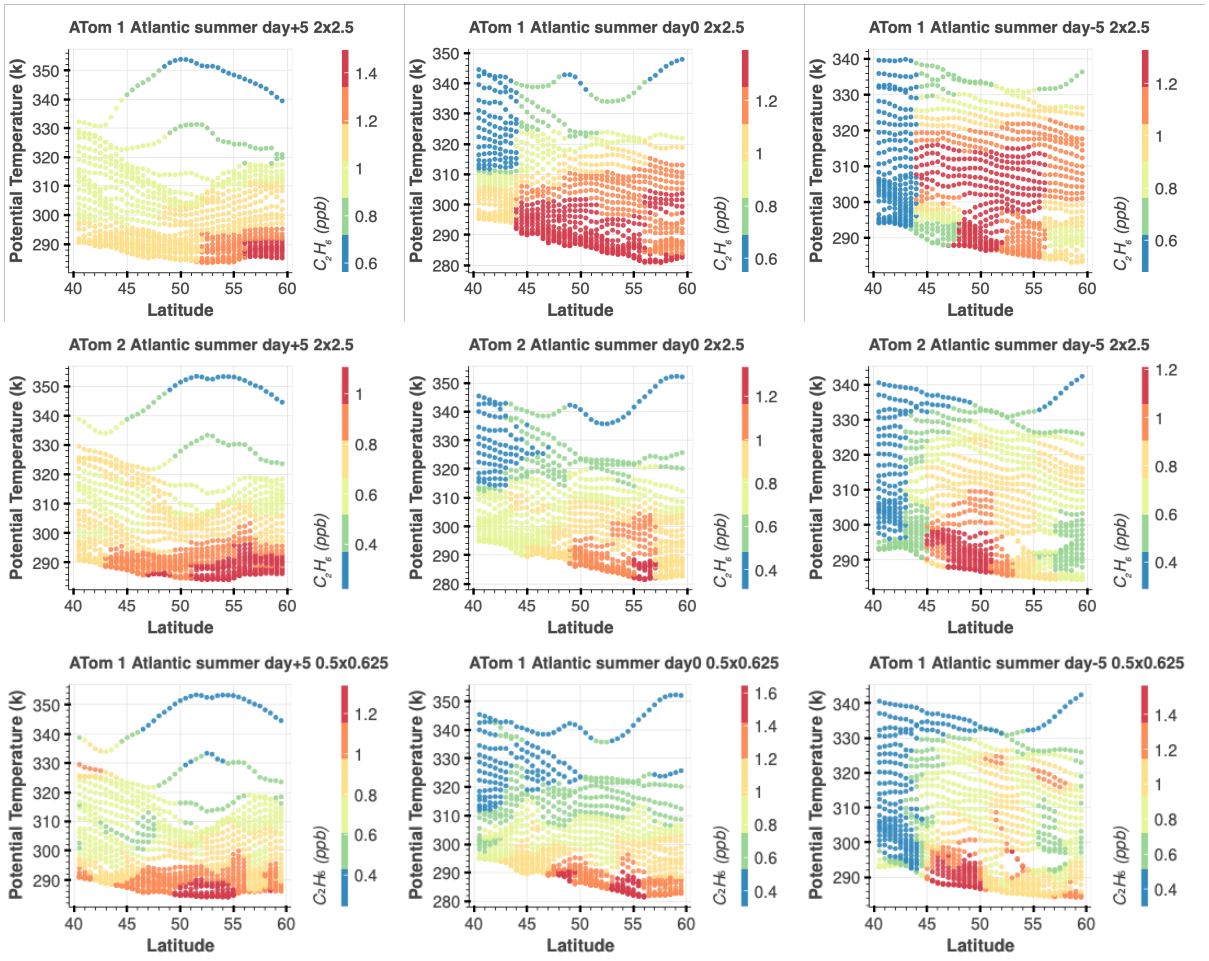
ATom 1 Atlantic summer day+5 2x2.5
ATom 1 Atlantic summer day0 2x2.5
ATom 1 Atlantic summer day-5 2x2.5
ATom 2 Atlantic summer day+5 2x2.5
ATom 2 Atlantic summer day0 2x2.5
ATom 2 Atlantic summer day-5 2x2.5
ATom 1 Atlantic summer day+5 0.5x0.625
ATom 1 Atlantic summer day0 0.5x0.625
ATom 1 Atlantic summer day-5 0.5x0.625
Potential Temperature (k)
Latitude
C2H6 (ppb)

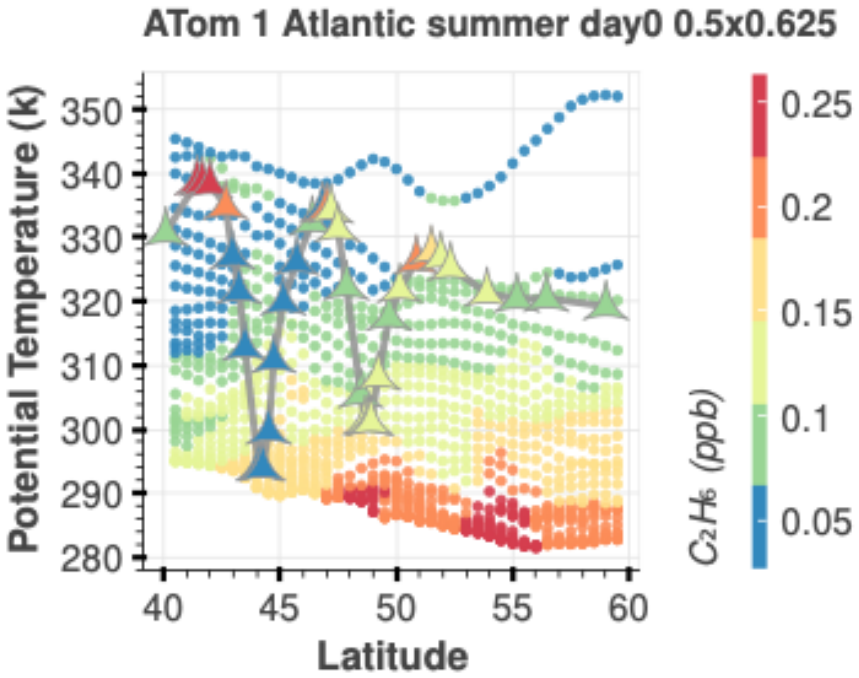
ATom 1 Atlantic summer day0 0.5x0.625
Potential Temperature (k)
Latitude
C2H6 (ppb)
0.25
0.2
0.15
0.1
0.05

Figure A6. GEOS-Chem-simulated C_2H_6 "curtain" during ATom 1 summer 2016 campaign, along potential temperature and latitude. All GEOS-Chem simulations were sampled along aircraft latitude and a single median time/longitude during the flight over the Atlantic ocean. Column 1 shows simulations sampled 5 days after the median aircraft time; Column 2 shows simulations sampled on the median aircraft time; Column 3 shows simulations sampled 5 days before the median aircraft time. FIRST row: 4x5 resolution. SECOND row: 2x2.5 resolution. THIRD row: 0.5x0.625 resolution. FOURTH row: a more detailed illustration of plot number r3,c2, with aircraft flight path shown in grey, the aircraft observations shown by triangle markers, and potential temperature contours shown in black.

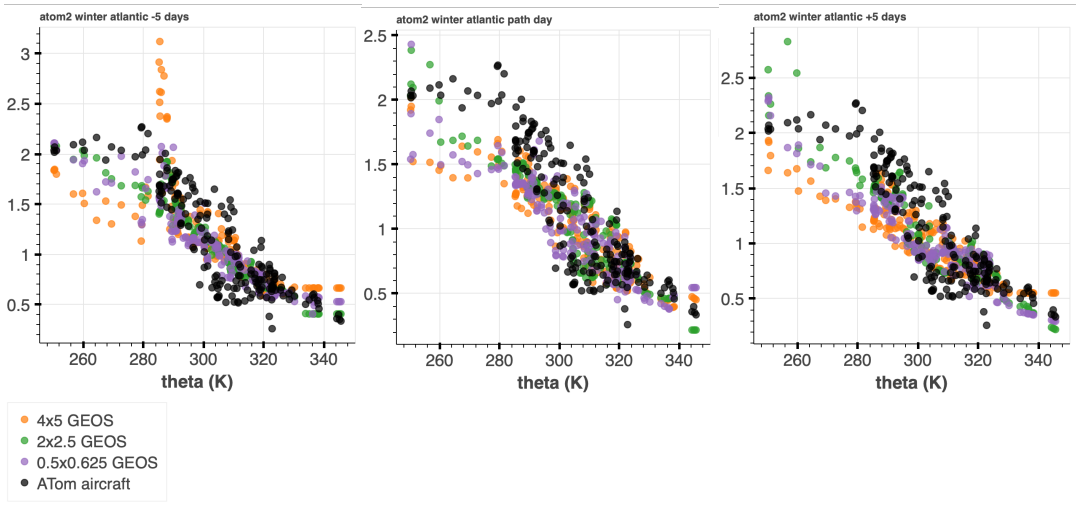

Figure A7. GEOS-Chem simulations and ATom aircraft C_2H_6 vs potential temperature. **Left**: Includes aircraft observations and simulations sampled 5 days after the aircraft flight path. **Middle**: Includes aircraft observations and simulations sampled during the aircraft flight path. **Right**: Includes aircraft observations and simulations 5 days before the aircraft flight path. C_3H_8 included in the main body.

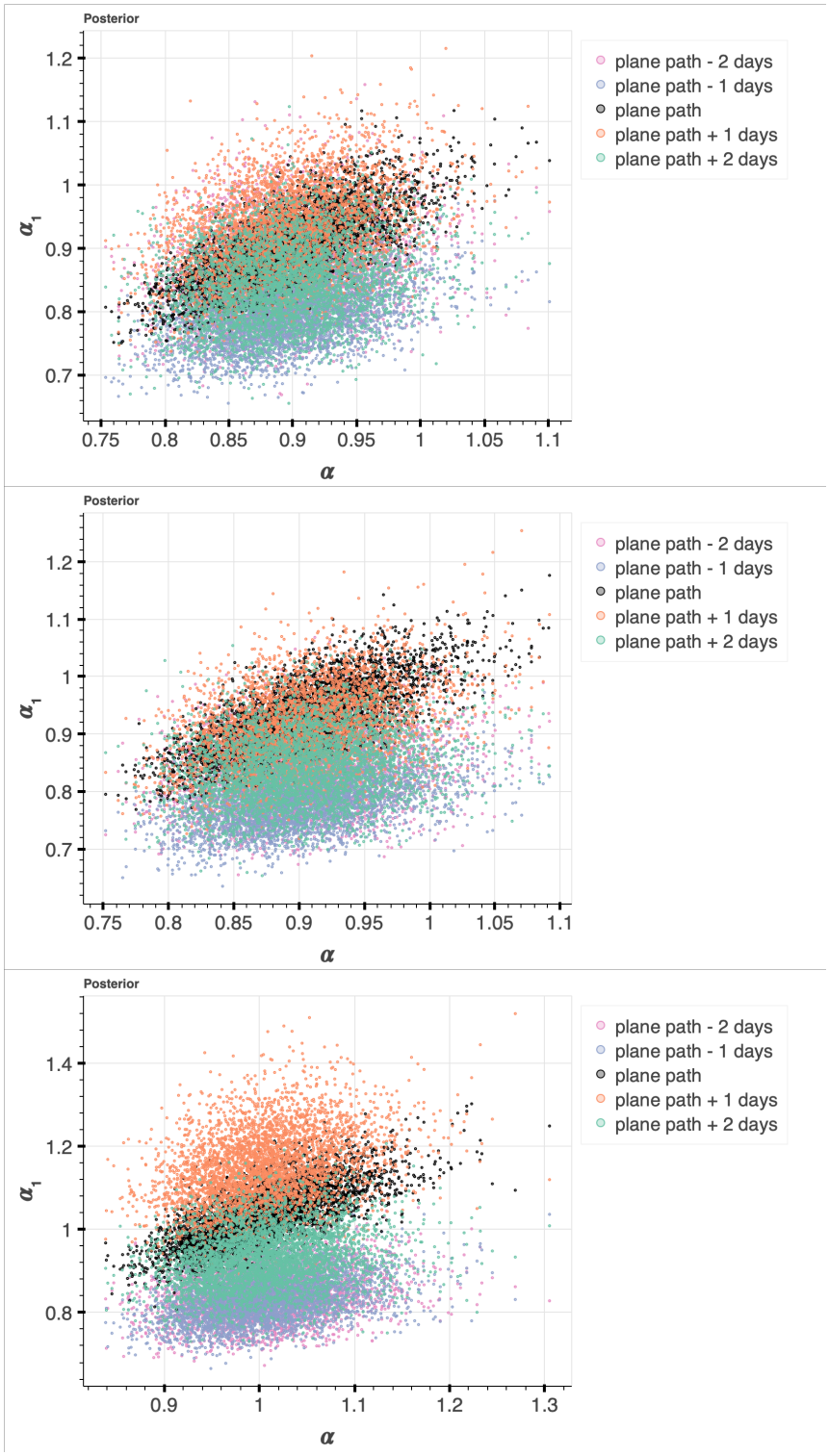

Figure A8. C_3H_8 posterior samples for the conditional parameter and the hyperparameter during ATom 2 winter 2017. **Top**: 4x5. Middle: 2x2.5. **Bottom**: 0.5x0.625.

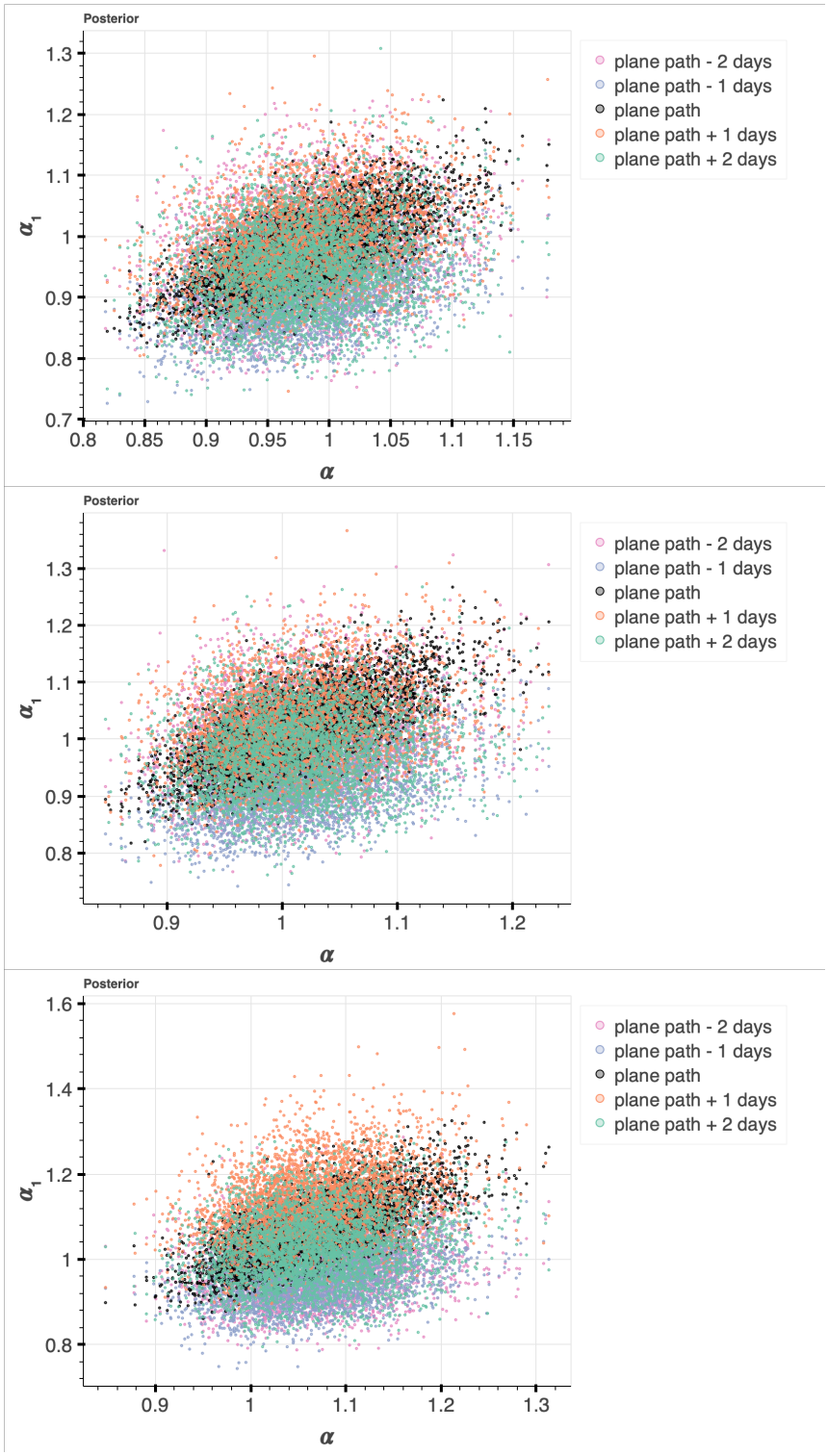

Figure A9. C_2H_6 posterior samples for the conditional parameter and the hyperparameter during ATom 2 winter 2017. **Top**: 4x5. **Middle**: 2x2.5. **Bottom**: 0.5x0.625.

As in Tribby et al. 2022, we conduct posterior predictive checks, which involve drawing parameter values out of the posterior, using those parameters in the likelihood to generate a pseudo dataset, and continue repeating. This allows us to see whether the Bayesian model reproduces the observed data. Below, we show all posterior predictive checks for ATom 2 atlantic aircraft campaign. The majority of the measured data fell into the 30th and 50th percentile of the simulated Bayesian model data.

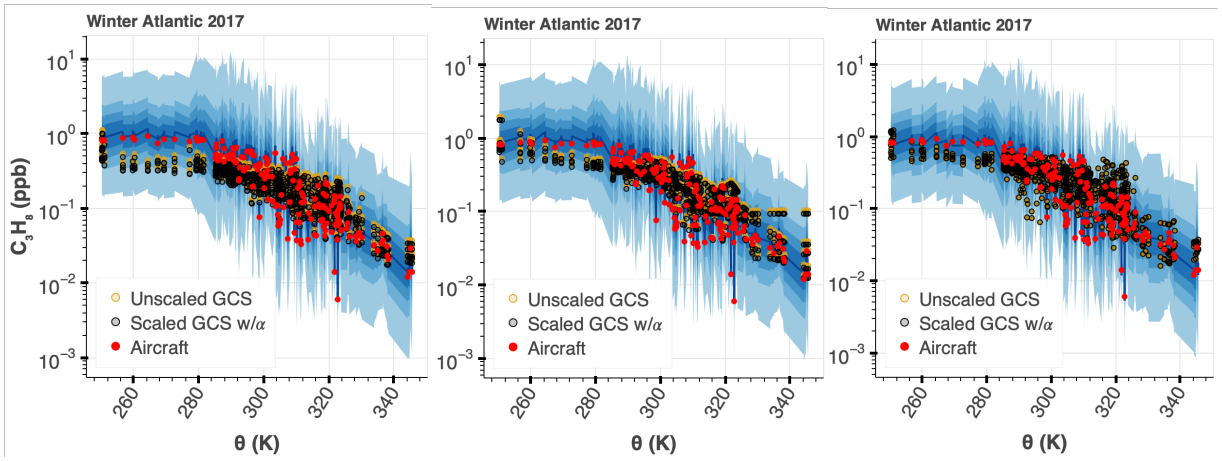

Figure A10. Posterior predictive check of C_3H_8 using ATom data. **Left**: 4x5. **Middle**: 2x2.5. **Right**: 0.5x0.625. Samples are during ATom 2 winter 2017. Pseudo data are shown in blue with 30, 50, 70, 99th percentiles. Please see Table 1 for values used to scale GCS data.

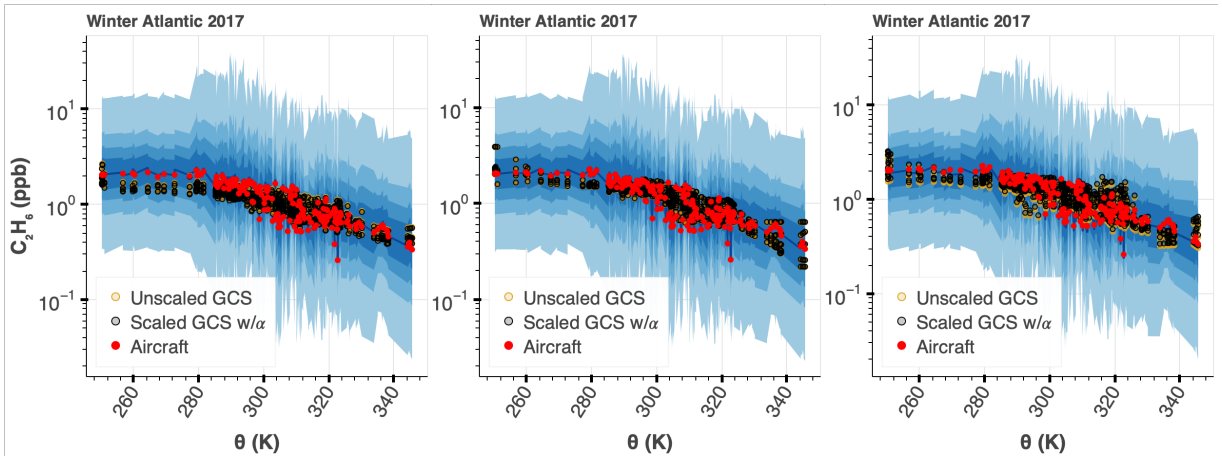

Figure A11. Posterior predictive check of C_2H_6 using ATom data. **Left**: 4x5. **Middle**: 2x2.5. **Right**: 0.5x0.625. Samples are during ATom 2 winter 2017. Pseudo data are shown in blue with 30, 50, 70, 99th percentiles. Please see Table 1 for values used to scale GCS data.

Table A1. Bayesian inference 97.5% confidence interval.

	α C_3H_8	α C_2H_6
4 x 5	[0.803 0.995]	[0.878 1.094]
2 x 2.5	[0.809 1.012]	[0.909 1.141]
0.5 x 0.625	[0.900 1.134]	[0.952 1.204]

Appendix B

Supplementary Information for "Towards Constraining Methane Emissions in Southern Oklahoma Using STILT Analysis of Remote Sensing and Flask Observations of Hydrocarbon Tracers"

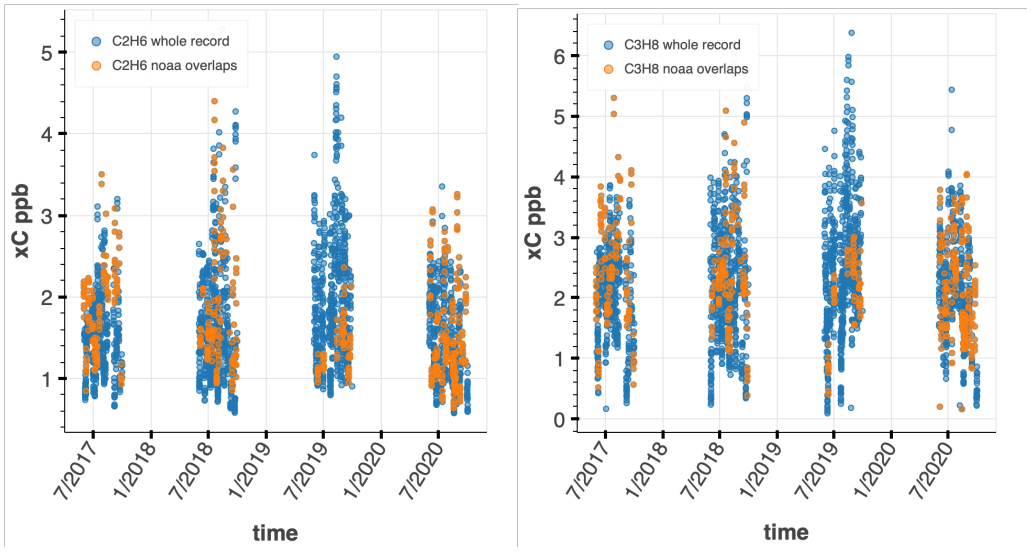

Figure B1. Temporal intersection between NOAA flask (aircraft + tower) and TCCON observations.

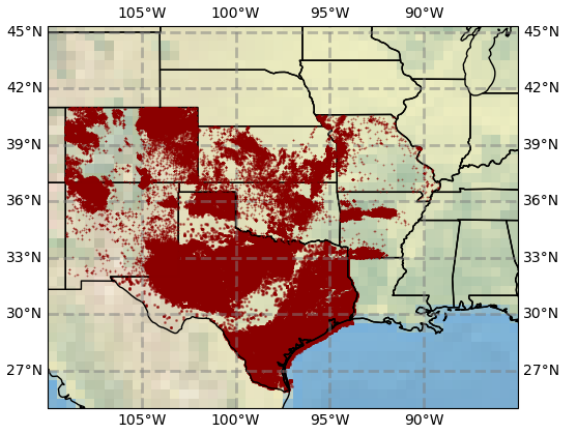

Figure B2. Oil and gas well geospatial data from FrackTracker.org.

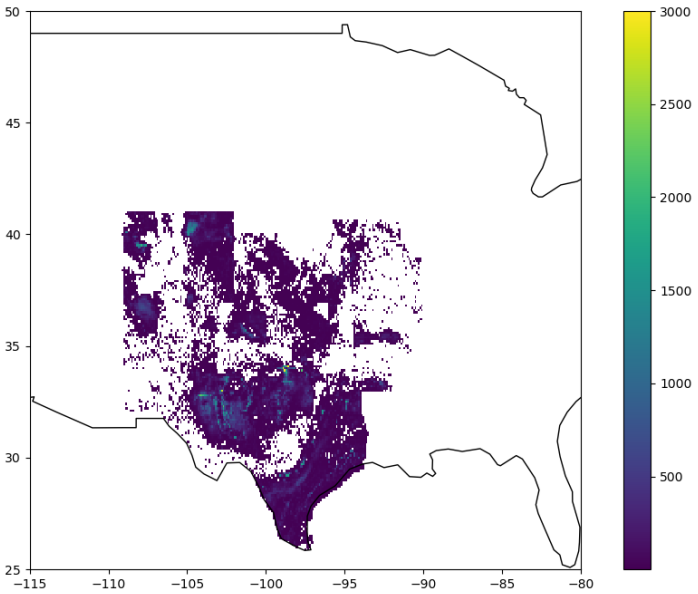

Figure B3. Density of oil and gas wells per .1x.1 degree grid.

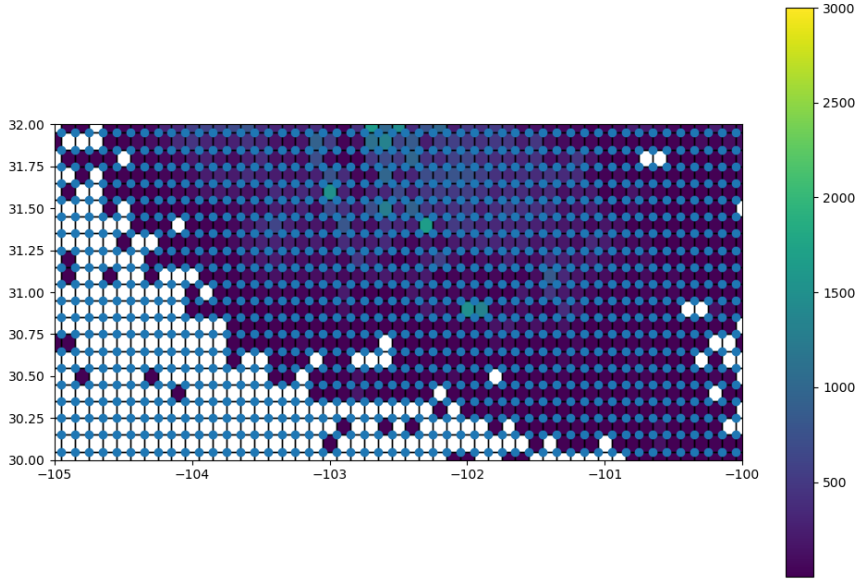

Figure B4. Well density (zoom in). The blue circles are the footprint lat/lon, and the squares are the 0.1x0.1 degree bins in which the density was calculated. The colorbar is in units of wells/cell.

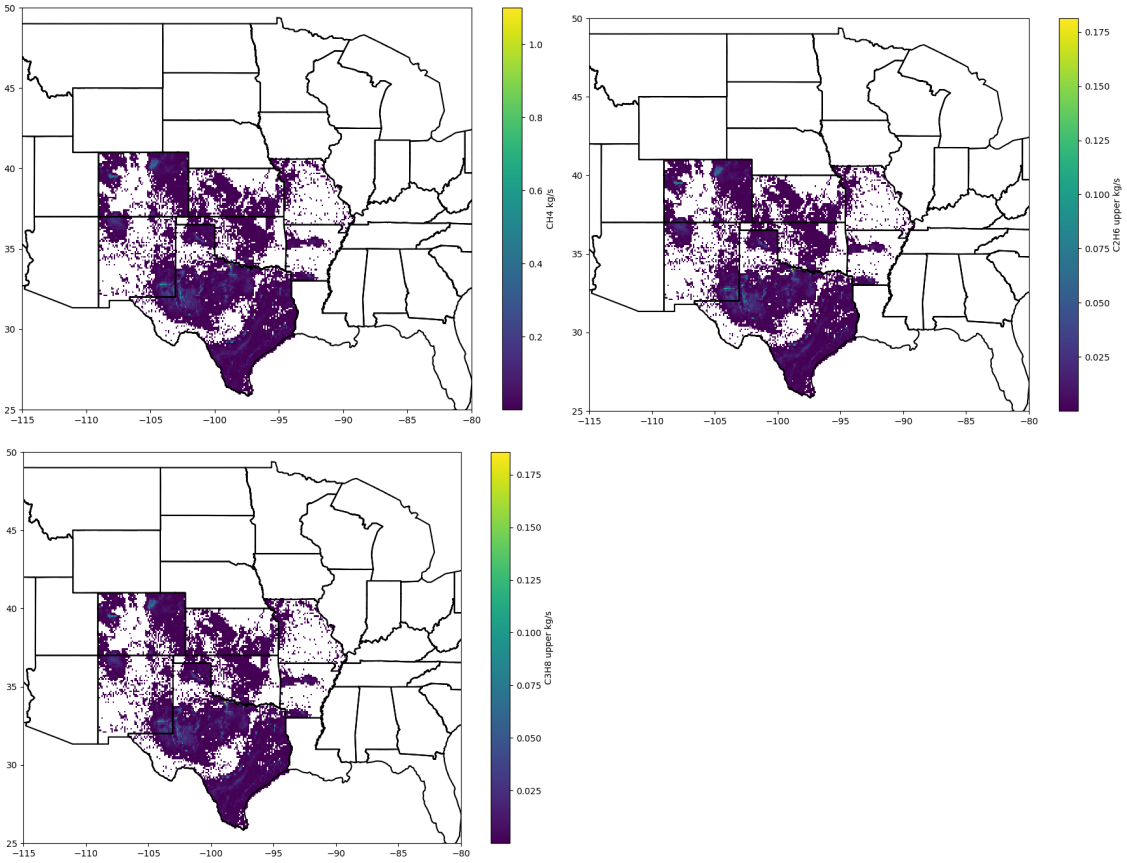

Figure B5. Emissions of methane, ethane, and propane used as a prior for the STILT analysis. These emissions were computed as described in the main text.

Emissions comparison to Alvarez et al. 2018 and Zhang et al. 2020

Our total emissions over the footprint area for CH_4, in units of Tg/yr, are 7.63 +/- 1.4. We calcula ted the uncertainty by scaling the 0.5Tg/yr uncertainty from Zhang et al. 2020 to our density calc ulation. In comparison, We sum several southwestern basin estimates from Alvarez et al. 2018 wi th the Permian 2.7 Tg (from Zhang et al. 2020) to obtain 5.5 Tg/yr. This sum is missing several k ey basins that would affect our receptor site, including Anadarko (northern Oklahoma), Ardmore (southern Oklahoma), Gulf Coast (of Texas), Cherokee Platform (central Oklahoma).

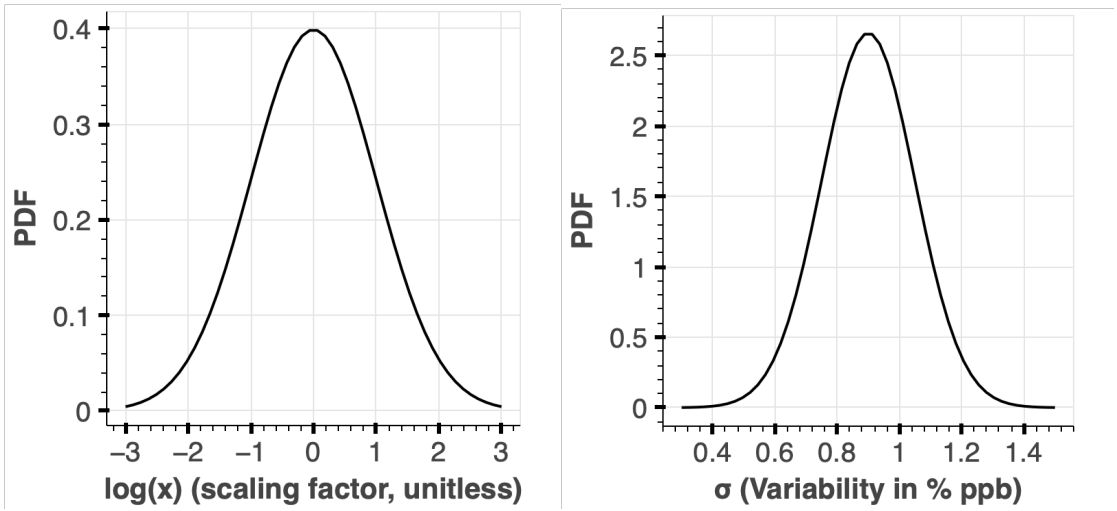

Figure B6. Priors for key parameters in our Bayesian analysis. Our methodology for choosing these priors is explained in the main text.